이학박사 학위논문

Unveiling Intrinsic Properties of Dusty Red AGNs

붉은 활동성 은하핵의 특성연구

2018년 2월

서울대학교 대학원
물리·천문학부 천문학 전공
김도형

Unveiling Intrinsic Properties of Dusty Red AGNs

by

Dohyeong Kim
(dohyeong@astro.snu.ac.kr)

A dissertation submitted in partial fulfillment of the requirements for the degree of

Doctor of Philosophy

in

Astronomy

in

Astronomy Program
Department of Physics and Astronomy
Seoul National University

Committee:

Professor	Hyung Mok Lee
Professor	Myungshin Im
Professor	Myung Gyoon Lee
Professor	Jong-Hak Woo
Doctor	Minjin Kim

ABSTRACT

Theoretical models suggest that dust-obscured active galactic nuclei (AGNs) appear for a certain period when merger-driven star forming galaxies evolve to galaxies harboring unobscured type 1 AGNs. These dust-obscured AGNs would look red due to the dust extinction, but observational properties of such an AGN population have not been studied extensively so far, leaving a hole in the understanding of the AGN evolution scheme. The most important expected property of the intermediate-stage, dusty AGNs is that they have higher accretion rates than unobscured type 1 AGNs, and this needs to be tested observationally. Red AGNs have been sampled in different ways in the hope of identifying the intermediate-stage dusty AGNs, but it is not yet clear if they really correspond to the dusty AGNs as suggested in the models.

In this thesis, we study the near-infrared (NIR) and mid-infrared (MIR) spectra of unobscured type 1 AGNs and red AGNs that are selected in various ways. There are three main themes: (i) derivation of black hole (BH) mass estimators and line diagnostics that can be used for red AGN study; (ii) investigation of red AGN selection methods to test its usefulness to identify dusty AGNs; and (iii) investigation of the accretion rates of red, dusty AGNs to see if they have properties consistent with the intermediate-stage, dusty AGNs as predicted in the models.

First, we derive methods to measure the BH masses of red AGNs using NIR and MIR hydrogen lines that are not strongly affected by dust extinction. It is necessary to find such a method, since the dust-obscuration in red AGNs will make it challenging to use the BH estimators that are based on the optical/UV lines. This is done by investigating the *AKARI* MIR spectra of unobscured type 1 AGNs. We derive Brβ- and Brα-based BH estimators and find that BH masses can be estimated with an accuracy of 0.20–0.36 dex using these estimators. We also investigate the Balmer/Paschen/Brackett line luminosity ratios of unobscured type 1 AGNs and

find that these line ratios are consistent with the theoretically expected line ratios from `CLOUDY` code. Together with Paschen line-based $M_{\rm BH}$ estimators and these line diagnostics provide tools to understand properties of red AGNs. Moreover, we examine how the hot and warm dust components of the type 1 AGNs behave by adding *AKARI* and *WISE* MIR data points to the analysis. The measured temperatures of the hot and warm dust components are $\sim$1100 K and $\sim$220 K, respectively, and the hot dust temperatures are somewhat cooler than the value quoted in previous studies ($\sim$1500 K).

Second, we test how effective the NIR or optical-NIR color selections of red AGNs are in identifying dusty AGNs. In order to test it, their rest-frame optical to NIR spectroscopic properties are examined to see if a reliable estimation of the dust extinction is possible. More specifically, we tested two red AGN selection methods, one by using NIR color ($J-K>2$ mag) and another using optical-NIR color ($r'-K>4$ mag and $J-K>1.3$ mag) with FIRST radio detection criteria. For the red AGNs selected from the NIR color, we measure the $E(B-V)$ values in two ways by using line luminosity ratios and continuum slopes, finding that all of the $g'-K \lesssim 4$ NIR-selected red AGNs ($\sim$40% of the NIR-selected red AGNs) have no significant dust extinction ($E(B-V)\sim 0$). In contrast, for the red AGNs selected from the optical-NIR colors, their $E(B-V)$ values are $\sim$0.804 (from 0.275 to 3.050), and the line luminosity ratios, from Hβ to Pα line, are difficult to explain without dust obscuration.

Third, armed with the knowledges gained through the first and second themes, we apply several hydrogen NIR-based BH mass estimators to derive the BH masses and the bolometric luminosities of red AGNs. This is done by using red AGNs $z\sim 0.3$ and $z\sim 0.7$ selected from the optical-NIR color selection. We find that the measured Eddington ratios of red AGNs ($\sim$0.69) are higher than those of unobscured type 1 AGNs by a factor of $\sim$4, consistent with the expectation from some merger-

driven galaxy evolution models.

We derived the NIR-line based $M_{\rm BH}$ estimators and the line ratio diagnostics to study dust-obscuration and BH masses in red AGNs. With these tools, we find that radio and optical-NIR colors can effectively select dust-obscured AGNs. Finally, we show that the red AGNs selected this way have high accretion rates, and we suggest that they are the intermediate-stage, dusty AGNs in the merger-driven galaxy evolution models.

Keywords: galaxies: evolution – (galaxies:) quasars: emission lines – (galaxies:) quasars: general – (galaxies:) quasars: supermassive black holes – methods: observational – techniques: spectroscopic

Student Number: 2011-30126

Contents

List of Figures

List of Tables

Chapter 1

Introduction

1.1 Active Galactic Nuclei

Over the past several decades, energetic sources have been found at the centers of galaxies, and these sources are called active galactic nuclei (AGNs) or quasi-stellar objects (quasars). Through many observational studies, it has been shown that AGNs emit enormous amount (10^{43}-$10^{48}\,\mathrm{erg\,s^{-1}}$; e.g., Woo & Urry 2002) of non-thermal radiations from X-ray to radio, and have a variability in various wavelengths (e.g., Giveon et al. 1999). The variability is known to have a short time scale of hours or days, implying that the size of the energy source is sub-parsec scale. Moreover, several high ionized emissions are shown, such as [O II] λ3727, [Ne III] λ3869, [O III] λ5007, and [S II] $\lambda\lambda 6716, 6731$, and some AGNs are known to have radio jets.

From these observational results, the AGN radiations are thought to the energy powered by accreting material into supermassive black holes (SMBHs). Moreover, the SMBHs are considered to play an important role in regulating the star formation in their host galaxies, by the AGN activities. The regulated star formation makes the accreting material decrease, resulting in the decline of the AGN activities.

This process is called the AGN feedback mechanism, and SMBHs are consid-

ered to closely related to their host galaxies, as expected results of the feedback mechanism. For examples, masses of SMBHs have a tight correlation with their host galaxy properties, such as (i) luminosities (Magorrian et al. 1998; Bentz et al. 2009; Bennert et al. 2010; Greene et al. 2010; Jiang et al. 2011; Park et al. 2015), (ii) stellar velocity dispersions (Ferrarese & Merritt 2000; Gebhardt et al. 2000; Tremaine et al. 2002; Gültekin et al. 2009; Woo et al. 2010), and (iii) Sersic indices (Graham et al. 2001; Graham & Driver 2007). Although these observational results can be explained by the co-evolution between the SMBHs and their host galaxies, the detail process of the co-evolution has not been clearly revealed so far, leaving the understanding the co-evolution as a major challenge of modern astrophysics.

1.2 Type 1 & 2 AGNs and unification model

AGNs can be broadly classified into two kinds, type 1 and type 2 AGNs. Spectra of type 1 AGNs show broad (2000–5000 $\mathrm{km\,s^{-1}}$; sometimes up to 10,000 $\mathrm{km\,s^{-1}}$) permitted emission lines, narrow ($< 500\,\mathrm{km\,s^{-1}}$) permitted and forbidden emission lines, and strong Fe complex on the UV-optical continuum that can be characterized crudely as a single power-law. Moreover, soft and hard X-rays can be detected, and the NIR spectrum is dominated by a black body radiation with a temperature of $\sim$1500 K (e.g., Barvainis 1987).

However, spectra of type 2 AGNs are different from those of type 1 AGNs. The spectra of type 2 AGNs show narrow permitted and forbidden emission lines on host galaxy dominated continuum spectra. These characteristics are similar to those of star-forming galaxies, and the flux ratios of two pairs of strong emission lines (BPT diagram; Veilleux & Osterbrock 1987; Rola et al. 1997; Lamareille et al. 2004) are used to distinguish them.

There was an attempt to explain these two kinds of AGNs with a simple model that is the unification model (Urry & Padovani 1995; Figure 1). They believe that an

AGN is composed of SMBH, accretion disk, dust torus, broad line regions (BLRs), narrow line regions (NLRs), and jets. Moreover, the broad lines, narrow lines, continuum are believed to come from BLRs, NLRs, and accretion disk, respectively, and the type of AGNs is believed to depends on whether or not the photon from the central region is blocked by the dust torus. In more detail, type 1 and 2 AGNs are physically the same, but the SMBH, accretion disk, and BLRs are hidden by the dust torus in type 2 AGNs, resulting that only the narrow lines are observable.

This model is supported by spectra of some type 2 AGNs. The polarized spectra of type 2 AGNs shows broad emission lines and strong Fe complex as type 1 AGNs as a result of (e.g., Antonucci 1984; Miller et al. 1991; Tran et al. 1992; Young et al. 1996; Moran et al. 2000; Ramos Almeida et al. 2016). Moreover, broad lines are detected in NIR or MIR for type 2 AGNs (e.g., Veilleux et al. 1997; Onori et al. 2017). These results imply that type 1 and type 2 AGNs are intrinsically the same.

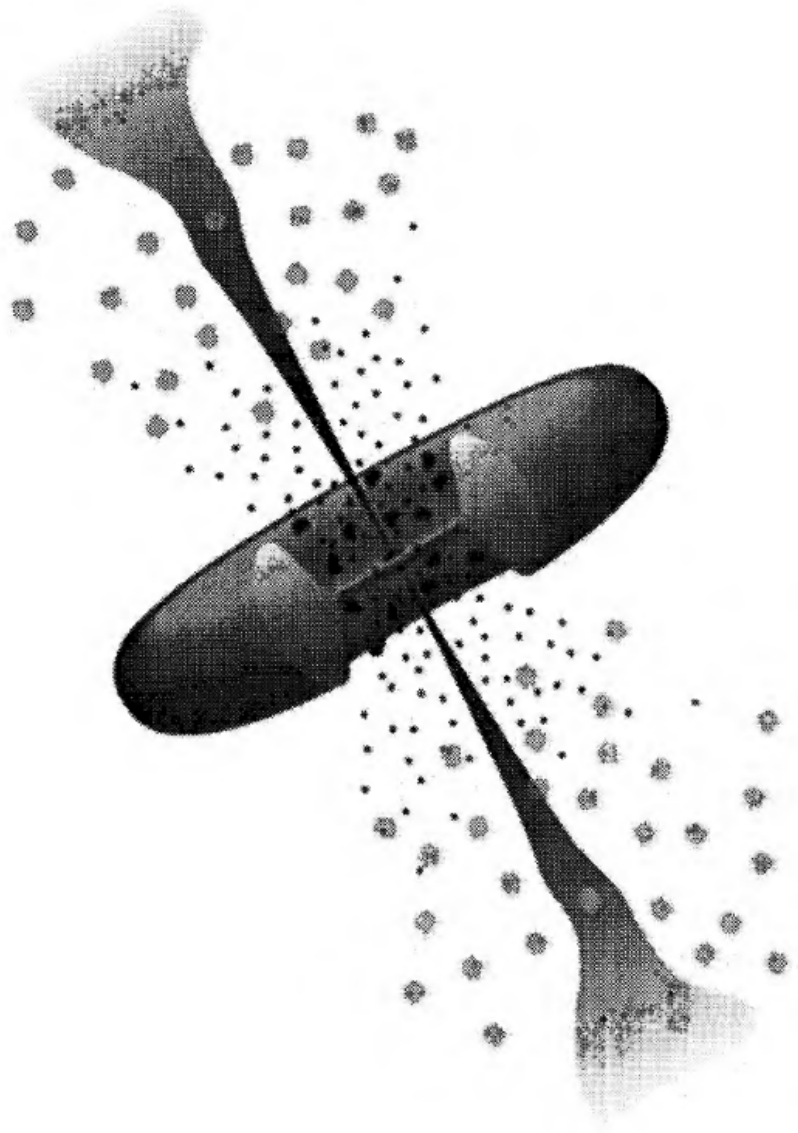

Figure 1.1 The unification schematic diagram for AGNs. The BLRs are orbiting around SMBH and accretion disk, and the NLRs are located at much farther from the SMBH than the BLRs. The dust torus obscures the SMBH, accretion disk, and BLRs, and the different types of AGNs are owing to the orientation angle with the dust torus. This figure is adopted from Urry & Padovani (1995).

Since type 1 AGNs offer direct views toward central engine, they are extremely luminous across a broad wavelength range from X-ray to radio, and their spectra are composed of strong broad emission lines and blue continuum due to the big blue bump peaks in the ultraviolet (UV; Malkan & Sargent 1982). Using these observational characteristics of type 1 AGNs, nearly a half million AGNs have been found to date by using surveys in X-ray, UV, optical, and radio wavelength (Grazian et al. 2000; Becker et al. 2001; Anderson et al. 2003; Croom et al. 2004; Risaliti & Elvis 2005; Schneider et al. 2005; Véron-Cetty & Véron 2006; Young et al. 2009; Pâris et al. 2014; Kim et al. 2015b). For this reason, most of our knowledge of AGNs come from the AGNs with the broad lines and blue continuum (hereafter, unobscured type 1 AGNs).

1.3 Intermediate-stage dusty AGNs

However, another missing type of AGNs has been proposed in several studies (Comastri et al. 2001; Tozzi et al. 2006; Polletta et al. 2008). In these studies, they expect that the missing AGNs are dust obscured and physically different from unobscured type 1 AGNs. Moreover, the dusty AGNs are expected to account for up to more than 50 % of whole AGN population.

Several simulations (Menci et al. 2004; Hopkins et al. 2005, 2006, 2008) expect the dusty AGNs as young AGNs. In these simulation, a major merger is considered to trigger massive star formation and buried BH activity, and which are ultra luminous infrared galaxies (ULIRGs; Sanders et al. 1988; Sanders & Mirabel 1996). After then, ULIRGs become unobscured type 1 AGNs after sweeping away gas and dust due to the BH activities. In this scenario, the dusty AGNs are expected to be intermediate galaxies between ULIRGs and unobscured type 1 AGNs as shown in Figure 2.

The intermediate stage is somewhat closed to the peak of the galaxy merging

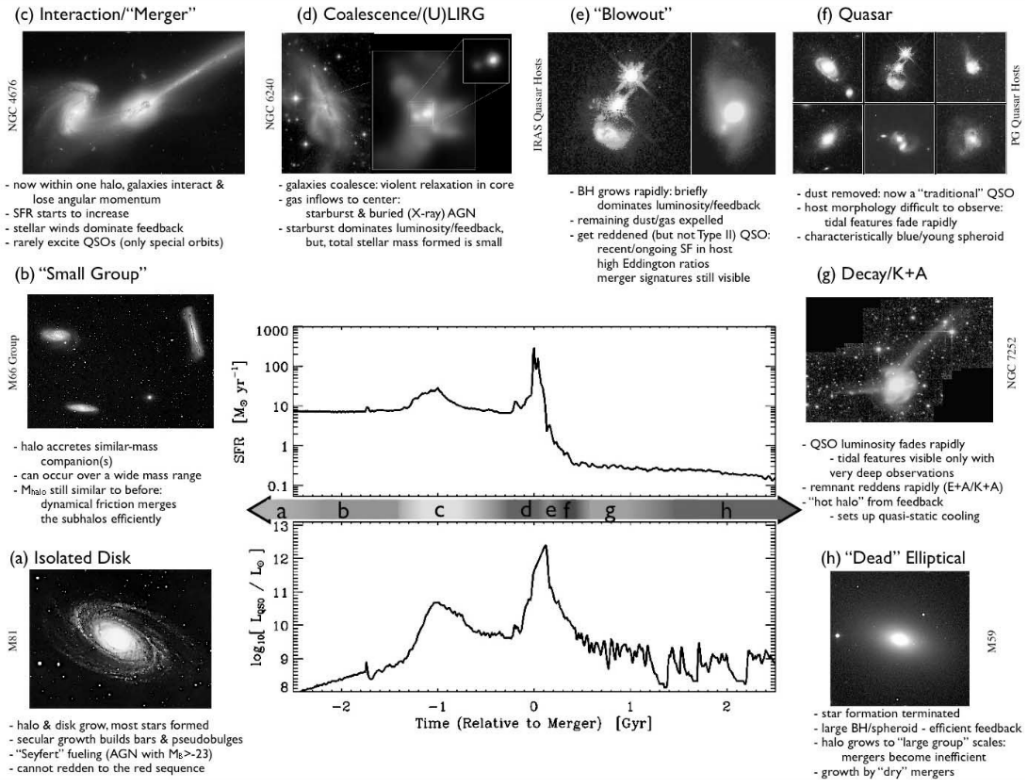

Figure 1.2 Schematic outline of the growth of a typical merger-driven galaxy. Red AGNs are expected to be in the intermediate stage between ULIRGs and unobscured type 1 AGNs, and correspond to the blowout phase in this figure. This figure is adopted from Hopkins et al. (2008).

activity, and it is expected to show recent or ongoing merging features with relatively strong star formation activities. Moreover, the nuclear regions are obscured by dust and gas in their host galaxies before sweeping away these intervening materials by the AGN activities. Due to this dust obscuration, it is difficult to observe the BH activities in UV or optical, but the intrinsic BH accretion rates are much higher than those of unobscured type 1 AGNs. The simulations expect that the life time of this intermediate stage is $\sim 10^8$ years that is considerable to that of AGN.

There have been several efforts to find the dusty AGNs. One way is to use X-ray surveys, because hard X-ray radiations are visible in the dust obscured system due to their high penetration ability. Even if, heavily obscured AGNs with column densities in excess of the Compton thick limit (Compton thick AGNs; $N_{\rm H} > 1.5 \times 10^{24}\,{\rm cm}^{-2}$) are able to be detected, and this Compton thick AGN population are known to reproduce the spectral shape of the cosmic X-ray background (Treister et al. 2009). Using this strength, there has been several Compton thick AGN surveys using X-ray surveys of XMM (Hasinger et al. 2007; Cappelluti et al 2009), *Chandra* (Elvis et al. 2009), and *Swift* (Baumgartner et al. 2013). However, the Compton thick AGNs include type 2 AGNs (e.g., Norman et al. 2002), and it is difficult to find Compton thick AGNs at low redshift (e.g., Georgantopoulos et al. 2009).

In addition to the Compton thick AGNs, there was another method that is using radio and hard X-ray both for identifying the dusty AGNs, since the low frequency radio can be visible in dusty systems. However, this is not efficient way due to the that only $\sim$10 % of AGNs are radio loud (Stern et al. 2000) and hard X-ray surveys have limited sensitivities.

1.4 Dusty red AGNs

The other attempt to find the dusty AGNs is to use the red colors due to the dust extinction, and such red, dusty AGNs (hereafter, red AGNs) are selected in several

ways. First, NIR color (e.g., $J-K>2$ mag in Cutri et al. 2001; $J-K>1.2$ mag in Francis et al. 2004) is used for selecting candidates, and ∼80 % (Cutri et al. 2001) of the candidates are confirmed as red AGNs using the follow up optical spectroscopic observations. Second, optical through NIR colors (e.g., $r'-K>5$ mag and $J-K>1.3$ mag in Urrutia et al. 2009; $g-r'>0.5$ mag in Young et al. 2008) are used to select candidates, and over 50 % (Urrutia et al. 2009) are classified as type 1 ($\mathrm{FWHM_{H\beta}} > 1000\,\mathrm{km\,s^{-1}}$) red AGNs by optical spectroscopic observations. Third, MIR color ($W1-W2>0.8$ mag in Stern et al. 2012) can be used, but only ∼15 % of the candidates are confirmed as type 1 red AGNs.

Overall, there have been quite a large numbers of surveys to find red AGNs using NIR or MIR surveys (Webster et al. 1995; Benn et al. 1998; Cutri et al. 2001; Francis et al. 2004; Glikman et al. 2007, 2012, 2013; Urrutia et al. 2009; Banerji et al. 2012; Stern et al. 2012; Assef et al. 2013; Fynbo et al. 2013; Lacy et al. 2013). In these red AGN surveys, the used NIR or MIR surveys are Two Micron All-Sky Survey (2MASS; Skrutskie et al. 2006), the UKIRT Infrared Deep Sky Survey (UKIDSS; Lawrence et al. 2007), the *Spitzer* Wide-area Infrared Extragalactic Survey (SWIRE; Lonsdale et al. 2003), or the *Wide field Infrared Survey Explorer* (*WISE*; Wright et al. 2010).

Most of these red AGNs are confirmed as type 1 AGNs, and type 2 AGNs are excluded. For these red AGNs, several observational studies support that red AGNs are the intermediate stage galaxies. For example, red AGNs have enhanced star formation activities (Georgakakis et al. 2009), a high fraction of merging features (Urrutia et al. 2008; Glikman et al. 2015), young radio jets (Georgakakis et al. 2012), and red continuum slopes possibly due to the dust extinction from their host galaxies (Glikman et al. 2007; Urrutia et al. 2009). These observational properties are consistent with the expected properties of the intermediate galaxies in the simulation studies, and imply that the redness of red AGNs come from the

dust extinction of the intervening gas and dust in their host galaxies (Webster et al. 1995; Cutri et al. 2002).

However, the origin of the redness of red AGNs is ongoing controversial issue yet. In contrast with the merger-driven galaxy evolution scenario, several studies have proposed different explanations for the redness. For example, the red colors could come from (i) a moderate viewing angle between type 1 and type 2 AGNs (Wilkes et al. 2002; Rose et al. 2013), (ii) an intrinsically red continuum (Puchnarewicz & Mason 1998; Whiting et al. 2001; Young et al. 2008; Ruiz et al. 2014), (iii) an unusual hot dust covering factor (Rose 2014), or (iv) a synchrotron emission peak at NIR wavelength (Whiting et al. 2011).

In addition to the alternative explains, Maddox & Hewett (2006) reported that some red AGNs (Cutri et al. 2001; Francis et al. 2004) may have the red colors contaminated from the host galaxy, since the red AGN surveys did not apply the minimum AGN absolute magnitude cut. Furthermore, the used NIR colors ($J-K >$ 2 mag in Cutri et al. 2001; $J - K > 1.2$ mag in Francis et al. 2004) are not enough to select red AGNs due to that some unobscured type 1 AGNs at low redshift could have such a NIR red color.

Moreover, the BH accretion rates of red AGNs are also one of controversial issues. In the simulations, the intermediate-stage galaxies are expected to have higher BH accretion rates than unobscured type 1 AGNs, but this quantities of red AGNs have not been revealed extensively. Because, the typical BH mass estimators were derived with flux and full width at half maximum (FWHM) measured in UV or optical (Kaspi et al. 2000; Vestergaard 2002; McLure & Dunlop 2004; Greene & Ho 2005), but these estimators are easily affected by the dust extinction, resulting that the BH accretion rates of red AGNs are an unveiled key property. For example, if the light is extincted as much as color excess of $E(B - V) = 2$ mag (typical color excess of red AGNs, e.g., Glikman et al. 2007; Urrutia et al. 2009), its Hβ and Hα

lines are suppressed by factors of 860 and 110, respectively (Galactic extinction law with R_V of 3.1; Cardelli et al. 1989).

1.5 NIR and MIR spectroscopy as a tool to study red AGNs

In order to alleviate the dust extinction effects, the NIR and MIR wavelength regions have become important windows for understanding red AGNs. The NIR and MIR wavelength regions include several hydrogen lines, such as Pβ (1.28 μm), Pα (1.88 μm), Brβ (2.63 μm), and Brα (4.05 μm) lines. The Paschen lines were used for deriving NIR BH mass estimators (Kim et al. 2010; Landt et al. 2011), and Figure 3 shows the Paschen line based BH mass estimators from Kim et al. (2010). The used Pβ and Pα line fluxes would be suppressed by a factors of 3.97 and 2.16, respectively, when the $E(B-V) = 2$ mag, and the flux declines are moderate.

Moreover, optical to NIR line analysis can be used to investigate the physical conditions of BLRs. Previous studies (e.g., Kim et al. 2010) showed that the line luminosity ratios of unobscured type 1 AGNs are well matched with theoretically computed line luminosity ratios with all possible physical conditions. The most successfully matched line luminosity ratio is reproduced with a set of physical parameters, $\alpha = -1$, $U = 10^{-1.5}$, and $n = 10^9\,\mathrm{cm}^{-3}$.

Furthermore, the NIR and MIR include several interesting features. For example, the NIR and MIR continua of AGNs are dominated by the radiations from the hot and warm dust components. The hot and warm dust components mean particular parts of the dust torus, and the hot dust temperature is $\sim 1500\,\mathrm{K}$ (Barvainis 1987). In addition to the continuum, the NIR and MIR spectra of AGNs show the polycyclic aromatic hydrocarbon (PAH) at 3.3 μm. The PAH line is a star formation tracer, and it has been suggested to have a correlation with the AGN activity.

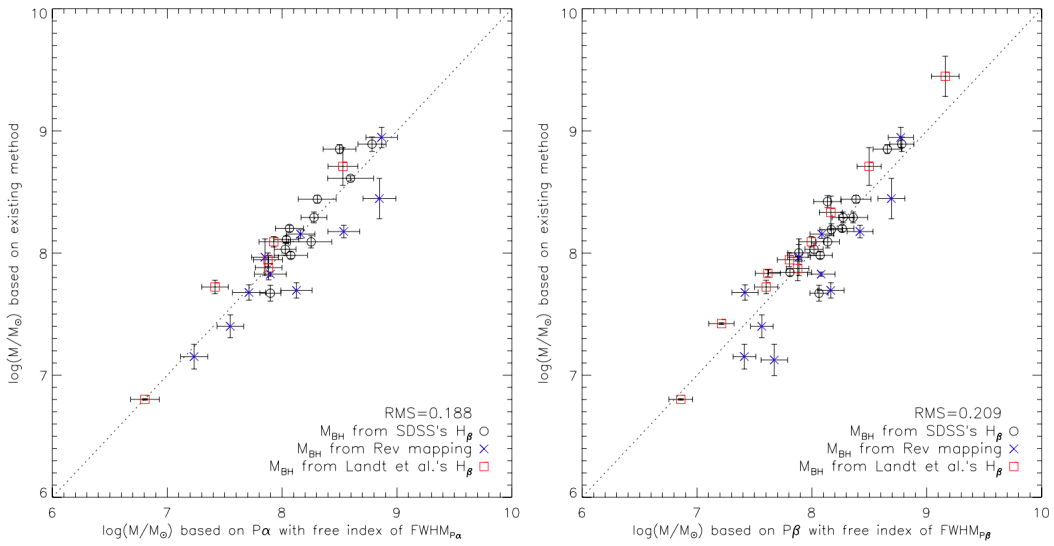

Figure 1.3 Comparison of the Paschen line based BH masses versus the BH masses from the reverberation mapping or Hβ line. Black circles and red squares represent the BH masses are derived from the Hβ line from SDSS and Landt et al. (2008) data, respectively. Blue crosses mean the BH masses are derived from the reverberation mapping (Vestergaard & Peterson 2006). This figure is adopted from Kim et al. (2010).

1.6 Thesis outline

As introduced above, in the merger-driven galaxy evolution scenario, ULIRGs are believed to unobscured type 1 AGNs, but the intermediate stage between ULIRGs and unobscured type 1 AGNs has not been investigated extensively. Red AGNs are suspected as the intermediate stage galaxies, and very important to understand this evolutionary scenario.

However, several key properties of red AGNs have not been revealed, such as the origin of the redness and the BH accretion rates. The redness of red AGNs are considered to come from the dust obscuration in their host galaxies, but there are other several alternative explanations for the redness. Furthermore, the BH accretion rates of red AGNs cannot be measured due to that previous BH mass estimators were derived based on UV/optical lines that can be easily affected by the dust extinction.

Chapter 2 provides new Brackett line-based BH mass estimators using the *AKARI* 2.5–5.0 μm spectra of 83 nearby unobscured type 1 AGNs. The derived BH mass estimators can be used for dusty AGNs. In Chapter 3, we present the investigation of red AGN selection methods to test its usefulness to identify dusty AGNs. For this investigations, high S/N and medium resolution optical and NIR spectra of 16 $J-K$ color-selected red AGNs are used. Chapter 4 introduces the investigation of the origin of the redness of red AGNs from the line ratio analysis, and the NIR spectra of 20 red AGNs at $z \sim 0.3$ and 0.7 are used. In Chapter 5, we compare the BH accretion rates of red AGNs to unobscured type 1 AGNs using 16 red AGNs at $z \sim 0.7$. In order to alleviate the dust extinction effects, the BH masses are measured by the Pβ line.

References

Anderson, S. F., Voges, W., Margon, B., et al. 2003, AJ, 126, 2209

Antonucci, R. R. J. 1984, ApJ, 278, 499

Assef, R. J., Stern, D., Kochanek, C. S., et al. 2013, ApJ, 772, 2

Banerji, M., McMahon, R. G., Hewett, P. C., et al. 2012, MNRAS, 427, 2275

Barvainis, R. 1987, ApJ, 320, 537

Baumgartner, W. H., Tueller, J., Markwardt, C. B., et al. 2013, ApJS, 207, 19

Becker, R. H., White, R. L., Gregg, M. D., et al. 2001, ApJS, 135, 227

Benn, C. R., Vigotti, M., Carballo, R., Gonzalez-Serrano, J. I., & Sánchez, S. F. 1998, MNRAS, 295, 451

Bennert, V. N., Treu, T., Woo, J.-H., et al. 2010, ApJ, 708, 1507

Bentz, M. C., Peterson, B. M., Pogge, R. W., & Vestergaard, M. 2009, ApJ, 694, L166

Cappelluti, N., Brusa, M., Hasinger, G., et al. 2009, A&A, 497, 635

Cardelli, J. A., Clayton, G. C., & Mathis, J. S. 1989, ApJ, 345, 245

Comastri, A., Fiore, F., Vignali, C., et al. 2001, MNRAS, 327, 781

Croom, S. M., Smith, R. J., Boyle, B. J., et al. 2004, MNRAS, 349, 1397

Cutri, R. M., Nelson, B. O., Kirkpatrick, J. D., Huchra, J. P., & Smith, P. S. 2001,

Elvis, M., Civano, F., Vignali, C., et al. 2009, ApJS, 184, 158

Ferrarese, L., & Merritt, D. 2000, ApJ, 539, L9

Francis, P. J., Nelson, B. O., & Cutri, R. M. 2004, AJ, 127, 646

Fynbo, J. P. U., Krogager, J.-K., Venemans, B., et al. 2013, ApJS, 204, 6

Gebhardt, K., Bender, R., Bower, G., et al. 2000, ApJ, 539, L13

Georgantopoulos, I., Akylas, A., Georgakakis, A., & Rowan-Robinson, M. 2009, A&A, 507, 747

Giveon, U., Maoz, D., Kaspi, S., Netzer, H., & Smith, P. S. 1999, MNRAS, 306, 637

Glikman, E., Helfand, D. J., White, R. L., et al. 2007, ApJ, 667, 673

Glikman, E., Urrutia, T., Lacy, M., et al. 2012, ApJ, 757, 51

Glikman, E., Urrutia, T., Lacy, M., et al. 2013, ApJ, 778, 127

Graham, A. W., Erwin, P., Caon, N., & Trujillo, I. 2001, ApJ, 563, L11

Graham, A. W., & Driver, S. P. 2007, ApJ, 655, 77

Grazian, A., Cristiani, S., D'Odorico, V., Omizzolo, A., & Pizzella, A. 2000, AJ, 119, 2540

Greene, J. E., & Ho, L. C. 2005, ApJ, 630, 122

Greene, J. E., Peng, C. Y., & Ludwig, R. R. 2010, ApJ, 709, 937

Gültekin, K., Richstone, D. O., Gebhardt, K., et al. 2009, ApJ, 698, 198

Hasinger, G., Cappelluti, N., Brunner, H., et al. 2007, ApJS, 172, 29

Hopkins, P. F., Hernquist, L., Cox, T. J., et al. 2005, ApJ, 630, 705

Hopkins, P. F., Hernquist, L., Cox, T. J., et al. 2006, ApJS, 163, 1

Hopkins, P. F., Hernquist, L., Cox, T. J., & Kereš, D. 2008, ApJS, 175, 356

Jiang, Y.-F., Greene, J. E., & Ho, L. C. 2011, ApJ, 737, L45

Kaspi, S., Smith, P. S., Netzer, H., et al. 2000, ApJ, 533, 631

Kim, D., Im, M., & Kim, M. 2010, ApJ, 724, 386

Kim, D., Im, M., Kim, J. H., et al. 2015, ApJS, 216, 17

Kim, Y., Im, M., Jeon, Y., et al. 2015, ApJ, 813, L35

Lacy, M., Ridgway, S. E., Gates, E. L., et al. 2013, ApJS, 208, 24

Lamareille, F., Mouhcine, M., Contini, T., Lewis, I., & Maddox, S. 2004, MNRAS, 350, 396

Landt, H., Bentz, M. C., Ward, M. J., et al. 2008, ApJS, 174, 282-312

Landt, H., Bentz, M. C., Peterson, B. M., et al. 2011, MNRAS, 413, L106

Lawrence, A., Warren, S. J., Almaini, O., et al. 2007, MNRAS, 379, 1599

Lonsdale, C. J., Smith, H. E., Rowan-Robinson, M., et al. 2003, PASP, 115, 897

Maddox, N., & Hewett, P. C. 2006, MNRAS, 367, 717

Magorrian, J., Tremaine, S., Richstone, D., et al. 1998, AJ, 115, 2285

Malkan, M. A., & Sargent, W. L. W. 1982, ApJ, 254, 22

McLure, R. J., & Dunlop, J. S. 2004, MNRAS, 352, 1390

Menci, N., Cavaliere, A., Fontana, A., et al. 2004, ApJ, 604, 12

Miller, J. S., Goodrich, R. W., & Mathews, W. G. 1991, ApJ, 378, 47

Moran, E. C., Barth, A. J., Kay, L. E., & Filippenko, A. V. 2000, ApJ, 540, L73

Norman, C., Hasinger, G., Giacconi, R., et al. 2002, ApJ, 571, 218

Onori, F., Ricci, F., La Franca, F., et al. 2017, MNRAS, 468, L97

Park, D., Woo, J.-H., Bennert, V. N., et al. 2015, ApJ, 799, 164

Pâris, I., Petitjean, P., Aubourg, É., et al. 2014, A&A, 563, A54

Polletta, M., Weedman, D., Hönig, S., et al. 2008, ApJ, 675, 960-984

Puchnarewicz, E. M., & Mason, K. O. 1998, MNRAS, 293, 243

Ramos Almeida, C., Martínez González, M. J., Asensio Ramos, A., et al. 2016, MNRAS, 461, 1387

Risaliti, G., & Elvis, M. 2005, ApJ, 629, L17

Rola, C. S., Terlevich, E., & Terlevich, R. J. 1997, MNRAS, 289, 419

Rose, M., Tadhunter, C. N., Holt, J., & Rodríguez Zaurín, J. 2013, MNRAS, 432, 2150

Rose, M. 2014, American Astronomical Society Meeting Abstracts #223, 223, #321.03

Ruiz, A., Della Ceca, R., Caccianiga, A., Severgnini, P., & Carrera, F. 2014, The X-ray Universe 2014, 314

Sanders, D. B., Soifer, B. T., Elias, J. H., et al. 1988, ApJ, 325, 74

Sanders, D. B., & Mirabel, I. F. 1996, ARA&A, 34, 749

Schneider, D. P., Hall, P. B., Richards, G. T., et al. 2005, AJ, 130, 367

Skrutskie, M. F., Cutri, R. M., Stiening, R., et al. 2006, AJ, 131, 1163

Stern, D., Djorgovski, S. G., Perley, R. A., de Carvalho, R. R., & Wall, J. V. 2000, AJ, 119, 1526

Stern, D., Assef, R. J., Benford, D. J., et al. 2012, ApJ, 753, 30

Tozzi, P., Gilli, R., Mainieri, V., et al. 2006, A&A, 451, 457

Tran, H. D., Miller, J. S., & Kay, L. E. 1992, ApJ, 397, 452

Treister, E., Cardamone, C. N., Schawinski, K., et al. 2009, ApJ, 706, 535

Tremaine, S., Gebhardt, K., Bender, R., et al. 2002, ApJ, 574, 740

Urrutia, T., Becker, R. H., White, R. L., et al. 2009, ApJ, 698, 1095

Urry, C. M., & Padovani, P. 1995, PASP, 107, 803

Veilleux, S., & Osterbrock, D. E. 1987, ApJS, 63, 295

Veilleux, S., Sanders, D. B., & Kim, D.-C. 1997, ApJ, 484, 92

Véron-Cetty, M.-P., & Véron, P. 2006, A&A, 455, 773

Vestergaard, M. 2002, ApJ, 571, 733

Vestergaard, M., & Peterson, B. M. 2006, ApJ, 641, 689

Webster, R. L., Francis, P. J., Petersont, B. A., Drinkwater, M. J., & Masci, F. J. 1995, Nature, 375, 469

Whiting, M. T., Webster, R. L., & Francis, P. J. 2001, MNRAS, 323, 718

Wilkes, B. J., Schmidt, G. D., Cutri, R. M., et al. 2002, ApJ, 564, L65

Woo, J.-H., & Urry, C. M. 2002, ApJ, 579, 530

Woo, J.-H., Treu, T., Barth, A. J., et al. 2010, ApJ, 716, 269

Wright, E. L., Eisenhardt, P. R. M., Mainzer, A. K., et al. 2010, AJ, 140, 1868

Young, S., Hough, J. H., Efstathiou, A., et al. 1996, MNRAS, 281, 1206

Young, M., Elvis, M., & Risaliti, G. 2008, ApJ, 688, 128-147

Young, M., Elvis, M., & Risaliti, G. 2009, ApJS, 183, 17

Chapter 2

The *AKARI* 2.5–5.0 Micron Spectral Atlas of Type-1 Active Galactic Nuclei: Black Hole Mass Estimator, Line Ratio, and Hot Dust Temperature

(This chapter has been published in The Astrophysical Journal Supplement Series[1])

2.1 INTRODUCTION

An active galactic nucleus (AGN) is a bright central part of a galaxy that shines via the energy released by materials that falls toward the super massive black hole (SMBH). During its active phase, the AGN luminosity can outshine that of the host

[1]Kim et al. 2015, ApJS, 216, 17

galaxy, emitting an enormous amount of energy (10^{43}–10^{48} erg s^{-1}; e.g., Woo et al. 2002) over a wide range of wavelengths from gamma-ray to radio. The spectrum of an AGN provides us with important information concerning the structure and the physics around the SMBH that powers the AGN activity. High-energy photons, such as X-ray and UV, probe the accretion disk around the SMBH that gives off hot thermal emission. Optical photons trace the accretion disk or the broad and narrow line regions farther away from the SMBH. Meanwhile, infrared (IR) observations can trace the dust-heated radiation from the dusty torus or the star forming regions. Finally, jets can be probed in the radio.

In recent years, the near-infrared (NIR) wavelength region has become an important window for understanding AGNs. In general, hot dust emission is known to be the main contributor to the NIR light from an AGN (e.g., Barvainis 1987; Kobayashi et al. 1993), and many studies have been carried out using observations in the NIR to understand the dust torus structures, such as the covering factor (Mor et al. 2009; Mor & Trakhtenbrot 2011), dust torus size (Minezaki et al. 2004; Suganuma et al. 2006), hot dust temperature ($T_{\rm HD} \sim 1500\,{\rm K}$; e.g., Barvainis 1987; Kobayashi et al. 1993; Landt et al. 2011), and the evolution of circumnuclear dust (Haas et al. 2003; Jiang et al. 2010; Hao et al. 2012; Jun & Im 2013).

Additionally, the NIR wavelength region includes interesting emission/absorption line features such as the hydrogen Paschen and Brackett lines, the polycyclic aromatic hydrocarbon (PAH) emission feature at $3.3\,\mu$m, and the absorption lines from H_2O ice ($3.1\,\mu$m), CO_2 ($4.26\,\mu$m), and CO ($4.67\,\mu$m) gas. These line features can be used to understand the BLR size, the BH mass ($M_{\rm BH}$), the star formation, and the materials surrounding the nuclear region as outlined below.

Recently, NIR Paschen lines have been put forward as a useful $M_{\rm BH}$ estimator (Kim et al. 2010; Landt et al. 2011; Landt et al. 2013), since they are much less affected by dust extinction than the common $M_{\rm BH}$ estimators using UV/optical

lines (Vestergaard & Peterson 2006; McLure & Dunlop 2004; Greene & Ho 2005). A similar study can be extended to the Brackett lines which would be even less affected by the dust than the Paschen lines. In the case of $E(B-V) = 2$ mag (a value corresponding to the typical color excess of dusty, red AGNs; e.g., Glikman et al. 2007; Urrutia et al. 2009), the Brα, Brβ, Pα, and Pβ line fluxes would be suppressed by factors of 1.31, 1.62, 2.16, and 3.97, respectively, assuming the galactic extinction law with $R_V = 3.07$ (McCall 2004). In other words, the Brα line is three times less affected by the dust extinction than the Pβ line in this example.

The 3.3 μm PAH feature has been suggested as a possible star formation indicator (Tokunaga et al. 1991), and has been detected in many local AGNs. A number of studies suggest that there may exist a correlation between the starburst (traced by the 3.3 μm PAH feature) and the AGN activity (traced, e.g., by 5100 Å continuum luminosity, hereafter, L_{5100}), although the correlation may break down at very high IR luminosities (Oi et al. 2010; Woo et al. 2012; Imanishi et al. 2011; Kim et al. 2012; Yamada et al. 2013). Finally, molecular lines such as H_2O ice, CO_2, and CO arise from molecular clouds or the diffused interstellar medium in the line of sight toward the AGN (Spoon et al. 2004), and they are useful tracers for the reservoir of molecular gas in the host galaxy and in the vicinity of an AGN. NIR hydrogen line ratios are also suggested as a useful means to understand the physical conditions of BLR (Ruff et al. 2012).

Studies of Brackett lines and PAH features have a special importance for understanding the evolutionary stages of galaxies, especially the dusty AGN phase. Dusty, red AGNs are AGNs whose optical light is obscured by the foreground dust (see Kim et al. 2010 for the demography of various types of red AGNs). They are suspected to be an intermediate population in the evolution of galaxies, situated between the dust enshrouded star forming phase (such as ultra luminous infrared galaxy, ULIRG) and the luminous AGN phase. During the red AGN stage, SMBHs are expected to

grow rapidly providing feedback to the star formation of host galaxies (Hopkins et al. 2005; Li et al. 2007), but heavy dust extinction in host galaxies prohibits observational studies of the activities occurring in red, dusty AGNs. Brackett lines and PAH features can possibly serve as NIR spectral diagnostics that can explore the AGN and star formation activity of dusty, red AGNs due to the low extinction of the light in NIR.

While studies of NIR spectra at $\lambda < 2.5\,\mu$m are common, studies based on the 2.5–5.0 μm spectra of nearby AGNs have been scarce, mainly due to the observational limitation caused either by atmospheric absorption or strong thermal background at $\lambda > 2.5\,\mu$m on the ground. In order to better understand the 2.5–5.0 μm spectra of AGNs, we conducted a spectroscopic study of 83 nearby AGNs using the *AKARI* Infrared Camera (IRC) (Murakami et al. 2007; Onaka et al. 2007) as a part of the *AKARI* mission program, Quasar Spectroscopic Observation with NIR Grism (QSONG; Im 2010). The *AKARI* IRC covers the wavelength range 2.5–5.0 μm with R $\sim$ 120 at 3.6 μm and offers high sensitivity at these wavelengths thanks to the cold and transparent environment in space. The scientific goals of our study are to (1) provide a spectral atlas of nearby, bright AGNs that have been studied extensively in previous works; (2) establish the $M_{\rm BH}$ estimator using Brackett lines so that we can estimate $M_{\rm BH}$ reliably by reducing the dust extinction effect (the Brackett-based $M_{\rm BH}$ estimator will be an improvement over Paschen line-based estimators); (3) understand the correlation between the hot dust emission and other AGN properties; and (4) study the 3.3 μm PAH feature in AGNs to understand the connection between AGN and star-formation activities. In this paper, we will describe the sample characteristics, present the 2.5–5.0 μm *AKARI* spectra of 83 AGNs, derive the $M_{\rm BH}$ estimator using the hydrogen Brackett lines of 10 AGNs where the Brackett lines are well detected, and investigate the correlation between the hot dust emission and AGN properties. The investigation of the PAH feature will appear in a future work.

2.2 THE SAMPLE AND OBSERVATION

2.2.1 The Sample

When constructing the sample, we impose the following two criteria. In order to place one of the redshifted Brackett lines (Brβ and Brα) in the IRC spectroscopic wavelength range of 2.5–5.0 μm, our sample is limited to AGNs at $z < 0.5$. In addition, we selected objects that are brighter than 14 mag in the K band to gain S/N > 10 for the continuum detection.

Using the above criteria, we constructed a sample of 108 nearby, bright AGNs that are culled from the three different AGN source catalogs below. The first source of the sample is a catalog of 35 bright and nearby type-1 AGNs with $M_{\rm BH}$ values measured from the reverberation mapping method (Peterson et al. 2004; Denney et al. 2010; Grier et al. 2008). The reverberation mapping method provides the reference $M_{\rm BH}$ values, which are used as the basis for deriving $M_{\rm BH}$ estimators using spectra taken at a single-epoch. Among the reverberation mapping sample, 31 AGNs were observed before *AKARI* stopped its operation in 2011. Note that two objects among these 31 AGNs, 3C 273 and NGC 7469, were observed through another *AKARI* mission program (AGNUL; PI: Takao Nakagawa). The AGNs that are selected from the reverberation mapping sample have a wide range of $M_{\rm BH}$ values, $10^{6.3}$–$10^{8.9} M_{\odot}$, and they are at $z = 0.002$ – 0.29. The second source is the PG QSO catalog (Green et al. 1986), since PG QSOs are optically very bright and have been extensively studied in previous works (Kaspi et al. 2000; Vestergaard 2002; Vestergaard & Peterson 2006). We find 69 PG QSOs at $z = 0.03$ – 0.48 to satisfy our selection criteria, excluding those that are already included in the reverberation mapping sample. Among them, 48 were observed by *AKARI*. For their $M_{\rm BH}$ values, we use the values derived from the Hβ line as listed in Vestergaard & Peterson (2006) where the $M_{\rm BH}$ values span the range of $10^{6.5}$–$10^{9.7} M_{\odot}$. Finally, we also supplement

the sample by four nearby bright quasars from Seoul National University Quasar Survey in Optical (SNUQSO; Im et al. 2007; Lee et al. 2008). SNUQSO is a survey of bright quasars missed by previous quasar survey at high and low galactic latitude (b $<$ | 20° |), and it provides additional bright QSOs to the sample. In total, 108 bright, low-redshift QSOs are selected, of which 83 were observed by *AKARI*

Figures 1 and 2 show the basic characteristics of the sample. AGNs in our sample are located at a redshift range of z = 0.002 – 0.48, and span over a wide range of $M_{\rm BH}$ ($10^{6.3}$–$10^{9.7} M_{\odot}$), bolometric luminosity ($L_{\rm bol}$; $10^{43.1}$–$10^{47.2}$ erg s^{-1}) and accretion rate (-2.35$\leq$ log(Eddington ratio) $\leq$0.43). The $L_{\rm bol}$ values of the PG QSOs and reverberation-mapped AGNs are estimated from L_{5100} using a bolometric correction factor of 10.3 (Richards et al. 2006), and their L_{5100} values are taken from Bentz et al. (2009); Vestergaard & Peterson (2006). For SNUQSOs, the Hα luminosity from Im et al. (2007); Lee et al. (2008) is converted to L_{5100} using Equation (1) of Greene & Ho (2005), and the converted L_{5100} is translated to $L_{\rm bol}$ with a correction factor of 10.3. All of the objects observed by *AKARI* in our sample and their basic properties are presented in Table 1. We note that the $M_{\rm BH}$ values in Table 1 are calculated with a recently updated virial factor of 5.1 (Woo et al. 2013).

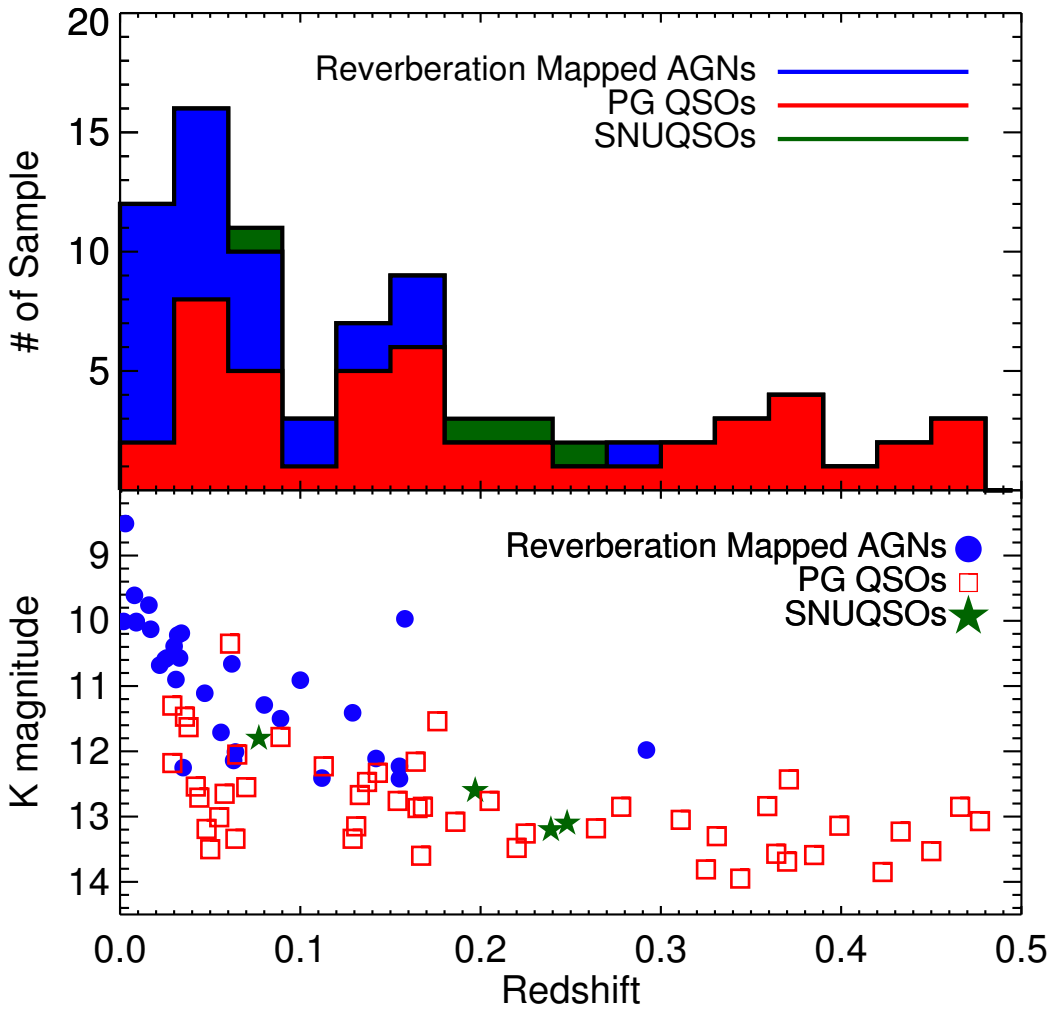

Figure 2.1 Top: redshift distribution of AGNs in our sample. The red, blue, and green histograms are for PG QSOs, reverberation mapped AGNs, and SNUQSOs, respectively. Bottom: redshift vs. K-band magnitude of our AGNs where the meaning of the colors is identical to the top panel. The K-band magnitudes include the host galaxy light. Note that PG QSOs are about two magnitude fainter than the reverberation mapped AGNs in apparent magnitude since they are in general at higher redshifts.

Table 2.1. Object List

Objects	α (J2000.0)	δ (J2000.0)	Redshift z	K (mag)	$\log(M_{\rm BH})$ ($M_\odot$)	Exposure Time (s)	Observed Dates
Mrk 335	00 06 19.5	+20 12 10	0.025	10.59	7.11[a]	1188	2008−06−30
PG 0026+129	00 29 13.6	+13 16 03	0.142	12.11	8.56[a]	1100	2008−07−02, 03
PG 0052+251	00 54 52.1	+25 25 38	0.155	12.23	8.53[a]	1144	2008−07−13, 14
Fairall 9	01 23 45.7	−58 48 20	0.047	11.11	8.37[a]	1188	2008−12−01, 02
Mrk 590	02 14 33.5	−00 46 00	0.026	10.57	7.64[a]	660	2009−07−24
3C 120	04 33 11.0	+05 21 15	0.033	10.57	7.71[a]	1188	2009−02−25
Ark 120	05 16 11.4	−00 08 59	0.032	10.22	8.14[a]	1056	2008−09−09
Mrk 79	07 42 32.7	+49 48 34	0.022	10.68	7.68[a]	1188	2008−10−10
PG 0804+761	08 10 58.6	+76 02 42	0.100	10.91	8.80[a]	1188	2008−10−04
PG 0844+349	08 47 42.4	+34 45 04	0.064	12.01	7.93[a]	1188	2009−04−24
Mrk 110	09 25 12.8	+52 17 10	0.035	12.25	7.36[a]	1056	2008−10−29, 2009−04−25
NGC 3516	11 06 47.4	+72 34 06	0.008	9.61	7.46[b]	1188	2008−10−25, 26
NGC 3783	11 39 01.7	−37 44 18	0.009	10.01	7.44[a]	1188	2008−07−03
NGC 4051	12 03 09.6	+44 31 52	0.002	10.01	6.20[b]	748	2009−05−29, 30
NGC 4151	12 10 32.5	+39 24 20	0.003	8.51	7.09[a]	1056	2008−06−03, 04
PG 1211+143	12 14 17.7	+14 03 12	0.080	11.29	8.13[a]	1144	2009−12−18, 19
3C 273	12 29 06.7	+02 03 08	0.158	9.97	8.91[a]	1848	2008−06−26, 27, 12−27
PG 1229+204	12 32 03.6	+20 09 29	0.063	12.14	7.83[a]	1188	2009−06−20
NGC 4593	12 39 39.4	−05 20 39	0.009	10.03	6.69[a]	1144	2008−07−02, 2009−01−01
PG 1307+085	13 09 47.0	+08 19 48	0.155	12.42	8.61[a]	1144	2008−07−03, 04
Mrk 279	13 53 03.4	+69 18 29	0.030	10.39	7.51[a]	1144	2008−11−14, 15, 16

Table 2.1 (cont'd)

Objects	α (J2000.0)	δ (J2000.0)	Redshift z	K (mag)	$\log(M_{\rm BH})$ ($M_\odot$)	Exposure Time (s)	Observed Dates
PG 1411+442	14 13 48.3	+44 00 14	0.089	11.50	8.61[a]	1144	2008−06−28, 29, 30
NGC 5548	14 17 59.5	+25 08 12	0.017	10.13	7.61[b]	1144	2008−07−13, 14
Mrk 817	14 36 22.0	+58 47 39	0.031	10.90	7.60[a]	660	2008−06−12
PG 1613+658	16 13 57.1	+65 43 09	0.129	11.41	8.41[a]	1144	2008−06−07, 08
PG 1617+175	16 20 11.2	+17 24 27	0.112	12.41	8.74[a]	1188	2008−08−21
PG 1700+518	17 01 24.8	+51 49 20	0.292	11.98	8.85[a]	924	2008−08−15, 17
3C 390.3	18 42 08.9	+79 46 17	0.056	11.71	8.42[a]	1188	2008−09−10
Mrk 509	20 44 09.7	−10 43 24	0.034	10.19	8.12[a]	1012	2009−04−30
PG 2130+099	21 32 27.8	+10 08 19	0.062	10.66	7.54[c]	1100	2009−05−20
NGC 7469	23 03 15.6	+08 52 26	0.016	9.762	7.05[a]	1100	2008−06−10, 11
PG 0003+158	00 05 59.2	+16 09 49	0.450	13.53	9.24[d]	1144	2008−06−30, 12−29, 30
PG 0007+106	00 10 31.0	+10 58 30	0.089	11.78	8.69[d]	1188	2009−12−28
PG 0043+039	00 45 47.3	+04 10 24	0.385	13.59	9.09[d]	1012	2010−01−02
PG 0049+171	00 51 54.8	+17 25 58	0.064	13.34	8.31[d]	1188	2010−01−09
PG 0050+124	00 53 34.9	+12 41 36	0.061	10.35	7.41[d]	1144	2008−07−08, 09
PG 0838+770	08 44 45.3	+76 53 10	0.131	13.15	8.12[d]	1188	2008−10−06
PG 0923+129	09 26 03.3	+12 44 04	0.029	11.30	8.56[d]	396	2009−11−12
PG 0934+013	09 37 01.0	+01 05 43	0.050	13.50	7.01[d]	792	2009−05−17
PG 0947+396	09 50 48.4	+39 26 51	0.205	12.76	8.64[d]	1188	2009−11−07
PG 1011−040	10 14 20.7	−04 18 40	0.058	12.65	7.28[d]	1144	2009−11−28
PG 1012+008	10 14 54.9	+00 33 37	0.186	13.08	8.21[d]	1100	2009−11−27

Table 2.1 (cont'd)

Objects	α (J2000.0)	δ (J2000.0)	Redshift z	K (mag)	$\log(M_{\rm BH})$ ($M_\odot$)	Exposure Time (s)	Observed Dates
PG 1022+519	10 25 31.3	+51 40 35	0.044	12.71	7.11[d]	396	2009−11−07
PG 1048−090	10 51 29.9	−09 18 10	0.344	13.95	9.17[d]	1188	2009−06−08
PG 1048+342	10 51 43.9	+33 59 27	0.167	13.60	8.33[d]	704	2009−11−22
PG 1049−005	10 51 51.4	−00 51 18	0.359	12.84	9.15[d]	1144	2009−06−04
PG 1100+772	11 04 13.7	+76 58 58	0.311	13.05	9.24[d]	1188	2008−10−18
PG 1103−006	11 06 31.8	−00 52 52	0.423	13.85	9.29[d]	792	2009−06−08
PG 1114+445	11 17 06.4	+44 13 33	0.143	12.33	8.56[d]	1144	2009−11−21, 22
PG 1115+407	11 18 30.3	+40 25 54	0.154	12.76	7.63[d]	1144	2009−11−24
PG 1116+215	11 19 08.7	+21 19 18	0.176	11.54	8.48[d]	1056	2009−12−03
PG 1121+422	11 24 39.2	+42 01 45	0.225	13.26	8.00[d]	396	2009−11−26
PG 1202+281	12 04 42.1	+27 54 12	0.165	12.87	8.58[d]	396	2009−12−11
PG 1216+069	12 19 20.9	+06 38 39	0.331	13.30	9.16[d]	616	2009−12−24
PG 1244+026	12 46 35.2	+02 22 09	0.048	13.19	6.49[d]	1100	2008−06−30, 12−31
PG 1259+593	13 01 12.9	+59 02 07	0.477	13.07	8.88[d]	1144	2009−11−27, 28
PG 1302−102	13 05 33.0	−10 33 19	0.278	12.85	8.84[d]	1100	2009−07−10, 11
PG 1322+659	13 23 49.5	+65 41 48	0.168	12.85	8.25[d]	1056	2009−11−21, 22
PG 1351+236	13 54 06.4	+23 25 49	0.055	13.01	8.53[d]	792	2008−07−09
PG 1402+261	14 05 16.2	+25 55 34	0.164	12.16	7.91[d]	1144	2008−07−09
PG 1415+451	14 17 00.7	+44 56 06	0.113	12.23	7.98[d]	1144	2008−12−29, 2009−06−28
PG 1416−129	14 19 03.8	−13 10 44	0.129	13.34	9.01[d]	1100	2010−01−27
PG 1425+267	14 27 35.6	+26 32 15	0.364	13.57	9.70[d]	1188	2008−07−16

Table 2.1 (cont'd)

Objects	α (J2000.0)	δ (J2000.0)	Redshift z	K (mag)	$\log(M_{\rm BH})$ ($M_\odot$)	Exposure Time (s)	Observed Dates
PG 1427+480	14 29 43.1	+47 47 26	0.220	13.48	8.05[d]	1188	2009−06−29, 07−01
PG 1448+273	14 51 08.7	+27 09 27	0.065	12.05	6.94[d]	1188	2009−07−22, 23
PG 1501+106	15 04 01.2	+10 26 16	0.036	11.47	8.49[d]	1188	2009−08−02
PG 1512+370	15 14 43.0	+36 50 50	0.370	13.69	9.34[d]	1100	2008−07−22
PG 1519+226	15 21 14.2	+22 27 44	0.137	12.47	7.91[d]	1188	2009−08−02, 03
PG 1534+580	15 35 52.3	+57 54 09	0.029	12.18	8.17[d]	1100	2008−06−29, 12−31, 2009−01−01
PG 1535+547	15 36 38.3	+54 33 33	0.038	11.63	7.16[d]	704	2008−07−06, 08
PG 1543+489	15 45 30.2	+48 46 09	0.399	13.14	7.96[d]	1188	2009−01−17, 20, 21
PG 1545+210	15 47 43.5	+20 52 17	0.264	13.18	9.28[d]	616	2008−08−11
PG 1626+554	16 27 56.1	+55 22 32	0.133	12.67	8.46[d]	1188	2010−01−22
PG 1704+608	17 04 41.4	+60 44 31	0.371	12.43	9.36[d]	1100	2008−07−23
PG 2112+059	21 14 52.6	+06 07 42	0.466	12.85	8.97[d]	1056	2009−05−13, 14
PG 2209+184	22 11 53.9	+18 41 50	0.070	12.55	8.73[d]	1144	2009−12−03, 05
PG 2233+134	22 36 07.7	+13 43 55	0.325	13.81	8.00[d]	1188	2009−12−07, 08
PG 2304+042	23 07 02.9	+04 32 57	0.042	12.54	8.53[d]	748	2009−12−12
PG 2308+098	23 11 17.7	+10 08 15	0.433	13.23	9.56[d]	1012	2008−12−14
SNUQSO 0644+3546	06 44 10.8	+35 46 44	0.077	11.82	8.86[e]	1188	2008−10−01
SNUQSO 1312+0641	13 12 04.7	+06 41 07	0.239	13.20	9.09[e]	1100	2008−07−06, 2009−01−03
SNUQSO 1935+5314	19 35 21.1	+53 14 11	0.248	13.14	8.61[e]	1188	2008−11−17, 2009−05−11
SNUQSO 2127+2719	21 27 56.4	+27 19 05	0.197	12.63	8.74[e]	396	2009−05−26

[a]The $M_{\rm BH}$ values are estimated from reverberation mapping method (Peterson et al. 2004).

[b]The $M_{\rm BH}$ values are estimated from reverberation mapping method (Denney et al. 2010).

[c]The $M_{\rm BH}$ values are estimated from reverberation mapping method (Grier et al. 2008).

[d]The $M_{\rm BH}$ values are based on $\rm FWHM_{H\beta}$ and L_{5100} (Vestergaard & Peterson 2006).

[e]The $M_{\rm BH}$ values are based on $\rm FWHM_{H\alpha}$ and $L_{\rm H\alpha}$ (Lee et al. 2008; Im et al. 2007).

2.2.2 The Observation

The 2.5–5.0 μm NIR spectra were obtained with the IRC infrared spectrograph (Onaka et al. 2007) on the *AKARI* satellite during phase 3 of the *AKARI* operation (Murakami et al. 2007), i.e., our observation was carried out during 2008–2011 after the helium cooling was over. We used the NG grism mode which provides a spectral resolution of R = 120 $\lambda/3.6\,\mu$m. The spectral resolution corresponds to the FWHM velocity resolution of 2500 km s^{-1} or σ = 1062 km s^{-1} at 3.6 μm which is adequate for studying the broad emission lines of quasars and AGNs whose typical FWHM velocity widths are greater than 2000 km s^{-1}. Also, the wavelength coverage of 2.5–5.0 μm enables us to sample Brβ, Brα, and PAH at low redshift.

For most of the targets, three-pointing observation was performed where one-pointing observation is made of seven to nine frames with 44 s of exposure each. For a few sources, 1, 2, or 5 pointings were assigned (total integration time of 396 to 1848 seconds) due to the observational constraints of the telescope. Each target was placed at the center of a square-shaped slit window ($1\farcm0 \times 1\farcm0$ size) designed to avoid confusing the spectrum with neighboring objects. Table 1 summarizes the observation of each target.

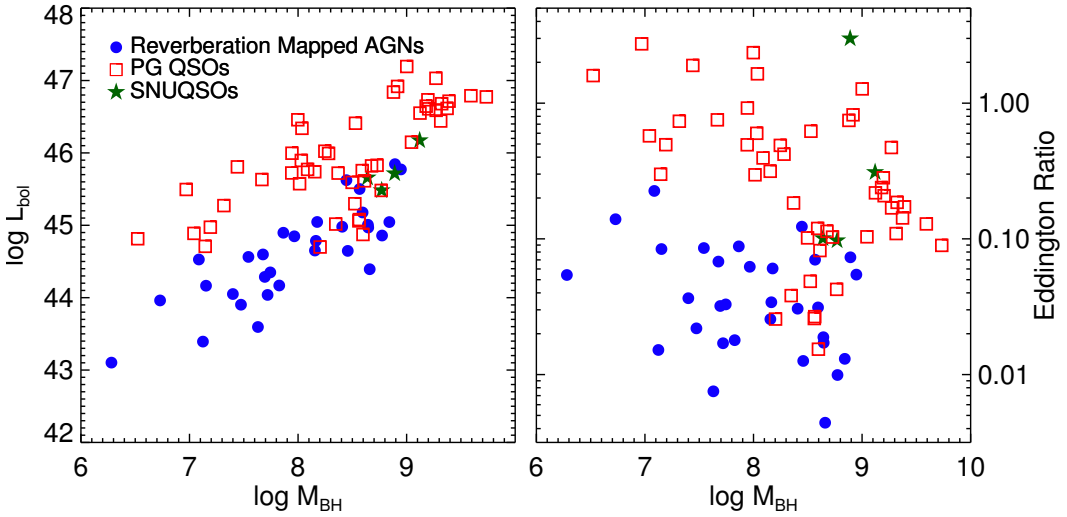

Figure 2.2 Left: $M_{\rm BH}$ values vs. $L_{\rm bol}$ values of AGNs in our sample. The meaning of the symbols are identical to Figure 1. Our sample covers a wide range in $M_{\rm BH}$ ($10^{6.3}$–$10^{9.7} M_{\odot}$) and $L_{\rm bol}$ ($10^{43.1}$–$10^{47.2}$ erg s^{-1}). Right: $M_{\rm BH}$ values vs. Eddington ratios of our AGNs. Our AGN sample covers an extensive range of BH accretion rates (-2.35 $\leq$ log(Eddington ratio) $\leq$ 0.43). Note that PG QSOs and SNUQSO AGNs are intrinsically more luminous and have higher accretion rates than the reverberation mapped AGNs.

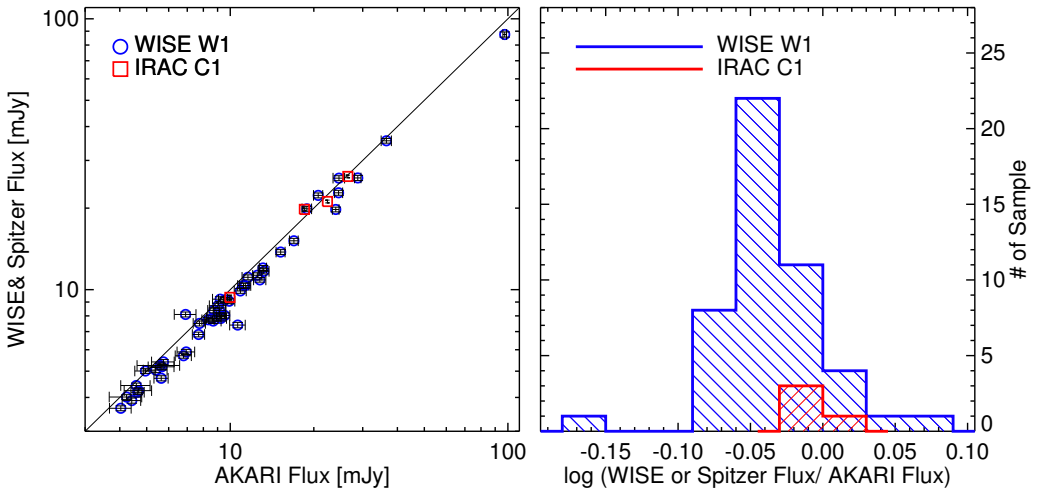

Figure 2.3 Left: comparison of the *WISE* $W1$ or *Spitzer* IRAC $Ch1$ magnitudes vs. the *WISE* $W1$ and *Spitzer* IRAC $Ch1$ magnitudes derived from the *AKARI* spectra. The blue circles and the red squares indicate the *WISE* $W1$ and the *Spitzer* IRAC $Ch1$ fluxes, respectively. The black solid line is for the case where the *AKARI*, and *WISE* or *Spitzer* fluxes are identical. Right: Distribution of the ratios of the *WISE* or *Spitzer* fluxes to the *AKARI* fluxes of PG QSOs. The blue and the red histograms indicate the ratios for *WISE* and the *Spitzer* fluxes, respectively.

2.2.3 Data Reduction

The data reduction was performed using the standard data reduction software package "IRC Spectroscopy Toolkit for Phase 3 data Version 20110301 (2011/03/01)" (Ohyama et al. 2007), but with an additional procedure for cosmic ray/hot pixel removal to improve quality of the final spectrum. First, we used the standard IRC pipeline on each pointing data separately, up to the point before the extraction of the one-dimensional spectrum. Then, we removed hot or bad pixels in the stacked two-dimensional spectrum using L.A.Cosmic (van Dokkum 2001) in spectroscopic mode, since the *AKARI* phase 3 images typically come with many hot pixels and we wanted to remove effectively the hot pixels. We set the hot or bad pixel detection limit to 4.5σ for removal of the hot pixels. Then, a one-dimensional spectrum of each pointing for each object was extracted using an extraction aperture width of 5 pixels, for which aperture correction is performed using the pipeline and assuming a point source PSF to correct for the missing flux due to the adoption of the finite aperture size. The extraction aperture width gives the optimal S/N since the FWHM of PSFs in the IRC data is about 5 pixels ($7\farcs3$). Note that the AGN spectrum can be contaminated by the host galaxy light, since the square-shaped slit window ($1\farcm0$) does not completely block the light from the extended regions of a host galaxy. Hence, we are effectively sampling the light from the AGN+host galaxy within an observational rectangular aperture of $7\farcs3 \times 1\farcm0$, which corresponds to physical scales of 1.49 kpc $\times$ 12.3 kpc at $z = 0.01$ and 32.5 kpc $\times$ 267 kpc at $z = 0.3$ where the long axis runs along the dispersion direction. In both cases, the aperture contains a significant portion of host galaxies, although we expect that the measured Brackett lines are dominated by emission from the nuclear region, as we describe in Section 4.1. Finally, the extracted one-dimensional spectra from all of the pointings of a source were combined. In this process, any remaining outlier pixels (hot or bad pixel features) in the one-dimensional spectrum were removed by σ clipping with

4.5σ where the median value and the σ of a data point were determined including two adjacent data points. The wavelength and flux calibration was performed in the IRC pipeline and the expected accuracies of the wavelengths and fluxes are about 0.01 μm and 10% (Ohyama et al. 2007), respectively.

To demonstrate the accuracy of the photometric calibration, we compare the fluxes of PG QSOs from the *AKARI* spectra to *WISE* $W1$ and *Spitzer* IRAC $Ch1$ magnitudes. To simplify the comparison, we restrict the sample for the comparison to point-like sources (i.e., unresolved) in all of the *AKARI*, *WISE*, and *Spitzer* images. Thus, we restrict the sample for the photometry comparison to those in the PG QSO sample. For this comparison, we used the *WISE* $W1$ magnitudes measured with a profile-fitting method provided by the *WISE* all-sky source catalog. However, for the *Spitzer* IRAC $Ch1$ magnitudes, we measured the magnitudes using IRAC $Ch1$ PBCD imaging data that we obtained from the *Spitzer* archive. In order to measure the magnitudes from the IRAC $Ch1$ PBCD imaging data, we used the IRAF daophot task with an aperture radius of 3×FWHM. Among the PG QSOs, five objects (PG 0007+106, PG 0050+124, PG 1100+772, PG 1501+106, and PG 1704+608) have IRAC $Ch1$ PBCD imaging data. Excluding PG 0050+124 which is too bright and saturated at the center of the IRAC image, we used four objects from the *Spitzer* archive for the comparison. Finally, using *AKARI* spectra, we calculated the corresponding *WISE* $W1$ and *Spitzer* $Ch1$ magnitudes by applying appropriate filter transmission curves. Figure 3 shows the comparison of the fluxes from *AKARI* with those from *WISE* and *Spitzer*. The *AKARI* fluxes are on average 10% larger than the *WISE* fluxes, while the *Spitzer* $Ch1$ fluxes are in good agreement with the *AKARI* flux values. Although the reason for the systematic offset in the flux is not clear, we find the 10% difference to be acceptable considering the general flux calibration uncertainty of *AKARI* (Ohyama et al. 2007).

The flux errors of the spectra from the pipeline appear somewhat larger than

the fluctuation of the data points (e.g., Figure 7). To check the flux error values from the pipeline, we used independent flux measurements derived from several pointing observations (Section 2.2), and we checked the determined uncertainty of the flux at each wavelength by adopting the rms value of the flux measurements from each pointing data. We find that the error derived this way agrees with the *AKARI* pipeline result, suggesting that the *AKARI* pipeline error measurement reflects unknown fluctuations in the continuum level determination or sensitivity fluctuations of IRC.

2.2.4 Construction of Composite Spectrum

In an attempt to increase the S/Ns of the AGNs without Brackett line detections, we created a composite spectrum of the 48 PG QSOs. The PG QSOs are less affected by host galaxy contamination than the reverberation-mapped sample due to bright luminosity ($L_{\rm bol}$: $10^{44.6}$–$10^{47.2}$ erg s^{-1}; Figure 2).

To construct the composite spectrum, we stacked, deredshifted, and flux-calibrated spectra of PG QSOs in logarithmic scale. Considering PG QSOs have different luminosity ranges, a geometric mean was used to construct the composite spectrum. We built a wavelength grid with a pixel resolution twice the spectral resolution of IRC (R = 120 $\lambda/3.6\,\mu$m). In each wavelength grid, the weighted mean flux of each object was stacked for the geometric mean flux.

Figure 4 shows the composite spectrum of PG QSOs in λ versus F_ν. The location of key lines are also displayed in the figure. The composite spectrum is available in the supplemental material accompanying the article. Although we could not detect Brackett lines in individual PG QSO spectra, some of the NIR Hydrogen emission lines are now visible in the composite spectrum.

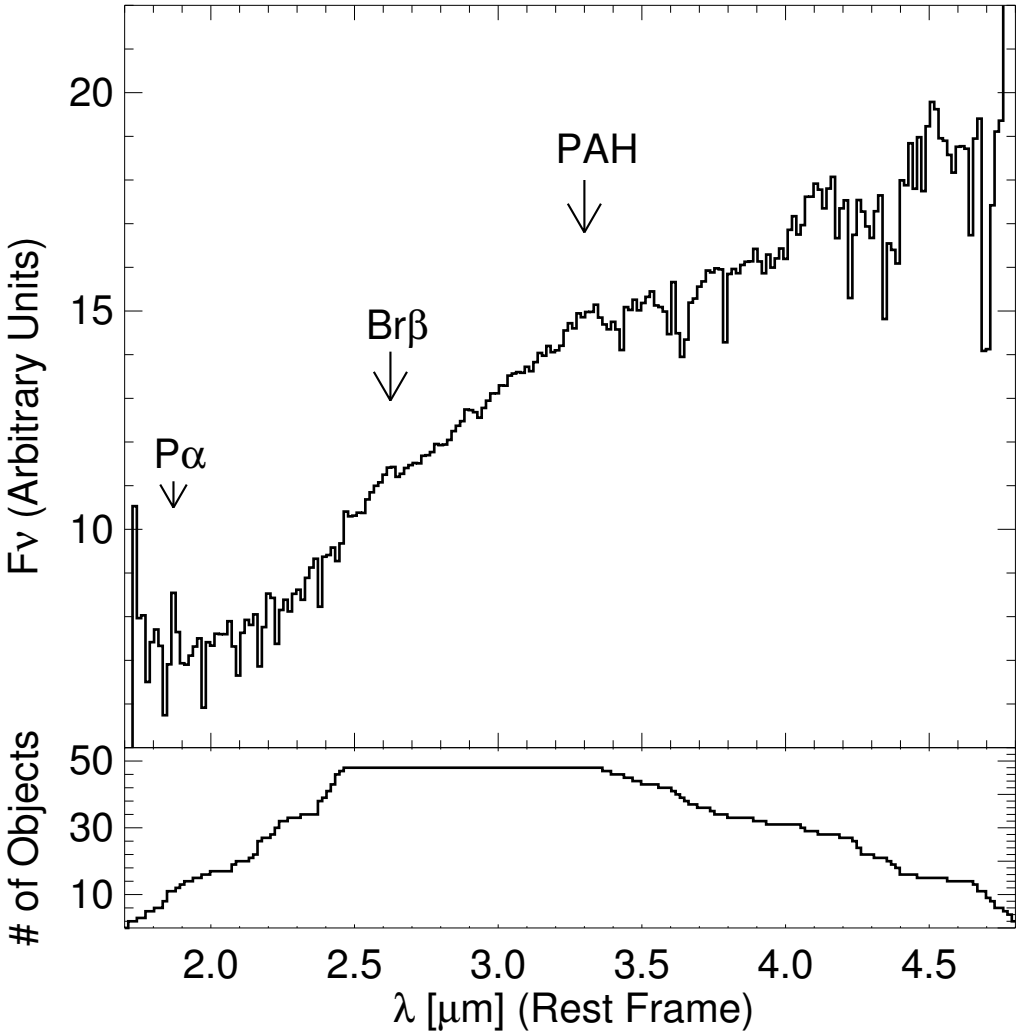

Figure 2.4 Top: composite spectrum of the 48 PG QSOs in arbitrary F_ν units. The composite spectrum indicates Pα, Brβ, and PAH lines. Bottom: the number of spectra contributing for the composite spectrum.

2.3 *AKARI* NIR SPECTRA

We show the *AKARI* spectra from our program in Figure 5. The machine-readable form of the spectra in Figure 5 are available. Several interesting lines are also indicated in Figure 5, such as the Hydrogen Brackett lines, 3.3 μm PAH, and other molecular/atomic lines. Brα and Brβ lines are identified in 9 and 7 objects at $S/N > 3$, respectively, and we mark the location of these lines in Figure 5 when they are identified. Potential detections are marked with a "?" sign. On the other hand, the Paschen lines are identified in 5 objects. All of the Brackett line detections come from the reverberation mapping sample whose members are brighter than the QSOs in the other two samples. The rather low detection rate of the Brackett lines reflect the reduced sensitivity and the increased number of detector defects during the warm mission phase of *AKARI*.

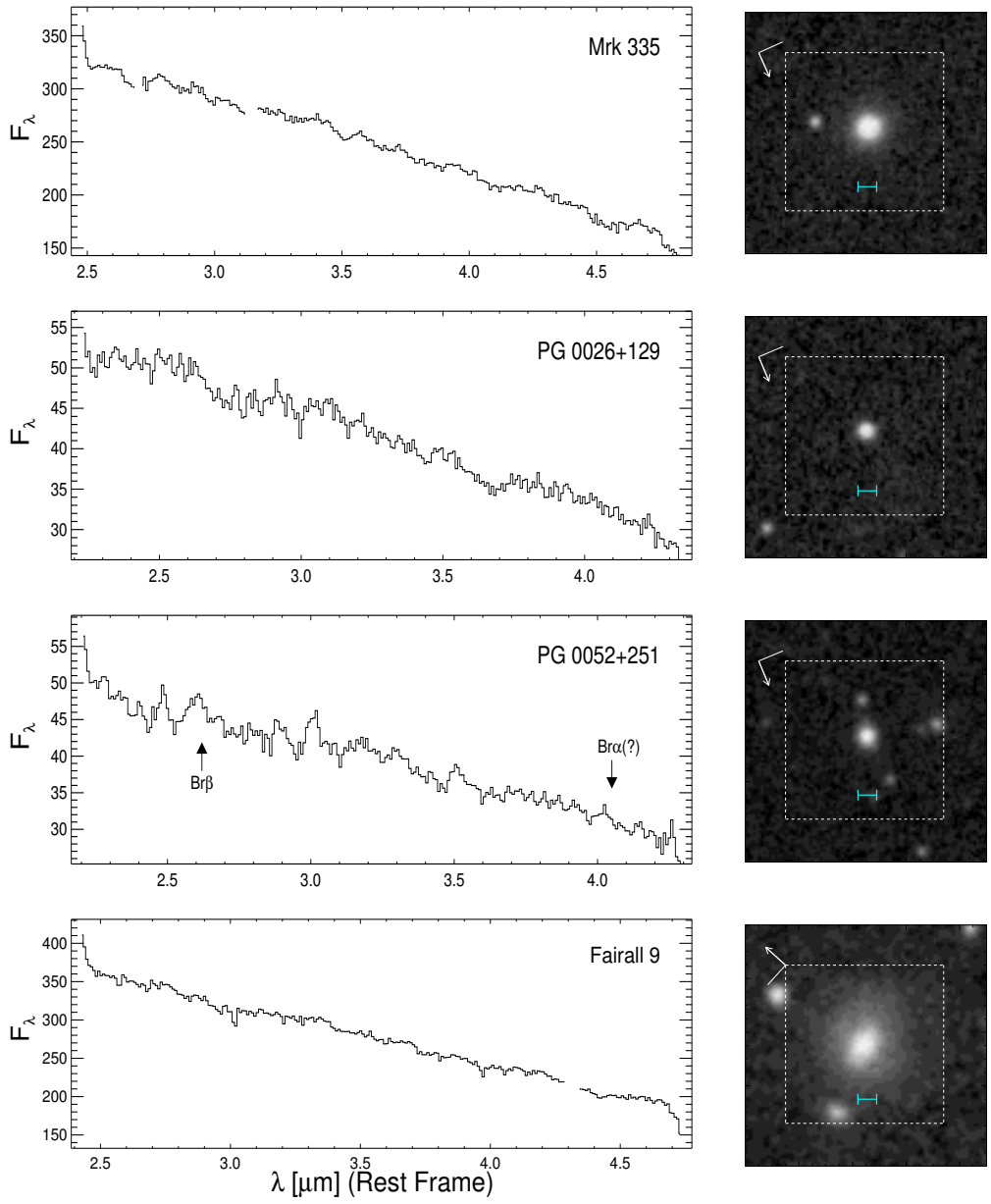

Figure 2.5 Spectra and images of AGNs in the QSONG sample. The left panels show de-redshifted 2.5–5.0 μm spectra and the spectral regions affected by remaining hot or bad pixels are masked out. The ordinate is in units of 10^{-13} erg s^{-1} cm^{-2} μm^{-1}. Several hydrogen lines (Pα, Brβ, and Brα) and molecular lines (PAH, CO_2, and CO) are marked on the spectra. When the line detection is not obvious, the line is marked with a question mark. The right panels indicate object images from the digitized sky survey (DSS). The white dashed line box and the cyan solid bar indicate $1\farcm0 \times 1\farcm0$ slit window and $7\farcs3$ width of extraction aperture, respectively. The arrow at the top left denotes north.

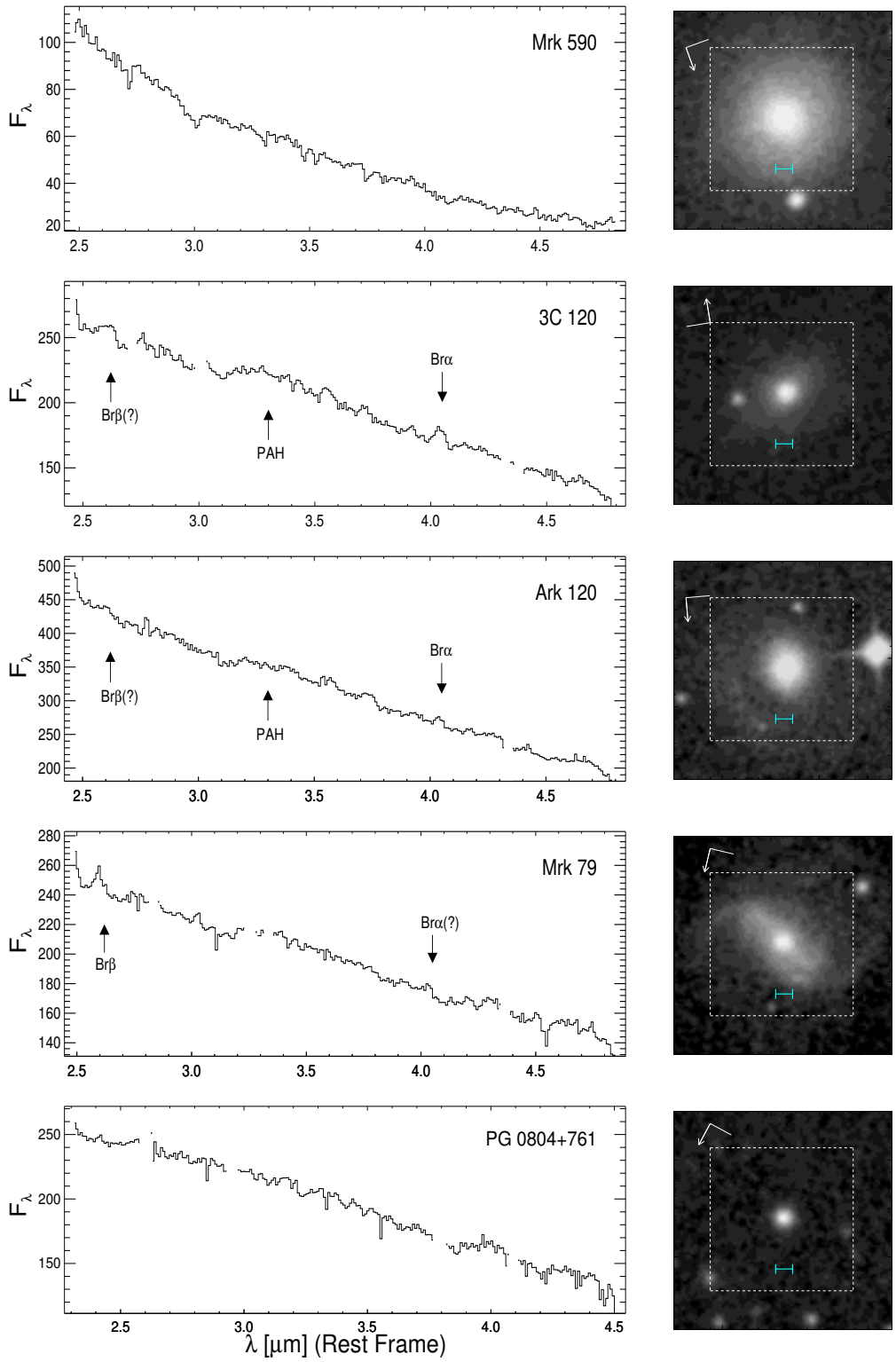

Figure 2.5 Continued

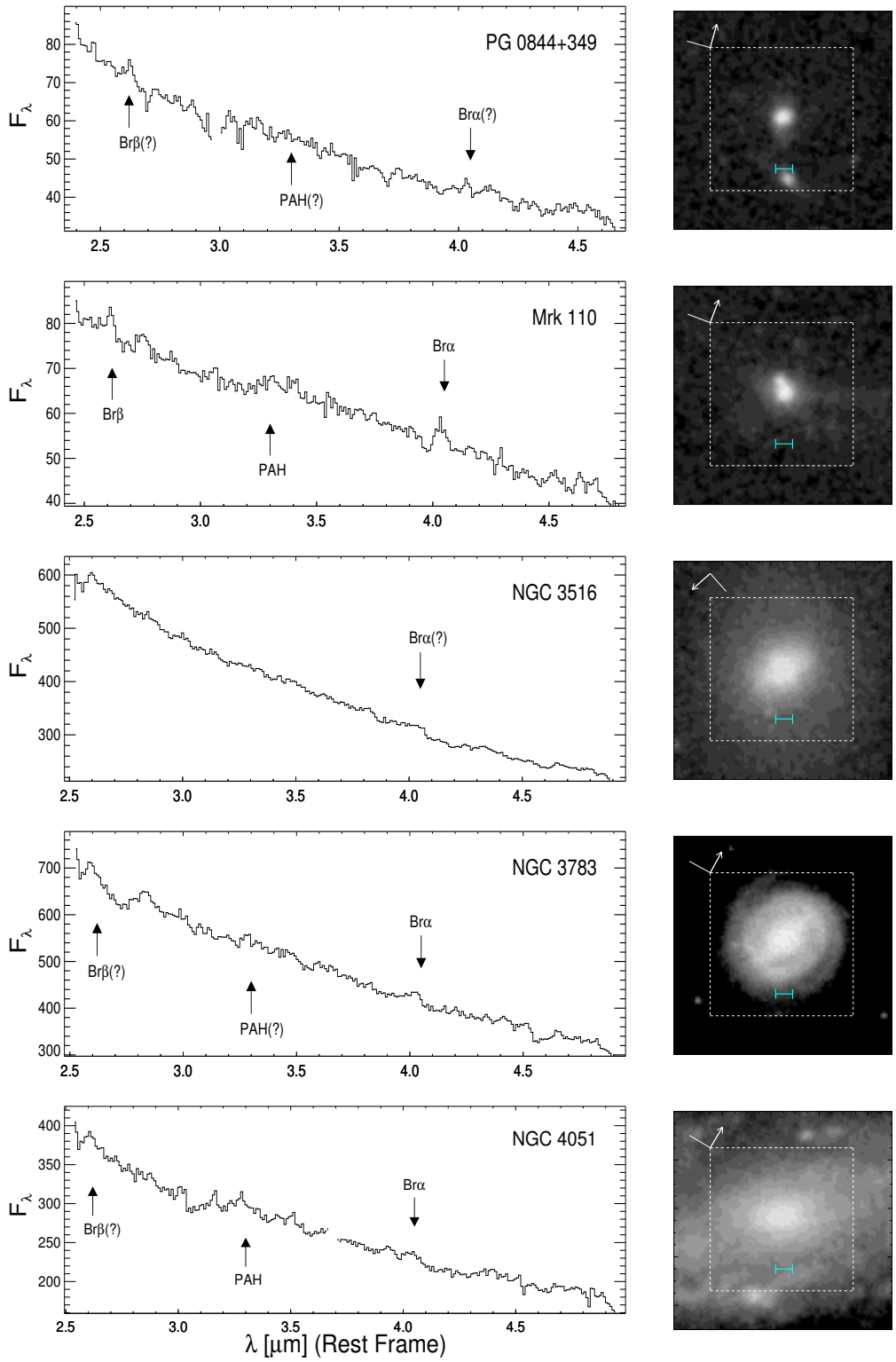

Figure 2.5 Continued

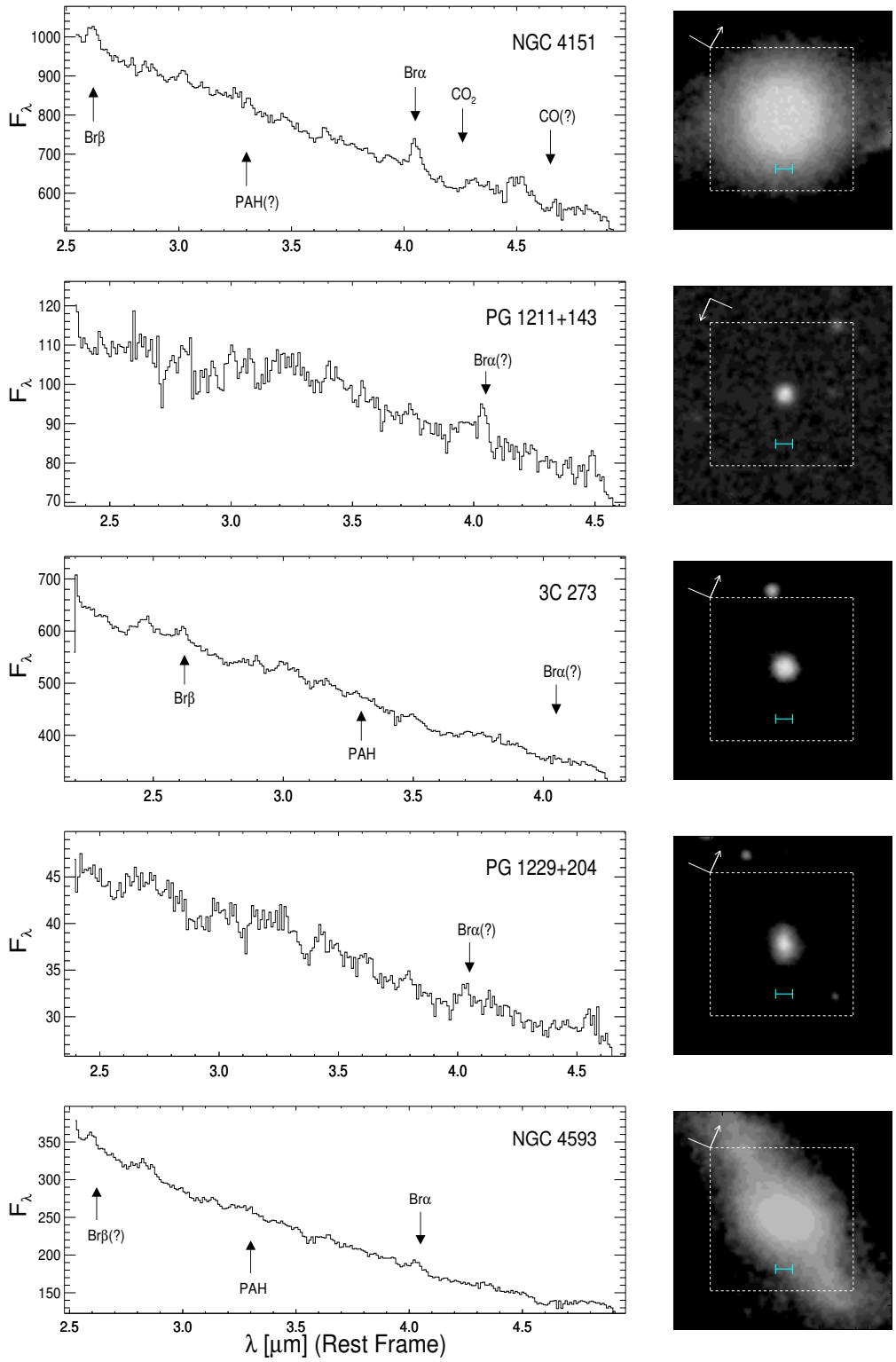

Figure 2.5 Continued

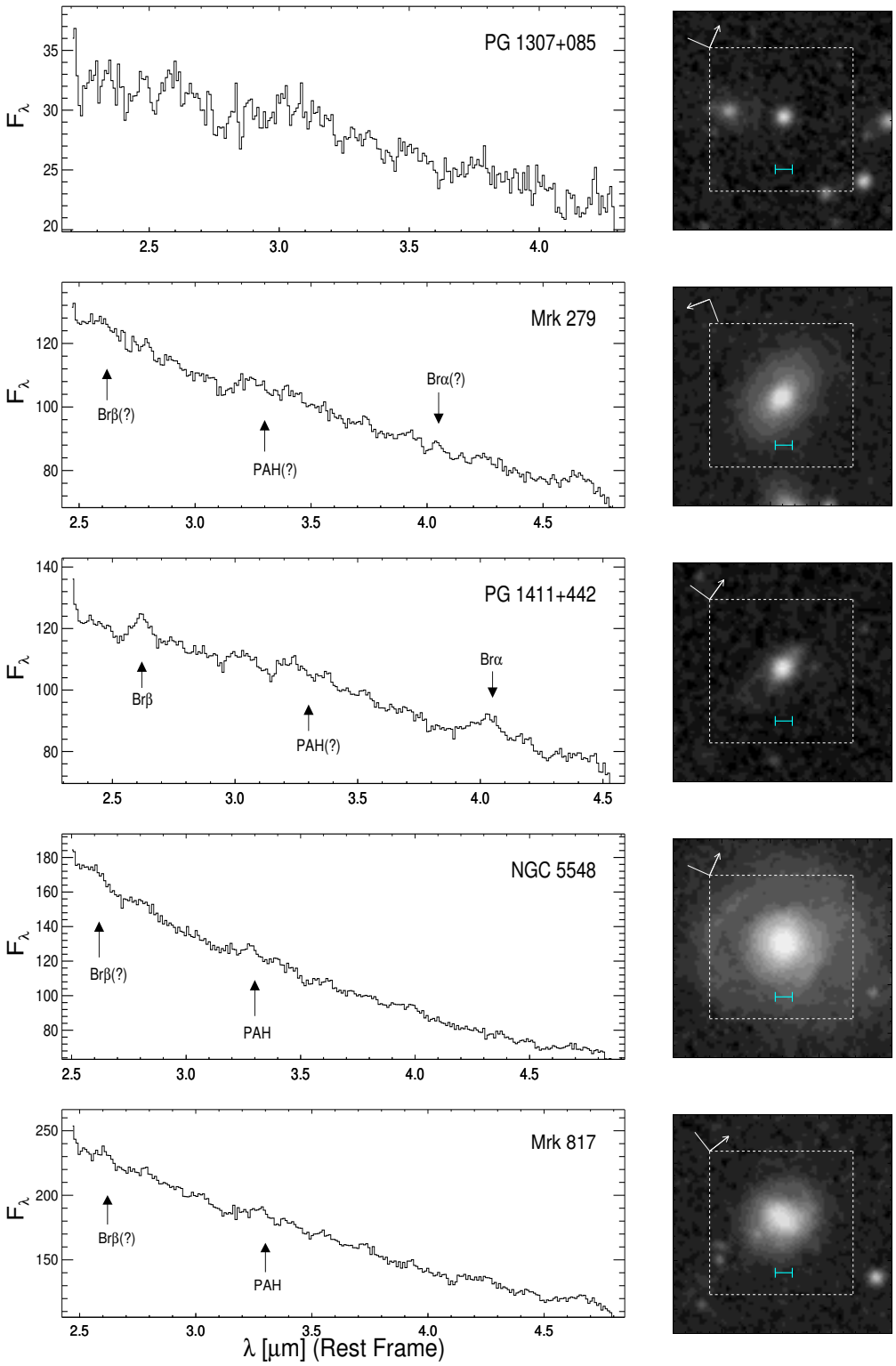

Figure 2.5 Continued

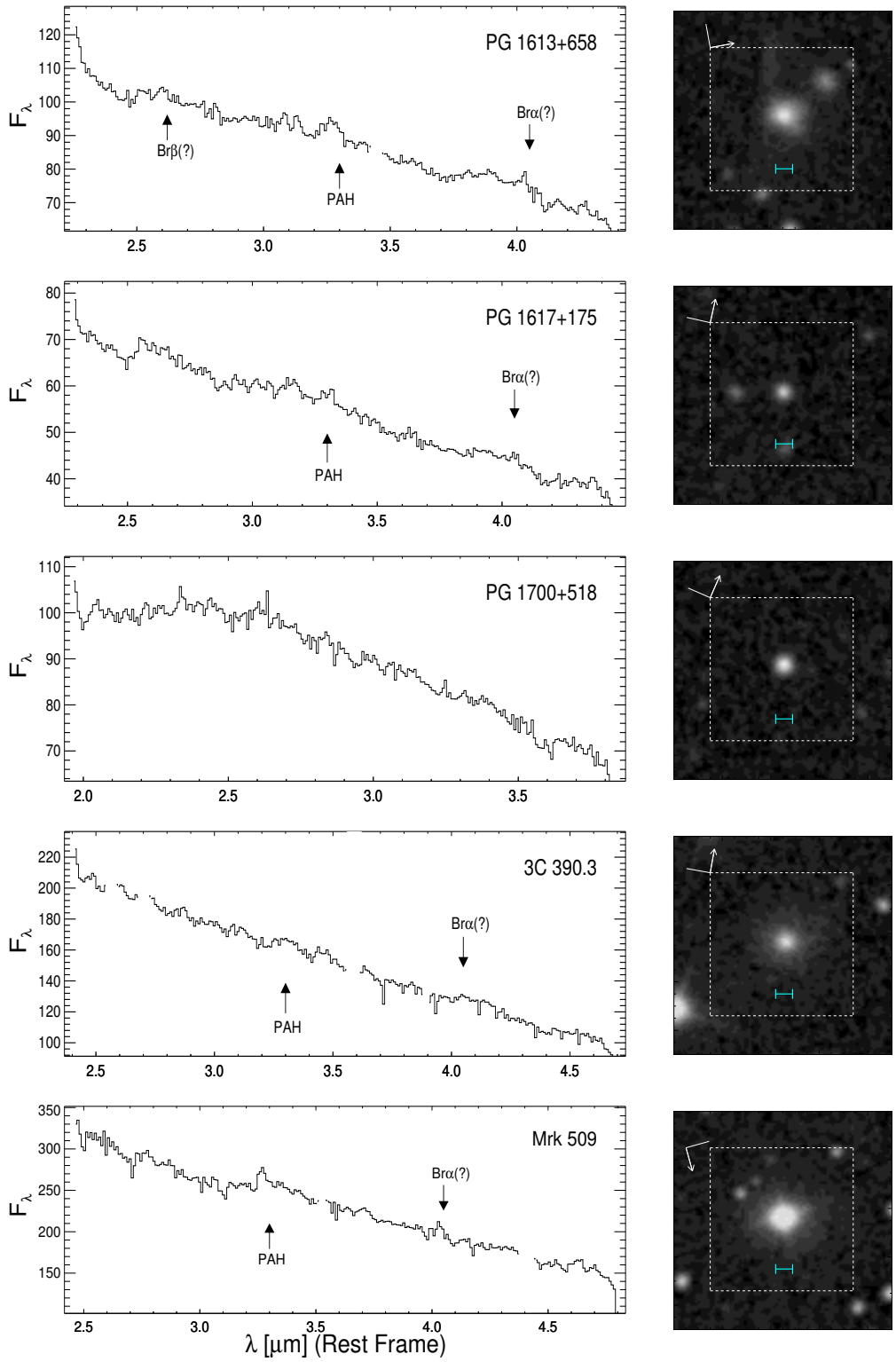

Figure 2.5 Continued

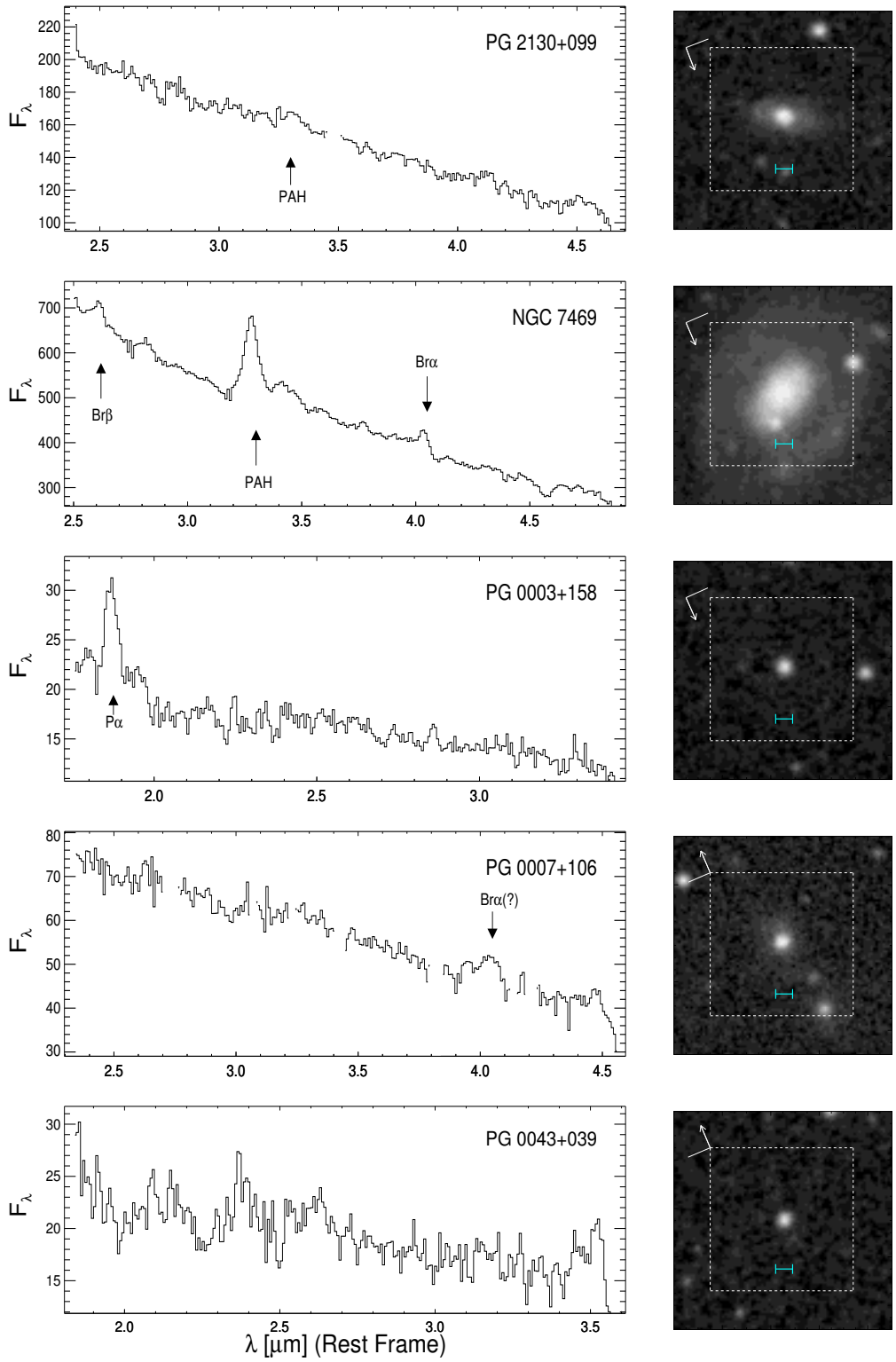

Figure 2.5 Continued

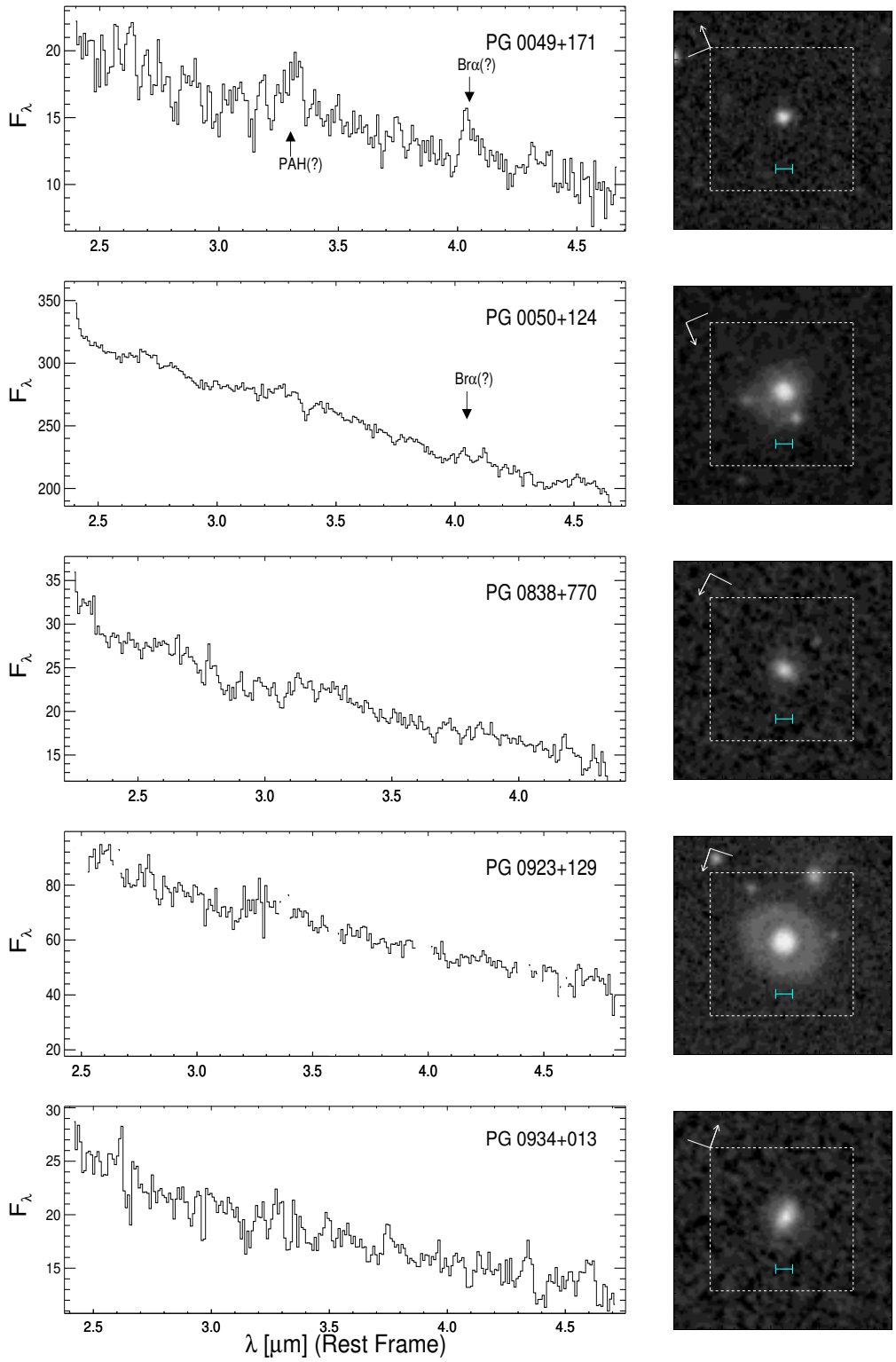

Figure 2.5 Continued

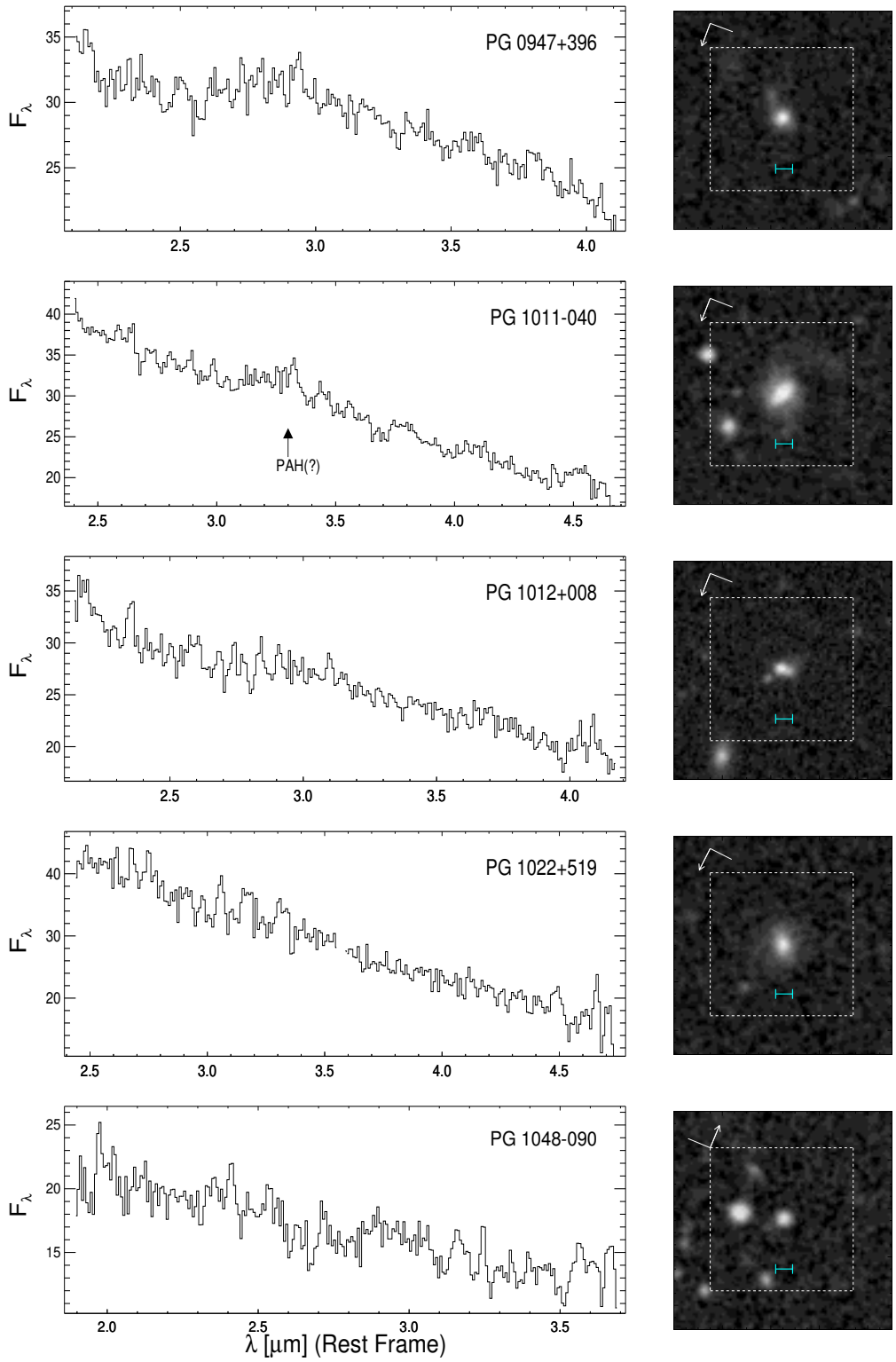

Figure 2.5 Continued

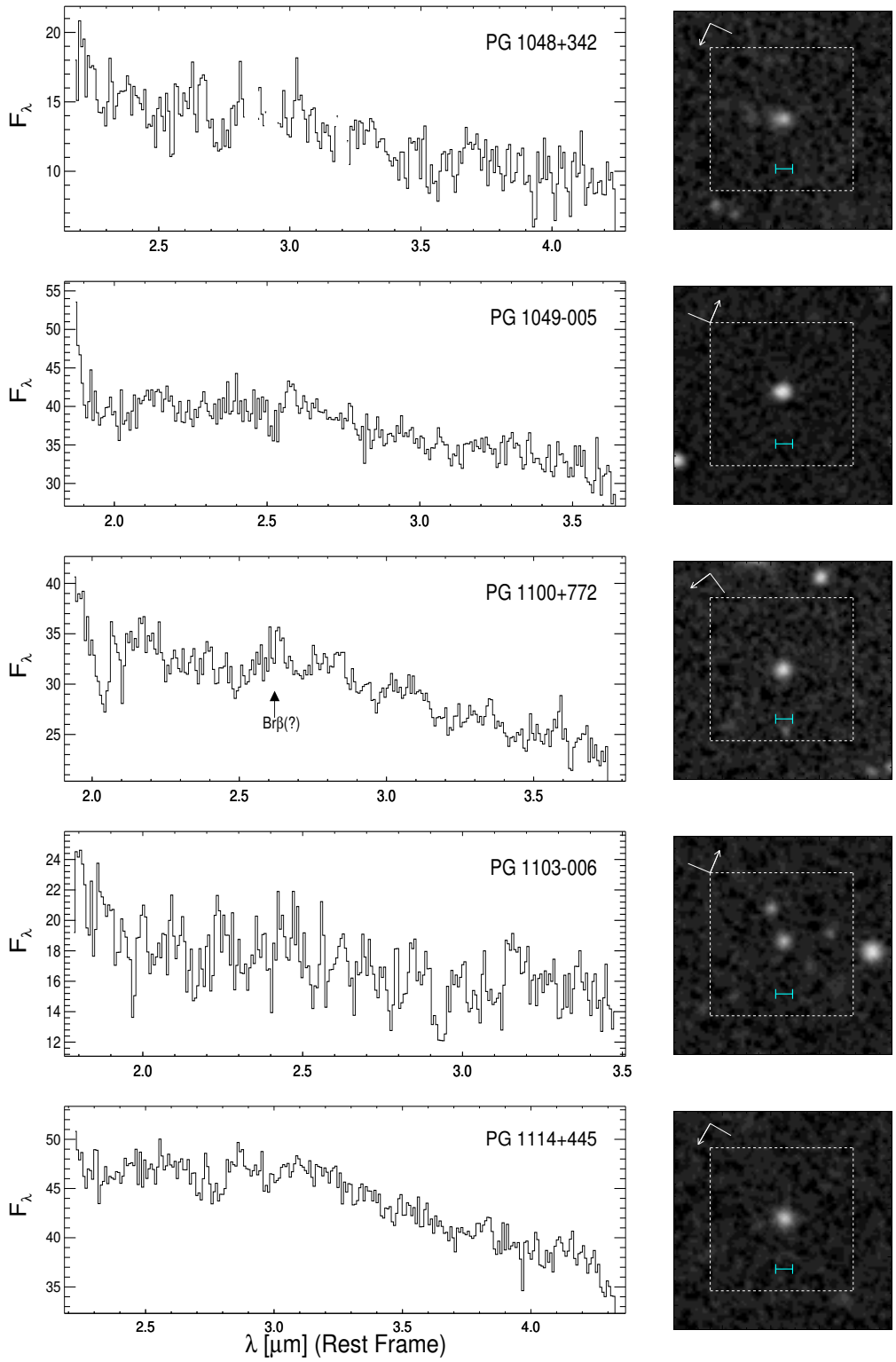

Figure 2.5 Continued

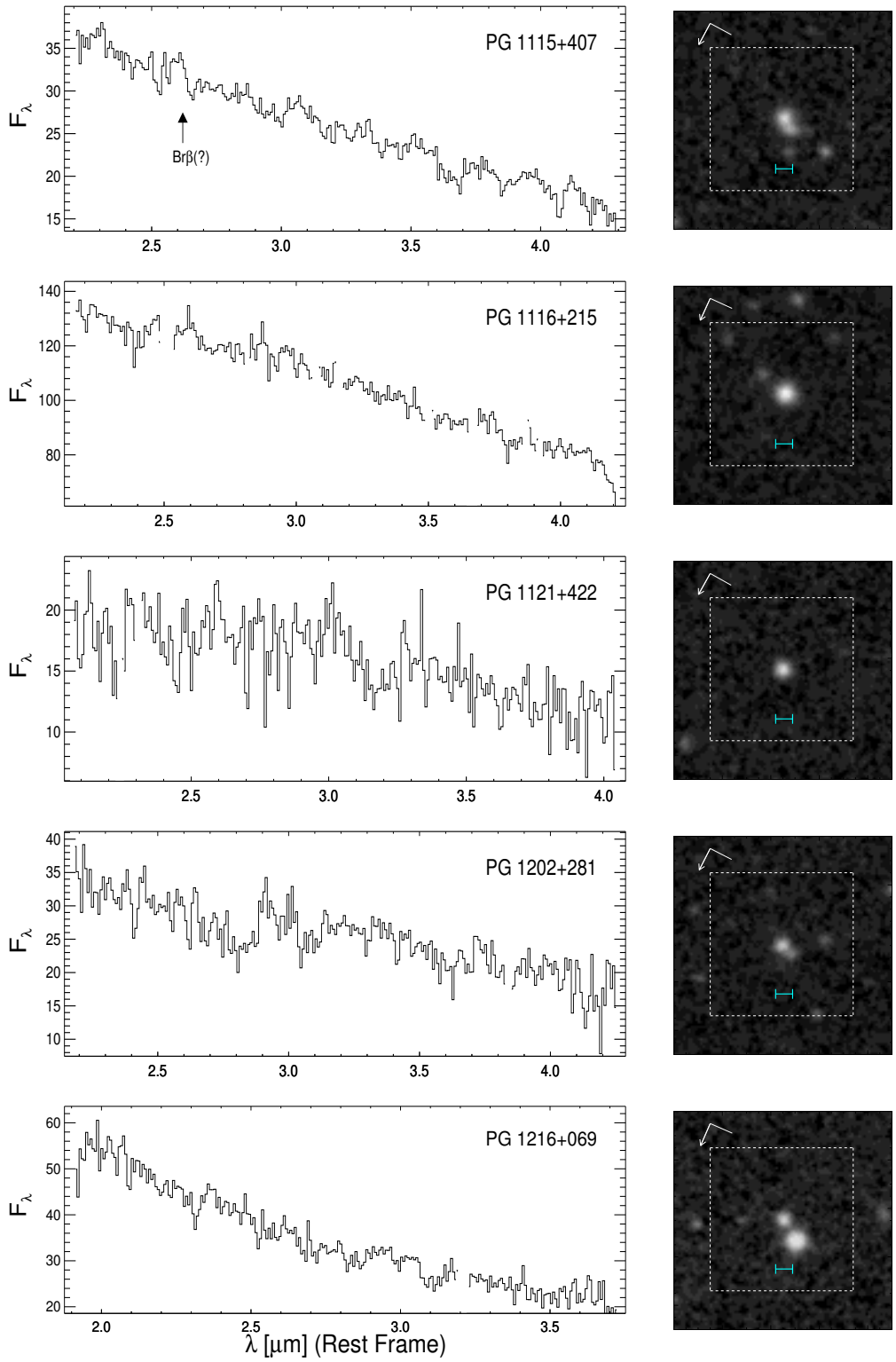

Figure 2.5 Continued

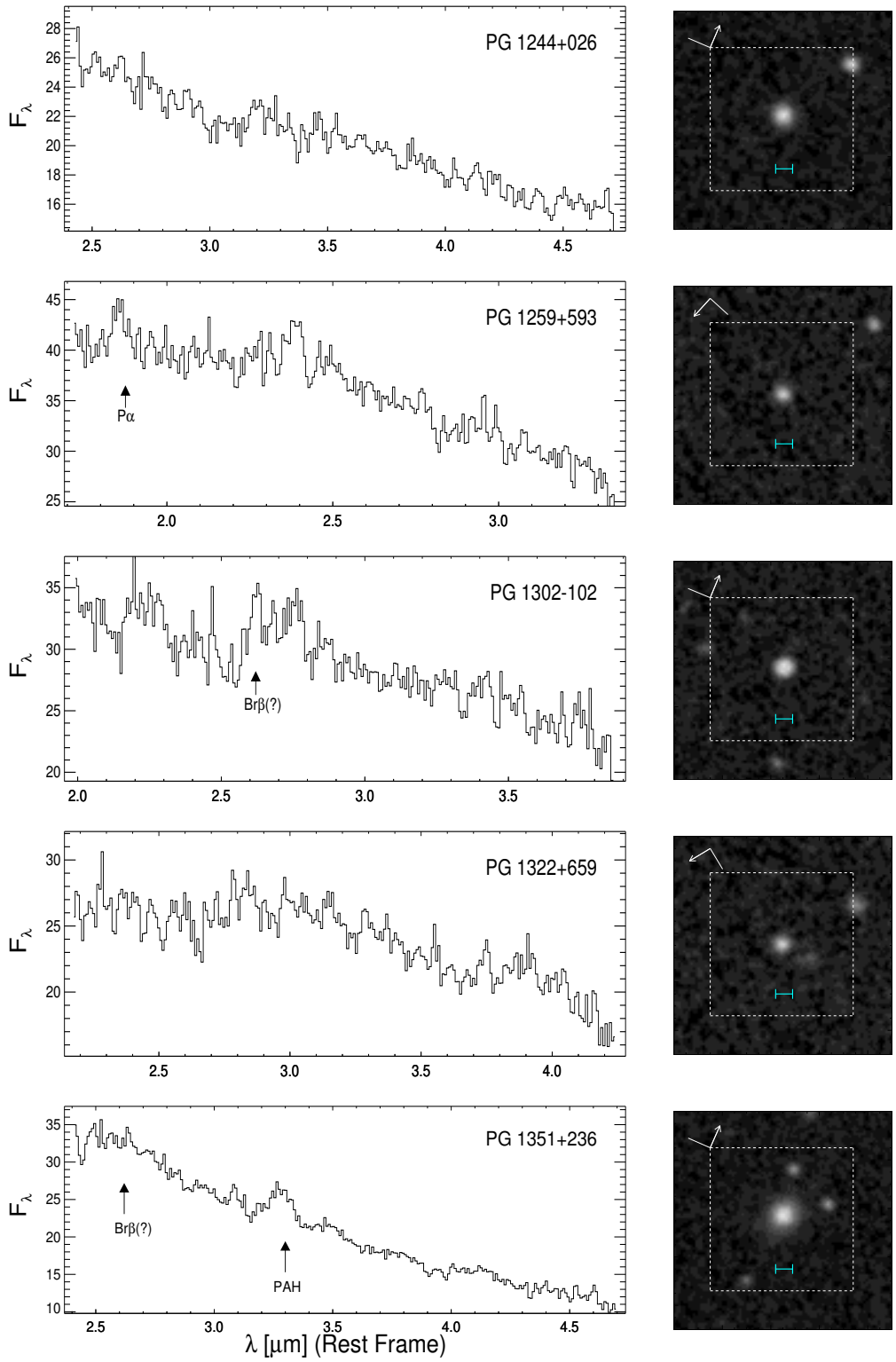

Figure 2.5 Continued

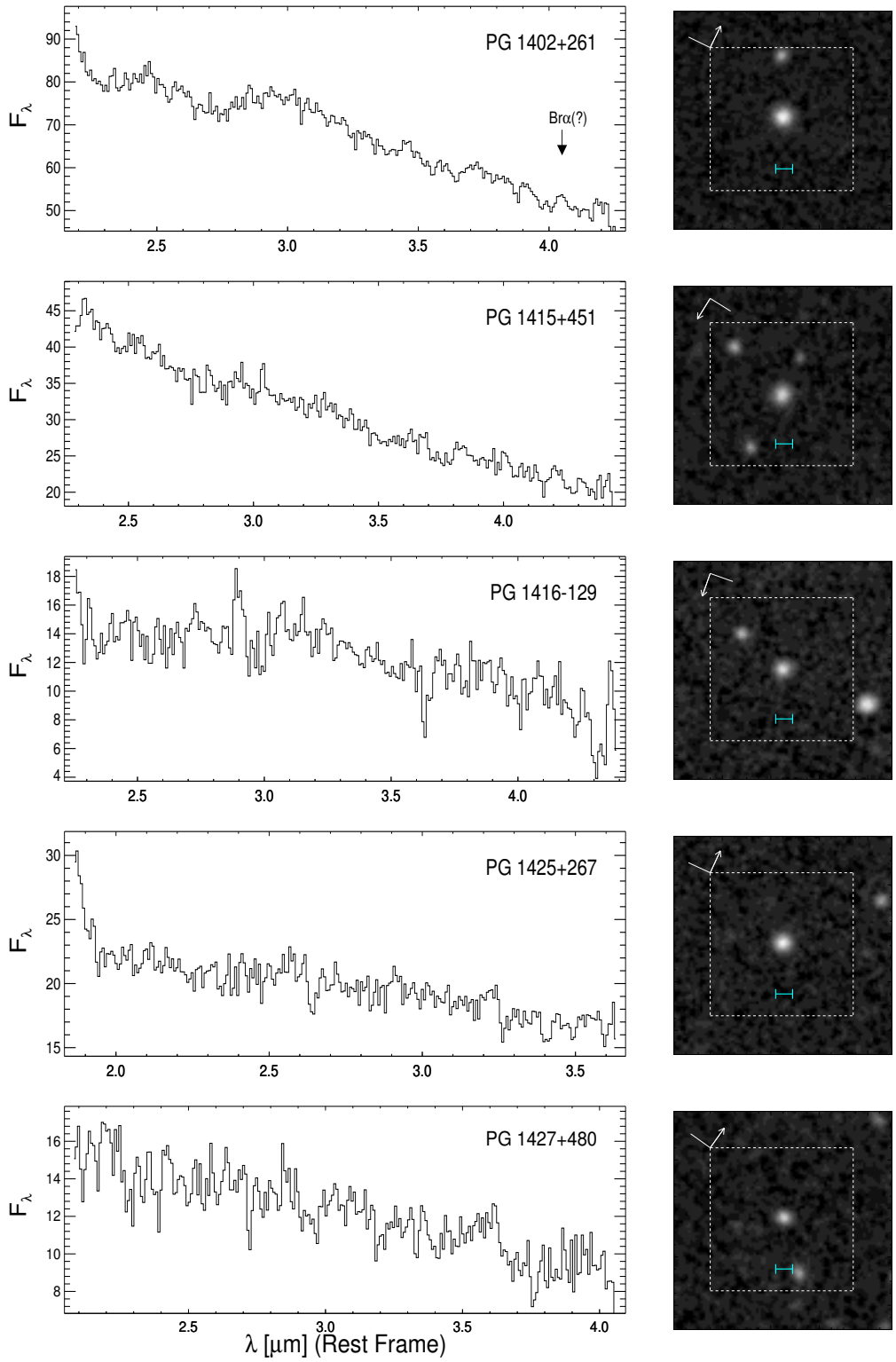

Figure 2.5 Continued

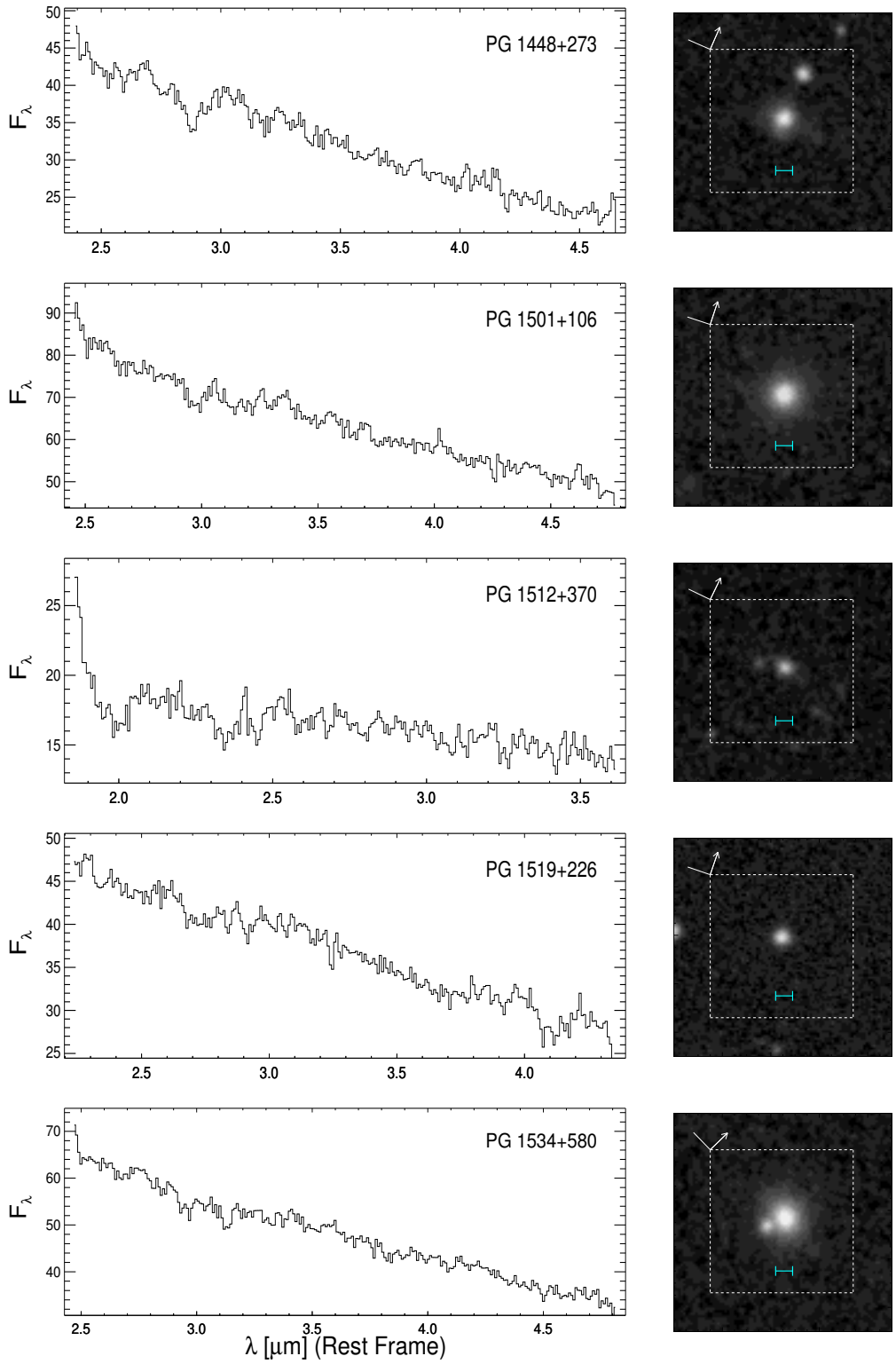

Figure 2.5 Continued

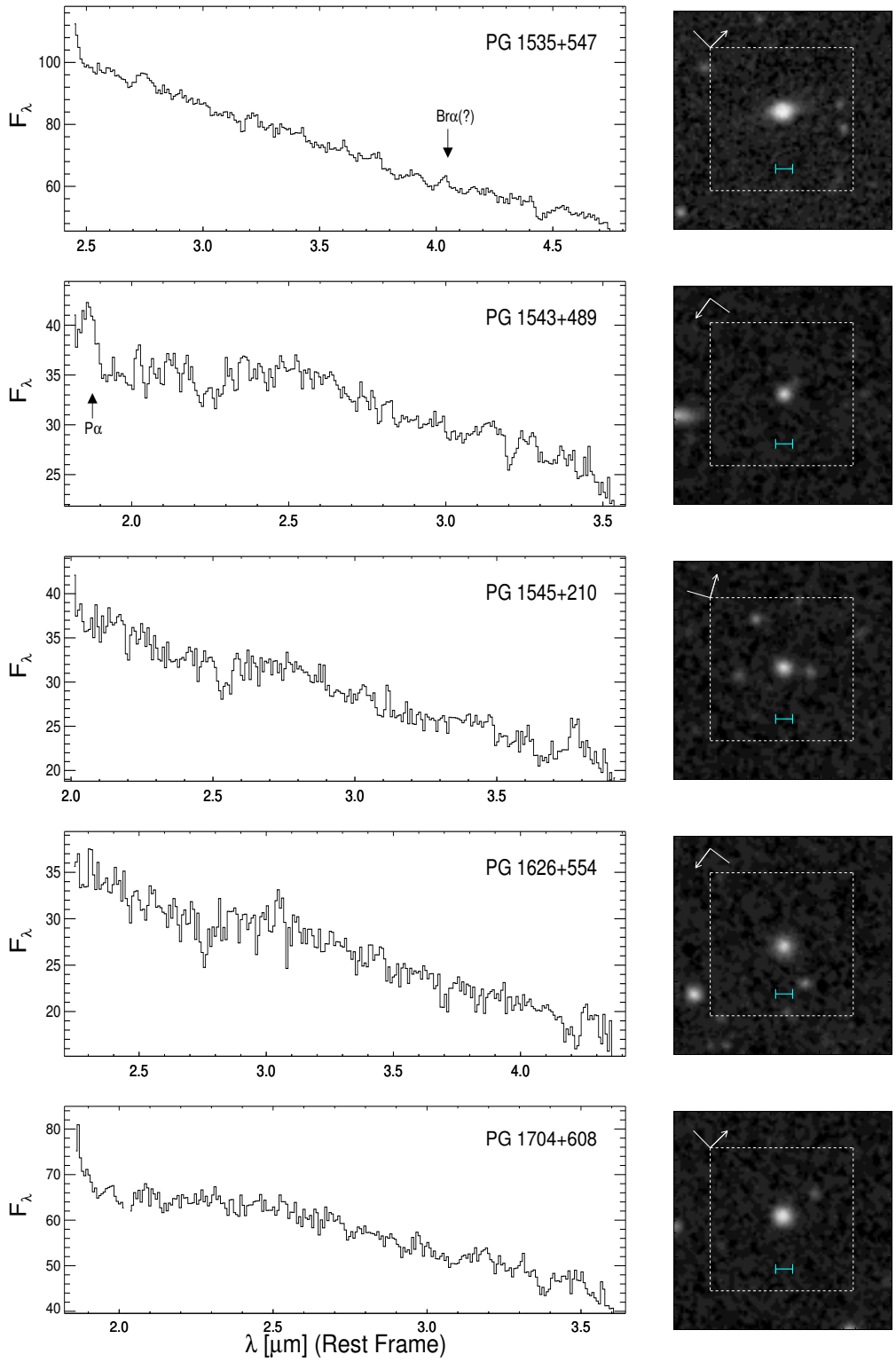

Figure 2.5 Continued

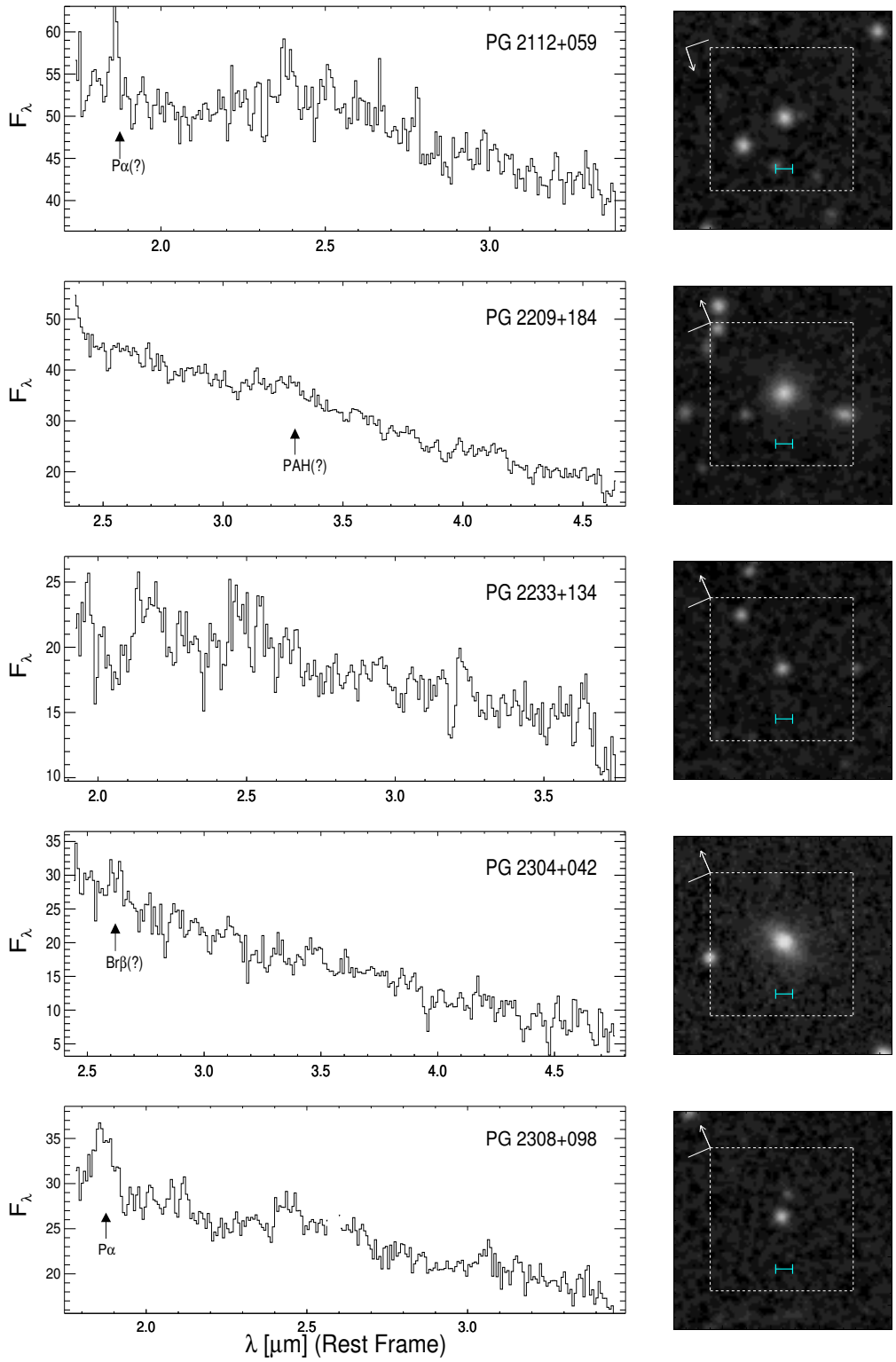

Figure 2.5 Continued

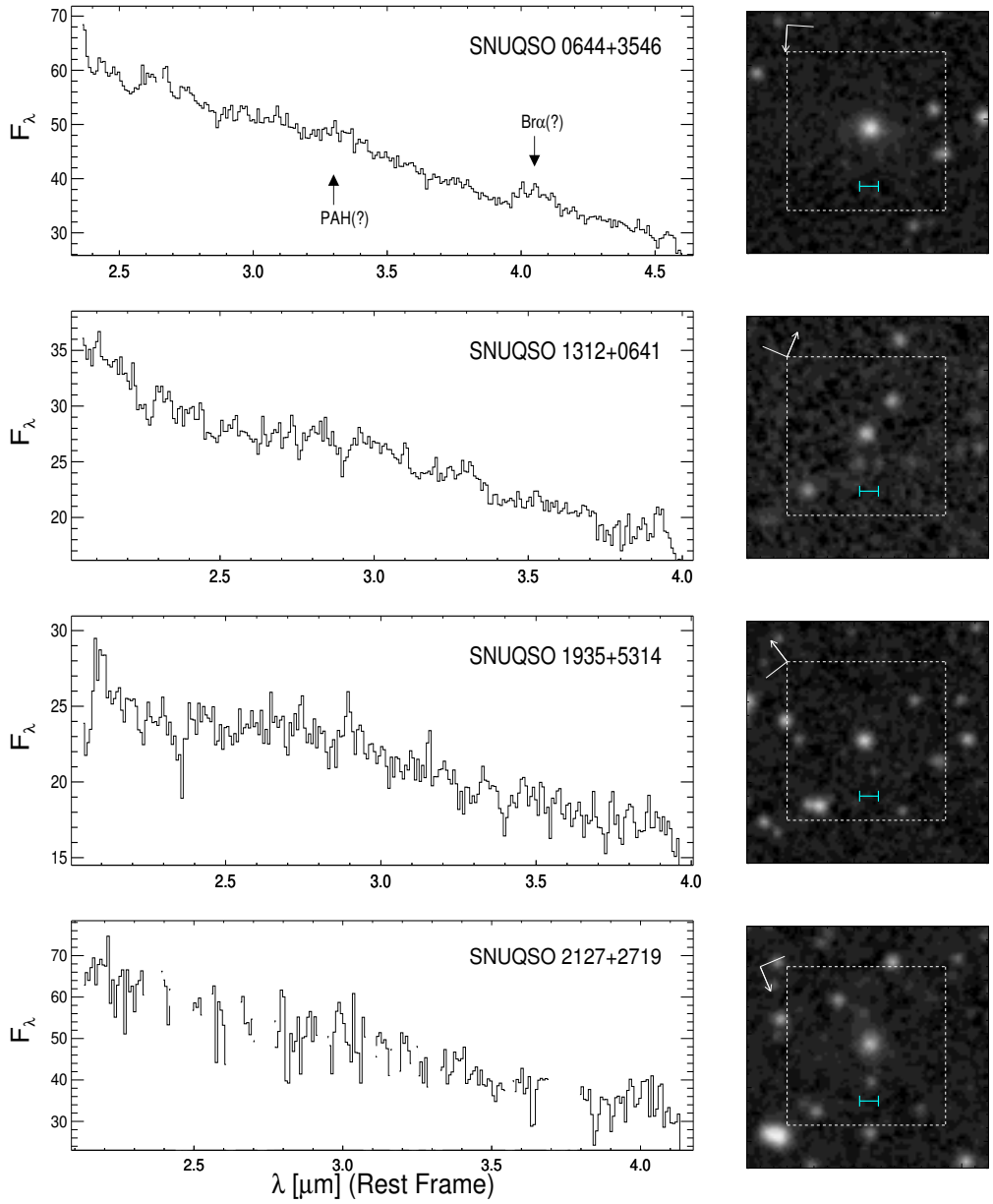

Figure 2.5 Continued

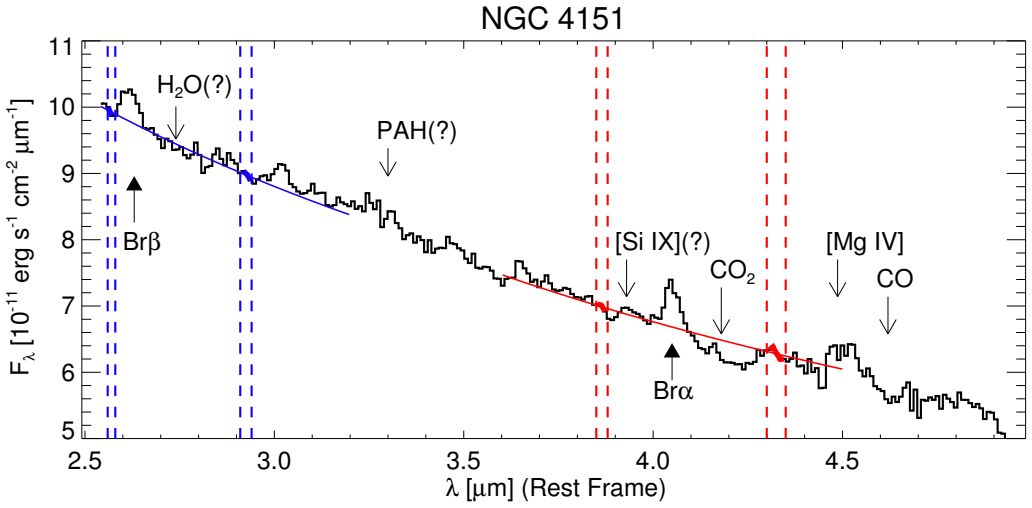

Figure 2.6 NIR spectrum (2.5–5.0 μm) of NGC 4151. The 2.5–5.0 μm wavelength window includes Brα and Brβ lines and various molecular lines such as H_2O, [Si IX], CO_2, [Mg IV], and CO. The blue and the red solid lines indicate the continuum fit to the regions around the Brβ and Brα lines, respectively. The dashed lines indicate the wavelength range used for the continuum fitting.

2.4 BRACKETT LINES

Using the spectra we presented in the previous section, we measured the line fluxes and widths of Brackett lines and used them to estimate the $M_{\rm BH}$ values and the physical conditions of the gas in BLR. In this section, we will describe the measurements of the line fluxes and widths, present the Brackett-line based $M_{\rm BH}$ estimators, and discuss the BLR physical condition inferred from the line luminosity ratios of the NIR Hydrogen lines.

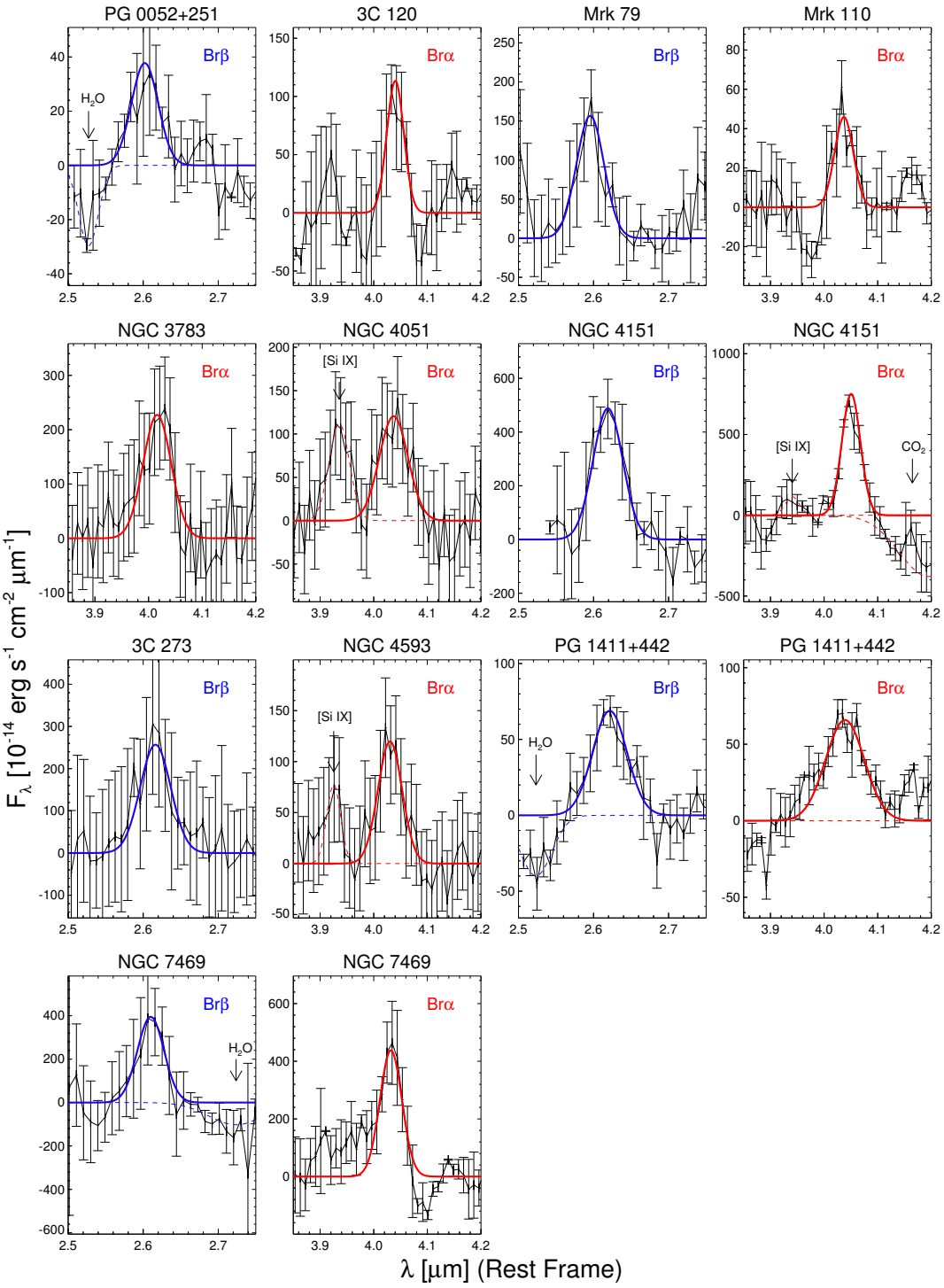

Figure 2.7 Gaussian fits of the Brackett lines of our sample. The black solid lines and bars indicate the observed spectra in rest frame and the associated errors. The blue and red lines indicate the fits for Brβ and Brα, respectively. The dashed lines show the fits to the molecular/atomic lines around Brackett lines, such as H_2O, [Si IX], and CO_2 lines. The solid lines indicate the Brackett line component of the best-fit spectra.

2.4.1 Brackett Line Luminosity and Width

In this subsection, we describe how the Brackett lines are fitted to derive line fluxes and widths. The fitting of the lines starts with the identification of the line in the deredshifted spectra. As mentioned already in the previous section, we find Brα and Brβ at $S/N > 3$ in 9 and 7 AGNs, respectively. After the line identification, the continuum around the Brackett lines were determined by fitting a linear function to both sides of each Brackett line. Although a NIR spectrum of a quasar is dominated by the black body radiation from the hot part of the dust torus, the linear fit of the continuum should provide a reasonable approximation of the local continuum around each emission line (Landt et al. 2008; Kim et al. 2010). However, determining the best wavelength region for the continuum is not a simple task, because many molecular absorption or atomic emission lines exist around the Brackett lines. Such lines are H_2O (2.53, 2.66, 2.73, 2.75–3.55 μm), [Si IX] (3.93 μm), CO_2 (4.26 μm) and CO (4.67 μm). Hence, we chose the continuum regions that are least affected by such lines. The wavelength regions adopted for the continuum determinations are listed in Table 2.

After continuum subtraction, we fit the Brackett lines and molecular/atomic lines simultaneously. Fitting of the molecular/atomic lines near the Brackett lines is necessary, since the fitting of the Brackett lines can be influenced by the presence of molecular/atomic lines such as the H_2O absorption lines at 2.53 and 2.66 μm (for Brβ), and the [Si IX] and CO_2 gas line at 3.93 and 4.1–4.4 μm (for Brα). Figure 6 shows a 2.5–5.0 μm spectrum of NGC 4151, which includes Brα, Brβ, H_2O, [Si IX], and CO_2 lines. The Blue and red solid lines are the continuum levels used for the Brβ and Brα emission line measurements. The region bracketed by the dashed lines indicates the wavelength range used for the continuum fitting of each Brackett line.

We used a single Gaussian function to fit each line considering the low spectral resolution of the *AKARI* spectroscopy, setting the central wavelength, the line

width, and the line flux to be free parameters. An interactive data language (IDL) procedure, `MPFITEXPR` (Markwardt 2009), was used to fit the lines. The fit provides the line-of-sight velocity dispersion, σ, and fluxes of the Brackett lines. Note that the narrow emission line does not significantly affect the line flux and σ measurements. As a test, we set a model spectrum with a broad (σ: 850 – 2500 km s^{-1}) and a narrow line component (σ: 170 km s^{-1}) at the *AKARI* spectral resolution. We adopt the flux ratios of the narrow to broad component flux to be 0.115 and 0.227 for Brβ and Brα, respectively. These ratios are derived by first taking a median Hα narrow/broad component flux ratio in Landt et al. (2008) for five objects (Mrk 110, Mrk 79, NGC 7469, NGC 4593, and NGC 4151), and then converting the Hα flux to the Brackett flux based on the computation from the CLOUDY code (version 10.00; Ferland et al. 1998) for the BLR condition (α = -1.0, $n = 10^9$ cm^{-3}, and $U = 10^{-1.5}$; Kim et al. 2010) and the narrow line condition ($n = 10^{4.5}$ cm^{-3} and $U = 10^{-2}$; Cox 2000). We fitted the degraded model emission line with a single Gaussian function. The measured flux and σ values are 108% (104 – 115%) and 95% (90 – 98%) compared to the original broad component properties, which would affect $M_{\rm BH}$ by a small amount, $\sim$0.03 dex. It is also confirmed that the narrow emission lines in the NIR do not affect the line flux and σ measurements as much ($< 10\%$) in a relatively low-resolution spectra (e.g., Kim et al. 2010).

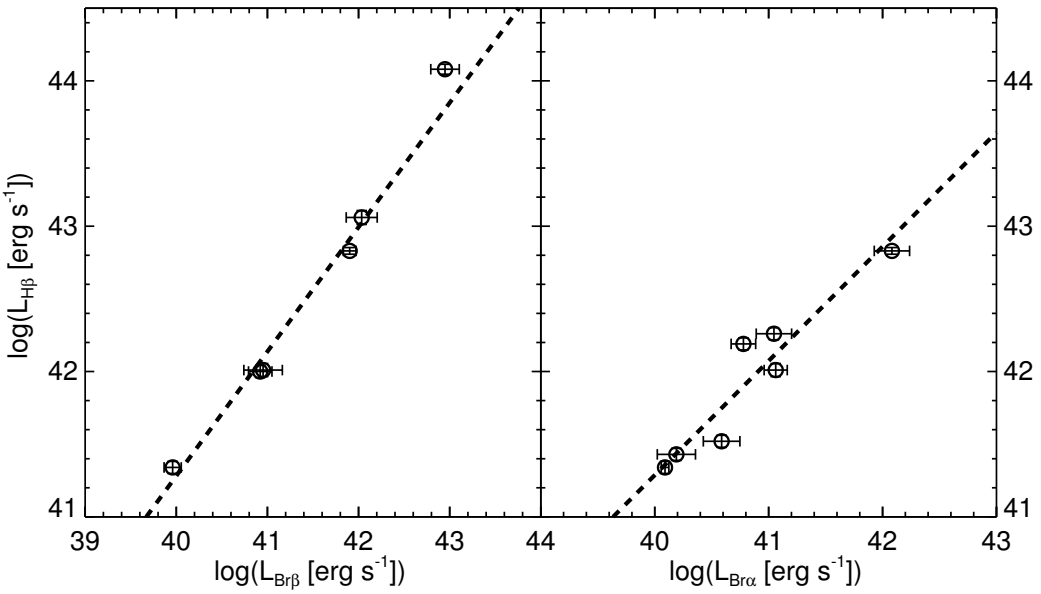

Figure 2.8 Comparison of the line luminosities of the Brackett lines vs. the Hβ line. The dotted line indicates the best-fit correlation between the luminosities of the Hβ and the Brackett lines.

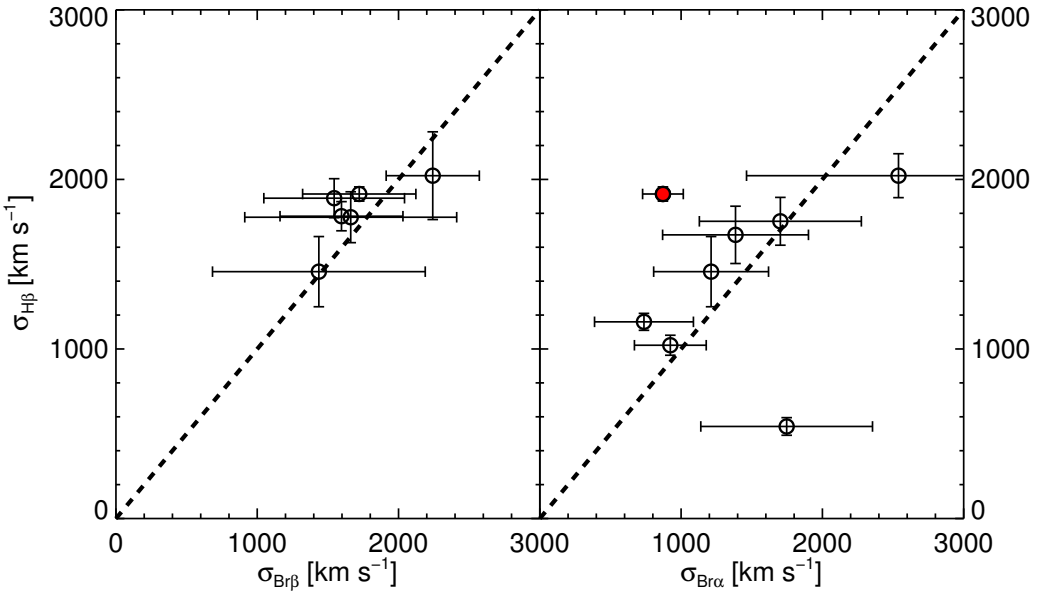

Figure 2.9 Comparison of the σ widths of the Brackett lines vs. those of the Hβ line. The dashed line indicates the case where the σ value of the Hβ and the Brackett lines are identical. The weak correlation for Brα is likely to be due to low S/N and the CO_2 absorption feature right next to the Brα line. The CO_2 absorption is the most prominently seen in the spectrum of NGC 4151, which is represented by the red filled circle.

For further analysis in the following subsections, we exclude objects with substantial σ errors (>60% of the measured σ value) or measured Brackett line FWHM ($2.35\,\sigma$) less than the spectral resolution ($\mathrm{R} = 120\,\lambda/3.6\,\mu\mathrm{m}$). The excluded cases are Mrk 110 (Brβ) and Ark 120 (Brα). Finally, eight Brα and seven Brβ lines are selected and used for further investigation of the line properties. All of these are from the reverberation mapping sample, since the PG QSOs are generally too faint for a reliable fitting of the lines (e.g., Figure 1).

Note that the selected Brackett lines show a small systematic shift in the wavelength of $\delta\lambda = (\lambda_{\mathrm{measured}} - \lambda_{\mathrm{lab}}) \sim -0.014\,\mu\mathrm{m}$ ($\langle\delta\lambda_{\mathrm{Br}\alpha}\rangle = -0.015\,\mu\mathrm{m}$ and $\langle\delta\lambda_{\mathrm{Br}\beta}\rangle = -0.013\,\mu\mathrm{m}$). The Br$\alpha$ and Brβ lines are shifted by a similar amount in wavelength ($\delta\lambda_{\mathrm{Br}\alpha} - \delta\lambda_{\mathrm{Br}\beta} = -0.001 \pm 0.005$), suggesting that the wavelength shift applies to the entire spectral range. The shift is a bit larger than the expected wavelength offset error in the *AKARI* IRC of $0.01\,\mu\mathrm{m}$ (Ohyama et al. 2007). The origin of the systematic offset is unclear, although it seems to be instrumental. A potential source of the offset is molecular/atomic absorption affecting the peak wavelength of the emission lines. However, if this were true, then we would expect a stronger offset in Brα than in Brβ since Brβ is generally much less affected by molecular absorption features than Brα, but this was not the case.

The formal fitting errors are found to be about 27% (between 7% and 49%) in σ and 28% (between 6% and 46%) in flux, due to low S/N and the necessity of simultaneously fitting the other lines in the vicinity. Another source of error comes from the determination of the continuum. We varied the wavelength regions for the continuum fit from the values noted in Table 2 to see how strongly the changes in the continuum level affect the line fitting results. We find that the variation in the continuum level changes the derived σ and flux values by 13% and 8% respectively. Overall, combining these two errors, we obtain the error in σ and flux to be 33% and 30%, which corresponds to 0.30 dex in M_{BH}.

Energy sources of the Brackett lines could be BH activity or star formation activity. Considering the large slit aperture of the IRC and the extraction width we adopted, the measured Brackett line fluxes may include the star formation contribution from the host galaxy. To determine the dominant energy source of the Brackett lines, we compared the expected $L_{\mathrm{Br}\alpha}$ from star formation to the measured $L_{\mathrm{Br}\alpha}$. The relationships $L_{3.3\mathrm{PAH}}/L_{\mathrm{IR}} \sim 10^{-3}$ (Mouri et al. 1990; Imanishi 2002) and $L_{\mathrm{Br}\alpha}/L_{\mathrm{IR}} \sim 10^{-4}$ (Imanishi et al. 2010) are expected for starburst galaxies, suggesting that the luminosity of the Brα line from star formation is 10% of the 3.3 μm PAH line luminosity. Among our seven Brα-detected AGNs, the 3.3 μm PAH emission line is detected in only two objects (NGC 4051 and NGC 7469) using the extraction width adopted in this study (Kim et al. in prep). The expected star formation contributions of the Brα line based on the 3.3 μm PAH line are 8% and 46% for NGC 4051 and NGC 7469, respectively. This assumes the above 10% flux ratio of $L_{\mathrm{Br}\alpha}$ to $L_{3.3\mathrm{PAH}}$, but the relation contains a large scatter of a factor of two to three. Therefore, we conclude that the contribution of star formation to the Bracket emission lines is negligible (no or weak detection of PAHs) for most of the AGNs in our sample. NGC 7469 is an exceptional case with a very strong 3.3 μm PAH. Even in this case, the star formation contribution is less than half for Brα, but we caution possible over-estimation of the line flux (134%) and under-estimation of the line width (80%) for NGC 7469.

The measured values of the σ and luminosities of the Brackett lines and the corresponding Hβ properties are presented in Table 2. Note that the σ values are corrected for the instrumental resolution by subtracting the instrumental resolution in quadrature ($\sigma^2 = \sigma^2_{\mathrm{obs}} - \sigma^2_{\mathrm{inst}}$) from the observed values. The derivation of the line luminosities assumes a standard ΛCDM cosmology of H_0=70 km s^{-1} Mpc^{-1}, Ω_m=0.3 and Ω_Λ=0.7 (e.g., Im et al. 1997)

Table 2.2. Brackett Parameters And References

Object Name	Brβ				Brα				Hβ	
	σ [km s^{-1}]	L [10^{40}erg s^{-1}]	SCDR [μm]	LCDR [μm]	σ [km s^{-1}]	L [10^{40}erg s^{-1}]	SCDR [μm]	LCDR [μm]	L [10^{42}erg s^{-1}]	σ [km s^{-1}]
(1)	(2)	(3)	(4)	(5)	(6)	(7)	(8)	(9)	(10)	(11)
3C 120	–	–	–	–	737 ± 349	11.1 ± 4.0	3.80–3.84	4.25-4.30	1.81[d]	1160[c]
PG 0052+251	1596 ± 435	108 ± 42	2.48–2.54	2.78–2.83	–	–	–	–	11.4[a]	1783[c]
Mrk 79	1544 ± 497	8.33 ± 2.46	2.52–2.54	2.72–2.73	–	–	–	–	1.00[e]	1889[c]
Mrk 110	–	–	–	–	923 ± 254	6.00 ± 1.48	3.85–3.88	4.30–4.35	1.54[e]	1022[c]
NGC 3783	–	–	–	–	1702 ± 573	3.86 ± 1.42	3.89–3.92	4.25–4.29	0.33[b]	1753[c]
NGC 4051	–	–	–	–	1747 ± 607	0.17 ± 0.07	3.83–3.87	4.26–4.30	–	543[c]
NGC 4151	1722 ± 400	0.91 ± 0.20	2.56–2.58	2.91–2.94	871 ± 144	1.23 ± 0.10	3.85–3.88	4.30–4.35	0.22[e]	1914[c]
3C 273	1661 ± 749	889 ± 319	2.53–2.56	2.68–2.73	–	–	–	–	120[a]	1770[c]
NGC 4593	–	–	–	–	1385 ± 516	1.54 ± 0.60	3.70–3.75	4.13–4.18	0.27[e]	1673[c]
PG 1411+442	2242 ± 329	79.9 ± 12.7	2.41–2.48	2.72–2.80	2538 ± 1075	120 ± 43	3.90–3.93	4.30–4.37	6.76[a]	2022[c]
NGC 7469	1436 ± 752	8.96 ± 4.35	2.54–2.57	2.65–2.68	1212 ± 406	11.5 ± 2.7	3.86–3.87	4.14–4.18	1.02[b]	1456[c]

Note. — Columns are as follow: (1) Object name; (2) Brα FWHM; (3) Brα luminosity; (4) Short wavelength side of continuum determination region for the Brα; (5) Long wavelength side of continuum determination region for the Brα; (6) Brβ FWHM; (7) Brβ luminosity; (8) Short wavelength side of continuum determination region for the Brβ; (9) Long wavelength side of continuum determination region for the Brβ; (10) luminosity and (11) FWHM of Hβ. For column (10) and (11), we adopted the luminosities and FWHMs of Hβ from literatures and make footnotes as their literatures: [a]Kaspi et al. (2000); [b]Marziani et al. (2003); [c]Peterson et al. (2004); [d]Vestergaard & Peterson (2006); [e]Landt et al. (2008)

2.4.2 Correlation between Balmer and Brackett Lines

In this section, we will investigate how the properties of the Brackett lines correlate with those of the Balmer lines. If the two lines arise from BLRs similar to each other, then we expect their line properties to correlate well. This would justify the use of the Brackett lines as an $M_{\rm BH}$ estimator (e.g., Kim et al. 2010), just like the Balmer lines that are commonly used as $M_{\rm BH}$ estimators (Greene & Ho 2005, 2007). For this comparison, we take the average of the multi-epoch σ values and the luminosities of the Hβ line from previous studies (Kaspi et al. 2000; Marziani et al. 2003; Peterson et al. 2004; Vestergaard & Peterson 2006; Landt et al. 2008). When there is a large discrepancy in the σ values ($> \times 1.5$) of Hβ and Hα, we take the average of the two. Such a case occurred for only one object (PG 1411+442). Note that we could not find the Hβ line luminosity data for NGC 4051, so we only adopted a σ value from Peterson et al. (2004) for NGC 4051.

Figures 8 and 9 show the correlations between the Brackett lines and the Hβ line in luminosity and σ. In Figure 8, we compare the luminosities of the Brackett lines with those of the Hβ line. The Pearson correlation coefficients are 0.991 and 0.947 for Brβ and Brα, respectively. By performing a linear bisector fit to these points, we find that the two quantities correlate with each other as

$$\log\left(\frac{L_{\rm H\beta}}{10^{42}\ {\rm erg\ s^{-1}}}\right) = (0.99 \pm 0.05) + (0.85 \pm 0.05) \log\left(\frac{L_{\rm Br\beta}}{10^{42}\ {\rm erg\ s^{-1}}}\right), \quad (2.1)$$

and

$$\log\left(\frac{L_{\rm H\beta}}{10^{42}\ {\rm erg\ s^{-1}}}\right) = (0.86 \pm 0.11) + (0.79 \pm 0.07) \log\left(\frac{L_{\rm Br\alpha}}{10^{42}\ {\rm erg\ s^{-1}}}\right). \quad (2.2)$$

In Figure 9, the dashed line indicates a perfect correlation between the σ values of the Brackett and Hβ lines. The figures show a reasonable correlation between the Brβ and Hβ line widths, but a weak correlation between the Brα and Hβ line

widths. The Pearson correlation coefficients are 0.735 and 0.273 for Brβ and Brα, respectively. The weak correlation in σ for Brα is likely due to low S/N and the difficulty in fitting some of the Brα lines. The zodiacal background increases rapidly at $\lambda > 4$ μm, causing the background noise to increase for Brα. Furthermore, the existence of the CO_2 absorption feature right next to Brα makes it challenging to provide a good fit. CO_2 absorption is the most prominent in the spectrum of NGC 4151, which also seems to be a significant outlier in Figure 9.The exclusion of the NGC 4151 point improves the σ correlation for Brα, with the correlation coefficient of 0.468.

We also compared the Brackett line luminosities to the BLR radii. For the radii of BLR, we adopted values from the time lags in the variability between the Hβ and the L_{5100} from Bentz et al. (2013). Figure 10 shows the correlation between the Brackett line luminosities and the BLR radii. The best-fit relations are

$$\log\left(\frac{R_{\rm BLR}}{\rm lt-days}\right) = (0.82 \pm 0.08) + (0.62 \pm 0.05)\log\left(\frac{L_{\rm Br\beta}}{10^{40}\ {\rm erg\ s^{-1}}}\right), \qquad (2.3)$$

and

$$\log\left(\frac{R_{\rm BLR}}{\rm lt-days}\right) = (0.75 \pm 0.03) + (0.66 \pm 0.06)\log\left(\frac{L_{\rm Br\alpha}}{10^{40}\ {\rm erg\ s^{-1}}}\right). \qquad (2.4)$$

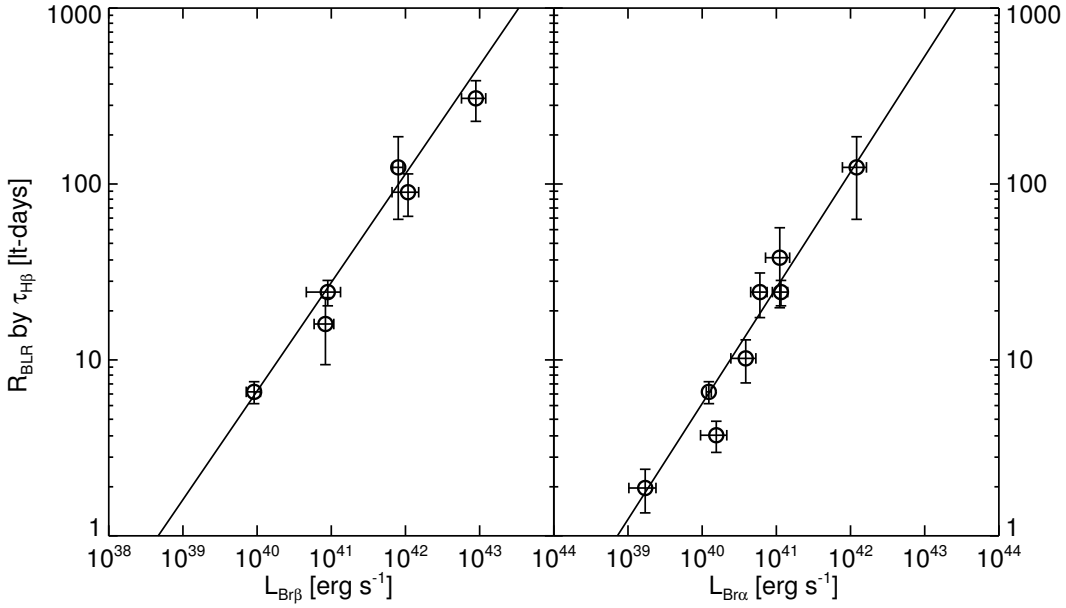

Figure 2.10 Comparison of the line luminosities of the Brackett lines vs. the BLR sizes. For the BLR size, we use the time lag in the variability between the Hβ and L_{5100} from Bentz et al. (2013). The solid line indicates the best-fit correlation between the luminosities of the Brackett lines and the BLR sizes.

2.4.3 BH Mass Estimators with Brackett Lines

In this section, we present $M_{\rm BH}$ estimators that are based on the Brβ and Brα lines. The idea here is that the radius and the velocity of the BLR can be inferred from the luminosity and σ of the Brackett lines, similar to the $M_{\rm BH}$ estimators based on the Balmer of the Paschen lines. Mathematically, we need to find three unknown parameters a, b, and c in the following equation:

$$\log(M) = a + b\log(L) + c\log(\sigma). \tag{2.5}$$

For simplicity, we fix the exponent of the velocity term, c to 2, as expected in the virial theorem. The exponent of the luminosity term, b, is expected to be 0.5 theoretically and empirically, i.e., $R_{\rm BLR} \sim L^{0.5}$ (Dibai 1977; Kaspi et al. 2000; Greene & Ho 2005; Kim et al. 2010). However, we will treat b as a free parameter. In order to derive the $M_{\rm BH}$ estimators, we used the `MPFITEXY` routine (Williams et al. 2010) to fit a linear relationship in the logarithmic scale as in Equation (5). `MPFITEXY` returns the fitted parameters with the uncertainties of the parameters and an intrinsic scatter in the fitted relation. The routine has been tested against several other similar routines, and has shown to return reliable outputs (Park et al. 2012). As a result, we obtain the following relations:

$$\frac{M_{\rm BH}}{M_\odot} = 10^{6.61\pm0.23}\left(\frac{L_{{\rm Br}\beta}}{10^{40}\ {\rm erg\ s^{-1}}}\right)^{0.68\pm0.13}\left(\frac{\sigma_{{\rm Br}\beta}}{10^{3}\ {\rm km\ s^{-1}}}\right)^{2}, \tag{2.6}$$

and

$$\frac{M_{\rm BH}}{M_\odot} = 10^{6.68\pm0.20}\left(\frac{L_{{\rm Br}\alpha}}{10^{40}\ {\rm erg\ s^{-1}}}\right)^{0.66\pm0.21}\left(\frac{\sigma_{{\rm Br}\alpha}}{10^{3}\ {\rm km\ s^{-1}}}\right)^{2}. \tag{2.7}$$

In Figure 11, we plot the $M_{\rm BH}$ from the reverberation mapping method versus the $M_{\rm BH}$ from the Brackett-line-based estimators, i.e., the values from Equations (6) and (7). The rms scatters of the data points (including measurement errors) with respect to the best-fit correlations of Equations (6) and (7) are 0.229 dex (Brβ) and

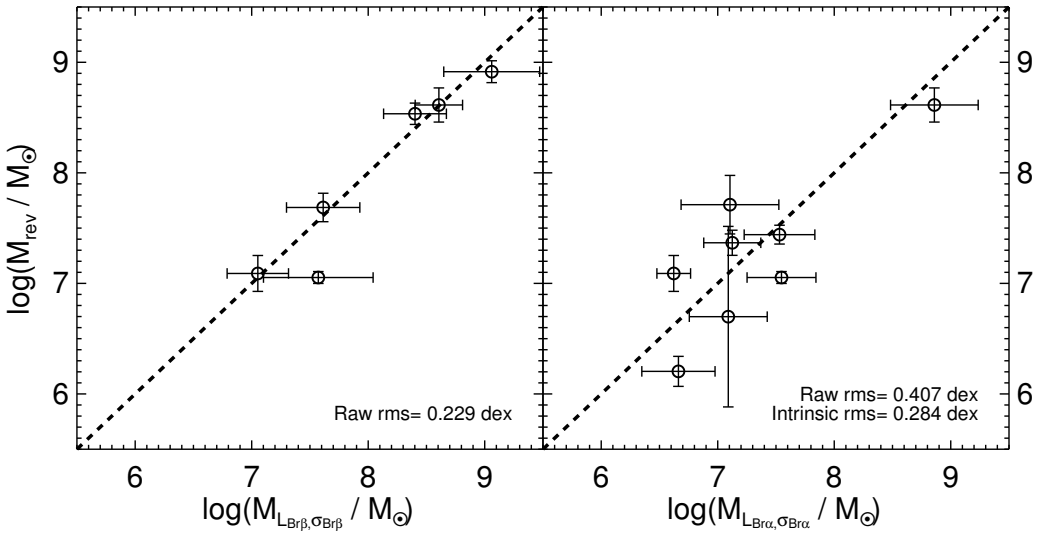

Figure 2.11 Comparison of the Brackett-line-based $M_{\rm BH}$ vs. $M_{\rm BH}$ derived from the reverberation mapping method. The Brackett-line-based $M_{\rm BH}$ is derived by using the L and σ of the Brackett lines as Equations (6) and (7). The dashed line indicates a line where $M_{\rm BH}$ from Brackett lines and the reverberation mapping methods are identical. In each panel, we indicate the intrinsic and the raw (no correction of the measurement errors) scatters of the points with respect to the dashed line.

0.407 dex (Brα). The intrinsic scatter of Equation (7) is 0.284 dex, but the intrinsic scatter of Equation (6) is not determined since the fit did not require intrinsic scatter. The value of the intrinsic scatter is expected to be small ($\lesssim$ 0.2 dex).

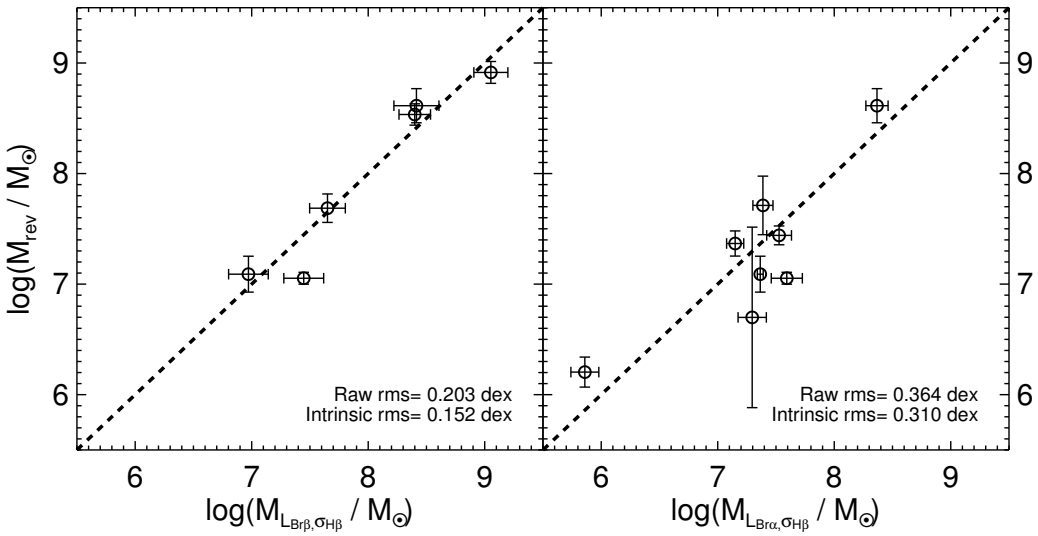

Figure 2.12 Comparison of $M_{\rm BH}$ from Equations (8) and (9) vs. $M_{\rm BH}$ derived from the reverberation mapping method. The Equations (8) and (9) are established by using the $L_{{\rm Br}\alpha,\beta}$ but adopting $\sigma_{{\rm H}\beta}$. The meaning of the line is identical to Figure 11.

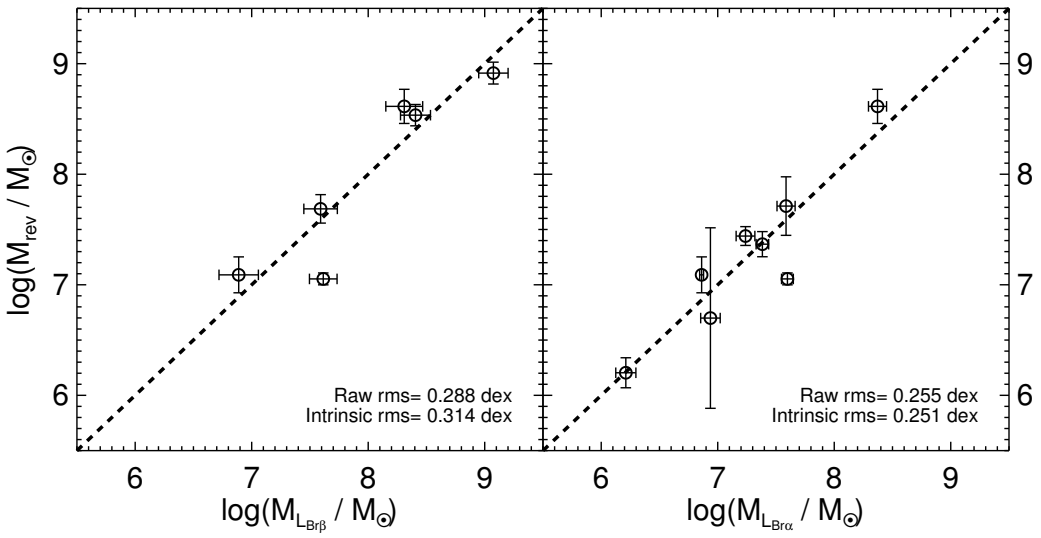

Figure 2.13 Comparison of $M_{\rm BH}$ from Equations (10) and (11) vs. $M_{\rm BH}$ derived from the reverberation mapping method. The Equations (10) and (11) are established by using only $L_{{\rm Br}\alpha,\beta}$. The meanings of the line is identical to Figure 11.

Since the σ values are rather poorly determined from the Brackett lines but we expect that they correlate closely with the σ values of the Hβ, we also derived the $M_{\rm BH}$ estimators using $L_{{\rm Br}\alpha,\beta}$ but adopting $\sigma_{{\rm H}\beta}$ as a proxy for $\sigma_{{\rm Br}\alpha,\beta}$. The $\sigma_{{\rm H}\beta}$ values are taken from Peterson et al. (2004). Since dust extinction in a host galaxy can reduce its line luminosity significantly but not as much for the line width, this is a plausible path to estimate $M_{\rm BH}$ of red AGNs whose $\sigma_{{\rm H}\beta}$ can be determined to a good accuracy, but its Hβ luminosity is quite uncertain due to an unknown amount of dust extinction. In this process, we also fixed the exponent of the velocity term, c, to 2. The resultant $M_{\rm BH}$ estimators using $L_{{\rm Br}\alpha,\beta}$ and $\sigma_{{\rm H}\beta}$ are given below and also in Figure 12 as

$$\frac{M_{\rm BH}}{M_\odot} = 10^{6.44\pm0.17} \left(\frac{L_{{\rm Br}\beta}}{10^{40}\ {\rm erg\ s^{-1}}}\right)^{0.72\pm0.10} \left(\frac{\sigma_{{\rm H}\beta}}{10^3\ {\rm km\ s^{-1}}}\right)^2, \tag{2.8}$$

and

$$\frac{M_{\rm BH}}{M_\odot} = 10^{6.76\pm0.17} \left(\frac{L_{{\rm Br}\alpha}}{10^{40}\ {\rm erg\ s^{-1}}}\right)^{0.48\pm0.17} \left(\frac{\sigma_{{\rm H}\beta}}{10^3\ {\rm km\ s^{-1}}}\right)^2. \tag{2.9}$$

The raw rms scatters (including measurement errors) with respect to a perfect correlation between the reverberation-mapping-based $M_{\rm BH}$ and $M_{\rm BH}$ for Equations (8) and (9) are 0.203 dex (Brβ) and 0.364 dex (Brα), while the intrinsic scatters are 0.152 dex (Brβ) and 0.310 dex (Brα). However, the intrinsic scatters are not better than the values for the purely Brackett-based $M_{\rm BH}$ estimators in Equations (6) and (7).

Since the σ values of Brackett lines, especially for Brα, show a weak correlation, we test whether or not the σ values of Brackett lines are adding useful information to the $M_{\rm BH}$ estimators. For this test, we derive $M_{\rm BH}$ estimators using only Brackett line luminosities:

$$\frac{M_{\rm BH}}{M_\odot} = 10^{6.92\pm0.26} \left(\frac{L_{{\rm Br}\beta}}{10^{40}\ {\rm erg\ s^{-1}}}\right)^{0.73\pm0.15}, \tag{2.10}$$

and

$$\frac{M_{\rm BH}}{M_\odot} = 10^{6.79\pm0.15} \left(\frac{L_{\rm Br\alpha}}{10^{40}\ {\rm erg\ s^{-1}}} \right)^{0.76\pm0.14}. \quad (2.11)$$

Figure 13 shows the $M_{\rm BH}$ values from the reverberation mapping method versus the $M_{\rm BH}$ values from the $M_{\rm BH}$ estimators using only $L_{\rm Br\beta}$ or $L_{\rm Br\alpha}$, i.e., the values from Equations (10) and (11). We find that the intrinsic scatters in these relations are 0.314 dex (Brβ), and 0.251 dex (Brα). Therefore, for Brβ, the intrinsic scatter in the $M_{\rm BH}$ estimators becomes smaller as we move from the luminosity-only estimator to the full Brβ luminosity+σ estimators, lending support to the usefulness of Equation (6). On other hand, the same cannot be said for the Brα-based estimators. This suggests that Brα σ measurement is more challenging with the current data, and the evaluation of the Brα-based $M_{\rm BH}$ estimators is needed with data sets with better sensitivity. Considering that the Eddington ratio of AGNs used for Equations (10) and (11) are between 0.015 and 0.225, Equations (10) and (11) could be useful when (i) the Brackett line luminosities are available but not for reliable σ values and (ii) the Eddington ratio of the sample is within a range of 0.015 to 0.225.

2.4.4 Line Luminosity Ratios

We investigate the physical conditions of BLR by comparing the observed line luminosity ratios of the Balmer through Brackett lines to the line luminosity ratios computed from the CLOUDY code (version 10.00; Ferland et al. 1998). The line luminosity ratios are computed by varying three physical parameters – the shape of the ionizing continuum (α = -1.0, -1.5), the ionization parameter ($U = 10^{-5.5}$ – $10^{0.5}$), and the hydrogen density ($n = 10^9$ – 10^{13} cm^{-3}). The hydrogen number densities are commonly taken as $n \simeq 10^9$ – 10^{10} cm^{-3} for type-1 AGNs (Davidson & Netzer 1979; Rees et al. 1989; Ferland & Persson 1989), but there are studies suggesting a high hydrogen number density ($n > 10^{12}$cm^{-3}) with a low ionization parameter of $U = 10^{-5}$ (e.g., Ruff et al. 2012) for BLR.

Figure 14 shows the observed line luminosity ratios (with respect to Hβ) as a function of wavelength for seven AGNs, for which we have at least one Brackett to Balmer line ratio and an additional line ratio of either Paschen or Brackett lines. The line luminosities are corrected for galactic extinction with the York Extinction Solver (McCall 2004), adopting $E(B-V)$ values from Schlafly & Finkbeiner (2011) and $R_V = 3.07$. No attempt is made to correct for internal dust extinction. Note that the Paschen line ratios are taken from Kim et al. (2010). The mean line ratios of the seven AGNs are $L_{\mathrm{Br}\alpha}/L_{\mathrm{Br}\beta} = 1.37 \pm 0.31$, $L_{\mathrm{Br}\beta}/L_{\mathrm{H}\beta} = 0.073 \pm 0.010$, and $L_{\mathrm{Br}\alpha}/L_{\mathrm{H}\beta} = 0.081 \pm 0.014$.

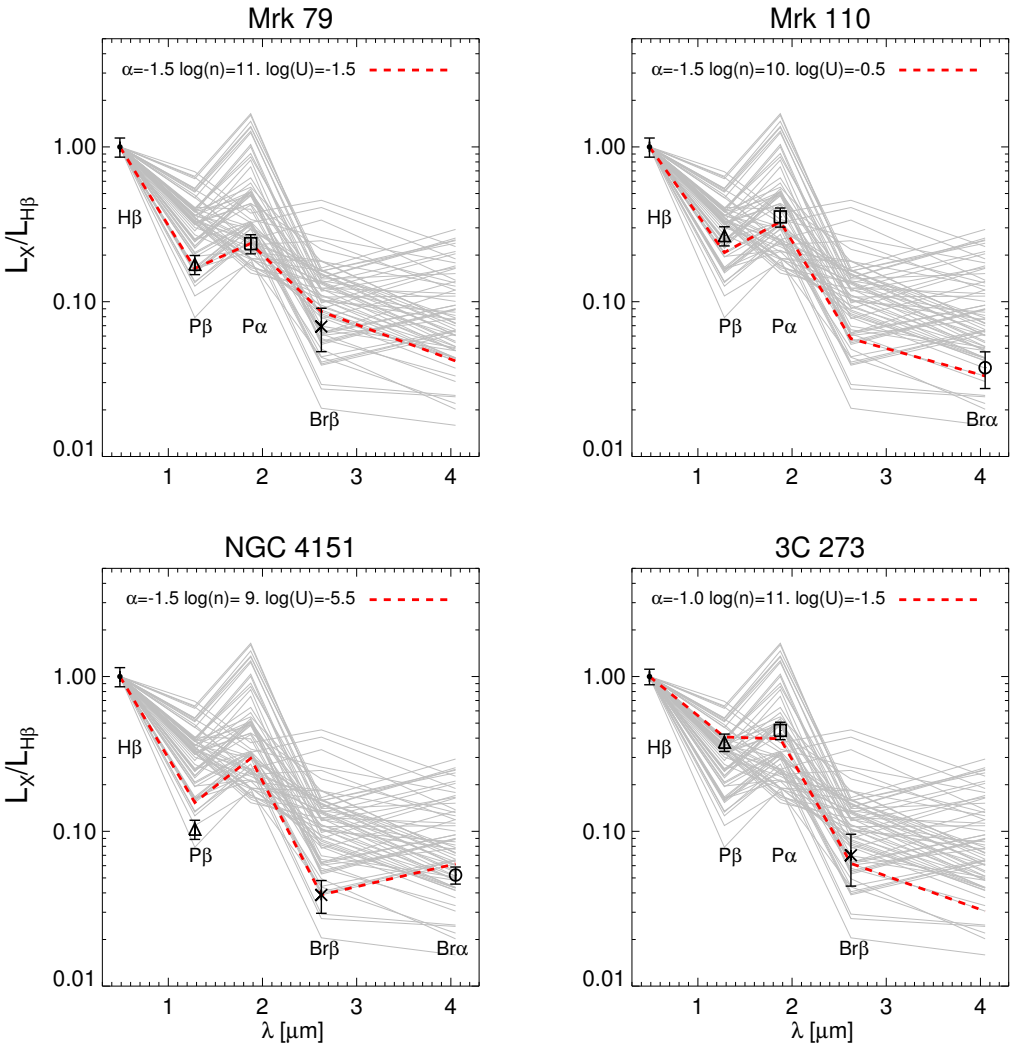

Figure 2.14 Line luminosity ratios of Paschen and Brackett with respect to Hβ. The crosses and the circles represent AGNs in the reverberation mapped sample with the Brackett line luminosity measurements. When available, we also plot the line luminosity ratios for Pα (squares) and Pβ (triangles) with respect to Hβ from Kim et al. (2010). The gray lines represent the expected line ratios from the CLOUDY code, assuming various parameters with different combinations of $\alpha = -1.0 \sim -1.5$, $n = 10^{9\sim13}$ cm^{-3}, and $U = 10^{-5.5\sim0.5}$. In each panel, we indicate the most likely set of the parameters, with the CLOUDY model predictions for such a parameter set in the red dashed line.

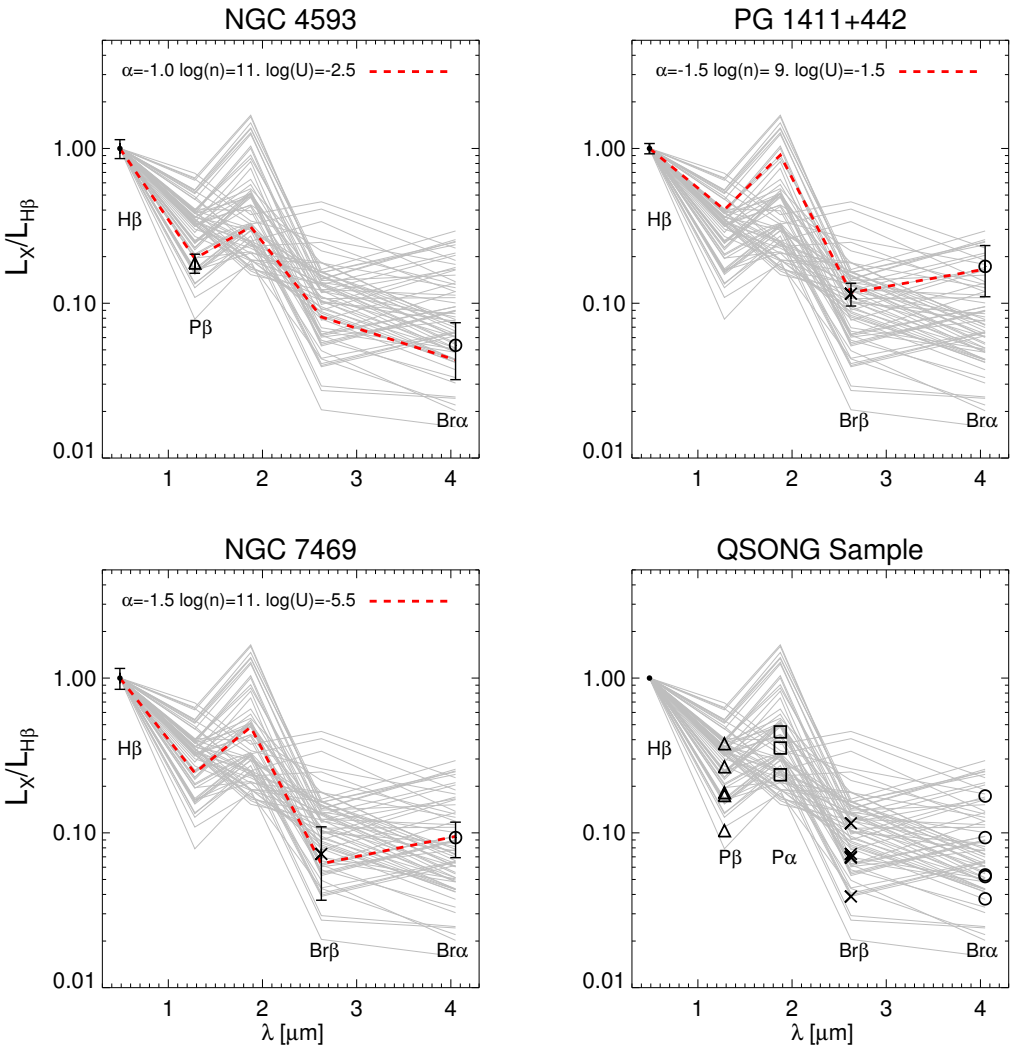

Figure 2.14 Continued

Table 2.3. BLR Conditions

Object Name	α	n $[\mathrm{cm}^{-3}]$	U
Mrk 79	-1.5	10^{11}	$10^{-1.5}$
Mrk 110	-1.5	10^{10}	$10^{-0.5}$
NGC 4151	-1.5	10^{9}	$10^{-5.5}$
3C 273	-1.0	10^{11}	$10^{-1.5}$
NGC 4593	-1.0	10^{11}	$10^{-2.5}$
PG 1411+442	-1.5	10^{9}	$10^{-1.5}$
NGC 7469	-1.5	10^{11}	$10^{-5.5}$

In order to find the most likely physical condition for each object, we searched for a parameter set that minimizes χ^2, which is a function of line ratios such as $L_{\mathrm{P}\beta}/L_{\mathrm{H}\beta}$, $L_{\mathrm{P}\alpha}/L_{\mathrm{H}\beta}$, $L_{\mathrm{Br}\beta}/L_{\mathrm{H}\beta}$, and $L_{\mathrm{Br}\alpha}/L_{\mathrm{H}\beta}$ following the approach by Ruff et al. (2012):

$$\chi^2 = \sum_{i=1}^{N} \frac{(R_{\mathrm{observed},i} - R_{\mathrm{model},i})^2}{\sigma_i^2}, \tag{2.12}$$

where N is the number of line luminosity ratios, and two types of R_i are the line luminosity ratios from either observation (when with a subscript, "observed") or the CLOUDY model (with a subscript, "model"), and σ_i is the error in the measured line ratio. The best-fit parameter sets are indicated for each object in Figure 14, and are summarized in Table 3. The best-fit line luminosity ratios are also plotted as a red dashed line in Figure 14.

The CLOUDY models can reproduce the observed line luminosity ratios, under commonly cited BLR physical conditions of $n = 10^9$ – 10^{11} cm^{-3} and $U = 10^{-2.5}$ – $10^{0.5}$, suggesting that most of the objects with Brackett line detections do not require a more exotic condition ($n > 10^{12}$ cm^{-3} and $U < 10^{-5}$), such as that found in Ruff et al. (2012). One exception is NGC 7469, for which we find a best-fit parameter set of $n = 10^{11}$ cm^{-3} and $U = 10^{-5.5}$. This is the case where the Brackett line luminosity may be affected by the star formation component (possibly by as much as 50%), and thus the interpretation of the line luminosity ratio result cannot be taken too seriously for this object.

2.5 DUST COMPONENT

In this section, we present hot (> 1000 K; e.g., Barvainis 1987; Glikman et al. 2006) and warm (~ 200 K; e.g., Netzer et al. 2007; Deo et a. 2009) dust temperatures and luminosities of the PG QSOs and the reverberation-mapped AGNs, and we investigate the correlation between hot dust luminosity ($L_{\rm HD}$) and $L_{\rm bol}$. For this purpose, we restrict our analysis to luminous AGNs with $L_{\rm bol} > 10^{45.7}$ erg s^{-1} for which the host galaxy light contribution is less than 10% at 0.51 μm (Shen et al. 2011), and even smaller at NIR.

To study the AGN dust components, we assembled a multi-wavelength data set from the optical to MIR by obtaining photometry of the objects from SDSS, 2MASS, *WISE* ($W3$ and $W4$), and *ISO* (7.3 μm: Haas et al. 2003). These multi-wavelength photometric data are combined with the *AKARI* spectra, and we fit them with a SED model that is composed of a single power law and a double black body radiation component as

$$F_\nu = C_0\nu^\alpha + C_1 B_\nu(T_{\rm HD}) + C_2 B_\nu(T_{\rm WD}), \tag{2.13}$$

where α is the slope of the underlying power-law continuum which dominates the

optical light, B_ν is the Planck function as a function of ν, $T_{\rm HD}$ and $T_{\rm WD}$ are the hot and warm dust temperatures, and C_0, C_1, and C_2 are the normalization constants of each component. The fitting result gives us the luminosities and the temperatures of the hot/warm dust components.

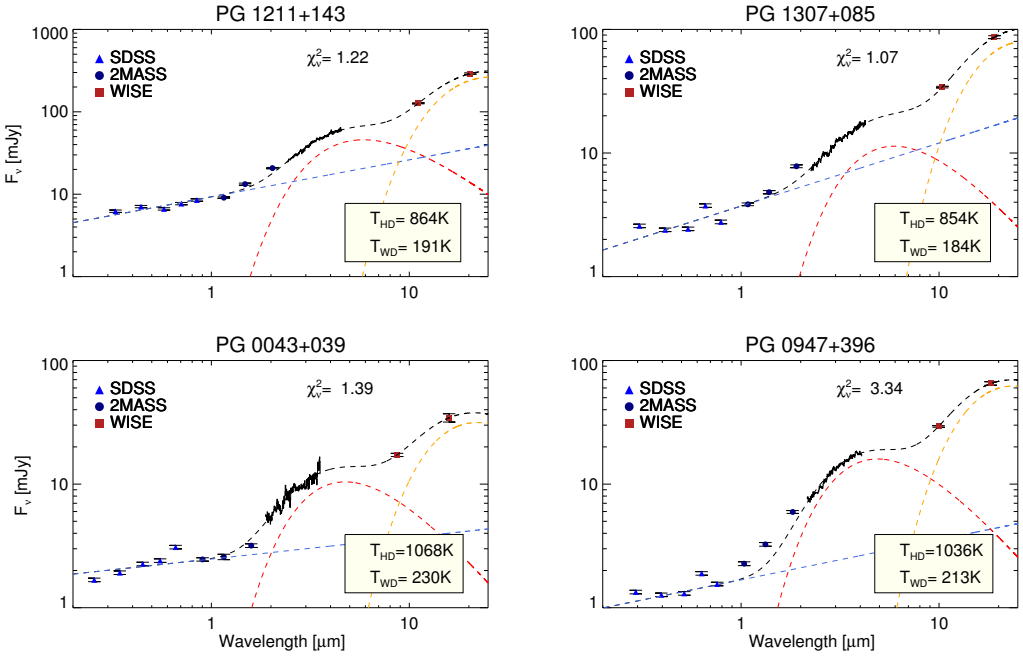

Figure 2.15 Photometric and spectroscopic SED. The SEDs are shown in rest-frame. Triangle, circle, square, and star indicate photometric data point from SDSS, 2MASS, *WISE* ($W3$ and $W4$), and *ISO* (7.3 μm), respectively. The black solid line denotes *AKARI* spectrum. The dashed lines are fitted results. The blue, red, and yellow dashed lines mean power-law, hot, and warm dust components, respectively, and the black dashed line is the sum of all components. The measured hot and warm dust temperatures are indicated in the lower right-hand corner. The dust properties are taken only if $\chi^2_\nu < 5$, and the χ^2_ν of each sample is indicated at top of each figure. The PG 1322+659 is excluded by the χ^2_ν limit, and the SED of the PG 1322+659 is indicated in last panel of this figure.

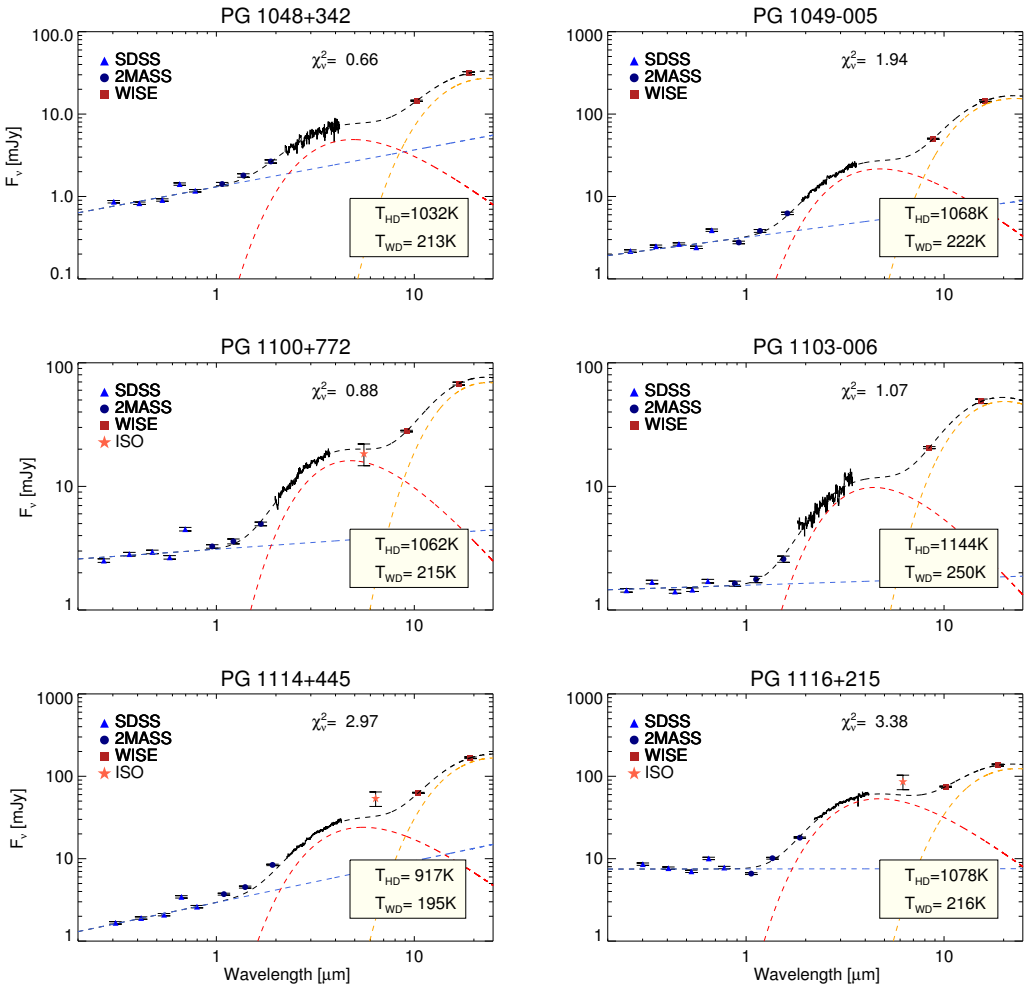

Figure 2.15 Continued

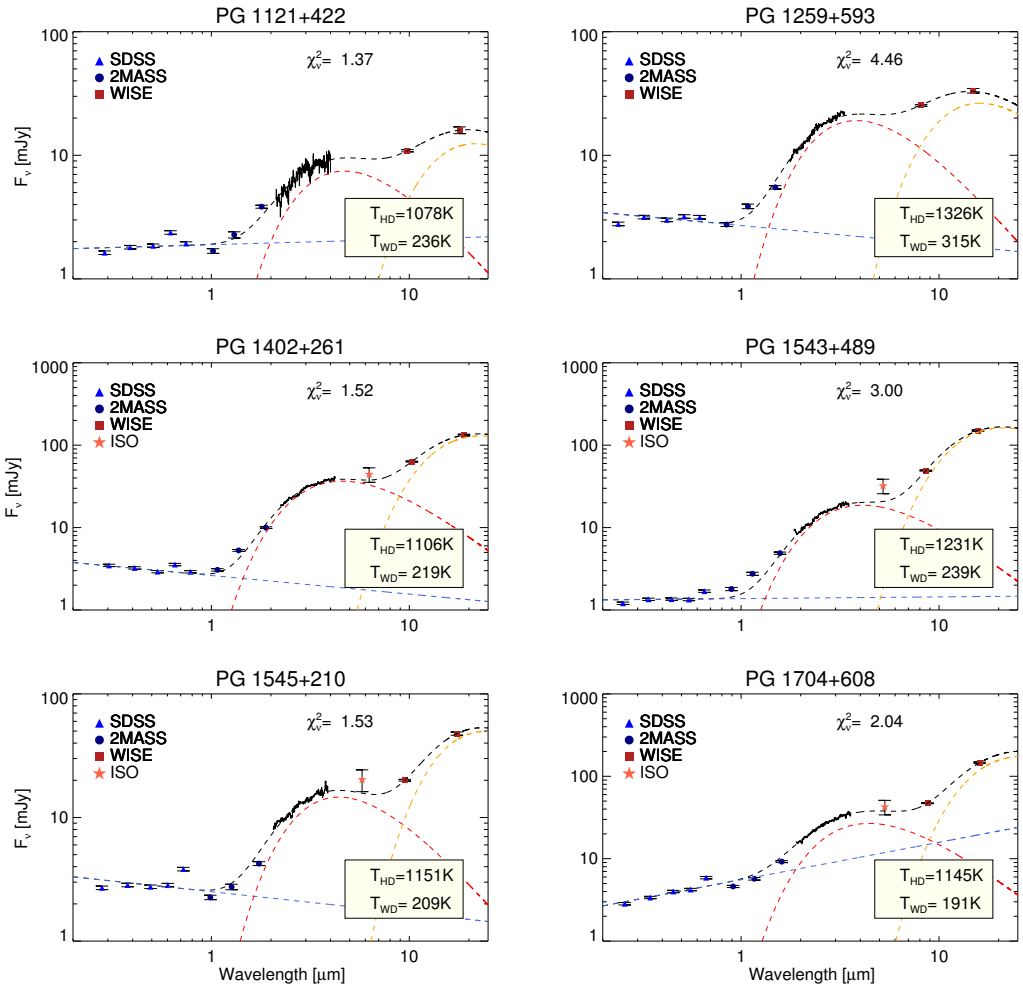

Figure 2.15 Continued

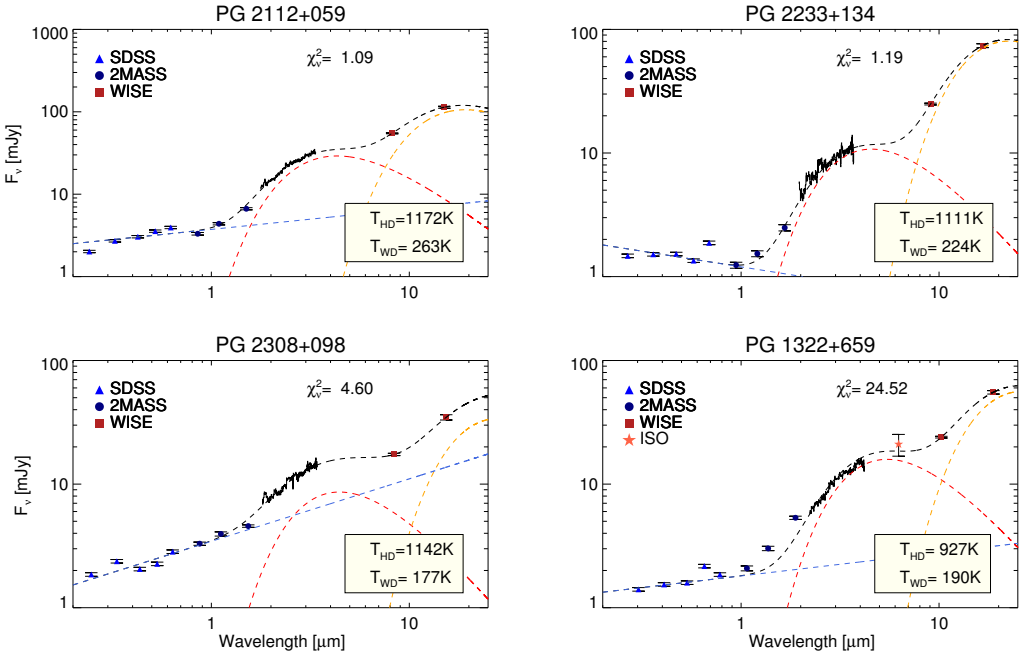

Figure 2.15 Continued

Table 2.4. Dust Components Fitting Results

Objects	$T_{\rm HD}$ [K]	$T_{\rm WD}$ [K]	$\log(L_{\rm HD})$ [erg s^{-1}]	$\log(L_{\rm WD})$ [erg s^{-1}]	$\rm CF_{HD}$	α
PG 1211+143	864±5	191±2	45.27±0.01	45.38±0.02	0.28	-1.55±0.02
PG 1307+085	854±13	184±3	45.27±0.03	45.45±0.03	0.18	-1.49±0.02
PG 0043+039	1068±14	230±9	46.22±0.02	46.04±0.07	0.23	-1.83±0.03
PG 0947+396	1036±2	213±3	45.78±0.00	45.68±0.03	0.60	-1.68±0.01
PG 1048+342	1032±20	213±5	45.06±0.03	45.12±0.04	0.25	-1.55±0.04
PG 1049−005	1068±6	222±2	46.48±0.01	46.65±0.02	0.43	-1.68±0.03
PG 1100+772	1062±9	215±3	46.20±0.02	46.14±0.03	0.29	-1.89±0.04
PG 1103−006	1144±17	250±5	46.33±0.03	46.37±0.03	0.35	-1.95±0.05
PG 1114+445	917±2	195±2	45.56±0.00	45.73±0.02	0.51	-1.50±0.01
PG 1116+215	1078±1	216±3	46.17±0.00	45.84±0.03	0.37	-2.00±0.02
PG 1121+422	1078±15	236±9	45.55±0.02	45.11±0.06	0.21	-1.95±0.04
PG 1259+593	1326±1	315±8	46.81±0.00	46.32±0.04	0.41	-2.15±0.01
PG 1402+261	1106±3	219±2	45.95±0.00	45.79±0.02	0.64	-2.23±0.01
PG 1543+489	1231±2	239±2	46.58±0.00	46.81±0.02	0.83	-1.98±0.01
PG 1545+210	1151±8	209±3	46.03±0.00	45.82±0.03	0.29	-2.17±0.04
PG 1704+608	1145±3	191±2	46.63±0.01	46.67±0.03	0.36	-1.55±0.01
PG 2112+059	1172±7	263±4	46.91±0.00	46.82±0.03	0.52	-1.75±0.03
PG 2233+134	1111±7	224±3	46.08±0.01	46.26±0.02	0.40	-2.25±0.05
PG 2308+098	1142±10	177±17	46.29±0.02	46.08±0.15	0.19	-1.50±0.03

We note three technical points that we took into account during the fit. First, we excluded SDSS photometry between 0.6 and 0.7 μm in the rest frame to avoid the inclusion of the Hα line which generally has a large equivalent width and produces a bump in the SED that deviates from a power law which is assumed as the continuum shape in the optical. Second, we increased the errors of the SDSS data points to represent the deviation of the optical continuum shape from a power law. Here, the deviation is caused by the intrinsic fluctuations in the continuum spectra due to Fe emission complex, emission lines other than Hα, and the host galaxy light. Without increasing the error, a fit to the SDSS photometry points with a simple power-law function ends up with a rather large reduced χ^2 values due to very small original SDSS photometry errors. From a composite spectrum of a quasar (Glikman et al. 2006) placed at $0 \leq z \leq 0.4$, we find the intrinsic fluctuation of the optical spectrum with respect to a simple featureless power law to be $\sigma_m = 0.035$ mag, and this value is added in quadrature to the original SDSS photometry error in each band. Third, we calculate the reduced chi-square, χ^2_ν of the fit, and the hot and warm dust properties are taken seriously only if $\chi^2_\nu < 5$. One object (PG 1322+659) is excluded by the χ^2_ν limit for which we had difficulty fitting the shape of the *AKARI* spectrum (the last object in Figure 15).

Through the procedure above, we obtain the temperatures and luminosities of the hot and warm dust components of 19 AGNs (2 reverberation mapped AGNs and 17 PG QSOs). The fitting results are presented in Figure 15, showing that both the hot and warm dust components exist and contribute to the NIR and MIR spectra of AGNs. However, four objects (PG 1114+445, PG 1116+215, PG 1543+489, and PG 1545+210) show an excess of 7.3 μm *ISO* photometry. This excess can hint at the existence of an intermediate-temperature dust component or a continuous dust temperature.

The SED fit provides formal fitting errors of 0.8% in $T_{\rm HD}$ and 3.1% in $L_{\rm HD}$,

where we obtain a small error in $T_{\rm HD}$ due to the strong constraints provided by the *AKARI* spectra. The errors in Table 4 indicate the formal fitting errors. Since the changes in the assumptions that went into the fitting model could influence the result more than the formal fitting errors, we explored how the derived quantities could be affected by changing the following conditions in the fit as an attempt to estimate more realistic errors: (1) fixing the power-law slope of the continuum, α, in Equation (13) to a value that deviates by five times the formal error from the fit; (2) the reduction of the fluxes of the *AKARI* data by 10%, since *AKARI* fluxes could be overestimated by that amount (Figure 3), and (3) the subtraction of the host galaxy contribution. The mean absolute differences in the fitted quantities from the change in the power law slope are 3.3% ($T_{\rm HD}$; between 0.6% and 8.7%) and 11% ($L_{\rm HD}$; between 2.6% and 36%), and from the flux of *AKARI* data are 2.7% (between <1% and 6.5%) in $T_{\rm HD}$ and 15% (between 11% and 22%) in $L_{\rm HD}$. The reduction in the *AKARI* flux leads to the reduction in $T_{\rm HD}$ and $L_{\rm HD}$. We note that the change of the power-law slope and the *AKARI* flux value keeps the χ^2_ν value to less than five, except for one object. We estimated the contribution of the host galaxy light in L_{5100} (Peterson et al. 2004; Vestergaard & Peterson 2006) using Equation (1) of Shen et al. (2011), and subtracted the host galaxy light assuming an elliptical galaxy SED shape (Bruzual & Charlot 2003) with the conditions of solar metallicity, $\tau = 0.1$ Gyr, t = 10 Gyr, and a Chabrier IMF. We examined how the fitting result changes with the subtraction of the host galaxy component, and find mean differences of 1.5% (between <1% and 7.5%) in $T_{\rm HD}$ and 7.5% (between <1% and 22%) in $L_{\rm HD}$, where $T_{\rm HD}$ decreases and $L_{\rm HD}$ increases in most cases. With these considerations, the error of $T_{\rm HD}$ is realistically ∼4%, while the error in $L_{\rm HD}$ could be as much as ∼14%. For the warm dust component, we have only two photometric data points for most AGNs and a single point in some AGNs; we caution that the fitted result have larger errors and can be affected more easily by the fitting method than the

hot dust component.

The left panel of Figure 16 shows $L_{\rm bol}$ versus $T_{\rm HD}$. The $L_{\rm bol}$ values are estimated from L_{5100} using a bolometric correction factor of 10.3 (Richards et al. 2006), and the L_{5100} values are taken from Bentz et al. (2009) and Vestergaard & Peterson (2006). The $L_{\rm bol}$ and the $T_{\rm HD}$ values have a positive correlation as

$$\frac{T_{\rm HD}}{1800\,{\rm K}} = 10^{-0.231\pm0.003}\left(\frac{L_{\rm bol}}{10^{46}\ {\rm erg\ s^{-1}}}\right)^{0.061\pm0.005}, \quad (2.14)$$

and the Pearson correlation coefficient is 0.690. We find that the mean $T_{\rm HD}$ and $T_{\rm WD}$ are 1083 K and 221 K, respectively, which is lower than the commonly cited $T_{\rm HD}$ of 1500 K (e.g., Barvainis 1987; Elvis et al. 1994), and somewhat lower than the value quoted in a recent study (1260 K, from Glikman et al. 2006). The difference does not seem to arise from technical parts of the fitting method. When we measure the $T_{\rm HD}$ using a composite spectrum of Glikman et al. (2006) with our method, we find the result to be identical to that of the previous study (i.e., 1260 K). Also, we estimate $T_{\rm HD}$ values of our sample using the methods of Glikman et al. (2006), and the measured $T_{\rm HD}$ values used in this way are consistent with our results.

The right panel of Figure 16 shows the hot dust luminosities versus the $L_{\rm bol}$ values for the 19 AGNs. For the bolometric luminosity, we use L_{5100} from our SED fitting multiplied by a bolometric correction factor of 10.3 (Richards et al. 2006). In the figure, we also indicate lines with three different values for the covering factor of the hot dust component ($\rm CF_{HD}$). Here, the covering factor is given by the ratio of the luminosity from the hot dust component to $L_{\rm bol}$ ($\rm CF_{HD}$=$L_{\rm HD}/L_{\rm bol}$; e.g., Maiolino et al. 2007). We find that $L_{\rm HD}$ correlates well with $L_{\rm bol}$, and their mean covering factor is found to be 0.38. The measured mean covering factor is similar to several previous results (Sanders et al. 1989; Elvis et al. 1994; Roseboom et al. 2013). However, we note that there is no significant downturn in $\rm CF_{HD}$ with $L_{\rm bol}$, in contrast to previous results which reported that $\rm CF_{HD}$ has an anti-correlation with $L_{\rm bol}$ at the high luminosity end of $10^{46.5}$ erg s^{-1} (Wang et al. 2005; Maiolino

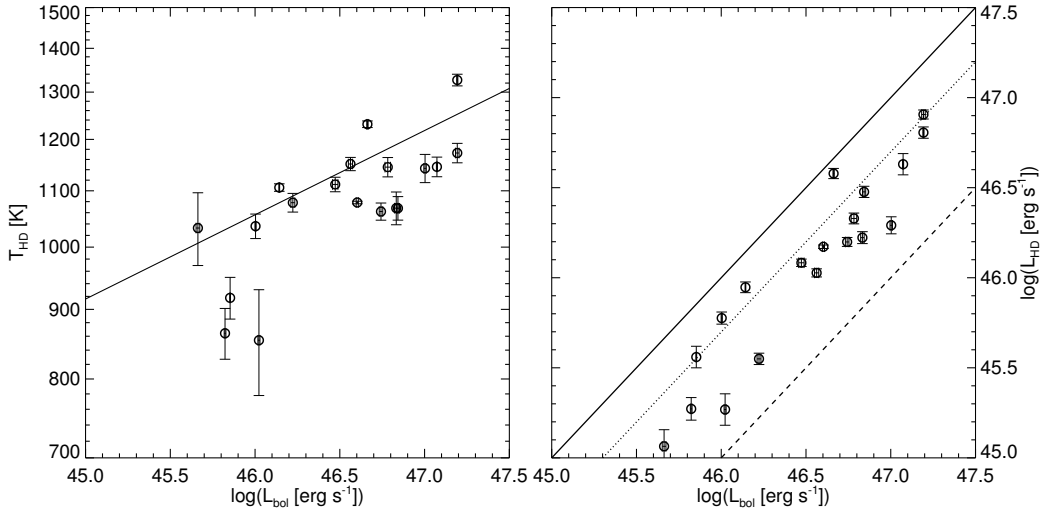

Figure 2.16 Left: $L_{\rm bol}$ vs. $T_{\rm HD}$ of the 19 AGNs. The solid line indicates the best-fit correlation. Right: comparison between $L_{\rm bol}$ and $L_{\rm HD}$. The solid, dotted, and dashed lines denote $\mathrm{CF_{HD}} = 1.0$, 0.5, and 0.1, respectively, and the measured mean $\mathrm{CF_{HD}}$ of the 19 AGNs is 0.38.

et al. 2007; Treister et al. 2008; Mor & Trakhtenbrot 2011; Mor & Netzer 2012). This discrepancy is quite possibly due to the low number statistics in our data, considering that the anti-correlation found by other groups has a large scatter.

2.6 SUMMARY

Using the *AKARI* IRC in grism mode, we obtained 2.5–5.0 μm spectra of 83 nearby (0.002< z <0.48), bright (K <14 mag) type-1 AGNs. The Brackett lines are identified in 11 AGNs in the sample, allowing us to derive $M_{\rm BH}$ estimators that are based on Brα and Brβ line properties. We find the Brβ-based $M_{\rm BH}$ estimator using the measured line width and luminosity so as to be useful with an intrinsic scatter of $\sim$0.1 dex or less with respect to the $M_{\rm BH}$ values from the reverberation mapping method. On the other hand, the Brα-based estimator shows a larger scatter and no strong dependence on $\sigma_{\rm Br\alpha}$, demonstrating the difficulty of $\sigma_{\rm Br\alpha}$ measurements and the need for future data to refine the estimator. However, both $M_{\rm BH}$ estimators can potentially be applied to derive $M_{\rm BH}$ values of dusty AGNs due to the low extinction in the Brackett line wavelengths. The continuum shape is well traced for all of the objects, and we derived the temperatures and luminosities of the hot and warm dust components of 19 luminous AGNs ($L_{\rm bol} > 10^{45.7}$ erg s^{-1}) for which host galaxy contamination is expected to be small (< 10%). The use of the *AKARI* spectra provides the advantage of tracing the NIR continuum densely, thus improving the dust temperature measurements. Our results show the hot dust temperature to be about 1100 K, which is lower than the commonly cited value of 1500 K but broadly consistent with most recent hot dust temperature measurements. The covering factor of the hot dust component is also derived with a mean $\rm CF_{HD}$ of 0.38, consistent with previous measurements. The *AKARI* spectral atlas and the tabulated spectral measurements can be downloaded from this article, revealing the rarely studied spectral range of 2.5–5.0 μm for low-redshift AGNs.

Table 2.5. Spectrum of Mrk 335

λ [μm]	f_λ [erg s^{-1} cm^{-2} μm^{-1}]	f_λ Uncertainty [erg s^{-1} cm^{-2} μm^{-1}]
2.543	3.500E-11	4.653E-13
2.552	3.363E-11	4.595E-13
2.562	3.207E-11	3.482E-13
2.572	3.133E-11	2.153E-13
2.581	3.106E-11	3.536E-13
2.591	3.118E-11	5.891E-13
2.601	3.128E-11	2.988E-13

Note. — This table display only a part of spectrum of Mrk 335. The entire spectra of 83 AGNs and the composite spectrum of 48 PG QSOs are available as a tar file in the electronic version of *Astrophysical Journal Supplement Series*.

References

Barvainis, R. 1987, ApJ, 320, 537

Bentz, M. C., Walsh, J. L., Barth, A. J., et al. 2009, ApJ, 705, 199

Bentz, M. C., Denney, K. D., Grier, C. J., et al. 2013, ApJ, 767, 149

Bruzual, G., & Charlot, S. 2003, MNRAS, 344, 1000

Cox, A. N. 2000, Allen's Astrophysical Quantities,

Davidson, K., & Netzer, H. 1979, Reviews of Modern Physics, 51, 715

Denney, K. D., Peterson, B. M., Pogge, R. W., et al. 2010, ApJ, 721, 715

Deo, R. P., Richards, G. T., Crenshaw, D. M., & Kraemer, S. B. 2009, ApJ, 705, 14

Dibai, E. A. 1977, Soviet Astronomy Letters, 3, 1

Elvis, M., Wilkes, B. J., McDowell, J. C., et al. 1994, ApJS, 95, 1

Ferland, G. J., & Persson, S. E. 1989, ApJ, 347, 656

Ferland, G. J., Korista, K. T., Verner, D. A., et al. 1998, PASP, 110, 761

Glikman, E., Helfand, D. J., & White, R. L. 2006, ApJ, 640, 579

Glikman, E., Helfand, D. J., White, R. L., et al. 2007, ApJ, 667, 673

Green, R. F., Schmidt, M., & Liebert, J. 1986, ApJS, 61, 305

Greene, J. E., & Ho, L. C. 2005, ApJ, 630, 122

Greene, J. E., & Ho, L. C. 2007, ApJ, 670, 92

Grier, C. J., Peterson, B. M., Bentz, M. C., et al. 2008, ApJ, 688, 837

Haas, M., Klaas, U., Müller, S. A. H., et al. 2003, A&A, 402, 87

Hao, H., Elvis, M., Bongiorno, A., et al. 2012, arXiv:1210.3044

Hopkins, P. F., Hernquist, L., Cox, T. J., et al. 2005, ApJ, 630, 705

Im, M., Griffiths, R. E., & Ratnatunga, K. U. 1997, ApJ, 475, 457

Im, M., Lee, I., Cho, Y., et al. 2007, ApJ, 664, 64

Im, M., 2010, IAU Symposium, 267, 40

Imanishi, M. 2002, ApJ, 569, 44

Imanishi, M., Nakagawa, T., Shirahata, M., Ohyama, Y., & Onaka, T. 2010, ApJ, 721, 1233

Imanishi, M., Ichikawa, K., Takeuchi, T., et al. 2011, PASJ, 63, 447

Jiang, L., Fan, X., Brandt, W. N., et al. 2010, Nature, 464, 380

Jun, H. D., & Im, M. 2013, ApJ, 779, 104

Kaspi, S., Smith, P. S., Netzer, H., et al. 2000, ApJ, 533, 631

Kim, D., Im, M., & Kim, M. 2010, ApJ, 724, 386

Kim, J. H., Im, M., Lee, H. M., et al. 2012, ApJ, 760, 120

Kobayashi, Y., Sato, S., Yamashita, T., Shiba, H., & Takami, H. 1993, ApJ, 404, 94

Landt, H., Bentz, M. C., Ward, M. J., et al. 2008, ApJS, 174, 282

Landt, H., Elvis, M., Ward, M. J., et al. 2011, MNRAS, 414, 218

Landt, H., Ward, M. J., Peterson, B. M., et al. 2013, MNRAS, 432, 113

Lee, I., Im, M., Kim, M., et al. 2008, ApJS, 175, 116

Li, Y., Hernquist, L., Robertson, B., et al. 2007, ApJ, 665, 187

Maiolino, R., Shemmer, O., Imanishi, M., et al. 2007, A&A, 468, 979

Markwardt, C. B. 2009, Astronomical Data Analysis Software and Systems XVIII, 411, 251

Marziani, P., Sulentic, J. W., Zamanov, R., et al. 2003, ApJS, 145, 199

McCall, M. L. 2004, AJ, 128, 2144

McLure, R. J., & Dunlop, J. S. 2004, MNRAS, 352, 1390

Minezaki, T., Yoshii, Y., Kobayashi, Y., et al. 2004, ApJ, 600, L35

Mor, R., Netzer, H., & Elitzur, M. 2009, ApJ, 705, 298

Mor, R., & Trakhtenbrot, B. 2011, ApJ, 737, L36

Mor, R., & Netzer, H. 2012, MNRAS, 420, 526

Mouri, H., Kawara, K., Taniguchi, Y., & Nishida, M. 1990, ApJ, 356, L39

Murakami, H., Baba, H., Barthel, P., et al. 2007, PASJ, 59, 369

Netzer, H., Lutz, D., Schweitzer, M., et al. 2007, ApJ, 666, 806

Ohyama, Y., Onaka, T., Matsuhara, H., et al. 2007, PASJ, 59, 411

Oi, N., Imanishi, M., & Imase, K. 2010, PASJ, 62, 1509

Onaka, T., Matsuhara, H., Wada, T., et al. 2007, PASJ, 59, 401

Park, D., Kelly, B. C., Woo, J.-H., & Treu, T. 2012, ApJS, 203, 6

Peterson, B. M., Ferrarese, L., Gilbert, K. M., et al. 2004, ApJ, 613, 682

Rees, M. J., Netzer, H., & Ferland, G. J. 1989, ApJ, 347, 640

Richards, G. T., Lacy, M., Storrie-Lombardi, L. J., et al. 2006, ApJS, 166, 470

Roseboom, I. G., Lawrence, A., Elvis, M., et al. 2013, MNRAS, 429, 1494

Ruff, A. J., Floyd, D. J. E., Webster, R. L., Korista, K. T., & Landt, H. 2012, ApJ, 754, 18

Sanders, D. B., Phinney, E. S., Neugebauer, G., Soifer, B. T., & Matthews, K. 1989, ApJ, 347, 29

Schlafly, E. F., & Finkbeiner, D. P. 2011, ApJ, 737, 103

Shen, Y., Richards, G. T., Strauss, M. A., et al. 2011, ApJS, 194, 45

Spoon, H. W. W., Armus, L., Cami, J., et al. 2004, ApJS, 154, 184

Suganuma, M., Yoshii, Y., Kobayashi, Y., et al. 2006, ApJ, 639, 46

Tokunaga, A. T., Sellgren, K., Smith, R. G., et al. 1991, ApJ, 380, 452

Treister, E., Krolik, J. H., & Dullemond, C. 2008, ApJ, 679, 140

Urrutia, T., Becker, R. H., White, R. L., et al. 2009, ApJ, 698, 1095

van Dokkum, P. G. 2001, PASP, 113, 1420

Vestergaard, M. 2002, ApJ, 571, 733

Vestergaard, M., & Peterson, B. M. 2006, ApJ, 641, 689

Wang, J.-M., Zhang, E.-P., & Luo, B. 2005, ApJ, 627, L5

Williams, M. J., Bureau, M., & Cappellari, M. 2010, MNRAS, 409, 1330

Woo, J.-H., & Urry, C. M. 2002, ApJ, 579, 530

Woo, J.-H., Kim, J. H., Imanishi, M., & Park, D. 2012, AJ, 143, 49

Woo, J.-H., Schulze, A., Park, D., et al. 2013, ApJ, 772, 49

Yamada, R., Oyabu, S., Kaneda, H., et al. 2013, arXiv:1307.6356

Chapter 3

A High S/N and Medium Resolution Optical and Near-Infrared Spectral Atlas of 16 2MASS-selected Red Active Galactic Nuclei at $z \sim 0.3$

(This chapter will be submitted to The Astrophysical Journal Supplement Series)

3.1 Introduction

In recent years, there has been increased interest in the role of supermassive black holes (SMBHs) in galaxy formation and evolution. Most massive spheroidal galaxies are believed to harbor SMBHs at their centers, and masses of the SMBHs have a correlation with the luminosities (Magorrian et al. 1998; Bentz et al. 2009; Bennert

et al. 2010; Greene et al. 2010; Jiang et al. 2011; Park et al. 2015), the stellar velocity dispersions (Ferrarese & Merritt 2000; Gebhardt et al. 2000; Tremaine et al. 2002; Gültekin et al. 2009; Woo et al. 2010), and Sersic indices (Graham et al. 2001; Graham & Driver 207) of their spheroids.

The proposed scenario for the growth of SMBHs is that they are assembled by gas accretion (Lynden-Bell 1969). The SMBHs are thought to grow very rapidly in an active phase, i.e., the period of active galactic nuclei (AGNs). During this phase, AGNs emit enormous amounts of energy (10^{43}–$10^{48}\,\mathrm{erg\,s^{-1}}$; e.g., Woo & Urry 2002) from gamma-ray to radio. Most of our knowledge of AGNs comes from unobscured type 1 AGNs, found by using surveys of X-ray, ultraviolet (UV), optical, and radio observations (Grazian et al. 2000; Becker et al. 2001; Anderson et al. 2003; Croom et al. 2004; Risaliti & Elvis 2005; Schneider et al. 2005; Véron-Cetty & Véron 2006; Young et al. 2009).

However, several studies (e.g., Comastri et al. 2001; Tozzi et al. 2006; Polletta et al. 2008) have reported that the soft X-ray, UV, and optical based AGN surveys could neglect quite a large number (e.g., up to more than 50%) of AGNs with very red colors, due to the dust extinction from the intervening dust and gas in their host galaxies (Webster et al. 1995; Cutri et al. 2002). From a similar but different point of view, there is another missing population of AGNs with red colors due to the interstellar medium in our galaxy (Im et al. 2007; Lee et al. 2008).

The AGNs with red colors are called red AGNs, and they are considered to be a different population from unobscured type 1 AGNs. In several simulation studies (Hopkins et al. 2005, 2006, 2008), red AGNs are expected to be in an intermediate phase between the merger-driven star-forming galaxies, such as ultra luminous infrared galaxies (ULIRGs; Sanders et al. 1988; Sanders & Mirabel 1996), and unobscured type 1 AGNs. Although this explanation for red AGNs is still controversial due to several reasons (e.g., Puchnarewicz & Mason 1998; Whiting et

al. 2001; Wilkes et al. 2002; Schawinski et al. 2011, 2012; Simmons et al. 2012; Kocevski et al. 2012; Rose et al. 2013), the scenario is further supported by several observational studies. For example, red AGNs have (i) high accretion rates (Urrutia et al. 2012; Kim et al. 2015b), (ii) enhanced star-forming activities (Georgakakis et al. 2009), (iii) a frequent occurrence of merging features (Urrutia et al. 2008; Glikman et al. 2015), (iv) young radio jets (Georgakakis et al. 2012), (v) red continua from dust extinction (Glikman et al. 2007; Urrutia et al. 2009), and (vi) line luminosity ratios explainable only when dust extinction is considered (Kim et al. 2017).

Since the observational results of red AGNs could arise from the limited sample size of red AGNs, there have been several efforts to search for more red AGNs (Webster et al. 1995; Benn et al. 1998; Cutri et al. 2001, 202; Smith et al. 2002; Glikman et al. 2007, 2012; Urrutia et al. 2009; Banerji et al. 2012; Stern et al. 2012; Assef et al. 2013; Fynbo et al. 2013; Lacy et al. 2013). A significant number of these studies found red AGNs using large area near-infrared (NIR) photometric surveys, such as the Two Micron All-Sky Survey (2MASS; Skrutskie et al. 2006), the UKIRT Infrared Deep Sky Survey (UKIDSS; Lawrence et al. 2007), and the *Wide-field Infrared Survey Explorer* (*WISE*; Wright et al. 2010) survey.

Compared to the contribution from large area NIR photometric surveys to our understanding of red AGNs, investigations based on NIR spectroscopic data (e.g., Glikman et al. 2007, 2012; Kim et al. 2015b) are limited. Despite the limited contribution, the NIR spectrum includes useful information to investigate the nature of red AGNs. For example, (i) BH masses (Paschen lines: Kim et al. 2010; Landt et al. 2011b, and Brackett lines: Kim et al. 2015a), (ii) bolometric luminosities (Kim et a. 2010), (iii) broad line region (BLR) sizes (Landt et al. 2011a), (iv) temperatures (Glikman et al. 2006; Landt et al. 2011b; Kim et al. 2015a) and covering factors of hot dust (Kim et al. 2015a), (v) stellar velocity dispersions (σ_*;

Woo et al. 2010; Kang et al. 2013), and (vi) star-forming activities (Imanishi et al. 2011; Kim et al. 2012) can be measured from the NIR spectra.

In this work, we present high S/N (up to several hundreds) and medium resolution ($R \sim 2000$) NIR spectra of a sample of 16 red AGNs at $z \sim 0.3$, for which optical images, spectra, and polarizations were obtained in previous studies (Smith et al. 2002; Marble et al. 2003; Canalizo et al. 2012). We concentrate on the detailed description of our sample and observation (§ 2), spectral fittings for hydrogen lines (§ 3), dust reddening measurements (§ 4), accretion rates (§ 5), and the $M_{\rm BH}$–σ_* relation for red AGNs (§ 6). In § 7, we briefly summarize our results. Throughout this work, we use a standard ΛCDM cosmological model of $H_0 = 70\,{\rm km\,s^{-1}}$ ${\rm Mpc^{-1}}$, $\Omega_m = 0.3$, and $\Omega_\Lambda = 0.7$, supported by observational studies in the past decades (e.g., Im et al. 1997).

3.2 The Sample and Observation

3.2.1 Sample

Our sample is drawn from the 29 2MASS-based red AGNs listed in Marble et al. (2003). The 29 objects were selected by the following procedures. First, Cutri et al. (2001, 2002) chose red AGN candidates by a combination of red color in NIR ($J - K_{\rm s} > 2$) and detection in each of the three 2MASS bands (complete to $K_s < 15.0\,{\rm mag}$). Then, among the candidates, 70 targets were spectroscopically confirmed in Smith et al. (2002). Furthermore, Smith et al. (2002) performed optical polarimetric observations using the Two-Holer Polarimeter/Photometer on the Steward Observatory 1.5 m telescope and the Bok 2.3 m reflector. Finally, Marble et al. (2003) selected 29 out of the 70 red AGNs within the redshift range of $0.136 \leq z \leq 0.596$, and observed them with the Wide Field Planetary Camera 2 (WFPC2) on board the *Hubble Space Telescope* (*HST*).

Among the 29 objects, we select 16 red AGNs at $z \sim 0.3$ (from 0.139 to 0.411) for which the redshifted Pβ or Pα line is observable within the sky window wavelength range. The 16 selected red AGNs span over a wide range of luminosities ($-29.0 < M_K < -26.0$). Figure 1 shows the redshifts vs. the M_K magnitudes and $g' - K$ colors versus $J - K$ colors of the 16 red AGNs and red quasars used in our previous studies (kim et al. 2015b, 2017; originally from Urrutia et al. 2009). These red AGNs have red colors of $J - K > 2$ and $g' - K \gtrsim 4$. Compared to the red quasars that we studied previously ($J - K > 1.3$ and $g' - K > 5$), the 16 red quasars include those that have $g' - K$ colors as blue as those of unobscured type 1 quasars.

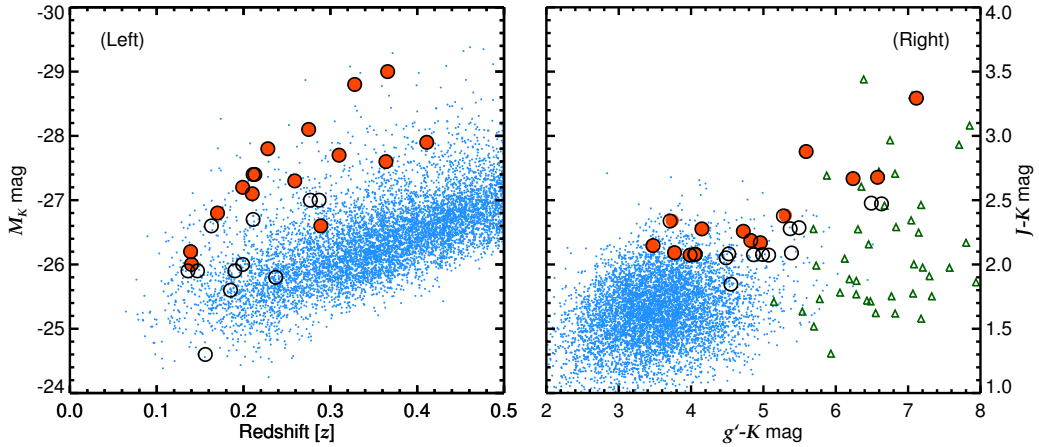

Figure 3.1 (Left) Redshifts versus M_K magnitudes for red AGNs and unobscured type 1 quasars. The circles represent 29 red AGNs listed in Marble et al. (2003) and the red filled circles denote 16 red AGNs used in this work. The blue dots represent the redshifts and M_K magnitudes of unobscured type 1 quasars listed in SDSS DR7 (Shen et al. 2011). (Right) color-color diagram using $g' - K$ and $J - K$ magnitudes. The meanings of the circles and the blue dots are identical to the left panel, and the green triangles denote the $g' - K$ and $J - K$ magnitudes of red quasars used in our previous studies (Kim et al. 2015b, 2017). Here, $g'-$, $J-$, and $K-$band magnitudes are corrected for the Galactic extinction (Schlafly & Finkbeiner 2011), and the g'-band magnitude is in AB unit, while $J-$ and $K-$band magnitudes are based on the Vega magnitudes.

For our sample, we emphasize the advantage of the availability of various types of high quality data. The 16 red AGNs have optical images from *HST* (Marble et al. 2003) and optical broadband polarimetry (Smith et al. 2002). We expect that a combined data set of the high quality images from the *HST* data, the optical polarization, and the optical/NIR spectra from this study will be unique and useful for the comprehensive investigations of the nature of red AGNs.

3.2.2 NIR Observation

We performed NIR spectroscopic observations with four telescopes and their respective instruments. Since the 16 red AGNs have different brightnesses and redshifts, the observations need to be performed with proper observational instruments and telescopes to fit the characteristics of the 16 red AGNs. We describe the details of our NIR observations below.

First, NIR spectra of nine red AGNs were obtained with the cross-dispersed mode of the Gemini Near-infrared Spectrograph (GNIRS; Elias et al. 2006) on the 8.1 m Gemini-North telescope. The observational configuration is a combination of a 110 l/mm grating, short blue camera, and $0\farcs675$ slit width, which provides a discontinuous spectral coverage from $\sim 1\,\mu$m to $\sim 2.1\,\mu$m with a spectral resolution of $R \sim 2600$.

Second, we used the newly updated SpeX (Rayner et al. 2003) on the 3.0 m NASA Infrared Telescope Facility (IRTF) for five red AGNs. In this observation, we used the short cross-dispersion mode (SXD) with a $0\farcs3$ slit width to achieve a spectral resolution of $R \sim 2000$ across $0.7-2.55\,\mu$m. Among these five red AGNs, one, 1543+1937, overlaps with the nine red AGNs observed with GNIRS/Gemini.

Third, in order to obtain the NIR spectra of two red AGNs, we used the Folded-port Infrared Echellette (FIRE) on the 6.5 m Magellan Baade telescope with a $1\farcs0$ slit width. This observational configuration allows the wavelength coverage to span

from 0.82 to 2.51 μm with a resolving power of $R \sim 3600$.

Fourth, a NIR spectrum of one red AGN was obtained with the Infrared Camera and Spectrograph (IRCS; Tokunaga et al. 1998; Kobayashi et al. 2000) on the 8.2 m Subaru telescope. In this observation, we used both grism and echelle modes. For the grism mode observation, we used a $0\farcs1$ slit width and HK band with the grism of 52 milli-arcsecond pixel scale, which provides a spectral coverage of 1.4 – 2.5 μm with a spectral resolution of $R \sim 440$. The Echelle mode observation was performed with a $0\farcs54$ slit width and K band, and this provides a spectral resolution of $R \sim 6600$ with a discontinuous wavelength coverage from 1.90 μm to 2.49 μm.

Our observations were performed under clear weather conditions with sub-arcsecond seeings of $\sim 0\farcs6$. For the flux calibration and telluric correction, we observed nearby A0V stars before or after the observations of the red AGNs. In order to produce fully reduced spectra, we used Gemini image reduction and analysis facility packages (Cooke & Rogers 2005), Spextool (Vacca et al. 2003; Cushing et al. 2004), FIREHOSE, and general reduction procedure of spectra with image reduction and analysis facility (Massey et al. 1988) for the spectra obtained with GNIRS, SpeX, FIRE, and IRCS, respectively. Even though we perform the standard reduction procedures, there is a possibility of photon loss due to the variable seeing conditions and unstable tracking systems. For this reason, the NIR spectra were scaled to match their $K-$band magnitudes of 2MASS. We perform a spectral energy distribution (SED) fit, and the host galaxy contribution in $K-$band is only $\sim$17 %. Moreover, the scaling factor is not significant, as much as a factor of $\sim$1.18.

In total, we obtained 0.7–2.55 μm NIR spectra of 16 red AGNs at $z \sim 0.3$ with a quite high resolution of $R > 2000$ from the four instruments and telescopes. We summarize the observation information in Table 1.

Table 3.1. Observing summary

						NIR spectroscopy			Optical Spectroscopy		
Object	R.A. (J2000.0)	Dec. (J2000.0)	Redshift (z)	K_s (mag)	M_{K_s}[a] (mag)	Telescope/ Instrument	Exp (sec)	Observing dates	Telescope/ Instrument	Exp (sec)	Observing dates
0106+2603	01 06 07.7	+26 03 34	0.411	14.6	-27.9	Subaru/IRCS	800[b]	Nov. 2015	Keck/ESI	3600	Oct. 2003
							6000[c]	Nov. 2015			
0157+1712	01 57 21.0	+17 12 48	0.213	13.2	-27.4	Gemini/GNIRS	3600	Aug. 2015	Keck/ESI	7200	Oct. 2003
0221+1327	02 21 50.6	+13 27 41	0.140	13.2	-26.0	Magellan/FIRE	6657	Jan. 2015	Keck/ESI	5400	Oct. 2003
0234+2438	02 34 30.6	+24 38 35	0.310	13.7	-27.7	Gemini/GNIRS	2160	Aug. 2015	–	–	–
0324+1748	03 24 58.2	+17 48 49	0.328	12.8	-28.8	Magellan/FIRE	3635	Jan. 2015	Keck/ESI	3600	Sep. 2004
0348+1255	03 48 57.6	+12 55 47	0.210	13.6	-27.1	Gemini/GNIRS	2880	Aug. 2015	Keck/ESI	3600	Sep. 2004
1258+2329	12 58 07.4	+23 29 21	0.259	13.4	-27.3	IRTF/SpeX	9000	Mar. 2016	SDSS		
1307+2338	13 07 00.6	+23 38 05	0.275	13.4	-28.1	IRTF/SpeX	18000	Mar. 2016	–	–	–
1453+1353	14 53 31.5	+13 53 58	0.139	13.1	-26.2	IRTF/SpeX	9600	Mar. 2016	SDSS		
1543+1937	15 43 07.7	+19 37 51	0.228	12.7	-27.8	Gemini/GNIRS	3600	Apr. 2016	Keck/ESI	3600	Jul. 2004
						IRTF/SepX	9600	Mar. 2016			
1659+1834	16 59 39.7	+18 34 36	0.170	12.9	-26.8	IRTF/SpeX	8400	Mar. 2016	Keck/ESI	5400	Jul. 2004
2222+1952	22 22 02.2	+19 52 31	0.366	13.3	-29.0	Gemini/GNIRS	2160	Aug. 2015	–	–	–
2222+1959	22 22 21.1	+19 59 47	0.211	12.9	-27.4	Gemini/GNIRS	2880	Aug. 2015	Keck/ESI	5400	Sep. 2004
2303+1624	23 03 04.3	+16 24 40	0.289	14.7	-26.6	Gemini/GNIRS	5040	Aug. 2015	–	–	–
2327+1624	23 27 45.6	+16 24 34	0.364	14.5	-27.6	Gemini/GNIRS	3600	Aug. 2015	Keck/ESI	5400	Sep. 2004
2344+1221	23 44 49.5	+12 21 43	0.199	12.9	-27.2	Gemini/GNIRS	2880	Aug. 2015	Keck/ESI	3600	Jul. 2004

[a]The M_{K_s} values are re-calculated using the method of Marble et al. (2003) with the standard ΛCDM cosmological model

[b]The grism mode observation

[c]The echelle mode observation

3.2.3 Optical Observation

In addition to the NIR spectra, we obtained optical spectra for 12 red AGNs. Two (G. Canalizo & M. Lazarova) of us observed 10 red AGNs with the Echellette Spectrograph and Imager (ESI; sheinis et al. 2002) on the Keck II telescope with a spectral wavelength range of 3900 Å to 11,000 Å and a spectral resolution of $R \sim 4000$. Descriptions of the observations for the 10 red AGNs are given in Table 1. The information about the data reduction is given in Canalizo et al. (2012). Among the 10 spectra from the Keck/ESI observation, five were used in Canalizo et al. (2012).

For the remaining two red AGNs, we obtained the optical spectra from Data Release 12 (DR12) of SDSS. The spectral coverage of the SDSS spectra is 3800 Å to 9200 Å and their spectral resolution is 1500–2500.

3.3 High S/N and Medium resolution Spectra

We show the fully reduced NIR spectra and the *HST* images of the 16 red AGNs in Figure 2, and the machine-readable form of the spectra are available in Table 2. Moreover, Figure 2 also shows the S/N of each spectrum, and we mark several interesting lines such as Pα (1.875 μm), Pβ (1.282 μm), Pγ (1.094 μm), Pδ (1.005 μm), Pϵ (0.955 μm), Pζ (0.923 μm), [Fe II] (1.600 and 1.257 μm), O I (1.129 and 0.845 μm), and He I (1.083 μm).

Table 3.2. NIR Spectrum of 0106+2603

λ [Å]	f_λ [erg s^{-1} cm^{-2} Å]	f_λ Uncertainty [erg s^{-1} cm^{-2} Å]
14439	4.6018E-17	2.2044E-17
14471	2.8404E-17	4.8711E-18
14504	1.9541E-17	4.8643E-18
14537	3.7478E-17	6.2486E-18
14570	2.5344E-17	3.7455E-18
14603	2.6977E-17	1.8525E-18
14636	3.1782E-17	2.4565E-18

Note. — This table represents only a part of NIR spectrum of 0106+2603. The entire NIR spectra of 16 red AGNs obtained with four telescopes are available in machine-readable format.

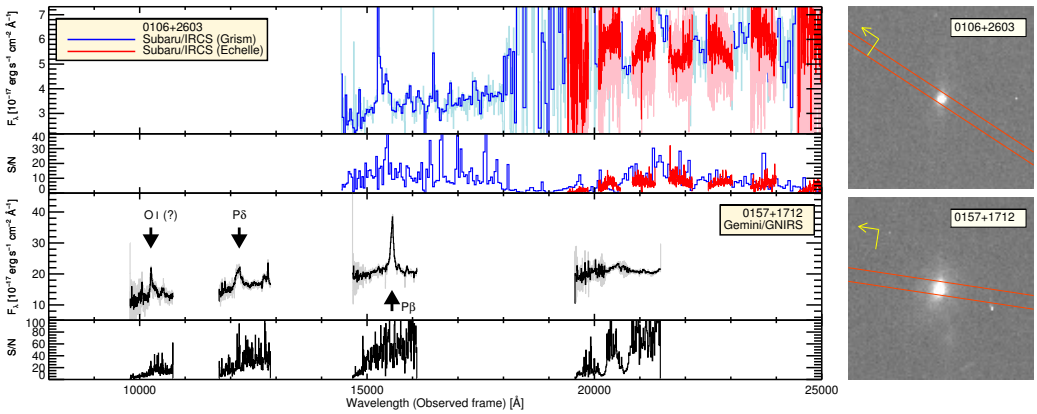

Figure 3.2 (Left) NIR spectra of 16 red AGNs and their S/N. The gray lines indicate observed spectra in the observed frame, and the black lines indicate binned spectra with the spectral resolution. For 0106+2603 and 1543+1937, the spectra were obtained with different two observing modes and instruments. The each binned spectrum from the individual observation is represented by the blue and red lines, and the sky blue and pink lines indicate their original spectra, respectively. Moreover, several emission lines (Pα: 1.8751 μm, Pβ: 1.2818 μm, Pγ: 1.0938 μm, Pδ: 1.0049 μm, Pϵ: 0.9546 μm, Pζ: 0.9229 μm, [Fe II]: 1.5995 and 1.2567 μm, O I: 1.1287 and 0.8446 μm, and He I: 1.0830 μm) are marked on the spectra. However, when the emission line is not obvious due to the low S/N or duplicated sky lines, the emission line is marked with a question mark. (Right) *HST* images of 16 red AGNs. The red boxes across the objects indicate slit widths and the yellow arrows at the top left denote north.

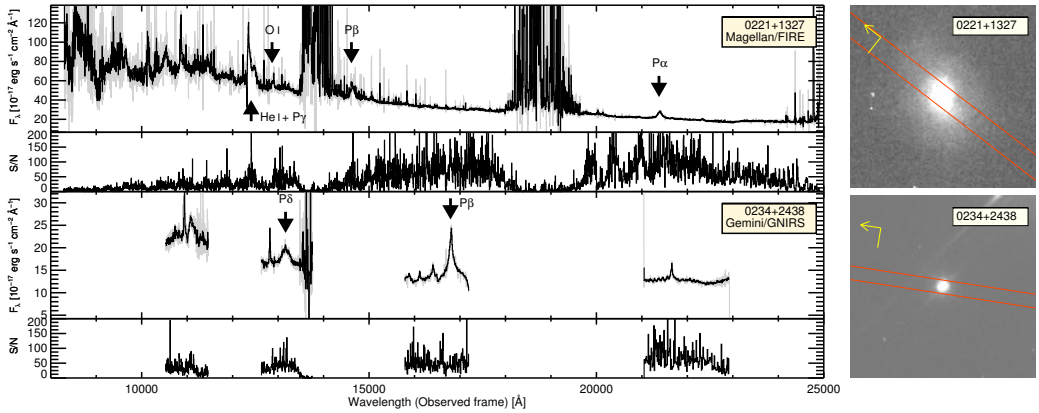

Figure 3.2 Continued

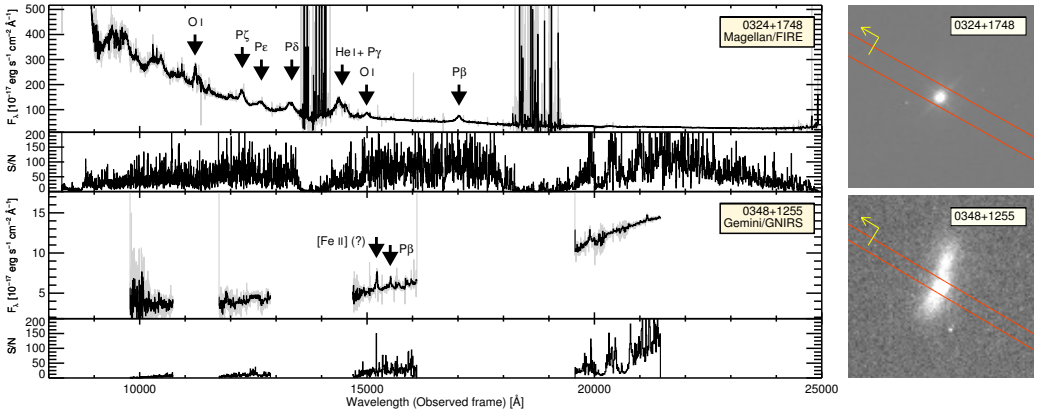

Figure 3.2 Continued

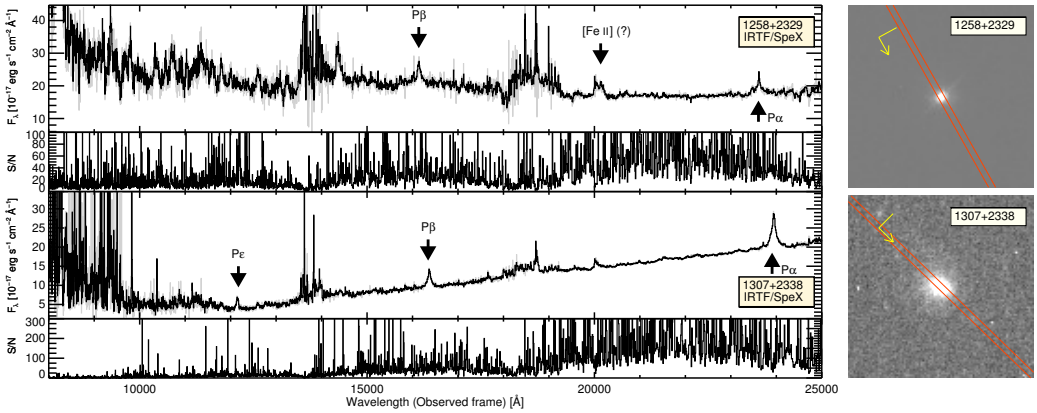

Figure 3.2 Continued

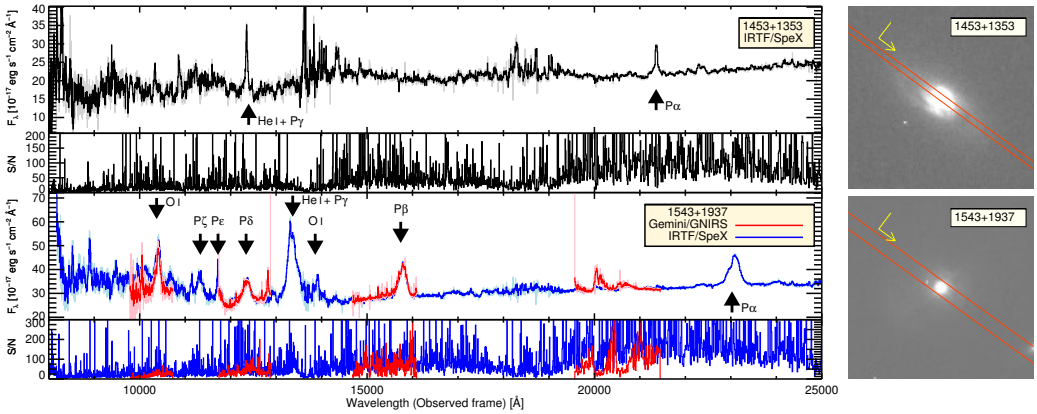

Figure 3.2 Continued

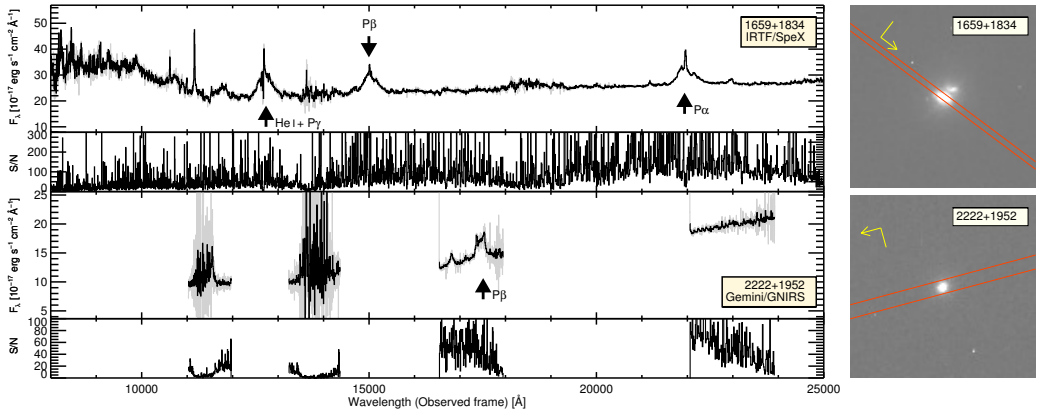

Figure 3.2 Continued

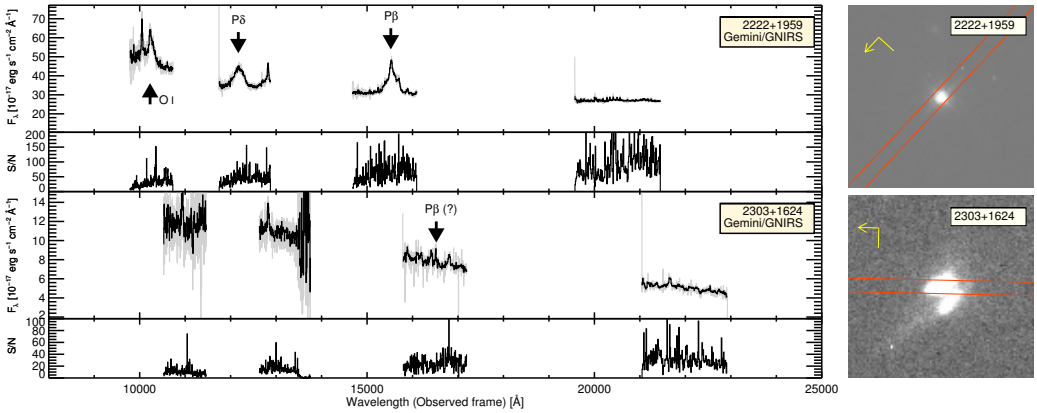

Figure 3.2 Continued

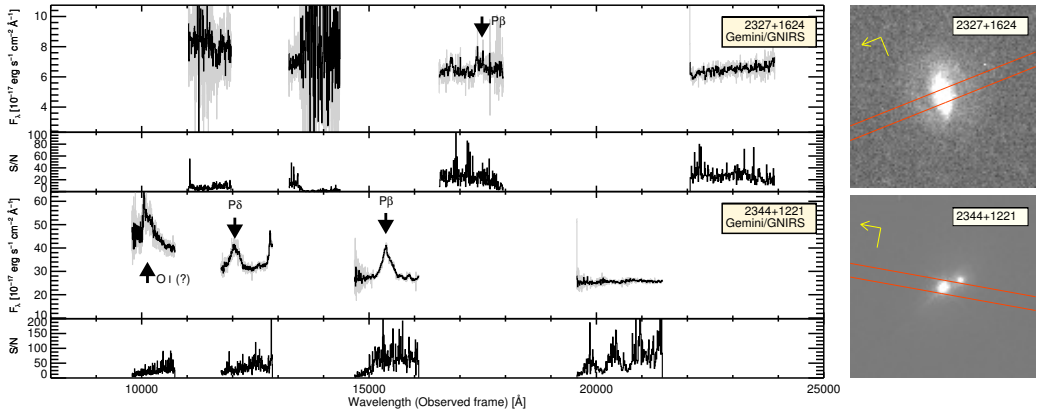

Figure 3.2 Continued

Table 3.3. Optical Spectrum of 0106+2603

λ [Å]	f_λ [erg s^{-1} cm^{-2} Å]	f_λ Uncertainty [erg s^{-1} cm^{-2} Å]
3899.4	8.3145E-17	6.4623E-18
3900.4	5.3173E-17	1.1044E-17
3901.3	2.6999E-17	3.4251E-18
3902.3	6.7212E-17	1.8250E-17
3903.3	1.2357E-16	1.4382E-17
3904.3	1.4238E-16	3.2512E-18
3905.2	1.1617E-16	1.4047E-17

Note. — This table represents only a part of optical spectrum of 0106+2603. The entire optical spectra of 12 red AGNs from the Keck/ESI observation and SDSS data are available in machine-readable format.

In addition to the NIR spectra, Figure 3 shows the reduced optical spectra of the 12 red AGNs, and several lines of [O II] (3727 Å), Hγ (4340 Å), Hβ (4861 Å), [O III] (4959 and 5007 Å), Hα (6563 Å), and [N II] (6548 and 6583 Å) are marked on the spectra. The optical spectra in ascii format are given in Table 3.

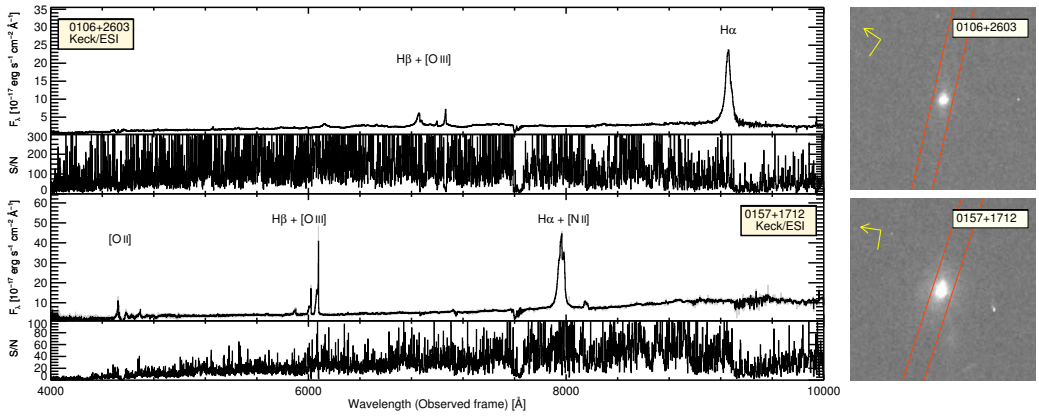

Figure 3.3 (Left) Optical spectra of 12 red AGNs and their S/N. The gray and black lines indicate observed and binned spectra in the observed frame, and we binned the spectra with the spectral resolution. We mark several emission lines in the optical wavelength region, such as [O II] (3727 Å), Hγ (4340 Å), Hβ (4861 Å), [O III] (4959 and 5007 Å), Hα (6563 Å), and [N II] (6548 and 6583 Å). (Right) *HST* images of 12 red AGNs. The red boxes and yellow arrows are identical to Figure 2, and red open circles mean SDSS fiber diameters.

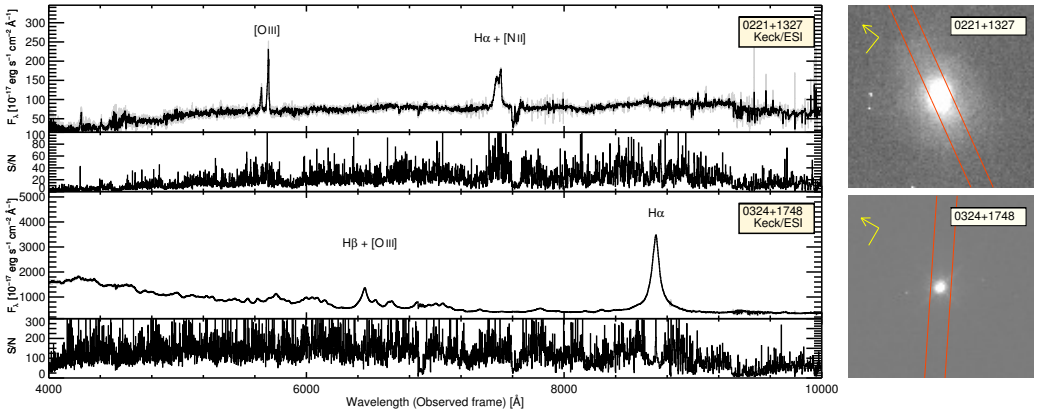

Figure 3.3 Continued

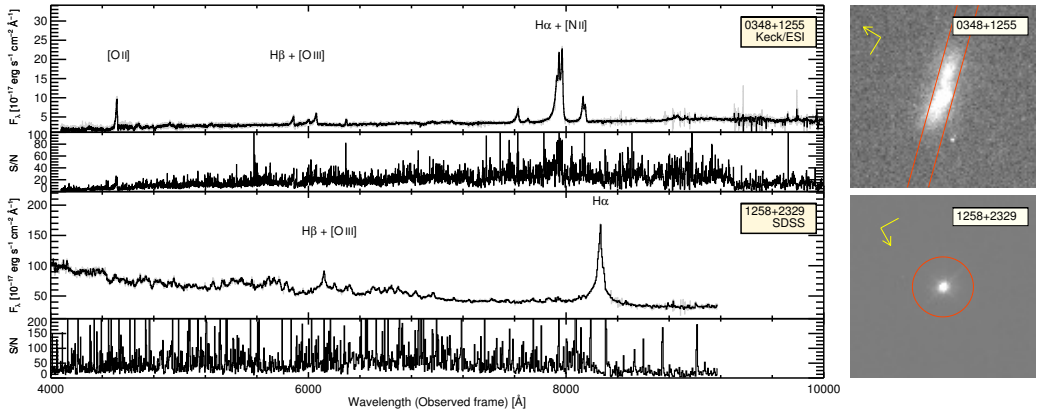

Figure 3.3 Continued

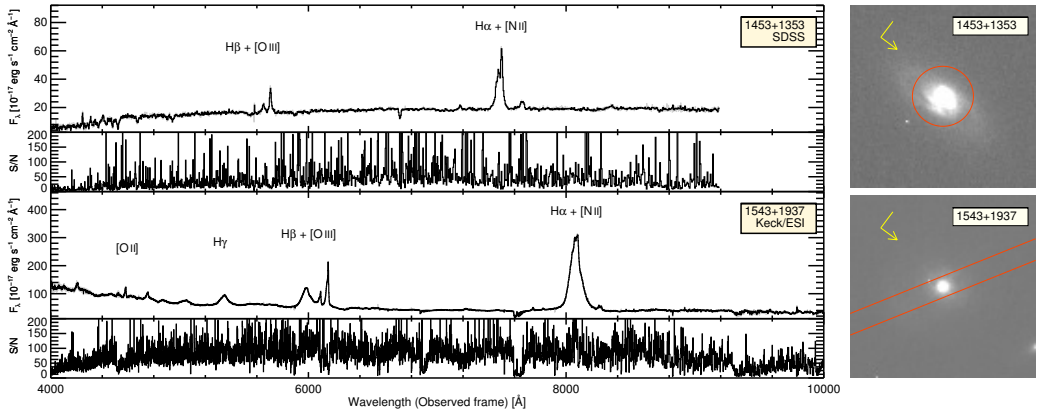

Figure 3.3 Continued

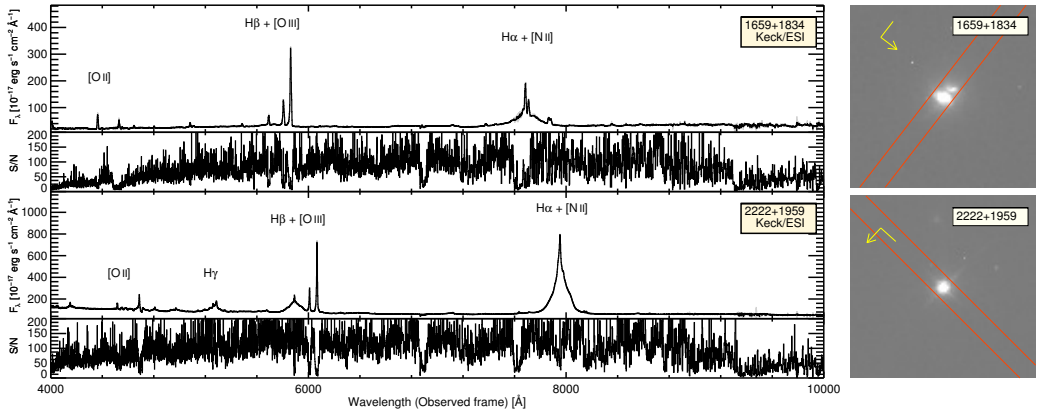

Figure 3.3 Continued

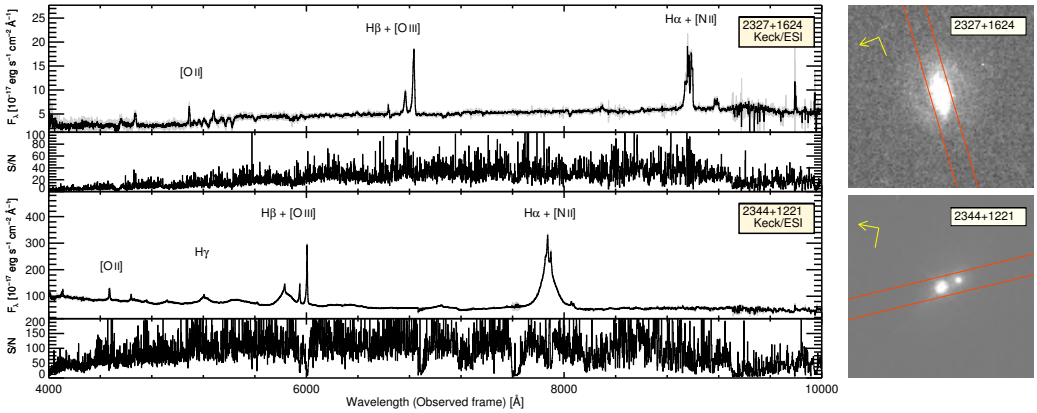

Figure 3.3 Continued

3.3.1 Spectral Fitting of Hydrogen Lines

In this subsection, we describe how the broad emission lines (BELs) of Hβ, Hα, Pβ, and Pα are fitted to measure the luminosities and FWHMs. The fitting of these lines starts with the identification of the line, and we find the Hβ, Hα, Pβ, and Pα lines in 11, 12, 14, and 6 red AGNs, respectively.

After the line identification, we correct the spectra for the Galactic extinction (Schlafly & Finkbeiner 2011) using the reddening law of Fitzpatrick (1999). Then, we transform the spectra to the rest frame and fit the continua for the Hβ, Hα, Pβ, and Pα lines. For Hα, Pβ, and Pα, the continuum around each line is fitted with a single power-law; however, an additional Fe component is required for the Hβ line. The Fe blends are determined by scaling and broadening the Fe template from the spectrum of IZw1 (Boroson & Green 1992), and this procedure is performed with `MPFIT` (Markwardt 2009) using Interactive Data Language (IDL). As an example, Figure 4 shows the spectra around the Hβ, Hα, Pβ, and Pα lines, along with the fitted continuum models, and the continuum-subtracted spectra.

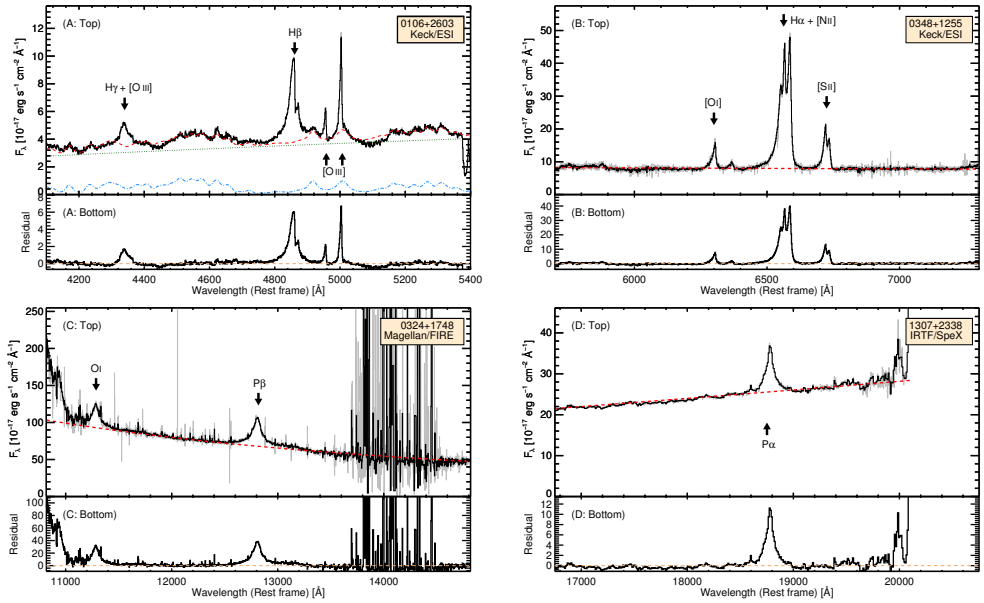

Figure 3.4 (A) Top: The optical spectrum of 0106+2603 obtained with the ESI on Keck telescope. The black solid line denotes the optical spectrum around Hβ line, and this spectrum includes several interesting emission lines, such as Hγ (4341 Å), [O III] (4363, 4959, and 5007 Å), and Hβ (4861 Å). The fitted model continuum spectrum is represented by the red dashed line, and this model is composed of a power-law component (the green dotted line) and a component for the Fe blends (the sky blue dot-dashed line). Bottom: The fitted model continuum-subtracted spectrum is represented, and this continuum-subtracted spectrum is used for estimating the line luminosity and FWHM. (B) The original and residual spectrum around the Hα line of 0348+1255, which is obtained with Keck/ESI. The meanings of the black solid line and the red dashed line are identical to panel (A). The black arrows represent [O I] (6300 Å), Hα (6563 Å), [N II] (6548 and 6583 Å), and [S II] (6716 and 6731 Å). (C) The original and residual spectrum around the Pβ line of 0324+1748, which is taken with Magellan/FIRE. The meanings of the black solid line and the red dashed line are identical to panel (A), and Pβ and O I (1.1287 μm) are marked with the black arrows. (D) The original and residual spectrum around the Pα line of 1307+2338, which is obtained with IRTF/SpeX. The meanings of the black solid line and the red dashed line are identical to panel (A), and Pα line is marked with the black arrow.

We note that several lines exist around the Hβ, Hα, Pβ, and Pα lines (e.g., Hγ λ4340, [O III] $\lambda\lambda$4956, 5007 doublet, [S II] $\lambda\lambda$6716, 6731 doublet, and O I λ11287). Hence, the continuum-fitting regions are chosen to avoid the nearby lines.

After the continuum subtraction, we model the narrow lines using the [O III] $\lambda\lambda$ 4956, 5007 and [S II] $\lambda\lambda$6716, 6731 doublets as templates. In order to fit the [S II] lines, we use two single Gaussian functions. However, the [O III] lines require double Gaussian functions for their asymmetric blue wings (Greene & Ho 2005). Although Greene & Ho (2005) suggest that the [O III] lines are not appropriate as a template for the narrow lines of unobscured type 1 quasars due to the blue wings, this template gives better results than the [S II] template when fitting the narrow components of the Hβ line, for a part of our red AGN sample. However, since the [S II] template is better to fit the narrow components of Hα, Pβ, and Pα lines, the template from the [S II] lines is primarily used to fit these lines, except when the [S II] lines are not detected.

Moreover, the [S II] narrow line template is also used for fitting the [N II] $\lambda\lambda$6548, 6583 doublet and the narrow component of the hydrogen lines. For the fitting of the [N II] lines, we fit the Hα and [N II] lines simultaneously. The width of the [N II] line is fixed to the width of the narrow line template, and its flux ratio is fixed to 2.96 (Kim et al. 2006).

We note that the narrow line template from the [O III] lines is used for 0106+2603 (Hβ and Hα), 0157+1712 (Hβ), 0221+1327 (Hβ, Hα, Pβ, and Pα), 0348+1255 (Hβ), 1659+1834 (Hβ), 2222+1959 (Hβ, Hα, and Pβ), 2327+1624 (Hβ), and 2344+1221 (Hβ), and the narrow line template from the [S II] lines is used for 0157+1712 (Hα and Pβ), 0348+1255 (Hα and Pβ), 1453+1353 (Hα and Pα), 1543+1937 (Hα), 1659+1834 (Hα, Pβ, and Pα), 2327+1624 (Hα), and 2344+1221 (Hα and Pβ). The measured FWHMs and luminosities of the [O III], [N II], and [S II] lines are listed in Table 4.

Table 3.4. Line measurements of [O III], [N II], and [S II] lines

Object Name	[O III] λ5007		[N II] λ6548		[S II] λ6716	
	L $[10^{38}\,\mathrm{erg\,s^{-1}}]$	FWHM $[\mathrm{km\,s^{-1}}]$	L $[10^{38}\,\mathrm{erg\,s^{-1}}]$	FWHM $[\mathrm{km\,s^{-1}}]$	L $[10^{38}\,\mathrm{erg\,s^{-1}}]$	FWHM $[\mathrm{km\,s^{-1}}]$
0106+2603	29.72±1.45	359.9±37.5	11.75±0.11	359.9±37.5	–	–
0157+1712	41.72±4.01	988.4±64.0	11.58±0.14	563.7±20.7	7.510±0.395	563.7±20.7
0221+1327	154.6±12.3	539.5±51.7	22.73±0.46	539.5±51.7	–	–
0234+2438	–	–	–	–	–	–
0324+1748	–	–	–	–	–	–
0348+1255	21.54±0.74	718.7±20.3	20.81±0.20	595.8±6.8	20.62±0.35	595.8±6.8
1258+2329	–	–	–	–	–	–
1307+2338	–	–	–	–	–	–
1453+1353	–	–	10.25±0.38	695.5±47.5	4.699±0.349	695.5±47.5
1543+1937	483.2±23.5	808.2±81.9	55.58±0.80	387.2±10.8	19.70±1.03	387.2±10.8
1659+1834	344.2±5.4	628.7±22.0	30.97±0.35	501.2±5.1	27.22±0.40	501.2±5.1

Table 3.4 (cont'd)

Object Name	[O III] λ5007		[N II] λ6548		[S II] λ6716	
	L $[10^{38}\,\mathrm{erg\,s^{-1}}]$	FWHM $[\mathrm{km\,s^{-1}}]$	L $[10^{38}\,\mathrm{erg\,s^{-1}}]$	FWHM $[\mathrm{km\,s^{-1}}]$	L $[10^{38}\,\mathrm{erg\,s^{-1}}]$	FWHM $[\mathrm{km\,s^{-1}}]$
2222+1952	–	–	–	–	–	–
2222+1959	987.2±41.4	538.9±41.7	84.91±0.84	538.9±41.7	–	–
2303+1624	–	–	–	–	–	–
2327+1624	116.3±20.8	719.6±76.5	29.92±0.52	518.9±33.1	13.76±1.59	518.9±33.1
2344+1221	248.9±10.1	449.3±29.0	52.69±0.99	301.1±10.0	17.00±0.97	301.1±10.0

Note. — The listed fluxes are not corrected from the dust extinction caused by their host galaxies.

For 1258+2329 (Pα) and 2303+1624 (Pβ), the narrow lines cannot be modeled due to the absence of the [O III] and [S II] lines, so Gaussian functions were fit to the lines. One of the fitted components is classified as the narrow component due to its FWHM being less than $600\,\mathrm{km\,s^{-1}}$.

Using the model of the narrow component, we simultaneously fit the broad line (FWHM $> 600\,\mathrm{km\,s^{-1}}$) with a single or double Gaussian function. Figure 5 shows the Hβ, Hα, Pβ, and Pα lines of red AGNs and its fitted models. For the fit, a single, double, or multiple Gaussian functions are used, so the measured line luminosities and FWHMs can be somewhat biased. To correct the bias, we adopt correction factors of $\mathrm{flux_{multi}/flux_{double}} = 1.05$, $\mathrm{flux_{multi}/flux_{single}} = 1.06$, $\mathrm{FWHM_{multi}/FWHM_{double}} = 0.85$, and $\mathrm{FWHM_{multi}/FWHM_{single}} = 0.91$ (Kim et al. 2010, 2017). Moreover, the FWHMs are corrected for the instrumental resolution as $\mathrm{FWHM^2 = FWHM^2_{obs} - FWHM^2_{inst}}$.

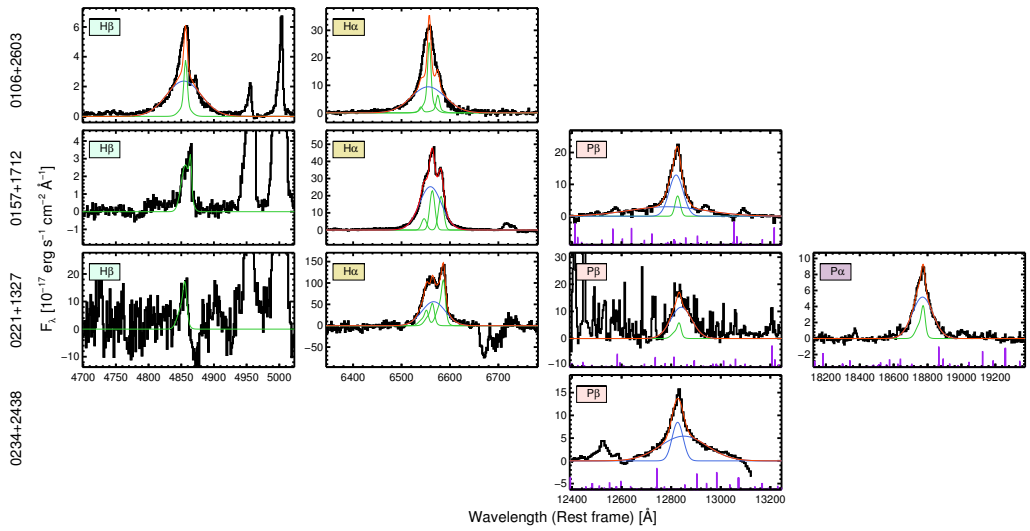

Figure 3.5 Results of the fitting of Hβ, Hα, Pβ, and Pα lines. The black lines indicate the continuum-subtracted observed spectra in the rest frame. The red lines represent the best-fit model, and the green and blue lines mean the narrow and broad component, respectively. Moreover, for the Pβ and Pα figures, the purple lines at the bottom show the sky OH emission lines.

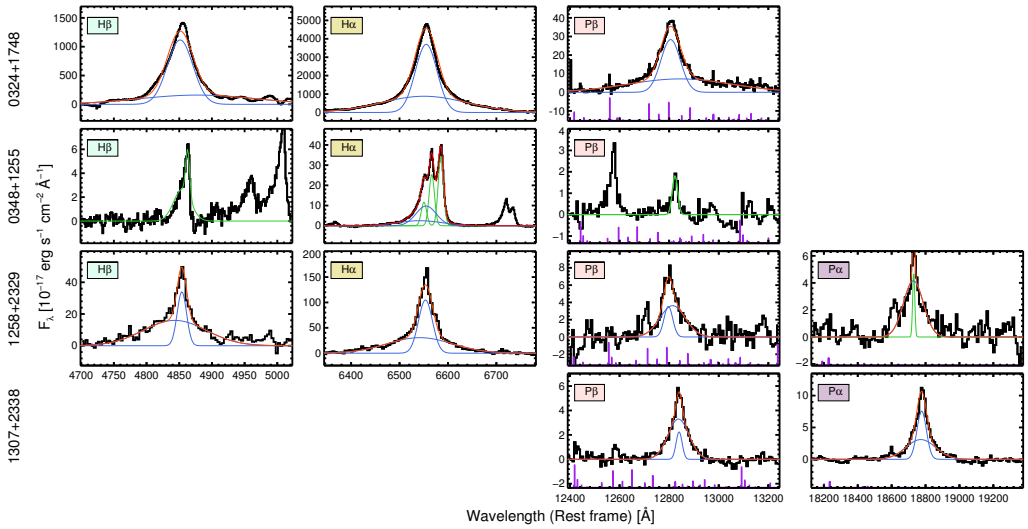

Figure 3.5 Continued

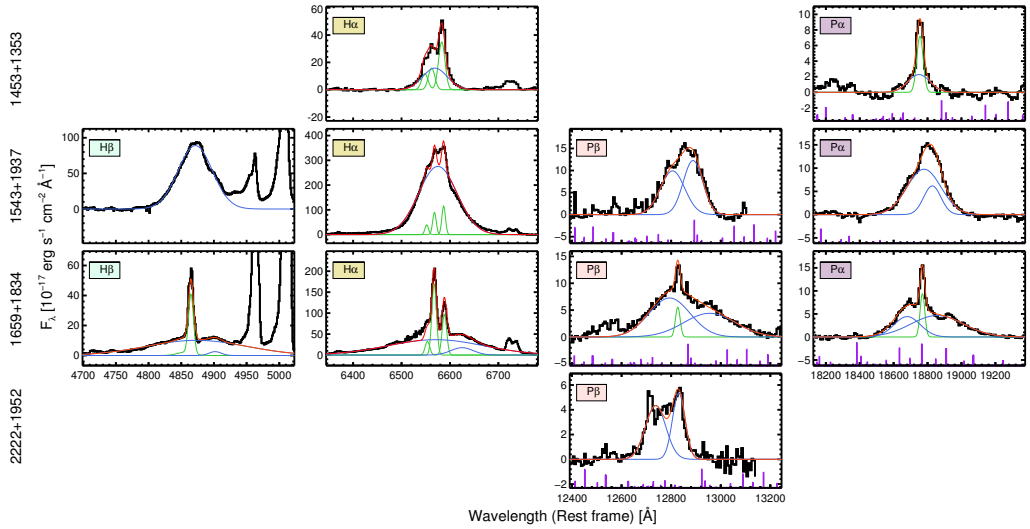

Figure 3.5 Continued

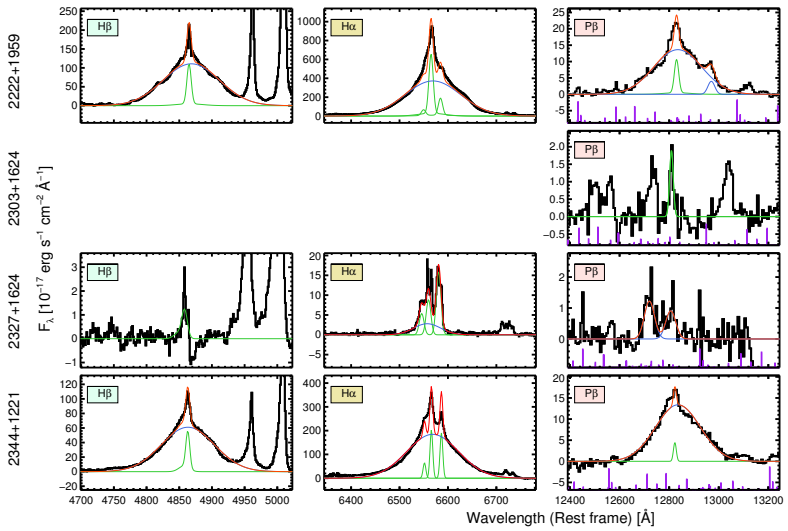

Figure 3.5 Continued

We note that the FWHM of the Pβ line of 2327+1624 is not measured, because the Pβ line is fitted by two Gaussian components that are broadly split. The broadly split components yield four half-maximum points, so the FWHM cannot be measured.

Strong correlations between the FWHMs of the Balmer and Paschen lines have been established for unobscured type 1 quasars (Landt et al. 2008; Kim et al. 2010). A tight correlation between the two quantities for our sample would imply that the luminosities originate from the same BLR, and the contribution of the narrow component is negligible. As shown in Figure 6, the measured FWHMs of Paschen lines are similar to those of Balmer lines, and the correlations between the two quantities are similar to those of unobscured type 1 quasars.

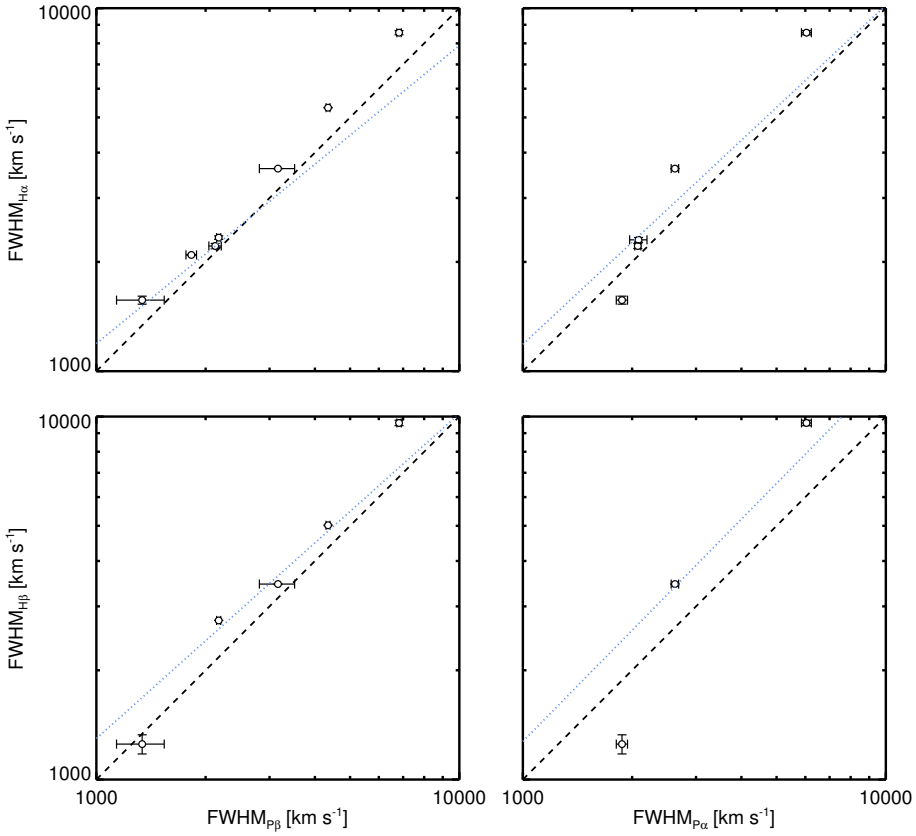

Figure 3.6 Comparisons of FWHMs of Balmer and Paschen lines. The black dashed lines show the two quantities are identical, and the blue dotted lines denote the adopted correlation of unobscured type 1 quasars from Kim et al. (2010).

In total, we obtain the broad line luminosities and FWHMs of seven Hβ, twelve Hα, twelve Pβ, and six Pα lines. The measured luminosities and FWHMs of the hydrogen lines for broad and narrow components are summarized in Table 5 and Table 6, respectively.

Table 3.5. Hydrogen line measurements for broad component

Object Name	Hβ		Hα		Pβ		Pα	
	FWHM [km s^{-1}]	L [10^{40} erg s^{-1}]	FWHM [km s^{-1}]	L [10^{40} erg s^{-1}]	FWHM [km s^{-1}]	L [10^{40} erg s^{-1}]	FWHM [km s^{-1}]	L [10^{40} erg s^{-1}]
0106+2603	3281±5	1.000±0.003	3227±8	5.312±0.028	–	–	–	–
0157+1712	–	–	2090±7	2.009±0.017	1827±62	2.729±0.130	–	–
0221+1327	–	–	2212±36	1.875±0.070	2125±84	0.682±0.043	2252±45	1.442±0.014
0234+2438	–	–	–	–	1515±74	5.741±0.202	–	–
0324+1748	2744±0	339.5±1.6	2333±26	1513±3	2173±29	24.67±0.42	–	–
0348+1255	–	–	2539±326	1.027±0.038	–	–	–	–
1258+2329	1252±56	5.601±0.137	1569±40	19.75±0.39	1337±204	1.368±0.152	1876±67	1.342±0.084
1307+2338	–	–	–	–	1125±105	1.040±0.073	1113±34	0.997±0.129
1453+1353	–	–	2301±35	0.541±0.033	–	–	1862±101	0.229±0.023
1543+1937	3456±10	9.554±0.038	3615±4	44.27±0.10	3165±334	3.926±0.375	2624±64	2.254±0.193
1659+1834	9603±166	1.603±0.023	8561±110	8.117±0.051	6822±91	2.128±0.036	6045±194	1.135±0.058

Table 3.5 (cont'd)

Object Name	Hβ		Hα		Pβ		Pα	
	FWHM [km s^{-1}]	L [10^{40} erg s^{-1}]	FWHM [km s^{-1}]	L [10^{40} erg s^{-1}]	FWHM [km s^{-1}]	L [10^{40} erg s^{-1}]	FWHM [km s^{-1}]	L [10^{40} erg s^{-1}]
2222+1952	–	–	–	–	3212±511	3.798±0.209	–	–
2222+1959	5316±9	16.28±0.04	5268±4	73.07±0.12	6099±64	4.470±0.083	–	–
2303+1624	–	–	–	–	–	–	–	–
2327+1624	–	–	2554±71	0.940±0.050	–	0.524±0.109	–	–
2344+1221	5018±13	7.423±0.030	5320±8	26.75±0.08	4348±54	3.551±0.064	–	–

Note. — The listed fluxes of Hβ, Hα, Pβ, and Pα lines are not corrected from the dust extinction caused by their host galaxies.

Table 3.6. Hydrogen line measurements for narrow component

Object Name	Hβ		Hα		Pβ		Pα	
	L [10^{38} erg s^{-1}]	FWHM [km s^{-1}]	L [10^{38} erg s^{-1}]	FWHM [km s^{-1}]	L [10^{38} erg s^{-1}]	FWHM [km s^{-1}]	L [10^{38} erg s^{-1}]	FWHM [km s^{-1}]
0106+2603	20.17±0.03	359.9±37.5	140.6±0.8	359.9±37.5	–	–	–	–
0157+1712	6.869±0.300	988.4±64.0	40.24±0.71	563.7±20.7	22.02±3.78	563.7±20.7	–	–
0221+1327	10.73±4.40	539.5±51.7	32.92±1.62	539.5±51.7	3.615±0.656	539.5±51.7	2.566±0.424	539.5±51.7
0234+2438	–	–	–	–	–	–	–	–
0324+1748	–	–	–	–	–	–	–	–
0348+1255	14.88±0.10	718.7±20.3	45.51±0.60	595.8±6.8	6.396±0.659	595.8±6.8	–	–
1258+2329	–	–	–	–	–	–	15.77±4.82	190.3±36.1
1307+2338	–	–	–	–	–	–	–	–
1453+1353	–	–	13.76±0.87	695.5±47.5	–	–	17.55±0.65	695.5±47.5
1543+1937	–	–	128.0±2.1	387.2±10.8	–	–	–	–
1659+1834	35.11±9.53	628.7±22.0	161.5±2.0	501.2±5.1	10.57±0.65	501.2±5.1	26.17±1.27	501.2±5.1

Table 3.6 (cont'd)

Object Name	Hβ		Hα		Pβ		Pα	
	L [10^{38} erg s^{-1}]	FWHM [km s^{-1}]	L [10^{38} erg s^{-1}]	FWHM [km s^{-1}]	L [10^{38} erg s^{-1}]	FWHM [km s^{-1}]	L [10^{38} erg s^{-1}]	FWHM [km s^{-1}]
2222+1952	–	–	–	–	–	–	–	–
2222+1959	144.6±1.3	538.9±41.7	875.9±5.3	538.9±41.7	14.12±1.04	538.9±41.7	–	–
2303+1624	–	–	–	–	9.334±3.732	394.6±116.0	–	–
2327+1624	7.587±9.783	719.6±76.5	49.27±1.45	518.9±33.1	–	–	–	–
2344+1221	60.26±0.91	449.3±29.0	166.5±2.7	301.1±10.0	7.326±1.189	301.1±10.0	–	–

Note. — The listed fluxes are not corrected from the dust extinction caused by their host galaxies.

3.4 Reddening

In this section, we assume that the red colors of red AGNs originate from the dust extinction in their host galaxies, as shown in several previous studies (Glikman et al. 2007; Urrutia et al. 2008, 2009; Kim et al. 2017). Hence, measuring the color excess, $E(B-V)$, is important to investigate the intrinsic, i.e., un-reddened properties of red AGNs. In the following subsections, $E(B-V)$ values are derived using two methods; comparison of line luminosity ratios and continuum slopes between unobscured and red AGNs. In this section, we use the reddening law, $k(\lambda)$, of Fitzpatrick (1999), based on the Galactic extinction curve from 1000 Å to 3.5 μm with $R_V = 3.1$.

3.4.1 Reddening derived from line luminosity ratios

We measure the reddening from line luminosity ratios ($E(B-V)_{\rm line}$) of red AGNs by using four line luminosity ratios of Balmer to Paschen lines ($L_{\rm H\beta}/L_{\rm P\beta}$, $L_{\rm H\alpha}/L_{\rm P\beta}$, $L_{\rm H\beta}/L_{\rm P\alpha}$, and $L_{\rm H\alpha}/L_{\rm P\alpha}$). We use the correlation between the Balmer and Paschen line luminosities of unobscured type 1 quasars adopted from Kim et al. (2010) as their intrinsic line luminosity ratios. By comparing the line luminosity ratios, the $E(B-V)_{\rm line}$ values can be measured for 10 out of the 16 red AGNs.

The $E(B-V)_{\rm line}$ values are computed by varying the amount of dust reddening to minimize χ^2, which is a function of the line luminosity ratios of red AGNs ($R_{\rm obs,i,j} = L_{\rm obs,\lambda j}/L_{\rm obs,\lambda i}$) and unobscured type 1 quasars ($R_{\rm int,i,j} = L_{\rm int,\lambda j}/L_{\rm int,\lambda i}$), expressed as

$$\chi^2 = \sum_{\rm i,j=1}^{N} \frac{(R_{\rm obs,i,j} - E(R_{\rm int,i,j}))^2}{\sigma_{\rm i,j}^2}. \quad (3.1)$$

Here, N is the number of line luminosity ratios, $\sigma_{\rm i,j}$ are the combined uncertainties of the line luminosity ratios and the adopted correlations from Kim et al. (2010), and E is a function for the dust reddening expressed as

$$\log\left(\frac{E(R_{\rm int,i,j})}{R_{\rm int,i,j}}\right) = \frac{E(B-V)}{1.086}(k(\lambda{\rm i}) - k(\lambda{\rm j})). \quad (3.2)$$

For estimating the uncertainty of $E(B-V)_{\rm line}$, we perform 1000 Monte-Carlo simulations. We calculate new line luminosity ratios by adding the measurement uncertainties of the line luminosities randomly to the observed line luminosities. The standard deviation of the 1000 newly measured $E(B-V)_{\rm line}$ values is taken as the uncertainty of $E(B-V)_{\rm line}$.

In Figure 7, we compare the observed and the dust extinction corrected line luminosities with the $E(B-V)_{\rm line}$ values. The measured $E(B-V)_{\rm line}$ values and uncertainties for the 10 red AGNs are summarized in Table 7.

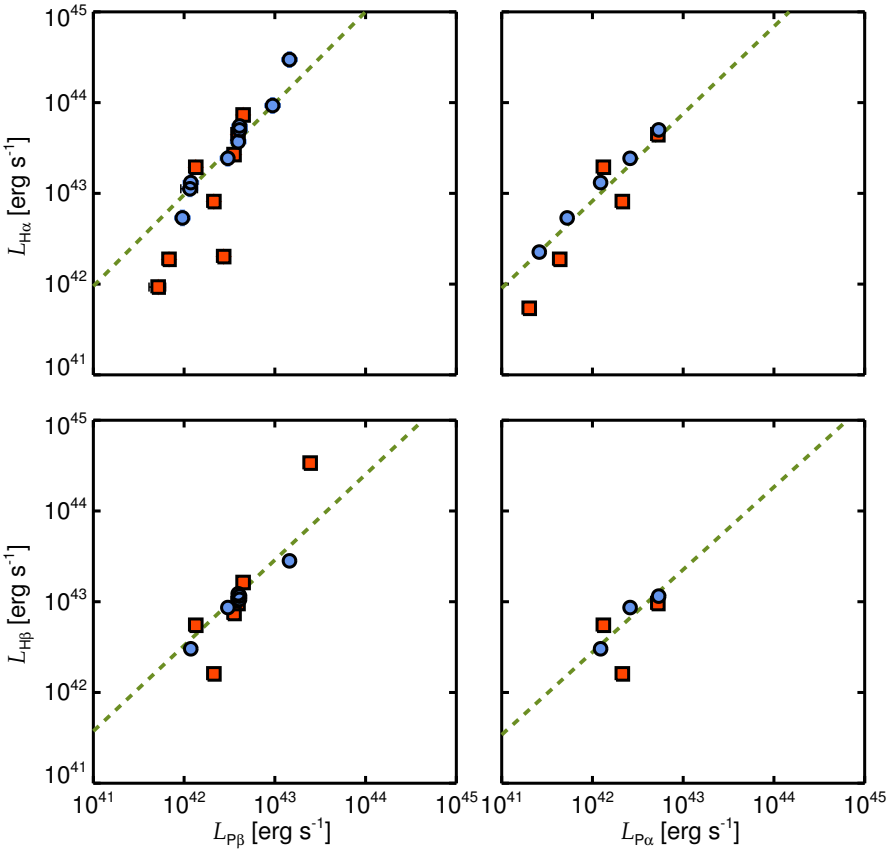

Figure 3.7 The observed and dust extinction corrected line luminosities of red AGNs. The red squares show the observed line luminosities, and the blue circles mean the dust extinction corrected line luminosities with the measured $E(B-V)_{\rm line}$ values. The green dotted lines represent the correlations between the Balmer and Paschen line luminosities (Kim et al. 2010), and these correlations are used for estimating the $E(B-V)_{\rm line}$ values.

Table 3.7. Four kinds of $E(B-V)$ values

Object	$E(B-V)_{\rm line}$ (mag)	$E(B-V)_{\rm cont}$ (mag)	$E(B-V)_{\rm BD1}$ (mag)	$E(B-V)_{\rm BD2}$ (mag)
0106+2603	–	0.676±0.001	0.137±0.005	0.371±0.005
0157+1712	1.766±0.028	2.051±0.004	–	–
0221+1327	0.484±0.031	0.983±0.007	–	–
0234+2438	–	–	–	–
0324+1748	-0.745±0.007	-0.167±0.000	-0.013±0.004	-0.003±0.004
0348+1255	–	0.816±0.001	–	–
1258+2329	-0.179±0.022	0.103±0.000	-0.213±0.027	-0.006±0.023
1307+2338	–	–	–	–
1453+1353	0.657±0.058	0.872±0.002	–	–
1543+1937	0.056±0.013	0.246±0.000	0.020±0.004	0.175±0.004
1659+1834	0.505±0.007	0.256±0.002	0.096±0.014	0.315±0.012
2222+1952	–	–	–	–
2222+1959	-0.129±0.008	0.271±0.000	-0.007±0.003	0.129±0.002
2303+1624	–	–	–	–
2327+1624	1.148±0.166	0.410±0.008	–	–
2344+1221	0.150±0.008	0.260±0.000	-0.194±0.004	-0.002±0.004

3.4.2 Reddening derived from continuum slopes

We measure the reddening from continuum slope ($E(B-V)_{\rm cont}$) of the red AGNs by comparing the observed spectrum, $f(\lambda)$, to model spectrum. A model spectrum combines a reddened quasar composite, $Q(\lambda)$, and reddened stellar template, $S(\lambda)$. The intrinsic quasar composite, $Q_0(\lambda)$, is adopted from Glikman et al. (2006), which is a composition of an optical quasar composite (Brotherton et al. 2001) and a NIR quasar composite (Glikman et al. 2006). They used unobscured type 1 quasars for constructing the optical and NIR quasar composites. For the intrinsic stellar template, $S_0(\lambda)$, we use a K type star spectrum adopted from SDSS (MJD=51816, plate=396, and fiber=605), since K type stars are the most dominant population of the stellar composite template for red AGNs (Canalizo et al. 2012).

In order to fit the $E(B-V)_{\rm cont}$ values, we fit the model spectrum to the observed spectrum, and the fitting function has a form of

$$f(\lambda) = Q(\lambda) + S(\lambda). \tag{3.3}$$

Here, $Q(\lambda)$ and $S(\lambda)$ are the reddened spectra of $Q_0(\lambda)$ and $S_0(\lambda)$, respectively, with their $E(B-V)$ values as

$$\log\left(\frac{X(\lambda)}{X_0(\lambda)}\right) = -\frac{k(\lambda)E(B-V)_X}{1.086}, \tag{3.4}$$

where $E(B-V)_Q$ is taken as $E(B-V)_{\rm cont}$. Here, $X(\lambda)$ denotes $Q(\lambda)$ or $S(\lambda)$, and $X_0(\lambda)$ is $Q_0(\lambda)$ or $S_0(\lambda)$.

For the fit, we use only a limited wavelength range (3790–10,000 Å), because Glikman et al. (2007) reported that fitting with the optical and NIR combined spectrum yields extremely poor results for one-third of red AGNs. Moreover, to exclude strong emission lines, wavelength regions of 3790–4700, 5100-6400, and 6700–10,000 Å are used. From this fitting procedure, we measure the $E(B-V)_{\rm cont}$ values for 12 red AGNs, and Figure 8 shows the fitting results. The measured $E(B-V)_{\rm cont}$ values and uncertainties are summarized in Table 7.

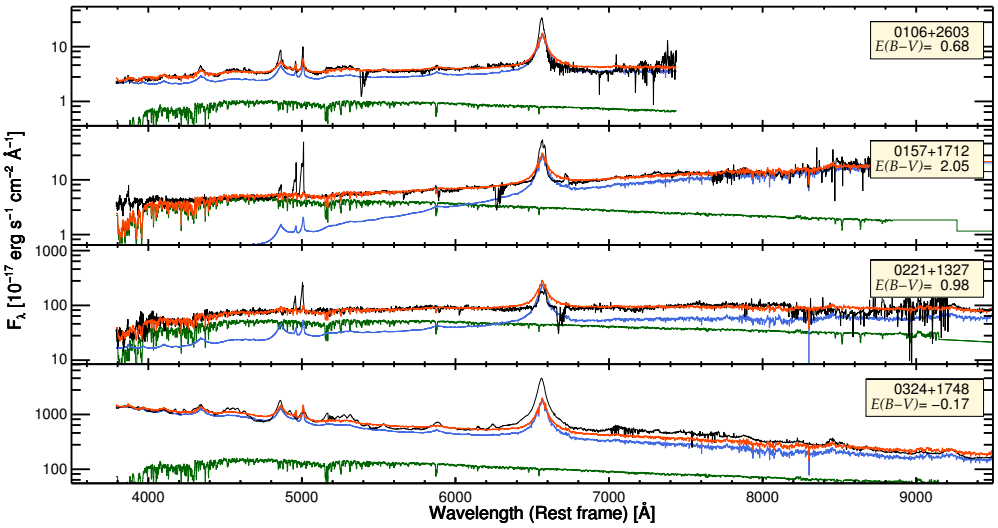

Figure 3.8 Spectra of red AGNs with the best-fit models are shown in rest frame. The shown wavelength range is from 3790 to 10,000 Å. The black lines denote the observed spectra. The green and blue lines mean the stellar and quasar spectra, respectively, and those spectra were applied by the dust reddening. The red line shows the sum of the dust extincted stellar and quasar spectra. The right-top box denotes the name of red AGN and the measured $E(B-V)_{\rm cont}$. Note that the host galaxy dominates the spectrum for 0157+1712 and 0221+1327 at short wavelength range (< 6500 Å) due to their quite big $E(B-V)_{\rm cont}$ values ($\gtrsim 1$).

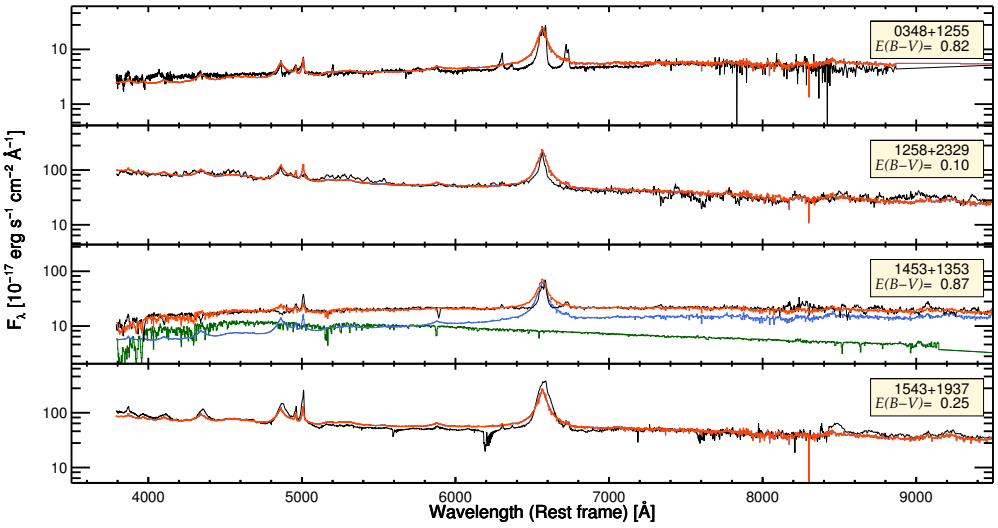

Figure 3.8 Continued

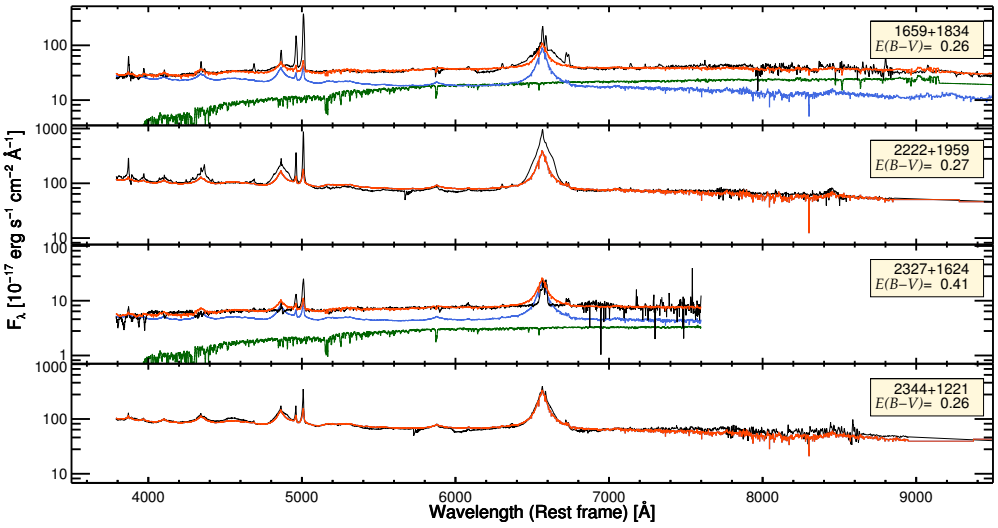

Figure 3.8 Continued

3.4.3 Discussion for the two types of reddening

We compare the $E(B-V)_{\rm line}$ values to the $E(B-V)_{\rm cont}$ values for the 10 red AGNs that have both $E(B-V)_{\rm line}$ and $E(B-V)_{\rm cont}$ in Figure 9. The two types of $E(B-V)$ values are consistent, and there is no significant trend in the difference between the two $E(B-V)$ values. We estimate the Pearson correlation coefficient between the two quantities. For estimating the coefficient, we exclude 0324+1748 that has negative values for both types of $E(B-V)$, and assume that the negative $E(B-V)$ values ($E(B-V)_{\rm line}$ values of 1258+2329 and 2222+1959) are 0. The measured coefficient is 0.822, and the rms scatter with respect to a one-to-one correlation is 0.249. This result supports that the two measurements of $E(B-V)$ are mutually verified.

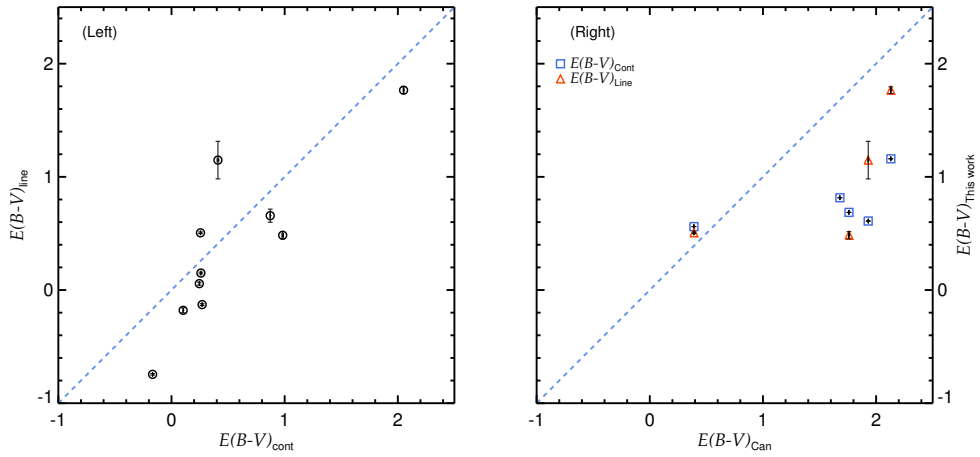

Figure 3.9 (Left) Comparison between the $E(B-V)_{\rm line}$ values and the $E(B-V)_{\rm cont}$ values of red AGNs. The blue dashed line denotes a line where the two values are identical. (Right) We compare the two types of $E(B-V)$ values with the $E(B-V)_{\rm Can}$ values. Blue squares and red triangles represent the $E(B-V)_{\rm cont}$ and $E(B-V)_{\rm line}$ values, respectively. The meaning of the blue dashed line is identical to the left panel.

Moreover, we compare the two types of $E(B-V)$ values to the $E(B-V)$ values adopted from Canalizo et al. (2012) (hereafter, $E(B-V)_{\rm Can}$), and this comparison is shown in Figure 9. They measured the $E(B-V)_{\rm Can}$ by comparing the observed continuum spectrum to the SDSS composite QSO spectrum (Vanden Berk et al. 2001) reddened with a Small Magellanic Cloud reddening law (Bouchet et al. 1985), and five red AGNs (0157+1712, 0221+1327, 0348+1255, 1659+1834, and 2327+1624) are overlapped with our sample. They showed that the $E(B-V)_{\rm Can}$ values were generally consistent with the $E(B-V)$ values derived by using Balmer decrements, and the difference between this two quantities was $\sim$0.3. Our $E(B-V)_{\rm cont}$ and $E(B-V)_{\rm line}$ values are generally, but somewhat weakly, consistent with the $E(B-V)_{\rm Can}$ values. Between the $E(B-V)_{\rm cont}$ and $E(B-V)_{\rm Can}$ values, the Pearson correlation coefficient is 0.603, and the rms scatter is 0.679. For the $E(B-V)_{\rm line}$ values, the result is generally same as the coefficient is 0.668 with the rms scatter of 0.546. We found a trend that the $E(B-V)$ values from this work is less than the $E(B-V)_{\rm Can}$ values, as much as $\Delta E(B-V) \sim 0.707$, but this trend is not significant due to small number statistics.

Unlike our result, previous studies (Glikman et al. 2007; Kim et al. 2017) reported that the two types of $E(B-V)$ values are far from a one-to-one correlation. The Pearson correlation coefficient between the two quantities is only -0.21 with a rms scatter of 0.68 (Kim et al. 2017).

In the previous studies, the $E(B-V)_{\rm cont}$ values are from Glikman et al. (2007) and Urrutia et al. (2009), and the $E(B-V)_{\rm line}$ values are from Glikman et al. (2007). To obtain the $E(B-V)_{\rm cont}$ values, they fit the continua using the quasar component only, without the stellar component. In this study, considering the continuum spectra of the most of red AGNs are dominated by the quasar component, the measurement technique for the $E(B-V)_{\rm cont}$ is almost same, and it is hard to believe that the contrasting result comes from the discrepancy of the $E(B-V)_{\rm cont}$

values.

However, in order to measure the $E(B-V)_{\rm line}$ values, Glikman et al. used somewhat different way. They measured the $E(B-V)_{\rm line}$ values using Balmer decrements (hereafter, $E(B-V)_{\rm BD1}$). The $E(B-V)_{\rm BD1}$ values were obtained by following formula:

$$E(B-V)_{\rm BD1} = \frac{1.086}{k({\rm H}\beta) - k({\rm H}\alpha)} \ln\left(\frac{[F_{{\rm H}\alpha}/F_{{\rm H}\beta}]_{\rm measured}}{[F_{{\rm H}\alpha}/F_{{\rm H}\beta}]_{\rm FBQS}}\right). \quad (3.5)$$

Here, k(X) is the extinction law of Calzetti et al. (1994) at the wavelength of X line, and $[F_{{\rm H}\alpha}/F_{{\rm H}\beta}]_{\rm measured}$ and $[F_{{\rm H}\alpha}/F_{{\rm H}\beta}]_{\rm FBQS}$ are the $F_{{\rm H}\alpha}/F_{{\rm H}\beta}$ from the spectra of red quasars and the FIRST Bright Quasar Survey (FBQS; Gregg et al. 1996) composite spectrum, respectively. In this equation, the $[F_{{\rm H}\alpha}/F_{{\rm H}\beta}]_{\rm FBQS}$ is used as the intrinsic $F_{{\rm H}\alpha}/F_{{\rm H}\beta}$ of red quasars, which is a fixed value of 4.526 when only broad component is treated (Glikman et al. 2007).

Using this technique, we can measure the $E(B-V)_{\rm BD1}$ values for seven red AGNs, and they are summarized in Table 7. We compare the $E(B-V)_{\rm BD1}$ values to the $E(B-V)_{\rm line}$ and $E(B-V)_{\rm cont}$ values in Figure 10. For the $E(B-V)_{\rm BD1}$ values vs. $E(B-V)_{\rm line}$ values, six red AGNs are used, and the measured Pearson correlation coefficient is 0.201 with the rms scatter of 0.264. For the comparison between the $E(B-V)_{\rm BD1}$ and $E(B-V)_{\rm cont}$ values, we used seven red AGNs that have both quantities, and the Pearson coefficient and the rms scatter are 0.453 and 0.235, respectively. These results show the $E(B-V)_{\rm BD1}$ values are significantly different from other $E(B-V)$ values.

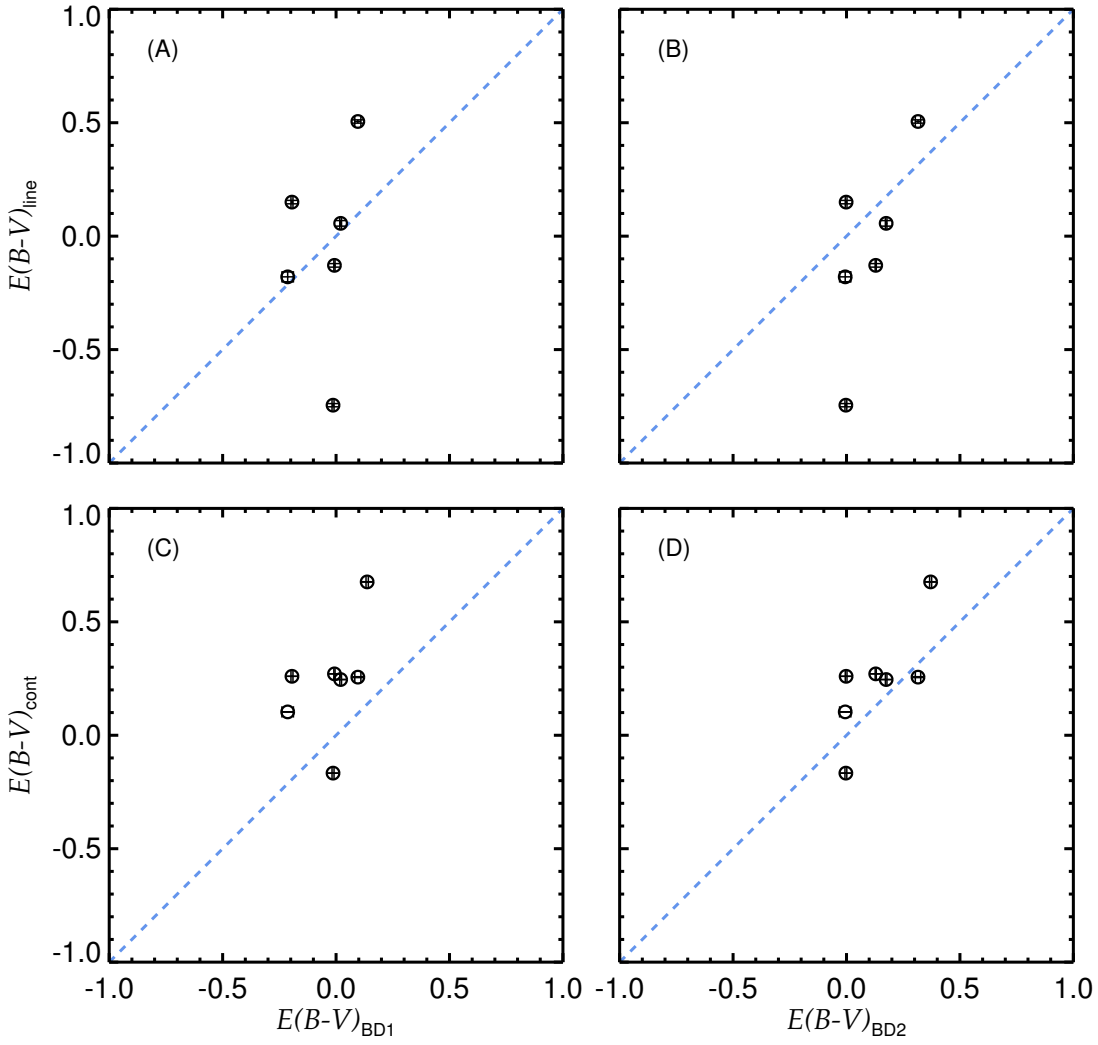

Figure 3.10 (A) Comparison between the $E(B-V)_{\rm BD1}$ and the $E(B-V)_{\rm line}$ values of red AGNs. The meaning of the blue dashed line is identical to Figure 9. (B) The $E(B-V)_{\rm BD2}$ vs. $E(B-V)_{\rm line}$ values. (C) The $E(B-V)_{\rm BD1}$ vs. $E(B-V)_{\rm cont}$ values. (D) The $E(B-V)_{\rm BD2}$ vs. $E(B-V)_{\rm cont}$ values.

In order to figure out what makes this different, we measure different type of Balmer decrement based-$E(B-V)$ values (hereafter, $E(B-V)_{\rm BD2}$). First, we combine two relations of $L_{\rm H\alpha}$–$L_{\rm P\alpha}$ and $L_{\rm H\beta}$–$L_{\rm P\alpha}$ from Kim et al. (2010) to make a relation of $L_{\rm H\alpha}$–$L_{\rm H\beta}$. The combined relation is

$$\log\left(\frac{L_{\rm H\alpha}}{10^{42}\,{\rm erg\,s^{-1}}}\right) = 0.509 + 1.056\log\left(\frac{L_{\rm H\beta}}{10^{42}\,{\rm erg\,s^{-1}}}\right) \tag{3.6}$$

that is used as the intrinsic $L_{\rm H\alpha}$–$L_{\rm H\beta}$ relation of red AGNs. Second, we measure the $E(B-V)_{\rm BD2}$ values by varying amount of dust reddening to minimize χ^2 that is a function of the $L_{\rm H\alpha}/L_{\rm H\beta}$ of red AGNs ($R_{\rm obs}$) and unobscured type 1 quasars ($R_{\rm int}$), expressed as

$$\chi^2 = \frac{(R_{\rm obs} - E(R_{\rm int}))^2}{\sigma^2}. \tag{3.7}$$

Here, the $R_{\rm int}$ is derived from the above relation of $L_{\rm H\alpha}$–$L_{\rm H\beta}$, E is a dust reddening function, and σ is the combined uncertainty of the $R_{\rm obs}$ and $R_{\rm int}$. The measured $E(B-V)_{\rm BD2}$ values are summarized in Table 7.

The $E(B-V)_{\rm BD2}$ values show tighter correlations with the $E(B-V)_{\rm line}$ and $E(B-V)_{\rm cont}$ values than the $E(B-V)_{\rm BD1}$ values, but this comparisons cannot be meaningful due to the small number statistics. The comparisons of the $E(B-V)_{\rm BD2}$ values with the $E(B-V)_{\rm line}$ and $E(B-V)_{\rm cont}$ values are shown in Figure 10. Between the $E(B-V)_{\rm BD2}$ and $E(B-V)_{\rm line}$ values, the Pearson correlation coefficient is 0.702 with the rms scatter of 0.245. For the $E(B-V)_{\rm BD2}$ and $E(B-V)_{\rm cont}$ values, the Pearson correlation coefficient and the rms scatter are 0.760 and 0.128, respectively. Although these Pearson correlation coefficients are slightly less than the quantity between the $E(B-V)_{\rm line}$ and $E(B-V)_{\rm cont}$ values of 0.850, which is significantly bigger than the comparison with the $E(B-V)_{\rm BD1}$ values.

Although the difference cannot be meaningful due to the small number statistics, if there is a difference, we suspect the different intrinsic $L_{\rm H\alpha}/L_{\rm H\beta}$ causes this conflicting results. Because, the intrinsic Balmer decrements are fixed to 4.526 for

deriving the $E(B-V)_{\rm BD1}$ values, but this quantities varies with the $L_{\rm H\beta}$ values for the $E(B-V)_{\rm BD2}$ values. For example, when the $L_{\rm H\beta}$ is increased from $10^{42}\,{\rm erg\,s^{-1}}$ to $10^{44}\,{\rm erg\,s^{-1}}$, the intrinsic Balmer decrement increases from 3.23 to 4.18, which makes $\sim$22% of discrepancy of the measured $E(B-V)$ values.

3.4.4 Color selection for red, dusty AGNs

In Urrutia et al. (2009), red AGNs were classified to have $E(B-V) > 0.1$. According to this criteria, among our sample, one (0324+1748) or four (0324+1748, 1258+2329, 1543+1937, and 2222+1959) objects cannot be classified as red AGNs based on the $E(B-V)_{\rm cont}$ or $E(B-V)_{\rm line}$ values, respectively. Compared to our sample, only two objects have $E(B-V) < 0.1$ in $\sim$50 candidates in Urrutia et al. (2009).

The difference between Urrutia et al. (2009) and our study may come from a lack of optical-NIR color criteria. Urrutia et al. (2009) used optical-NIR ($r'-K > 5$) and NIR color ($J-K > 1.3$), but our sample was selected by only NIR color ($J-K > 2$). As shown in Figure 11, a change of the $E(B-V)$ with the $J-K$ increase is not significant, but the $E(B-V)$ values are positive when $g'-K > 5$.

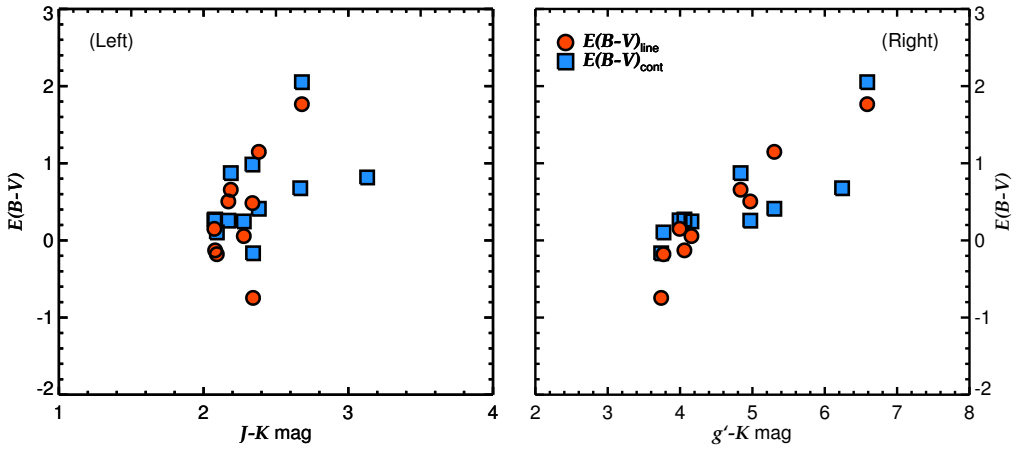

Figure 3.11 (Left) The comparison between the measured $E(B-V)$ values and $J-K$ magnitudes. Blue squares and red circles mean that the $E(B-V)$ values are the $E(B-V)_{\rm cont}$ and $E(B-V)_{\rm line}$ values, respectively. (Right) The comparison of $g'-K$ magnitudes vs. the $E(B-V)$ values. The meanings of the blue squares and red circles are identical to the left panel.

These red in NIR but blue in optical-NIR AGNs can be explained by (i) an unusual high hot dust covering factor ($CF_{HD} = L_{HD}/L_{bol}$; Rose 2014) or (ii) a synchrotron emission peak at NIR wavelength from jet (Whiting et al. 2001), and they are red but not dusty AGNs. This result suggests that optical-NIR color criteria is needed to select red, dusty red AGNs that is expected as the intermediate stage galaxies in the simulation studies.

However, considering the quite big rms scatter of the measured $E(B-V)$ values, 0.249, the objects with small $E(B-V)$ values cannot be concluded as not dusty AGNs within the imperfect information. Therefore, we use our sample as red, dusty AGNs in this study, but there is a possibility that some of our sample are red in NIR but not dusty AGNs.

3.5 Accretion rates

In this section, we measure the Eddington ratios ($\lambda_{Edd} = L_{bol}/L_{Edd}$, where L_{Edd} is the Eddington luminosity) of red AGNs at $z \sim 0.3$. To obtain the quantities, we derive BH masses and bolometric luminosities after correcting for the dust extinction by using the $E(B-V)_{line}$ values (if unavailable, $E(B-V)$cont values) to avoid the effects of dust extinction. If the taken $E(B-V)$ is negative, we did not correct the dust extinction under an assumption that there is no dust extinction.

As a comparison sample, we use the unobscured type 1 quasars in the quasar property catalog (Shen et al. 2011) of SDSS Seventh Data Release (DR7; Abazajian et al. 2009). To avoid the effects of sample bias, we set the sample selection criteria to be identical to those of our red AGNs: (i) $0.139 \leq z \leq 0.411$ and (ii) detection in all three 2MASS bands. Finally, we select 4130 unobscured type 1 quasars through the sample selection criteria.

On the aspect that the λ_{Edd} values may have dependence on the L_{bol} and M_{BH} values (e.g., Lusso et al. 2012; Suh et al. 2015), these selected control sample may

cause the sample bias effects. Thus, we address this issue in Section 5.3 by restraint on these samples with limited ranges of the $L_{\rm bol}$ and $M_{\rm BH}$.

3.5.1 BH masses

In order to measure the BH masses of red AGNs, NIR $M_{\rm BH}$ estimators (e.g., Kim et al. 2010, 2015a; Landt et al. 2011b) are used to alleviate the effects of the dust extinction. We adopt the Paschen-line-based $M_{\rm BH}$ estimators (Kim et al. 2010), to which we applied a recent virial coefficient of $\log f = 0.05$ (Woo et al. 2015). The modified, new virial-coefficient-applied, Paschen-line-based $M_{\rm BH}$ estimators are

$$\frac{M_{\rm BH}}{M_\odot} = 10^{7.04\pm0.02} \left(\frac{L_{\rm P\beta}}{10^{42}\,{\rm erg\,s^{-1}}}\right)^{0.48\pm0.03} \left(\frac{\rm FWHM_{P\beta}}{10^3\,{\rm km\,s^{-1}}}\right)^2 \tag{3.8}$$

and

$$\frac{M_{\rm BH}}{M_\odot} = 10^{7.07\pm0.04} \left(\frac{L_{\rm P\alpha}}{10^{42}\,{\rm erg\,s^{-1}}}\right)^{0.49\pm0.06} \left(\frac{\rm FWHM_{P\alpha}}{10^3\,{\rm km\,s^{-1}}}\right)^2. \tag{3.9}$$

We measure the BH masses for 11 and 6 red AGNs by using the Pβ- and Pα-based $M_{\rm BH}$ estimators, respectively. There is no significant difference between the measured Pβ- and Pα-based BH masses as shown in Figure 12, and the measured BH masses are listed in Table 8.

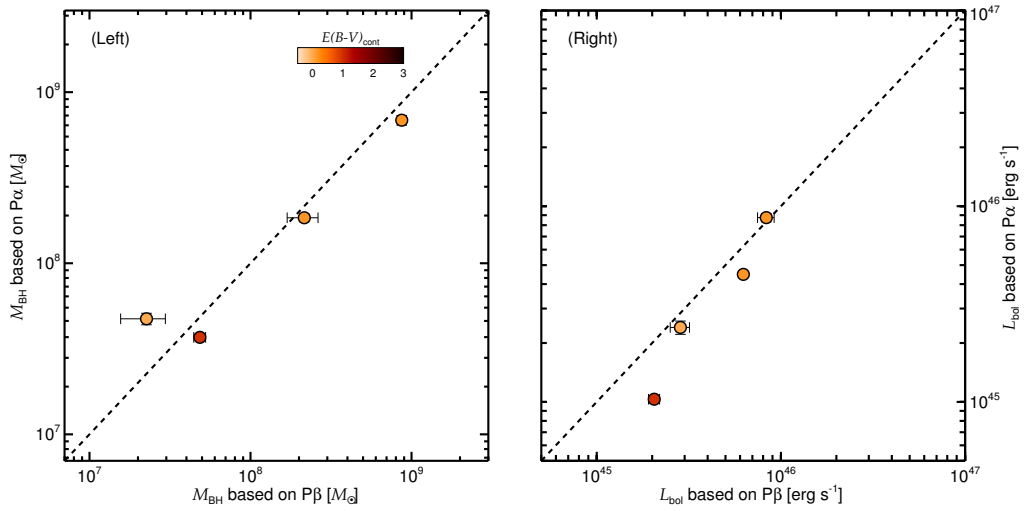

Figure 3.12 (Left) The comparison between the measured $M_{\rm BH}$ based on Pβ and Pα lines. The BH masses are represented by circles, and the colors in the circles mean their $E(B-V)_{\rm cont}$ values. (Right) The comparison of the $L_{\rm bol}$ values derived from Pβ vs. Pα lines. The circles denote the $L_{\rm bol}$ values, and the meaning of the colors in the circles is identical to the left panel.

Table 3.8. BH masses, bolometric luminosities, and $\lambda_{\rm Edd}$ values of red AGNs

Object Name	Pβ			Pα		
	$\log M_{\rm BH}$ $[M_\odot]$	$\log L_{\rm bol}$ $[{\rm erg\,s^{-1}}]$	$\lambda_{\rm Edd}$	$\log M_{\rm BH}$ $[M_\odot]$	$\log L_{\rm bol}$ $[{\rm erg\,s^{-1}}]$	$\lambda_{\rm Edd}$
0106+2603	–	–	–	–	–	–
0157+1712	8.032±0.031	46.27±0.02	1.381±0.126	–	–	–
0221+1327	7.607±0.024	45.37±0.02	0.462±0.031	7.358±0.009	45.09±0.01	0.428±0.013
0234+2438	–	–	–	–	–	–
0324+1748	8.381±0.012	46.67±0.01	1.551±0.053	–	–	–
0348+1255	–	–	–	–	–	–
1258+2329	7.354±0.121	45.45±0.05	1.000±0.344	7.675±0.032	45.38±0.03	0.403±0.044
1307+2338	–	–	–	–	–	–
1453+1353	–	–	–	7.420±0.048	44.73±0.04	0.162±0.026
1543+1937	8.334±0.091	45.92±0.04	0.306±0.078	8.266±0.021	45.94±0.02	0.376±0.026
1659+1834	8.939±0.012	45.80±0.01	0.057±0.002	8.836±0.028	45.65±0.02	0.052±0.004

Table 3.8 (cont'd)

Object Name	Pβ			Pα		
	$\log M_{\rm BH}$ $[M_\odot]$	$\log L_{\rm bol}$ $[{\rm erg\,s^{-1}}]$	$\lambda_{\rm Edd}$	$\log M_{\rm BH}$ $[M_\odot]$	$\log L_{\rm bol}$ $[{\rm erg\,s^{-1}}]$	$\lambda_{\rm Edd}$
2222+1952	–	–	–	–	–	–
2222+1959	8.923±0.009	45.96±0.01	0.086±0.003	–	–	–
2303+1624	–	–	–	–	–	–
2327+1624	–	45.39±0.09	–	–	–	–
2344+1221	8.603±0.011	45.91±0.01	0.160±0.005	–	–	–

Note. — The listed properties of red AGNs are measured after correcting for the dust extinction by using the $E(B-V)_{\rm cont}$ values.

To obtain the BH masses of unobscured type 1 quasars, we use an optical $M_{\rm BH}$ estimator (McLure & Dunlop 2004) consisting of $\lambda L_{5100\,\mathring{\rm A}}$ (L5100) and $\rm FWHM_{H\beta}$. For the optical $M_{\rm BH}$ estimator, we apply the virial coefficient of Woo et al. (2015) as

$$\frac{M_{\rm BH}}{M_\odot} = 5.27 \left(\frac{\rm L5100}{10^{44}\,{\rm erg\,s^{-1}}} \right)^{0.61} \left(\frac{\rm FWHM_{H\beta}}{\rm km\,s^{-1}} \right)^2. \tag{3.10}$$

The L5100 and $\rm FWHM_{H\beta}$ values of unobscured type 1 quasars are adopted from Shen et al. (2011).

3.5.2 Bolometric luminosities

For estimating the bolometric luminosities of red AGNs, we combine several empirical relations between the bolometric luminosity ($L_{\rm bol}$), the continuum luminosity, and the line luminosity. We bootstrap the empirical relations between $L_{\rm bol}$ and L5100 (Shen et al. 2011), L5100 and $L_{\rm H\alpha}$ (Jun et al. 2015), and $L_{\rm H\alpha}$ and the two Paschen line luminosities (Kim et al. 2010). The combined relations between $L_{\rm bol}$ and the Paschen line luminosities are

$$\log(\frac{L_{\rm bol}}{10^{44}\,{\rm erg\,s^{-1}}}) = 1.33 + 0.966\ \log(\frac{L_{\rm P\beta}}{10^{42}\,{\rm erg\,s^{-1}}}) \tag{3.11}$$

and

$$\log(\frac{L_{\rm bol}}{10^{44}\,{\rm erg\,s^{-1}}}) = 1.27 + 0.920\ \log(\frac{L_{\rm P\alpha}}{10^{42}\,{\rm erg\,s^{-1}}}). \tag{3.12}$$

We measured the $L_{\rm bol}$ values for 12 and 6 red AGNs by using $L_{\rm P\beta}$ and $L_{\rm P\alpha}$, respectively. The $L_{\rm bol}$ measured from Pβ and Pα show no significant difference, as shown in Figure 12, and the measured $L_{\rm bol}$ values are listed in Table 8.

To obtain the $L_{\rm bol}$ values of unobscured type 1 quasars, we use L5100 values, with the bolometric correction factor (9.26) for L5100, both of which are adopted from Shen et al. (2011).

3.5.3 Eddington ratios of red AGNs

When comparing the $\lambda_{\rm Edd}$ values of red AGNs to those of unobscured type 1 quasars, we prefer to use the $\lambda_{\rm Edd}$ values from Pα than those from Pβ when both quantities are available, to minimize the effects from the dust extinction. The $\lambda_{\rm Edd}$ values of nine red AGNs are used for the comparison, among which four (0157+1712, 0324+1748, 2222+1959, and 2344+1221) and five (0221+1327, 1258+2329, 1453+1353, 1543+1937, and 1659+1834) $\lambda_{\rm Edd}$ values are derived from Pβ and Pα, respectively.

The $M_{\rm BH}$ and $L_{\rm bol}$ values of red AGNs and unobscured type 1 quasars are shown in Figure 13, and Figure 14 shows their distributions of $\lambda_{\rm Edd}$ values. We find that $\lambda_{\rm Edd}$ values of red AGNs, $\log(\lambda_{\rm Edd}) = -0.654 \pm 0.500$, are higher than those of unobscured type 1 quasars, $\log(\lambda_{\rm Edd}) = -0.961 \pm 0.506$. For quantifying how significantly these two distributions of the $\lambda_{\rm Edd}$ values differ from each other, we perform the Kolmogorov-Smirnov test (K-S test) by using the `KSTWO` code based on IDL. The maximum deviation between the cumulative distributions of these two $\lambda_{\rm Edd}$ values, D, is 0.392, and the probability of the result given the null hypothesis, p, is 0.094.

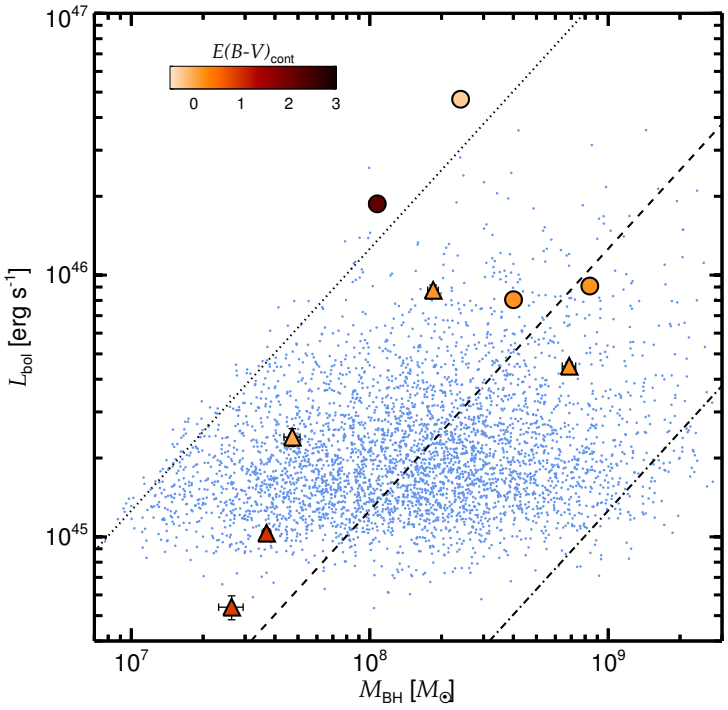

Figure 3.13 The $L_{\rm bol}$ and $M_{\rm BH}$ values of red AGNs and unobscured type 1 quasars. Circles and triangles show the $L_{\rm bol}$ and $M_{\rm BH}$ values of red AGNs derived from Pβ and Pα, respectively. The meaning of the colors in the circles and triangles is identical to Figure 11. The blue dots mean the $L_{\rm bol}$ and $M_{\rm BH}$ values of unobscured type 1 quasars. The dotted, dashed, and dash-dotted lines denote $\lambda_{\rm Edd}$ of 1, 0.1, and 0.01, respectively.

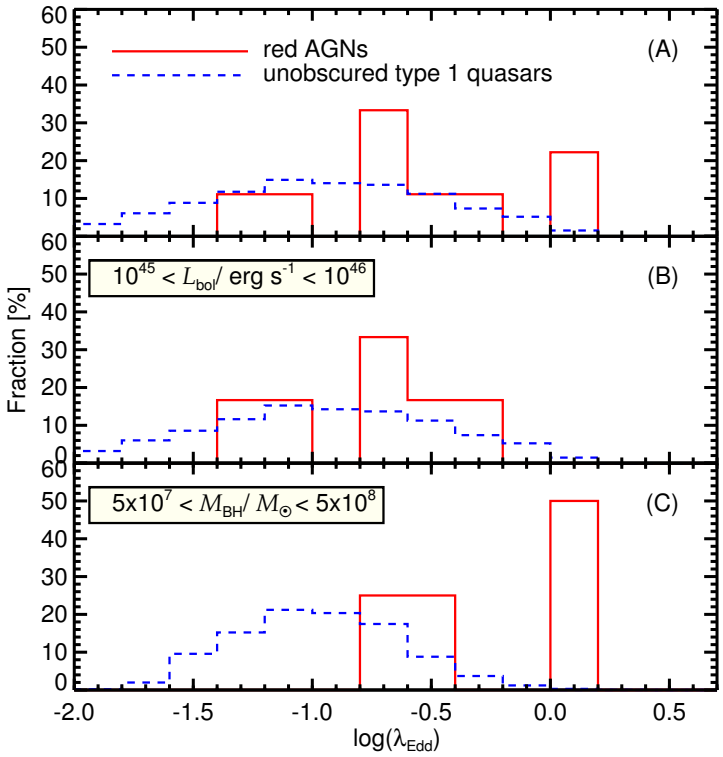

Figure 3.14 (A) Distributions of the $\lambda_{\rm Edd}$ values of red AGNs and unobscured type 1 quasars. The red solid and blue dashed histograms show the $\lambda_{\rm Edd}$ distributions of red AGNs and unobscured type 1 quasars, respectively. (B) Distributions of the $\lambda_{\rm Edd}$ values of red AGNs and unobscured type 1 quasars in the limited $L_{\rm bol}$ range of $10^{45}\,{\rm erg\,s^{-1}} < L_{\rm bol} < 10^{46}\,{\rm erg\,s^{-1}}$. The meanings of the histograms are identical to panel (A). (C) Distributions of the $\lambda_{\rm Edd}$ values for the BH mass limited red AGNs and unobscured type 1 quasars, where the BH mass range is $5 \times 10^{7}\,M_{\odot} < M_{\rm BH} < 5 \times 10^{8}\,M_{\odot}$. The meanings of the histograms are identical.

Since the $\lambda_{\rm Edd}$ values can depend on the $L_{\rm bol}$ and $M_{\rm BH}$ values (e.g., Lusso et al. 2012; Suh et al. 2015), we compare the $\lambda_{\rm Edd}$ values of red AGNs and unobscured type 1 quasars in limited $L_{\rm bol}$ and $M_{\rm BH}$ ranges. First, we compare the $\lambda_{\rm Edd}$ values in a limited $L_{\rm bol}$ range of $10^{45}\,{\rm erg\,s^{-1}} < L_{\rm bol} < 10^{46}\,{\rm erg\,s^{-1}}$. For the comparison, 6 red AGNs and 3839 unobscured type 1 quasars are selected, and their BH masses have ranges of $10^{7.57}$–$10^{8.92}\,M_{\odot}$ and $10^{6.94}$–$10^{10.41}\,M_{\odot}$, respectively. For the $L_{\rm bol}$-limited sample, the $\lambda_{\rm Edd}$ values of red AGNs, $\log({\rm Edd}) = -0.654 \pm 0.354$, are higher than those of unobscured type 1 quasars, $\log({\rm Edd}) = -0.956 \pm 0.502$. From the K–S test between these two $\lambda_{\rm Edd}$ values, the measured D is 0.279, and p is 0.661. Second, we compare the $\lambda_{\rm Edd}$ values of red AGNs and unobscured type 1 quasars in a limited BH mass range of $5 \times 10^7\,M_{\odot} < M_{\rm BH} < 5 \times 10^8\,M_{\odot}$. For the $M_{\rm BH}$-limited sample, 4 red AGNs and 2727 unobscured type 1 quasars are chosen, and their $L_{\rm bol}$ values have ranges of $10^{45.91}$–$10^{46.67}\,{\rm erg\,s^{-1}}$ and $10^{44.73}$–$10^{46.55}\,{\rm erg\,s^{-1}}$, respectively. The log(Edd) of red AGNs and unobscured type 1 quasars are 0.140±0.474 and -0.987±0.344, respectively. The K-S test between these two $\lambda_{\rm Edd}$ distributions yields D of 0.689 and p of 0.023.

Although the measured p values of these three comparisons are inferred rather inconclusive, the result is more skewed in favor of the red AGNs at $z \sim 0.3$ having higher $\lambda_{\rm Edd}$ values than unobscured type 1 quasars by a factor of 3. The somewhat large p values are likely to have come from the small number statistics. This result is consistent with the conclusion from previous studies that the red quasars have higher accretion rates and they are the intermediate stage galaxies between the merger-driven star-forming galaxies and unobscured type 1 quasars (Urrutia et al. 2012; Kim et al. 2015b, 2017).

3.6 $M_{\rm BH}$–σ_* relation

Red AGNs are expected to be in the young quasar phase, and their BHs grow very rapidly (Hopkins et al. 2008). Therefore, the discrepancy or similarity of the $M_{\rm BH}$–σ_* relation of red AGNs compared to that of unobscured type 1 quasars will be a key to understand the co-evolution of SMBHs and galaxies. For example, if red AGNs have smaller σ_* for a fixed BH mass, which imply that BHs grow first and host galaxies catch up later. Canalizo et al. (2012) measured the $M_{\rm BH}$–σ_* relation of red AGNs at $z \sim 0.3$, which is similar to that of unobscured type 1 AGNs at similar redshift. However, the BH masses of red AGNs used in this paper were derived from L5100 and FWHM$_{\rm H\alpha}$ values that could have been affected by the dust extinction.

In this section, we replace the BH masses of the $M_{\rm BH}$–σ_* relation of red AGNs (Canalizo et al. 2012) with the Pβ- and Pα- based BH masses to alleviate the effects of the dust extinction. As for the σ_* values in the relation, they are derived from the spectra at 3900–5500 Å (Canalizo et al. 2012). By compiling the $M_{\rm BH}$ and σ_* values, we find three red AGNs (0157+1712, 0221+1327, and 1659+1834) that have both $M_{\rm BH}$ and σ_* available.

We compare the Paschen-line-based BH masses to the optical-based BH masses. In Canalizo et al. (2012), the BH masses based on L5100 and FWHM$_{\rm H\alpha}$ are $10^{8.35}$, $10^{8.42}$, and $10^{8.68}\,M_\odot$ for 0157+1712, 0221+1327, and 1659+1834, respectively, whereas the BH masses derived from the Paschen lines are $10^{8.03}$, $10^{7.57}$, and $10^{8.84}\,M_\odot$. Although there is no significant difference in the BH masses for 0157+1712 and 1659+1834, the BH mass of 0221+1327 is decreased by a factor of ~ 7. The discrepancy for the BH mass of 0221+1327 does not come from the dust extinction but from the spectral line fitting. In Canalizo et al. (2012), they measured the FWHM as $4279\,{\rm km\,s^{-1}}$ that is estimated from the Hα line. However, in this study, the FWHM is measured for three times with the Hα, Pβ, and Pα line, which are 2212, 2125, and $2252\,{\rm km\,s^{-1}}$, respectively, and these values are

significantly smaller than the previous result.

In Figure 15, the newly established $M_{\rm BH}$–σ_* relation of red AGNs is presented, along with those for local quiescent galaxies (Gültekin et al. 2009) and unobscured type 1 AGNs at $z \simeq 0$, 0.36, and 0.57 (Woo et al. 2006, 2008, 2010). The $M_{\rm BH}$–σ_* relations of unobscured type 1 AGNs are modified by applying the virial coefficient of $\log f = 0.05$ (Woo et al. 2015), as we did for red AGNs.

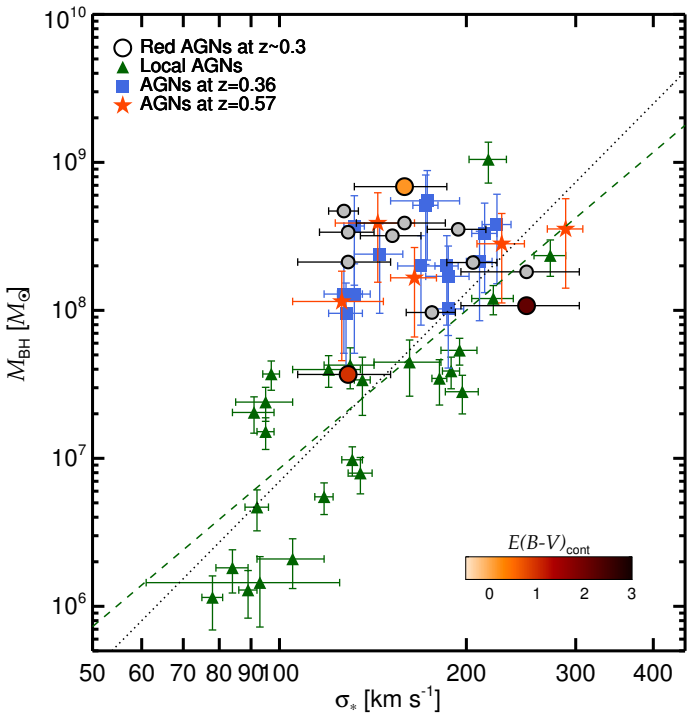

Figure 3.15 $M_{\rm BH}$–σ_* relations of AGNs. Circles denote the $M_{\rm BH}$ and σ_* values of red AGNs, and the meaning of the colors in the circles is identical to Figure 11. The gray circles denote the quantities of red AGNs measured in Canalizo et al. (2012). The $M_{\rm BH}$ and σ_* values of unobscured type 1 AGNs at $z \simeq 0$ (Woo et al. 2010), 0.36 (Woo et al. 2006), and 0.57 (Woo et al. 2008) are represented by green triangles, blue squares, and red stars. Green dashed and black dotted lines show the $M_{\rm BH}$–σ_* relations for local AGNs (Woo et al. 2010) and quiescent local galaxies (Gültekin et al. 2009).

The $M_{\rm BH}$–σ_* relation of red AGNs seems to be similar to that of local unobscured type 1 AGNs (Woo et al. 2010). By comparing the $M_{\rm BH}$–σ_* relation of red AGNs and local unobscured type 1 AGNs, we find offsets of $\Delta \log M_{\rm BH}$ = -0.313, 0.243, and 1.119 for 0157+1712, 0221+1327, and 1659+1834, respectively, resulting in a mean offset of $\Delta \log M_{\rm BH} = 0.373$. However, this mean offset is not significant when the intrinsic scatter of 0.43 dex in the relation of local unobscured type 1 AGNs is considered.

In comparison to the $M_{\rm BH}$–σ_* relation of unobscured type 1 AGNs at similar redshift ($z = 0.36$), the offset of red AGNs seem to be smaller than that ($\Delta \log M_{\rm BH} = 0.62 \pm 0.10 \pm 0.25$; Woo et al. 2006) of unobscured type 1 AGNs. Although based on only three red AGNs, the implication of this result is that red AGNs, which are young when following the scenario presented above, have smaller BH masses at a given host galaxy mass, implying that the host galaxy grows first and the BH catches up later. Moreover, this result implies that the AGN phase is preceded by the star-forming phase, which points to the picture that ULIRGs evolve into AGNs (Sanders et al. 1988; Sanders & Mirabel 1996; Dasyra et al. 2007) through the red AGN phase as expected from simulation studies (e.g., Hopkins et al. 2008).

3.7 Summary

By performing NIR spectroscopic observations with four telescopes, Gemini, IRTF, Magellan, and Subaru, we obtained 0.7–2.5 μm medium resolution ($R > 2000$) and high S/N (up to several hundreds) spectra of 16 red AGNs at $z \sim 0.3$. In addition to the NIR spectra, we obtained optical (0.4–1.0 μm) medium resolution ($R \sim 4000$) spectra of 12 red AGNs taken with Keck/ESI and SDSS data. Using both spectra, we measured the line luminosities and FWHMs of Hβ, Hα, Pβ, and Pα lines for 7, 12, 12, and 6 red AGNs, respectively.

Before analyzing the physical properties of red AGNs, we derived the $E(B-V)$ values of red AGNs in two ways. First, we estimated the $E(B-V)_{\rm line}$ values by using the luminosity ratios of Hβ, Hα, Pβ, and Pα lines. Second, the $E(B-V)_{\rm cont}$ values were measured by comparing the continuum slopes at 3790–10,000 Å. Through these two methods, we measured the $E(B-V)_{\rm line}$ and $E(B-V)_{\rm cont}$ values for ten and 12 red AGNs, respectively. These two $E(B-V)$ values are consistent, and their Pearson correlation coefficient is 0.841.

After correcting for the dust extinction with the measured $E(B-V)$ values, we measured the $\lambda_{\rm Edd}$ values of red AGNs. For the $M_{\rm BH}$ and $L_{\rm bol}$ values, we used Paschen-line-based $M_{\rm BH}$ and $L_{\rm bol}$ estimators to alleviate the effects of the dust extinction. The newly estimated $\lambda_{\rm Edd}$ values of red AGNs, with a distribution of $\log({\rm Edd}) = -0.654 \pm 0.500$, are higher than those of unobscured type 1 quasars, same as above $\log({\rm Edd}) = -0.961 \pm 0.506$. This result is consistent with the picture that red AGNs are in the intermediate stage between merger-driven star-forming galaxies and unobscured type 1 quasars, as expected from several previous studies (Glikman et al. 2007; Urrutia et al. 2012; Kim et al. 2015b, 2017).

Using the measured BH masses, we compared the $M_{\rm BH}$–σ_* relation of red AGNs to that of unobscured type 1 AGNs at similar redshift. Although only three objects were used, red AGNs show a tendency to have smaller BH masses at a fixed σ_*. This result points to a picture in which the host galaxy grows first and the BH catches up later, as expected from simulation studies (e.g., Hopkins et al. 2008).

References

Abazajian, K. N., Adelman-McCarthy, J. K., Agüeros, M. A., et al. 2009, ApJS, 182, 543

Anderson, S. F., Voges, W., Margon, B., et al. 2003, AJ, 126, 2209

Assef, R. J., Stern, D., Kochanek, C. S., et al. 2013, ApJ, 772, 2

Banerji, M., McMahon, R. G., Hewett, P. C., et al. 2012, MNRAS, 427, 2275

Becker, R. H., White, R. L., Gregg, M. D., et al. 2001, ApJS, 135, 227

Benn, C. R., Vigotti, M., Carballo, R., Gonzalez-Serrano, J. I., & Sánchez, S. F. 1998, MNRAS, 295, 451

Bennert, V. N., Treu, T., Woo, J.-H., et al. 2010, ApJ, 708, 1507

Bentz, M. C., Peterson, B. M., Pogge, R. W., & Vestergaard, M. 2009, ApJ, 694, L166

Boroson, T. A., & Green, R. F. 1992, ApJS, 80, 109

Bouchet, P., Lequeux, J., Maurice, E., Prevot, L., & Prevot-Burnichon, M. L. 1985, A&A, 149, 330

Brotherton, M. S., Tran, H. D., Becker, R. H., et al. 2001, ApJ, 546, 775

Calzetti, D., Kinney, A. L., & Storchi-Bergmann, T. 1994, ApJ, 429, 582

Canalizo, G., Wold, M., Hiner, K. D., et al. 2012, ApJ, 760, 38

Cattaneo, A., Blaizot, J., Devriendt, J., & Guiderdoni, B. 2005, MNRAS, 364, 407

Comastri, A., Fiore, F., Vignali, C., et al. 2001, MNRAS, 327, 781

Cooke, A., & Rodgers, B. 2005, Astronomical Data Analysis Software and Systems XIV, 347, 514

Croom, S. M., Smith, R. J., Boyle, B. J., et al. 2004, MNRAS, 349, 1397

Cushing, M. C., Vacca, W. D., & Rayner, J. T. 2004, PASP, 116, 362

Cutri, R. M., Nelson, B. O., Kirkpatrick, J. D., Huchra, J. P., & Smith, P. S. 2001, The New Era of Wide Field Astronomy, 232, 78

Cutri, R. M., Nelson, B. O., Francis, P. J., & Smith, P. S. 2002, IAU Colloq. 184: AGN Surveys, 284, 127

Dasyra, K. M., Tacconi, L. J., Davies, R. I., et al. 2007, ApJ, 657, 102

Di Matteo, T., Springel, V., & Hernquist, L. 2005, Nature, 433, 604

Elias, J. H., Joyce, R. R., Liang, M., et al. 2006, Proc. SPIE, 6269, 62694C

Ferrarese, L., & Merritt, D. 2000, ApJ, 539, L9

Fitzpatrick, E. L. 1999, PASP, 111, 63

Fynbo, J. P. U., Krogager, J.-K., Venemans, B., et al. 2013, ApJS, 204, 6

Gebhardt, K., Bender, R., Bower, G., et al. 2000, ApJ, 539, L13

Georgakakis, A., Clements, D. L., Bendo, G., et al. 2009, MNRAS, 394, 533

Georgakakis, A., Grossi, M., Afonso, J., & Hopkins, A. M. 2012, MNRAS, 421, 2223

Glikman, E., Helfand, D. J., & White, R. L. 2006, ApJ, 640, 579

Glikman, E., Helfand, D. J., White, R. L., et al. 2007, ApJ, 667, 673

Glikman, E., Urrutia, T., Lacy, M., et al. 2012, ApJ, 757, 51

Glikman, E., Simmons, B., Mailly, M., et al. 2015, arXiv:1504.02111

Graham, A. W., Erwin, P., Caon, N., & Trujillo, I. 2001, ApJ, 563, L11

Graham, A. W., & Driver, S. P. 2007, ApJ, 655, 77

Grazian, A., Cristiani, S., D'Odorico, V., Omizzolo, A., & Pizzella, A. 2000, AJ, 119, 2540

Greene, J. E., & Ho, L. C. 2005, ApJ, 630, 122

Greene, J. E., Peng, C. Y., & Ludwig, R. R. 2010, ApJ, 709, 937

Gregg, M. D., Becker, R. H., White, R. L., et al. 1996, AJ, 112, 407

Gültekin, K., Richstone, D. O., Gebhardt, K., et al. 2009, ApJ, 698, 198

Hopkins, P. F., Hernquist, L., Cox, T. J., et al. 2005, ApJ, 630, 705

Hopkins, P. F., Hernquist, L., Cox, T. J., et al. 2006, ApJS, 163, 1

Hopkins, P. F., Hernquist, L., Cox, T. J., & Kereš, D. 2008, ApJS, 175, 356

Im, M., Griffiths, R. E., & Ratnatunga, K. U. 1997, ApJ, 475, 457

Im, M., Lee, I., Cho, Y., et al. 2007, ApJ, 664, 64

Imanishi, M., Ichikawa, K., Takeuchi, T., et al. 2011, PASJ, 63, 447

Jiang, Y.-F., Greene, J. E., & Ho, L. C. 2011, ApJ, 737, L45

Jun, H. D., Im, M., Lee, H. M., et al. 2015, ApJ, 806, 109

Kang, W.-R., Woo, J.-H., Schulze, A., et al. 2013, ApJ, 767, 26

Kim, M., Ho, L. C., & Im, M. 2006, ApJ, 642, 702

Kim, D., Im, M., & Kim, M. 2010, ApJ, 724, 386

Kim, J. H., Im, M., Lee, H. M., et al. 2012, ApJ, 760, 120

Kim, D., Im, M., Kim, J. H., et al. 2015, ApJS, 216, 17

Kim, D., Im, M., Glikman, E., Woo, J.-H., & Urrutia, T. 2015, ApJ, 812, 66

Kim, D., & Im, M. Accepted to A&A

Kocevski, D. D., Faber, S. M., Mozena, M., et al. 2012, ApJ, 744, 148

Lacy, M., Ridgway, S. E., Gates, E. L., et al. 2013, ApJS, 208, 24

Landt, H., Bentz, M. C., Ward, M. J., et al. 2008, ApJS, 174, 282

Landt, H., Bentz, M. C., Peterson, B. M., et al. 2011, MNRAS, 413, L106

Landt, H., Elvis, M., Ward, M. J., et al. 2011, MNRAS, 414, 218

Lawrence, A., Warren, S. J., Almaini, O., et al. 2007, MNRAS, 379, 1599

Lee, I., Im, M., Kim, M., et al. 2008, ApJS, 175, 116

Lusso, E., Comastri, A., Simmons, B. D., et al. 2012, MNRAS, 425, 623

Lynden-Bell, D. 1969, Nature, 223, 690

Kobayashi, N., Tokunaga, A. T., Terada, H., et al. 2000, Proc. SPIE, 4008, 1056

Marble, A. R., Hines, D. C., Schmidt, G. D., et al. 2003, ApJ, 590, 707

Magorrian, J., Tremaine, S., Richstone, D., et al. 1998, AJ, 115, 2285

Markwardt, C. B. 2009, Astronomical Data Analysis Software and Systems XVIII, 411, 251

Massey, P., Strobel, K., Barnes, J. V., & Anderson, E. 1988, ApJ, 328, 315

McLure, R. J., & Dunlop, J. S. 2004, MNRAS, 352, 1390

Menci, N., Cavaliere, A., Fontana, A., et al. 2004, ApJ, 604, 12

Park, D., Woo, J.-H., Bennert, V. N., et al. 2015, ApJ, 799, 164

Polletta, M., Weedman, D., Hönig, S., et al. 2008, ApJ, 675, 960-984

Puchnarewicz, E. M., & Mason, K. O. 1998, MNRAS, 293, 243

Risaliti, G., & Elvis, M. 2005, ApJ, 629, L17

Rose, M., Tadhunter, C. N., Holt, J., & Rodríguez Zaurín, J. 2013, MNRAS, 432, 2150

Rose, M. 2014, American Astronomical Society Meeting Abstracts #223, 223, #321.03

Ruff, A. J., Floyd, D. J. E., Webster, R. L., Korista, K. T., & Landt, H. 2012, ApJ, 754, 18

Sanders, D. B., Soifer, B. T., Elias, J. H., et al. 1988, ApJ, 325, 74

Sanders, D. B., & Mirabel, I. F. 1996, ARA&A, 34, 749

Scannapieco, E., Silk, J., & Bouwens, R. 2005, ApJ, 635, L13

Schawinski, K., Treister, E., Urry, C. M., et al. 2011, ApJ, 727, L31

Schawinski, K., Simmons, B. D., Urry, C. M., Treister, E., & Glikman, E. 2012, MNRAS, 425, L61

Schlafly, E. F., & Finkbeiner, D. P. 2011, ApJ, 737, 103

Schneider, D. P., Hall, P. B., Richards, G. T., et al. 2005, AJ, 130, 367

Sheinis, A. I., Bolte, M., Epps, H. W., et al. 2002, PASP, 114, 851

Shen, Y., Richards, G. T., Strauss, M. A., et al. 2011, ApJS, 194, 45

Shen, Y., Greene, J. E., Ho, L. C., et al. 2015, ApJ, 805, 96

Silk, J., & Rees, M. J. 1998, A&A, 331, L1

Simmons, B. D., Urry, C. M., Schawinski, K., Cardamone, C., & Glikman, E. 2012, ApJ, 761, 75

Skrutskie, M. F., Cutri, R. M., Stiening, R., et al. 2006, AJ, 131, 1163

Smith, P. S., Schmidt, G. D., Hines, D. C., Cutri, R. M., & Nelson, B. O. 2002, ApJ, 569, 23

Stern, D., Assef, R. J., Benford, D. J., et al. 2012, ApJ, 753, 30

Suh, H., Hasinger, G., Steinhardt, C., Silverman, J. D., & Schramm, M. 2015, ApJ, 815, 129

Tokunaga, A. T., Kobayashi, N., Bell, J., et al. 1998, Proc. SPIE, 3354, 512

Tozzi, P., Gilli, R., Mainieri, V., et al. 2006, A&A, 451, 457

Tremaine, S., Gebhardt, K., Bender, R., et al. 2002, ApJ, 574, 740

Treu, T., Woo, J.-H., Malkan, M. A., & Blandford, R. D. 2007, ApJ, 667, 117

Urrutia, T., Lacy, M., & Becker, R. H. 2008, ApJ, 674, 80-96

Urrutia, T., Becker, R. H., White, R. L., et al. 2009, ApJ, 698, 1095

Urrutia, T., Lacy, M., Spoon, H., et al. 2012, ApJ, 757, 125

Vacca, W. D., Cushing, M. C., & Rayner, J. T. 2003, PASP, 115, 389

Vanden Berk, D. E., Richards, G. T., Bauer, A., et al. 2001, AJ, 122, 549

Véron-Cetty, M.-P., & Véron, P. 2006, A&A, 455, 773

Webster, R. L., Francis, P. J., Petersont, B. A., Drinkwater, M. J., & Masci, F. J. 1995, Nature, 375, 469

Whiting, M. T., Webster, R. L., & Francis, P. J. 2001, MNRAS, 323, 718

Wilkes, B. J., Schmidt, G. D., Cutri, R. M., et al. 2002, ApJ, 564, L65

Woo, J.-H., & Urry, C. M. 2002, ApJ, 579, 530

Woo, J.-H., Treu, T., Malkan, M. A., & Blandford, R. D. 2006, ApJ, 645, 900

Woo, J.-H., Treu, T., Malkan, M. A., & Blandford, R. D. 2008, ApJ, 681, 925-930

Woo, J.-H., Treu, T., Barth, A. J., et al. 2010, ApJ, 716, 269

Woo, J.-H., Yoon, Y., Park, S., Park, D., & Kim, S. C. 2015, ApJ, 801, 38

Wright, E. L., Eisenhardt, P. R. M., Mainzer, A. K., et al. 2010, AJ, 140, 1868

Young, M., Elvis, M., & Risaliti, G. 2009, ApJS, 183, 17

Chapter 4

What makes red quasars red?: Observational evidence for dust extinction from line ratio analysis

(This chapter has been accepted for publication in Astronomy & Astrophysics)

4.1 Introduction

Large area surveys in X-ray, ultraviolet (UV), optical, and radio wavelengths have uncovered nearly a half million quasars to date (Grazian et al. 2000; Becker et al. 2001; Anderson et al. 2003; Croom et al. 2004; Risaliti & Elvis 2005; Schneider et al. 2005; Véron-Cetty & Véron 2006; Im et al. 2007; Lee et al. 2008; Young et al. 2009; Pâris et al. 2014; Kim et al. 2015c). In the UV to optical wavelength range, the spectra of quasars show a blue power-law continuum with broad and narrow

emission lines or a host galaxy continuum with only narrow emission lines, which are classified as type 1 and 2 quasars, respectively. The unification model (Urry & Padovani 1995) has been proposed to explain different types of quasars. In the model, a quasar is composed of a black hole (BH), accretion disk, dust torus, broad line regions (BLRs), and narrow line regions (NLRs). Under the unification model, the type 1 and 2 quasars are physically the same, but an obscuring dust torus prevents us from seeing the accretion disk and the BLR in a certain line-of-sight direction for type 2 quasars.

However, our knowledge about quasars is still incomplete, especially with a population of quasars called red quasars, which have been identified in recent infrared surveys (Webster et al. 1995; Benn et al. 1998; Cutri et al. 201; Glikman et al. 2007, 2012, 2013; Urrutia et al. 2009; Banerji et al. 2012; Stern et al. 2012; Assef et al. 2013; Fynbo et al. 2013; Lacy et al. 2013). Red quasars typically indicate quasars with red continua from UV or optical through NIR (e.g., $r' - K > 5$ mag and $J - K > 1.3$ mag in Urrutia et al. 2009; $g - r > 0.5$ in Young et al. 2008), red mid-infrared (MIR) colors (Lacy et al. 2004), or detections in X-rays while being obscured in UV and optical wavelengths (Norman et al. 2002; Anderson et al. 2003; Risaliti & Elvis 2005; Young et al. 2009; Brusa et al. 2010).

Interestingly, red quasars are expected in simulations where merger-driven galaxy evolution is stressed (Menci et al. 2004; Hopkins et al. 2005, 2006, 2008). In such simulations, major mergers of galaxies trigger both star formation and quasar activity, often appearing as ultra-luminous infrared galaxies (ULIRGs; Sanders et al. 1988; Sanders & Mirabel 1996). After that, the central BH grows rapidly but it is still obscured by the remaining dust in their host galaxies. Finally, the obscured quasar evolves to an unobscured quasar after the feedback from the central BH sweeps away cold gas and dust. In this picture, red quasars should appear during the intermediate stage between ULIRGs and unobscured quasars. These quasars are

red owing to dust extinction by the remaining dust and gas in their host galaxies. So far, observational signatures of red quasars tend to support this picture. For example, red quasars have (i) higher BH accretion rates than unobscured type 1 quasars by factors of 4 to 5 (Urrutia et al. 2012; Kim et al. 2015b), (ii) enhanced star formation activities (Georgakakis et al. 2009), (iii) a high fraction of merging features (Urrutia et al. 2008; Glikman et al. 2015), and (iv) young radio jets (Georgakakis et al. 2012).

However, several studies have proposed varying explanations for the red continuum of red quasars. Wilkes et al. (2002) and Rose et al. (2013) suggested that the red $J-K$ colors ($J-K>2$) of red quasars come from a moderate viewing angle in the unification model when the photons from the accretion disk and the BLR are blocked by the dust torus and not by the dust in host galaxies. Other studies suggest that some ($\sim$40%; Young et al. 2008) red quasars have intrinsically red continuum (Puchnarewicz & Mson 1998; Whiting et al. 2001; Young et al. 2008; Rose et al. 2013; Ruiz et al. 2014) or an unusual covering factor of hot dust (Rose 2014). Also a synchrotron emission peak at NIR wavelength from radio jet (Whiting et al. 2001) has been proposed as a possible reason for the intrinsically red continuum of red quasars.

The hydrogen line ratios can be used to infer the amount of dust extinction over the BLRs. Rose et al. (2013) showed that 2MASS selected ($J-K>2$) red quasars have higher $L_{\mathrm{H}\alpha}/L_{\mathrm{H}\beta}$ ratios than unobscured type 1 quasars. However, the difference is modest (4.9 ± 0.5 versus 3.2 ± 0.4 for red and unobscured type 1 quasars, respectively) and the modest difference could originate from not only the dust extinction but also different physical condition in the BLRs.

In this study, we use Pβ and Pα lines with Balmer lines to investigate the red colors of red quasars that are shown to have broad emission lines (i.e., type 1). The use of the line ratios over a wide range of wavelength makes it easier to understand

if the red colors are due to dust extinction or other mechanisms. Additionally, the use of AGN NIR diagnostics (e.g., Kim et al. 2010) allows us to measure black hole masses and bolometric luminosities in a way that is almost dust free. This fact is very advantageous when trying to distinguish several plausible mechanisms for red colors. For example, in a simple viewing angle scenario, we expect to find red quasars to have Eddington ratios similar to ordinary type 1 quasars, but not so in the intermediate population scenario. Throughout this paper, we use a standard ΛCDM cosmological model of H_0=70 km s^{-1} Mpc^{-1}, Ω_m=0.3, and Ω_Λ=0.7, supported by previous observations (e.g., Im et al. 1997).

4.2 Sample and data

In this work, we used 20 red quasars at $0.186 < z < 0.842$ that are composed of 16 red quasars ($z > 0.5$ and $L_{\rm bol} > 10^{46}\,{\rm erg\,s^{-1}}$) studied in Kim et al. (2015b) and four additional red quasars ($z < 0.5$ and $L_{\rm bol} \sim 10^{46}\,{\rm erg\,s^{-1}}$). These 20 red quasars are a subsample of $\sim$ 80 spectroscopically confirmed red quasars in Glikman et al. (2007) and Urrutia et al. (2009), which were selected to be red quasars based on their broadband colors ($R - K > 4$ and $J - K > 1.7$ mag in Glikman et al. 2007; $r' - K > 5$ and $J - K > 1.3$ mag in Urrutia et al. 2009) from radio-detected 2MASS point sources. In this work, "radio-detected" means the detection of the object in the FIRST radio catalog (Becker et al. 1995). We note that radio-detected AGNs are not necessarily radio-loud. We define radio-loudness as $R_i = \log(f(1.4\,{\rm GHz})/f(7480\,{\rm \AA}))$ (Ivezić et al. 2002). In our red quasars sample, we find that only one-third are radio-loud (e.g., $R_i > 2$; Karouzos et al. 2014) and the remaining two-thirds are in the radio-intermediate regime ($1 < R_i < 2$). Additionally, these quasars are chosen to be at $z \sim 0.3$ or $z \sim 0.7$ so that we can sample both the Balmer and Paschen lines.

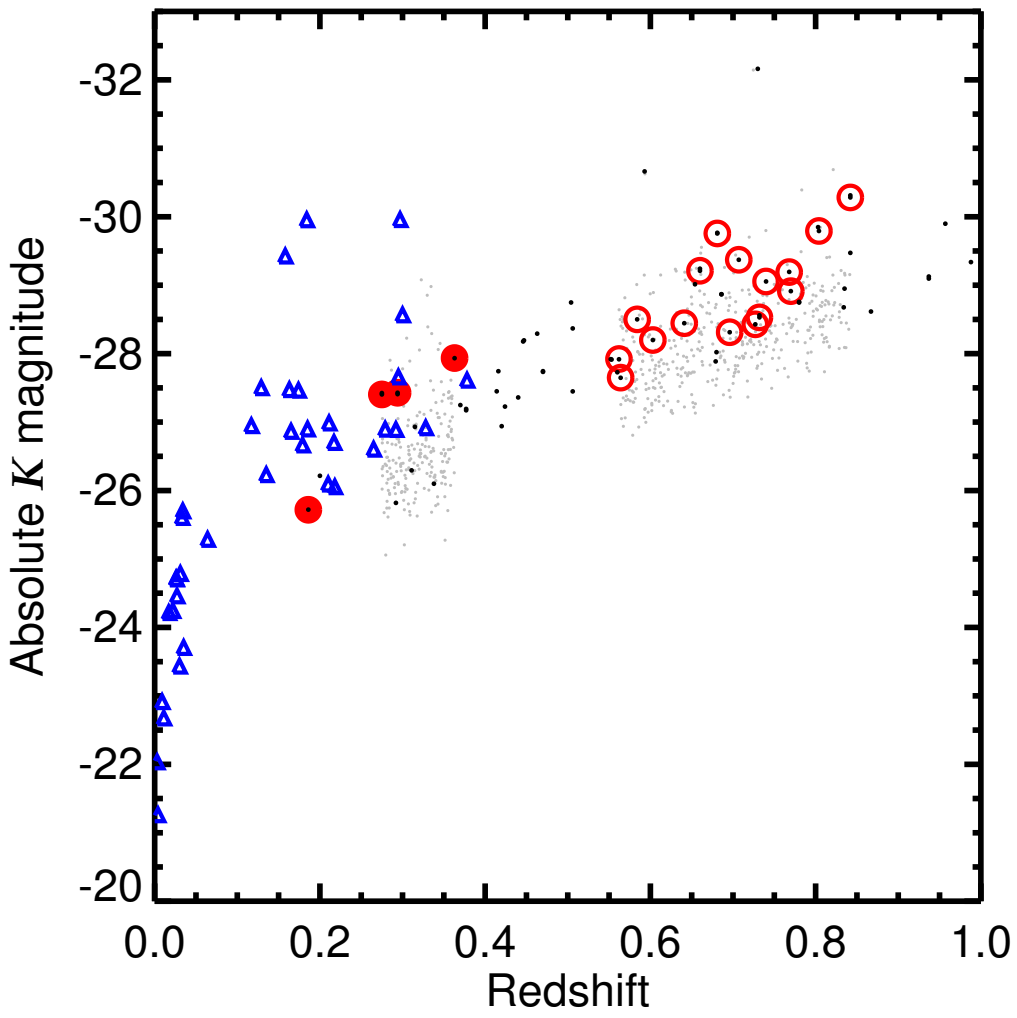

Figure 4.1 Redshifts and absolute K-band magnitudes of red quasars and unobscured type 1 quasars. The 20 red quasars used in this study are denoted by red open circles, and the black dots indicate the red quasars listed in Glikman et al. (2007) and Urrutia et al. (2009) from which our sample is drawn. Four red quasars (0036−0113, 0817+4354, 1209−0107, and 1307+2338), which were not used in Kim et al. (2015b), are denoted by filled red circles. The comparison sample is made of 37 unobscured type 1 quasars from Kim et al. (2010; blue open triangles), and 623 SDSS unobscured type 1 quasars at $0.275 < z < 0.363$ and $0.562 < z < 0.842$ (gray dots).

In this study, we compare several properties of red quasars to those of unobscured type 1 quasars. We used 623 unobscured type 1 quasars at $z \sim 0.3$ and 0.7, both selected from Sloan Digital Sky Survey (SDSS) in an approach similar to the red quasars (also see Section 5.3), and 37 unobscured type 1 quasars at $z < 0.5$ for which Paschen line information is available from Kim et al. (2010). The 37 unobscured type 1 quasars are relatively bright ($K < 14.5$ mag). The unobscured type 1 quasars cover a wide range in the K band luminosities ($-30.0 < K\,\mathrm{mag} < -21.3$), which overlaps well with the K-band luminosities of our red quasars ($-30.3 < K\,\mathrm{mag} < -25.7$). Although the unobscured type 1 quasars from Kim et al. (2010) include six faint ($K\,\mathrm{mag} > -24$) sources, the host galaxy contamination is negligible ($< 8\,\%$) due to a narrow slit width (Glikman et al. 2006; Kim et al. 2010).

Figure 1 indicates the redshifts and absolute K-band magnitudes of the 20 red quasars and the comparison quasar sample. The absolute K-band magnitudes are $K-$corrected using a composite spectrum of unobscured type 1 quasars (NIR: Glikman et al. 2006; MIR: Kim et al. 2015a). Here, we do not apply the dust extinction correction, and we note that the amount of extinction is rather small for K band. The mean $E(B-V)$ of red quasars is 0.88 ($A_K = 0.45$ mag).

For 13 of the 20 red quasars, both the optical and NIR spectra are available and the remaining objects have only NIR spectra. The optical spectra of the red quasars come from Glikman et al. (2007, 2012) while the NIR spectra are from Glikman et al. (2007, 2012) and Kim et al. (2015b). Additionally, new NIR spectra were obtained for two red quasars (0036−0113 and 1307+2338) using the SpeX instrument (Rayner et al. 2003) on the NASA Infrared Telescope Facility (IRTF). The observation was performed with a set of the short cross-dispersion mode (SXD; 0.8–2.5 μm) and a $0\farcs8$ slit width to achieve a resolution of $R \sim 750$ (400 km s^{-1} in FWHM) under clear weather and good seeing conditions of $\sim 0\farcs7$. In order to get fully reduced spectra, we used the Spextool software (Vacca et al. 2003;

Cushing et al. 2004). The spectrophotometric calibration was carried out using the standard star spectra taken before or after the spectrum of each quasar was obtained. These flux-calibrated spectra were matched with a $K-$band photometry from 2MASS and additional flux scaling was performed when necessary. The fully reduced and calibrated NIR spectra of the two red quasars are provided in Table 3 by a machine readable table form.

Among our sample, we detected Pβ in 19 and Pα in two red quasars (only one red quasar is detected in both Pβ and Pα lines) at signal-to-noise ratios (S/N) of > 5. Among 13 red quasars with optical spectra, we detected Hβ in 11 and Hα in 3 red quasars at S/N of > 5. For 2 red quasars (0817+4354 and 1656+3821), we derived upper limits of their Hβ line luminosities. For the remainder, the spectra at Hβ and Hα lines are not readily available.

For the lines with no detection, we set upper limits. For the upper limits of the Hβ line luminosity, we assume the FWHM of typical red quasars of $3000\,\mathrm{km\,s^{-1}}$ (Kim et al. 2015b). Then, the 5-sigma limit of the integrated luminosity density within the wavelength width of the FWHM value is adopted.

As summarized in Table 1, 12 red quasars have both Hβ and Pβ detections or upper limits, while only Pβ line is detected for 7 red quasars. A few red quasars have Hα or Pα line detected.

4.3 Analysis

We corrected the spectra for the Galactic extinction by adopting the reddening map of Schlafly & Finkbeiner (2011), and the extinction curve with $R_V = 3.1$ of Fitzpatrick (1999). Then, we shifted the corrected spectra to the rest frame. In order to estimate the Hβ luminosity, first we determined the continuum spectrum around the Hβ line. Spectrum of type 1 quasar around the Hβ line is generally complex, which contains a power-law continuum component, a host galaxy component,

blended Fe II multiplets, and several narrow emission lines (e.g., [O II] λ3726, Hγ λ4340, and [O III] $\lambda\lambda$4959, 5007 doublet).

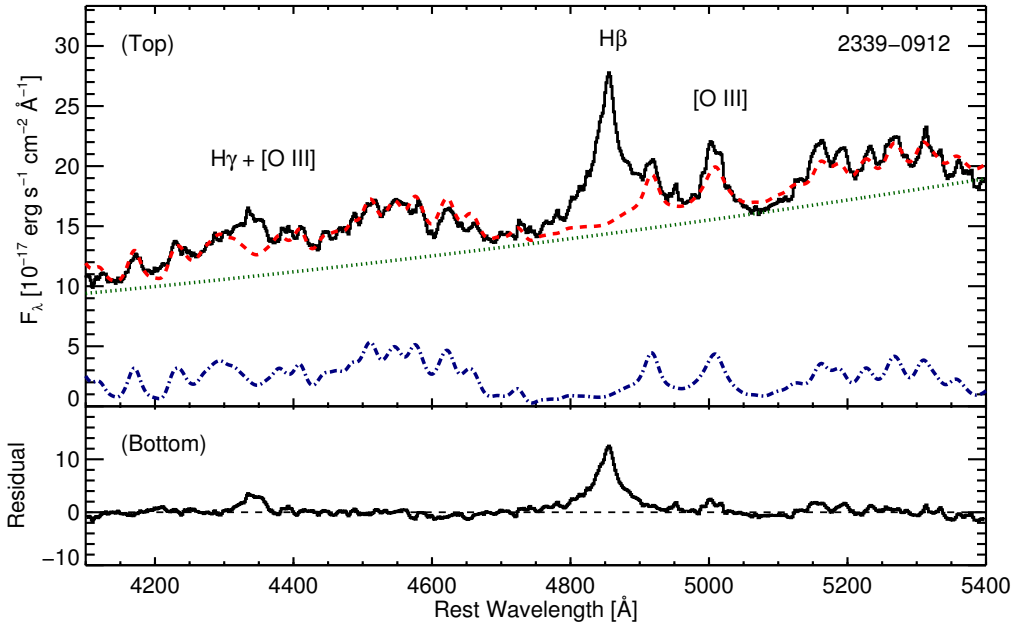

Figure 4.2 (Top) Optical spectrum of 2339−0912 (the black solid line) and its model spectrum components. The optical spectrum includes several emission lines such as Hγ, Hβ, and [O III]. The red dashed line indicates the fitted continuum spectrum that is composed of a power-law component (green dotted line) and a component for the Fe blends (blue dot-dashed line). (Bottom) The continuum-subtracted spectrum showing broad Balmer emission lines. The continuum-subtracted spectra are used for fitting the lines.

We fit the continuum of the red quasars with the power-law component and Fe template (Boroson & Green 1992). To avoid contamination from the several narrow emission lines around the Hβ line, the continuum-fitting regions were chosen as 4150–4280 Å, 4400–4750 Å, 4910–4945 Å, and 5070–5400 Å. For the fit, a `MPFIT` (Markwardt 2009) code based on an interactive data language (IDL) procedure was used to determine the power-law continuum and Fe blends. The Fe blends were determined by broadening and scaling the Fe template from the spectrum of IZw1 (Boroson & Green 1992). Figure 2 shows the optical spectrum of 2339−0912 with the fitted continuum model (the power-law continuum and Fe blends) and the continuum-subtracted spectrum.

We omitted the host galaxy component from the fit for two reasons. First, among the 11 Balmer line measurable red quasars, the measured rest-frame 5100 Å continuum luminosities ($L_{5100} = \lambda L_{\lambda}$ at 5100 Å) of 6 red quasars (0825+4716, 1113+1244, 1227+5053, 1434+0935, 1720+6156, and 2339−0912) are very luminous (extinction-corrected $L_{5100} = L_{\rm bol}/9.2 > 10^{45}\,{\rm erg, s^{-1}}$; Table 2). For type 1 AGNs as luminous as the red quasars in L_{5100} (after the extinction correction), the host galaxy contamination is known to be well below 1% (Shen et al. 2011), and we assume the same for the red quasars. Then, even if we assume that the dust extinction occurs only in the nuclear part [1] with $E(B-V) = 1$, the host contamination would be $< 30\,\%$ at 5100 Å. Second, we measured the equivalent width (EW) of Ca II K λ3934 absorption line for the remaining 5 red quasars, since an EW of 1.5 Å for Ca II K corresponds to the host galaxy contribution of $\sim$10 % (Greene & Ho 2005; Kim et al. 2006). We could not detect the Ca II K absorption line for 3 red quasars, and for the remaining 2, we measured EWs of 3.8 Å, which corresponds to the host galaxy contribution of $\sim$25 % (0036−0113 and 1307+2338), by scaling the results of Greene

[1] If the dust extinction obscures the light from both the nucleus and host galaxy by the same amount, then the host galaxy contamination stays at $< 1\,\%$.

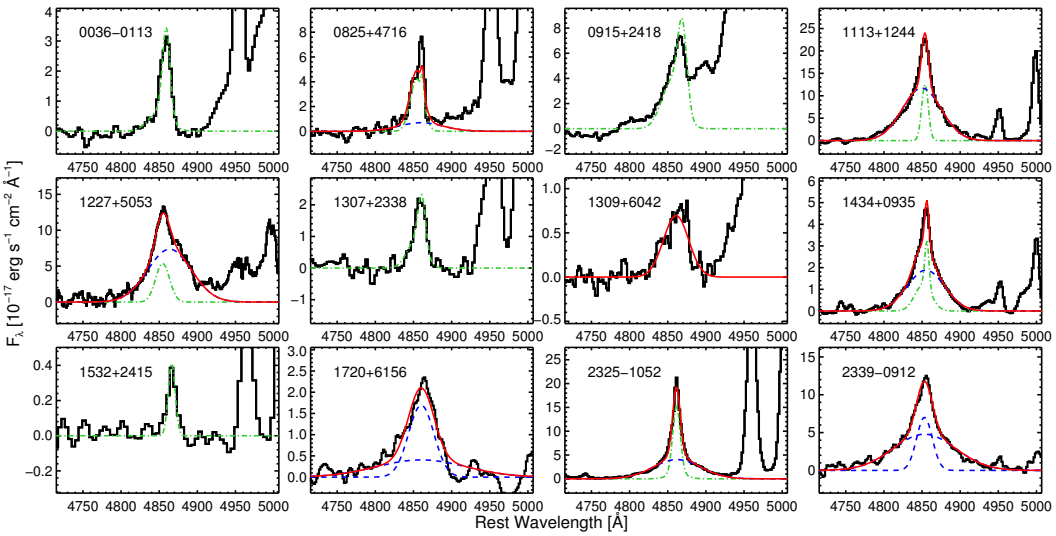

Figure 4.3 Results of the fitting of the Hβ lines. The continuum is already subtracted. The black and red solid lines indicate the observed spectra and best-fit model, respectively. The narrow component of Hβ line is fitted by using the nearby [O III] line at 5007 Å as a template, and the fitted narrow component is represented by the green dash-dotted line. The dashed blue lines represent the broad component (FWHM $> 800\,\mathrm{km}^{-1}$) of the Hβ line.

& Ho (2005) and Kim et al. (2006). Even if the host galaxy contamination of red quasars is bigger than 25 %, we stress that it will not affect the line luminosity and width measurements much since the continuum is well subtracted for each object.

After the continuum subtraction, we fit the narrow component of Hβ line using [O III] line at 5007 Å as a template when possible. The [O III] line was fitted with a double Gaussian function to reproduce both the symmetric component and asymmetric outflow component (Greene & Ho 2005), and the fitted result was used as the template. This was possible for nine red quasars.

Among the nine [O III]-fitted red quasars, the Hβ line of four red quasars (0036−0113, 0915+2418, 1307+2338, and 1532+2415) is well fitted by the narrow component only, although 0036−0113 and 1307+2338 were reported to have a broad Hβ component (Glikman et al. 2007). For these four red quasars, we estimated the upper limit of the Hβ line luminosities. In order to estimate the upper limit of the Hβ line luminosities, we performed the same procedures (see Section 2) in the narrow component subtracted spectra.

For the remaining five [O III]-fitted red quasars (0825+4716, 1113+1244, 1227+5053, 1434+0935, and 2325−1052), the Hβ line is fitted by a composition of the broad and narrow component. For the fit, we set the central wavelength, line width, and line flux of the broad component as free parameters. We set the lower limit of FWHM of broad component as 800 km s^{-1} that is twice of the typical FWHM of narrow emission line (400 km s^{-1}; Schneider et al. 2006) and the FWHMs of the fitted broad component are bigger than 800 km s^{-1}.

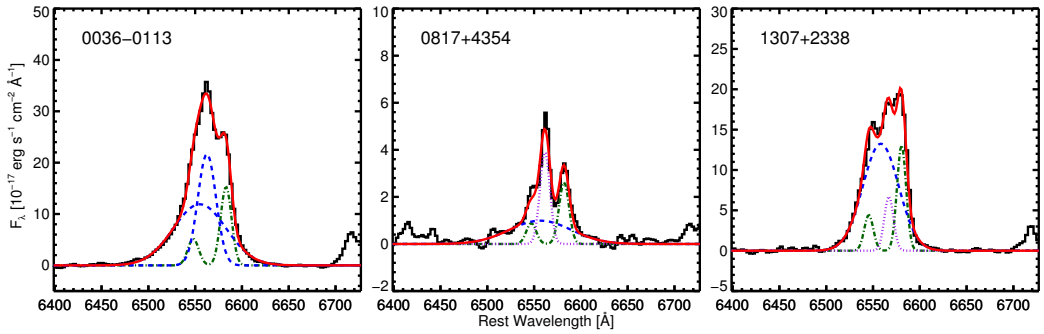

Figure 4.4 Results of the fitting of the Hα lines. The black and red solid lines indicate the continuum subtracted spectra and best-fit model, respectively. The blue dashed and purple dotted lines are the best-fit models for the broad and narrow component of the Hα line, respectively, and the green dot-dashed lines indicate the best-fit models for the [N II] doublet.

For the [O III]-unfitted three red quasars (1309+6042, 1720+6156, and 2339−0912), we fit broad Hβ line with a single (1309+6042) or double (1702+6156 and 2339−0912) Gaussian function, and the fit is performed by the `MPFIT`. Similar to the procedure above, the central wavelength, line width, and line flux are set to be free parameters. The FWHMs of the fitted components of the three red quasars are bigger than 800 km s^{-1} and this result means that the fitted component represent the broad components. The flux of the Hβ line is taken to be the sum of the two broad components for 1704+6156 and 2339−0912, while only the flux of the single broad component is taken to be the broad line flux for 1309+6042. Figure 3 shows the Hβ line-fitting results.

To fit the Hα line, we used a similar procedure as for Hβ line fitting. However, for the fitting the continuum, we use a single power-law component only because of the negligible contribution of the Fe blends around the Hα line. After the continuum subtraction, fitting the Hα is somewhat more complicated than fitting the Hβ line because the Hα line is blended with a [N II] $\lambda\lambda$ 6548, 6583 doublet. For Hα line measurable red quasars 0036−0113, 0817+4354, and 1307+2338, we constructed a model for narrow component of Hα and [N II] doublet using nearby [S II] $\lambda\lambda$ 6716, 6731 doublet. Using the model of narrow component, we simultaneously fit the Hα line and [N II] doublet. The [N II] doublet is also fitted by two single Gaussian functions, but the central wavelength and flux ratio (2.96; Kim et al. 2006) are fixed. For two red quasars (0817+4354 and 1307+2338), the Hα line is fitted by a composition of broad and narrow component, and the narrow component is from the model of the [S II] doublet. For the other red quasar (0036-0113), the Hα line is fitted by double broad components. Only the flux of the broad component is taken to be the broad Hα flux for 0817+4354 and 1307+2338, but the sum of the fluxes from the two broad components is taken to be the broad component flux of Hα line for 0036−0113. We show the fitting results of the Hα lines in Figure 4.

The Pβ and Pα lines are detected for 19 and 2 red quasars, respectively. Among these, the Pβ luminosities of 16 red quasars are adopted from Kim et al. (2015b). The Paschen line luminosities of the other red quasars are newly measured, following the procedure in Kim et al. (2010). Figure 5 shows the fitting of the Paschen lines.

This procedure fits the line with a single or double Gaussian functions, neglecting the NLR component, since the S/N and the resolution of the spectra do not allow us to measure the NLR component. The measured line luminosities and line widths are taken as the values for the broad line. Hence, the derived broad line luminosities and widths can be somewhat biased. To correct for the bias we applied the mean correction factors that are derived from well-resolved Balmer lines of 26 local unobscured type 1 quasars (Kim et al. 2010). They measured the fluxes and FWHMs of the well-resolved Balmer lines with a single, double, and multiple Gaussian functions, and derived the correction factors by comparing the measured properties. The mean correction factors are $\mathrm{flux_{multi}/flux_{double}} = 1.05$ and $\mathrm{flux_{multi}/flux_{single}} = 1.06$ for correcting the luminosities and $\mathrm{FWHM_{multi}/FWHM_{double}} = 0.85$ and $\mathrm{FWHM_{multi}/FWHM_{single}} = 0.91$ for correcting FWHM values. For more details, see Section 2.3 of Kim et al. (2010).

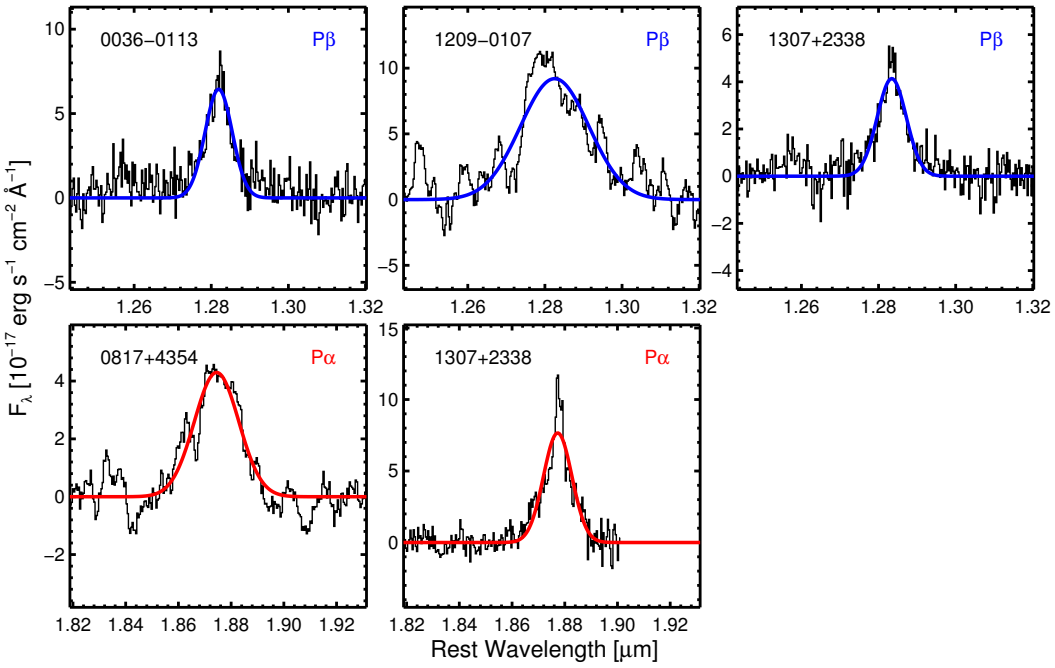

Figure 4.5 Fitting results of the Pβ and Pα lines. The black solid lines are the continuum subtracted spectra. The blue and red solid lines are the best-fit models for the Pβ and Pα lines, respectively.

When no Hβ line is detected (0817+4354 and 1656+3821), we estimated the upper limit of the Hβ line luminosity. In order to estimate the upper limit of the Hβ line luminosity, we used the same procedure mentioned above. The measured upper limits of Hβ line luminosities of the two red quasars are provided in Table 1.

Table 4.1. Luminosities and FWHMs of BLRs for red quasars

Object Name	Redshift (z)	$\log L_{\mathrm{H}\beta}$ (erg s^{-1})	$\mathrm{FWHM}_{\mathrm{H}\beta}$ (km s^{-1})	$\log L_{\mathrm{H}\alpha}$ (erg s^{-1})	$\mathrm{FWHM}_{\mathrm{H}\alpha}$ (km s^{-1})	$\log L_{\mathrm{P}\beta}$ (erg s^{-1})	$\mathrm{FWHM}_{\mathrm{P}\beta}$ (km s^{-1})	$\log L_{\mathrm{P}\alpha}$ (erg s^{-1})	$\mathrm{FWHM}_{\mathrm{P}\alpha}$ (km s^{-1})
0036−0113	0.294	<40.9	–	42.58±0.04	1476±135	42.22±0.02	1765±73	–	–
0817+4354	0.186	<40.7	–	41.02±0.11	3022±452	–	–	41.97±0.04	3172±270
0825+4716	0.804	42.21±0.17	4199±1541	–	–	43.62±0.04	3940±393	–	–
0911+0143	0.603	–	–	–	–	42.74±0.04	2907±206	–	–
0915+2418	0.842	<43.1	–	–	–	43.77±0.09	3527±729	–	–
1113+1244	0.681	43.20±0.06	3699±350	–	–	43.28±0.03	2054±107	–	–
1209−0107	0.363	–	–	–	–	42.99±0.02	4451±246	–	–
1227+5053	0.768	43.18±0.06	4160±409	–	–	42.98±0.08	2781±446	–	–
1248+0531	0.752	–	–	–	–	42.95±0.02	2697±123	–	–
1307+2338	0.275	<40.8	–	42.17±0.05	2050±69	41.99±0.02	1891±107	42.41±0.03	2029±124
1309+6042	0.641	41.70±0.07	2275±245	–	–	42.71±0.02	2673±89	–	–
1313+1453	0.584	–	–	–	–	43.08±0.01	3793±96	–	–
1434+0935	0.770	42.52±0.08	3538±387	–	–	42.99±0.01	1398±34	–	–

Table 4.1 (cont'd)

Object Name	Redshift (z)	$\log L_{\mathrm{H}\beta}$ (erg s^{-1})	FWHM$_{\mathrm{H}\beta}$ (km s^{-1})	$\log L_{\mathrm{H}\alpha}$ (erg s^{-1})	FWHM$_{\mathrm{H}\alpha}$ (km s^{-1})	$\log L_{\mathrm{P}\beta}$ (erg s^{-1})	FWHM$_{\mathrm{P}\beta}$ (km s^{-1})	$\log L_{\mathrm{P}\alpha}$ (erg s^{-1})	FWHM$_{\mathrm{P}\alpha}$ (km s^{-1})
1532+2415	0.562	<40.9	–	–	–	42.88±0.16	4071±1549	–	–
1540+4923	0.696	–	–	–	–	42.88±0.14	5397±1518	–	–
1600+3522	0.707	–	–	–	–	43.31±0.06	1887±228	–	–
1656+3821	0.732	<43.3	–	–	–	43.15±0.04	3028±246	–	–
1720+6156	0.727	42.51±0.16	2866±305	–	–	42.70±0.06	1818±205	–	–
2325−1052	0.564	42.63±0.04	4522±2871	–	–	42.90±0.13	2778±772	–	–
2339−0912	0.660	43.12±0.01	2191±196	–	–	43.29±0.03	2927±140	–	–

In total, we obtained the broad line luminosities of eight Hβ, three Hα, 19 Pβ, and two Pα lines. The line luminosities and FWHMs are summarized in Table 1. We note that all the values in Table 1 are only corrected for Galactic extinction.

4.4 Results

In order to investigate the factor leading to the red color of red quasars, we compared the luminosity ratios of the Pβ/Hβ, Pβ/Hα, Pα/Hβ, and Pα/Hα of red quasars to those of unobscured type 1 quasars. For a typical red quasar with the $E(B-V) = 2$ mag, its Hα and Hβ luminosities would be suppressed by a factor of 100 and 1000, respectively, but the Pα and Pβ fluxes are suppressed by a factor of only 2.3 and 4.7, respectively. Therefore, the analysis using optical to NIR emission lines is a useful way to investigate the dust obscuration, where the Paschen lines can serve as a good measure of the unobscured light.

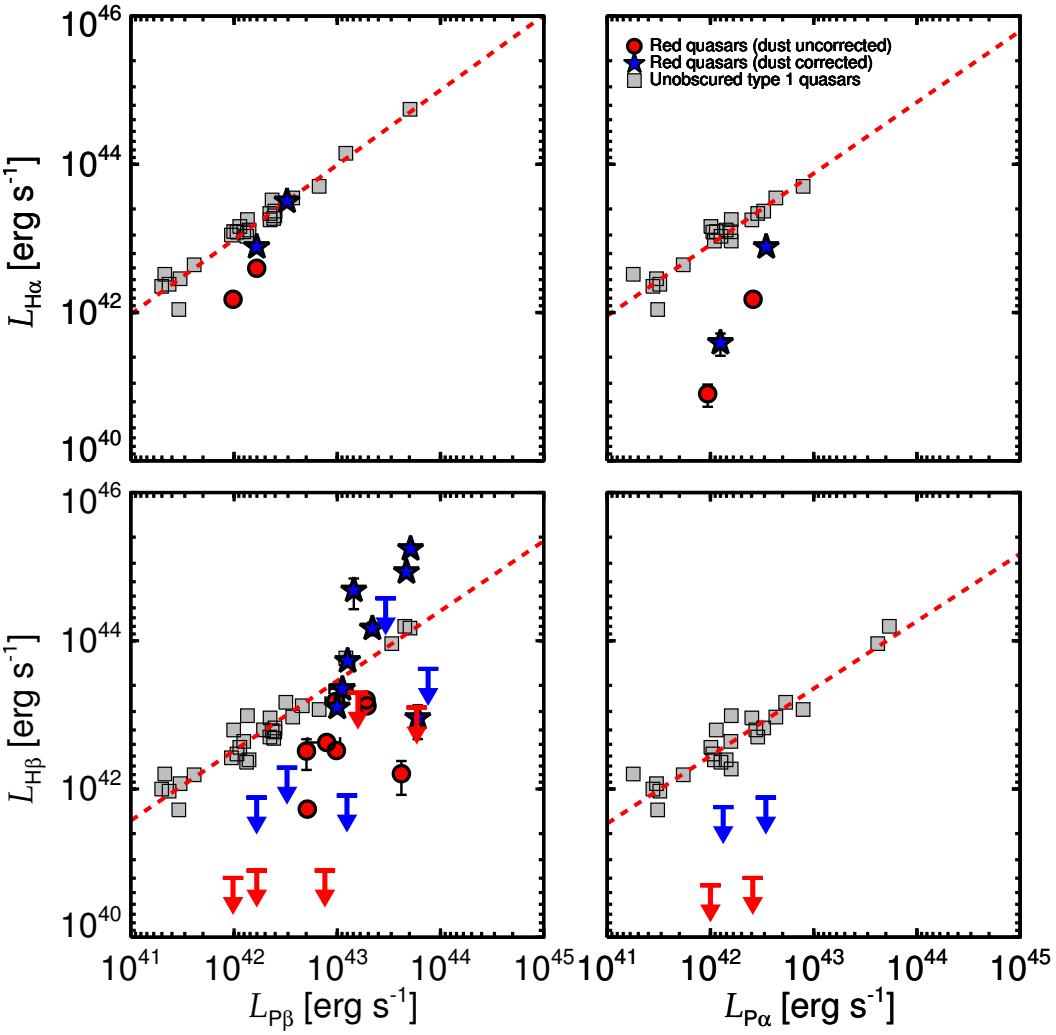

Figure 4.6 Comparison between the Paschen and Balmer line luminosities of red quasars and unobscured type 1 quasars (gray squares). The dashed red lines mean the best-fit lines between the Paschen and Balmer line luminosities of unobscured type 1 quasars. The blue stars and red circles indicate the dust-corrected and uncorrected luminosities of the red quasars, respectively. The blue and red arrows represent the upper limits of dust corrected and uncorrected $L_{\mathrm{H}\beta}$ vs. $L_{\mathrm{P}\beta}$ of 0036−0113, 0915+2418, 1307+2338, 1532+2415, and 1656+3821, respectively, and $L_{\mathrm{H}\beta}$ vs. $L_{\mathrm{P}\alpha}$ of 0817+4354 and 1307+2338, respectively. The left two panels show the comparison of the Pβ and Balmer line luminosities, and the right two panels compare the Pα with the Balmer line luminosities. Before extinction correction and at a given Paschen line luminosity, the Balmer line luminosities of red quasars are much weaker than those of unobscured type 1 quasars, while extinction corrections bring the red quasars close to the unobscured type 1 quasars.

For this analysis, the line luminosity ratios of unobscured type 1 quasars are adopted from Kim et al. (2010). Although several faint ($L_{\rm Paschen} < 10^{42}\,{\rm erg\,s^{-1}}$) unobscured type 1 quasars are included in this comparison, the line luminosity ratios are insensitive to the luminosity (see Figure 6 in Kim et al. 2010). Figure 6 compares line luminosities of the red quasars and unobscured type 1 quasars. We find that the observed Balmer line luminosity for a given Paschen line luminosity is 1.5–290 ($\sim$12 on average) times weaker for the red quasars than for unobscured type 1 quasars.

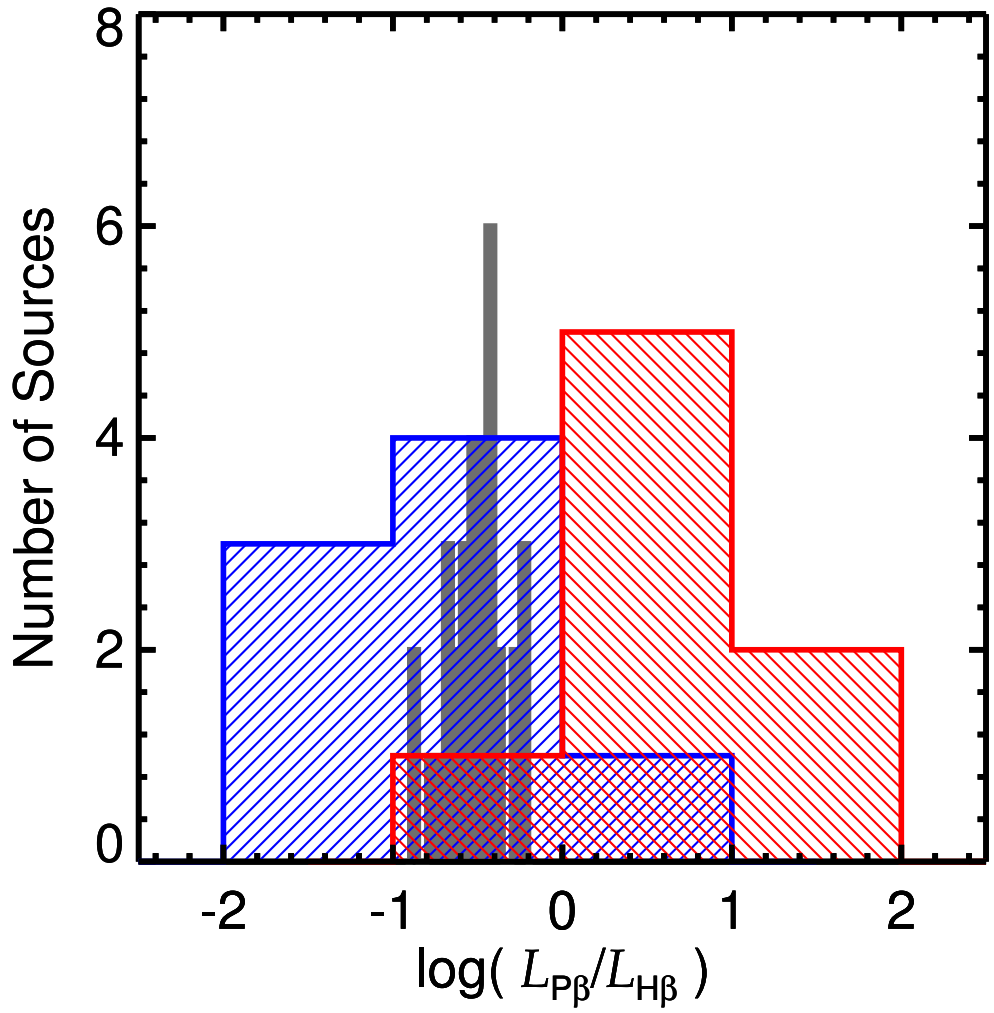

Figure 4.7 Distributions of the Pβ/Hβ luminosity ratios of the red quasars (color-hatched histogram) and unobscured type 1 quasars (gray histogram). The blue and red histograms indicate the distributions of the extinction corrected and uncorrected Pβ/Hβ luminosity ratios of the red quasars, respectively. After applying the extinction correction, the Pβ/Hβ distribution of red quasars agree broadly with that of unobscured type 1 quasars, but with a much larger scatter suggesting that the extinction-correction prescription is not perfect.

Figure 7 shows the distributions of the Pβ/Hβ luminosity ratios of the red quasars and unobscured type 1 quasars. We find that red quasars have the $\log(L_{\mathrm{P}\beta}/L_{\mathrm{H}\beta})$ values much higher than those of the unobscured type 1 quasars; median $\log(L_{\mathrm{P}\beta}/L_{\mathrm{H}\beta})$ of the red quasars are 0.27$\pm$0.53, in contrast to that of unobscured type 1 quasars (-0.49$\pm$0.17). The Kolmogorov-Smirnov (K-S) test confirms this significant difference in the line luminosity ratios between the two quasar populations. We performed the K-S test using the `KSTWO` code based on the IDL. The maximum deviation between the cumulative distributions of these two Pβ/Hβ luminosity ratios, D, is 1.0, and the probability of the result given the null hypothesis, p, is only 9.22×10^{-7}.

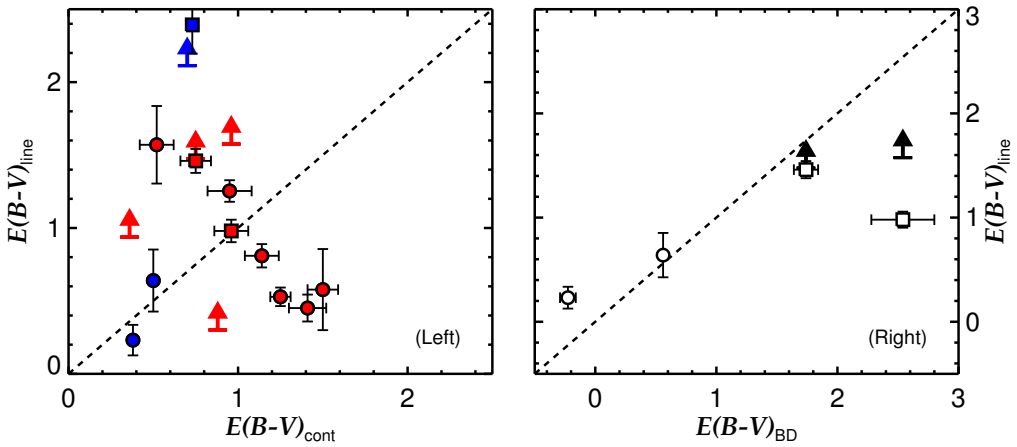

Figure 4.8 (Left) Comparison between the continuum-based and the line ratio-based $E(B-V)$ values of red quasars. The $E(B-V)_{\rm line}$ values are composed of $E(B-V)_{\rm line1}$ and $E(B-V)_{\rm line2}$ values. The $E(B-V)_{\rm line1}$ and $E(B-V)_{\rm line2}$ are represented by the circles and squares, respectively. The $E(B-V)_{\rm cont}$ values are adopted from previous studies (Glikman et al. 2007; Urrutia et al. 2009), for which uncertainties for some of the values are not available. The red and blue colors indicating the $E(B-V)_{\rm cont}$ values are adopted from Urrutia et al. (2009) and Glikman et al. (2007), respectively. The arrows representing the $E(B-V)_{\rm line1}$ values are measured using the upper limits luminosities of Hβ and $L_{\rm P\beta}$, and their colors have the same meanings. The dashed line indicates a line where the two values are identical. The correlation between these two quantities are nonexistent, suggesting large uncertainties that are associated with the determination of the dust extinction from the continuum that may be affected by the modeling of the continuum components. (Right) The $E(B-V)_{\rm BD}$ vs. $E(B-V)_{\rm line}$. The meaning of the circles, square, and arrows are identical to the left panel. The $E(B-V)_{\rm BD}$ values are adopted from Glikman et al. (2007), and they agree well with the $E(B-V)_{\rm line}$.

If red quasars are dust-reddened, we expect the dust-corrected line luminosity ratios of the red quasars to be consistent with those of unobscured type 1 quasars. For this test, we adopted the $E(B-V)$ values from previous studies (Glikman et al. 2007; Urrutia et al. 2009) and applied the extinction correction assuming the Galactic extinction curve with $R_V = 3.1$ (Schultz & Wiemer 1975). Glikman et al. (2007) and Urrutia et al. (2009) provide two types of $E(B-V)$ values derived from the continuum shape and the Balmer decrement. In this study, we used the $E(B-V)$ values from the continuum shape because the $E(B-V)$ values from the continuum shape are available for all objects in the sample. The extinction-corrected line luminosities ratios of red quasars are indicated in Figures 6 and 7.

The extinction-corrected median $\log(L_{\mathrm{P}\beta}/L_{\mathrm{H}\beta})$ of the red quasars is -0.63±0.81, that is almost the same as that of unobscured type 1 quasars. Furthermore, our K-S test for the histogram of the extinction-corrected Pβ/Hβ luminosity ratios show that the measured D and p values of the K-S statistic are 0.44 and 0.12, respectively, against unobscured type 1 quasars. For this K-S test, we broadened the Pβ/Hβ luminosity ratios distribution of unobscured type 1 quasars by adding scatters to Pβ/Hβ luminosity ratios through a Monte Carlo simulation by the amount that could be produced during de-reddening of Pβ/Hβ luminosity ratios of red quasars assuming a typical scatter in $E(B-V)$ of 0.5 (Glikman et al. 2007). Therefore, we conclude that, on average, both the continuum colors and the line ratios of red quasars can be explained by dust extinction.

One interesting question is whether we can accurately determine $E(B-V)$ values of red quasars. In an attempt to make this determination, we compared $E(B-V)$ values from the Paschen and Balmer line luminosity ratios ($E(B-V)_{\mathrm{line}}$) versus $E(B-V)$ values from the continuum shape ($E(B-V)_{\mathrm{cont}}$). In this study, the $E(B-V)_{\mathrm{line}}$ is composed of the two values $E(B-V)_{\mathrm{line1}}$ and $E(B-V)_{\mathrm{line2}}$. The $E(B-V)_{\mathrm{line1}}$ is derived by finding a proper value of $E(B-V)$ that brings the

observed $L_{\mathrm{P}\beta}/L_{\mathrm{H}\beta}$ ratio to the observed mean of unobscured type 1 quasars, where the Galactic extinction curve and $R_V = 3.1$ are assumed. On the other hand, the $E(B-V)_{\mathrm{line2}}$ is determined by using the ratios of $L_{\mathrm{P}\beta}$ (0817+4354 and 1307+2338) or $L_{\mathrm{P}\alpha}$ (0036−0113) to $L_{\mathrm{H}\alpha}$. The measured $E(B-V)_{\mathrm{line1}}$ and $E(B-V)_{\mathrm{line2}}$ values are listed in Table 2. In Figure 8, we compare $E(B-V)_{\mathrm{line}}$ versus $E(B-V)_{\mathrm{cont}}$. The Pearson correlation coefficient between the two quantities is -0.21 and a rms scatter of 0.68 with respect to a one-to-one correlation. The result can be considered as no correlation or a one-to-one correlation with a very large scatter of 0.72 in $E(B-V)$. On the same plot, we also compare $E(B-V)_{\mathrm{line}}$ versus $E(B-V)$ from the Balmer decrement ($E(B-V)_{\mathrm{BD}}$). The $E(B-V)_{\mathrm{BD}}$ values are taken from Glikman et al. (2007) and determined using the ratios between the $L_{\mathrm{H}\alpha}$ and $L_{\mathrm{H}\beta}$. We note that the $E(B-V)_{\mathrm{BD}}$ values were determined using total line intensity or broad component luminosity. Among the two types of $E(B-V)_{\mathrm{BD}}$, we use the $E(B-V)_{\mathrm{BD}}$ from the broad component luminosity except for 1227+5053 for which $E(B-V)_{\mathrm{BD}}$ from the broad line is not available. For the comparison between the $E(B-V)_{\mathrm{BD}}$ and $E(B-V)_{\mathrm{line}}$, only four data points are available, but we find a reasonably good agreement between $E(B-V)_{\mathrm{line}}$ and $E(B-V)_{\mathrm{BD}}$. The Pearson correlation coefficient between the two quantities is 0.80.

The large scatter between $E(B-V)_{\mathrm{cont}}$ and $E(B-V)_{\mathrm{line}}$ is likely due to the wide range of continuum slopes that quasars can have and the difficulty in estimating the intrinsic continuum shape in advance. Another possible reason is that the dust obscuration region varies between the continuum emitting and line emitting regions. We suggest that $E(B-V)$ estimated through the continuum shape contains a large scatter (~ 0.72 in $E(B-V)$). This agrees with what we saw in Figure 7, where the histogram of $L_{\mathrm{P}\beta}/L_{\mathrm{H}\beta}$ after the extinction correction with $E(B-V)_{\mathrm{cont}}$ is much broader than the same histogram for unobscured type 1 quasars and the two histograms are virtually indistinguishable after taking into account this broadening

effect.

4.5 Discussion

4.5.1 Physical condition as a cause for high line luminosity ratio

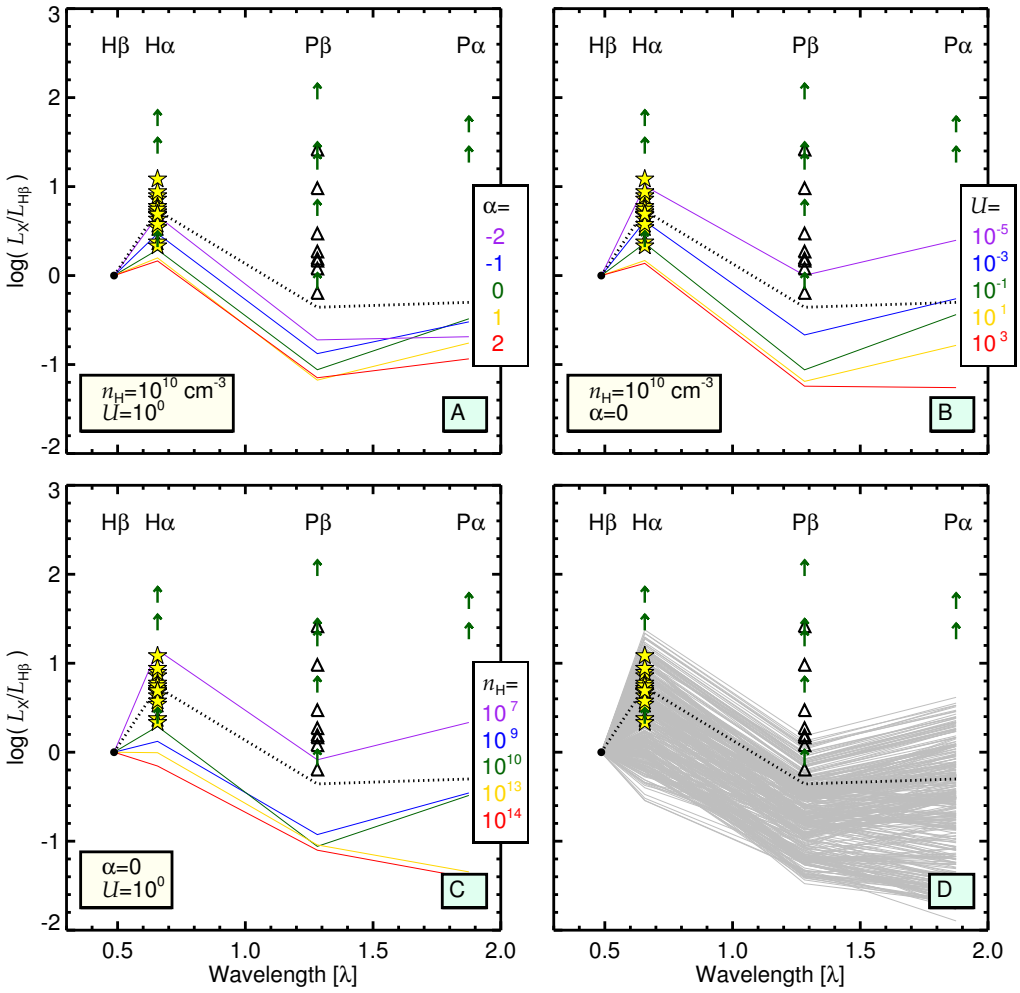

Figure 4.9 Line luminosity ratios of Hα, Pβ, and Pα with respect to Hβ of red quasars. The Pβ/Hβ luminosity ratios of eight red quasars are indicated by the open triangles, and the yellow stars are the Hα/Hβ luminosity ratios of the local red AGNs from Rose et al. (2013). The green arrows indicate the lower limits. The dotted line is the line luminosity ratio reproduced by the `CLOUDY` code with a set of parameters ($\alpha = -1.0$, $U = 10^{-1.5}$, and $n_{\rm H} = 10^9$ cm^{-3}), which is consistent with the line luminosity ratios of unobscured type 1 quasars from Hβ to Pα (Kim et al. 2010). (A) The five colored solid lines represent the line luminosity ratios from the `CLOUDY` code with $n_{\rm H} = 10^{10}$ cm^{-3}, $U = 10^0$, and various α from -2 to 2. The various α is represented by color, i.e., the purple, blue, green, yellow, and red lines indicate α is -2, -1, 0, 1, and 2, respectively. (B) The meanings of the symbols and lines are identical to (A), but the five colored lines are the line luminosity ratios with $n_{\rm H} = 10^{10}$ cm^{-3}, $\alpha = 0$, and various U from 10^{-5} to 10^3. (C) The meanings of the symbols and lines are identical to (A), but the five colored lines are the line luminosity ratios with $\alpha = 0$, $U = 10^0$, and various $n_{\rm H}$ from 10^7 to 10^{14} cm^{-3}. (D) The meanings of the symbols and the dotted line are identical to (A), and the gray lines represent the line luminosity ratios computed from the `CLOUDY` code with various physical conditions, within $\alpha = -2$ to 2, $n_{\rm H} = 10^7 - 10^{14}$ cm^{-3}, and $U = 10^{-5} - 10^5$.

Here, we test a hypothesis that the observed $L_{\rm Paschen}/L_{\rm Balmer}$ of red quasars are due to a different physical condition of broad emission line regions (BELRs) without dust extinction. To do so, we explore what physical conditions of BELRs can reproduce the observed line luminosity ratios by computing theoretically expected line luminosity ratios under different physical conditions using the `CLOUDY` code (version 13.03; Ferland et al. 1998).

We set the plausible ranges of input parameters as the following. Quasars do not show any broad forbidden lines (e.g., see Glikman et al. 2007; Urrutia et al. 2009). The absence of the broad forbidden lines implies that the hydrogen density ($n_{\rm H}$) in the BELR is higher than the critical density of the forbidden lines, which gives us the lower limit of $n_{\rm H} = 10^7$ cm^{-3}. The upper limit of $n_{\rm H}$ is set to 10^{14} cm^{-3} considering the existence of strong Fe blends ($\sim 10^{12}$ cm^{-3}; Collin-Souffrin et al. 1982; Rees et al. 1989). For the other parameters, we vary the values of the shape of the ionizing continuum ($\alpha = -2 \sim 2$) and the ionization parameter ($U = 10^{-5} \sim 10^5$) to cover various physical conditions.

Line luminosity ratios of $L_{\rm P\alpha}/L_{\rm H\beta}$, $L_{\rm P\beta}/L_{\rm H\beta}$, and $L_{\rm H\alpha}/L_{\rm H\beta}$ are sensitive to $n_{\rm H}$ and U. The line luminosity ratios decrease when the $n_{\rm H}$ and U values are increased, which is indicated in the B and C panels of Figure 9.

Figure 9 shows the line luminosity ratios as a function of wavelength for red quasars and those from the `CLOUDY` calculation. The line luminosity ratios of unobscured type 1 quasars can be successfully reproduced by the `CLOUDY` calculation with a set of parameters, $\alpha = -1.0$, $U = 10^{-1.5}$, and $n_{\rm H} = 10^9$ cm^{-3} (Kim et al. 2010), which is represented by the dotted line in Figure 9. For the Balmer lines, although the Hα/Hβ luminosity ratios of red quasars are not measured in this study, these luminosity ratios of local red AGNs are only moderately different from those of unobscured type 1 quasars (Rose et al. 2013).

However, the line luminosity ratios start to demand unusual physical conditions

when Paschen lines are included. The median $\log(L_{\mathrm{P}\beta}/L_{\mathrm{H}\beta})$ is 0.43 ± 0.53 for red quasars, while it is only -0.48 ± 0.17 for unobscured type 1 quasars. Among the eight $L_{\mathrm{P}\beta}/L_{\mathrm{H}\beta}$ ratios measured red quasars, five (63 %) red quasars have higher line ratios than the maximum line luminosity ratios in the `CLOUDY` calculation ($\log(L_{\mathrm{P}\beta}/L_{\mathrm{H}\beta}) \leq 0.18$). In other words, the $L_{\mathrm{P}\beta}/L_{\mathrm{H}\beta}$ ratios of the five red quasars are much higher than the line luminosity ratios from all the plausible physical parameters for BLR. For the remaining three (38 %) red quasars, the $L_{\mathrm{P}\beta}/L_{\mathrm{H}\beta}$ ratios can be explained with a condition of low $n_{\mathrm{H}} = 10^7\,\mathrm{cm}^{-3}$, low $U = 10^{-3}$, and $\alpha = 2$. The parameters are found by minimizing χ^2, which is a function of the line luminosity ratios

$$\chi^2 = \sum_{i=1}^{N} \frac{(R_{\mathrm{observed},i} - R_{\mathrm{model},i})^2}{\sigma_i^2}, \tag{4.1}$$

where N is the number of line luminosity ratios, and two types of R_i are the line luminosity ratios either from observation or the CLOUDY model, and σ_i is the uncertainty in the measured line luminosity ratio. However, this physical condition, that is, low n_{H} and low U, is somewhat similar to that of NLRs (e.g., $n_{\mathrm{e}} = 10^{3.5} \sim 10^{7.5}\,\mathrm{cm}^{-3}$ and $U \sim 10^{-2}$; Osterbrock 1991; Netzer 2013), rather than the broad lines that we are studying here (FWHM $> 800\,\mathrm{km\,s}^{-1}$), and this disfavors the physical condition as a reason for the observed line luminosity ratios.

4.5.2 High hot dust covering factor as a cause for redness

Rose et al. (2013) suggested that some of AGNs with red $J-K$ colors are red owing to a relatively large hot dust covering factor ($\mathrm{CF_{HD}} = L_{\mathrm{HD}}/L_{\mathrm{bol}}$; Maiolino et al. 2007; Kim et al. 2015a). We address this point here with our sample.

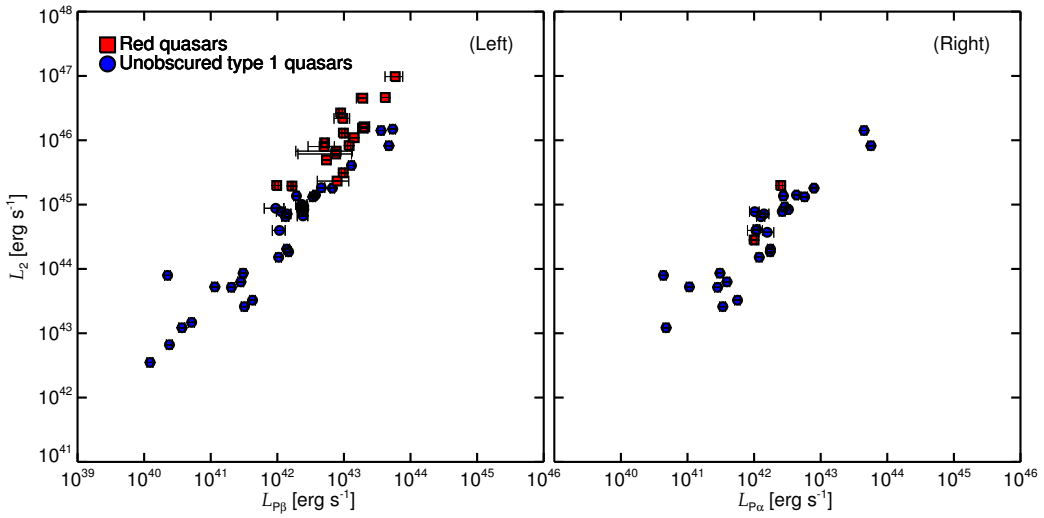

Figure 4.10 (Left) Values of L_2 vs. $L_{\mathrm{P}\beta}$ of red quasars (the red filled squares) and unobscured type 1 quasars (the blue filled circles). (Right) The L_2 values vs. the $L_{\mathrm{P}\alpha}$ values. The meanings of the symbols are identical. This figure shows that red quasars do not have unusual hot dust emission that is much stronger (> 1 dex) than that of unobscured type 1 quasars, although their NIR emission may be a bit stronger (~ 0.3 dex) than unobscured type 1 quasars.

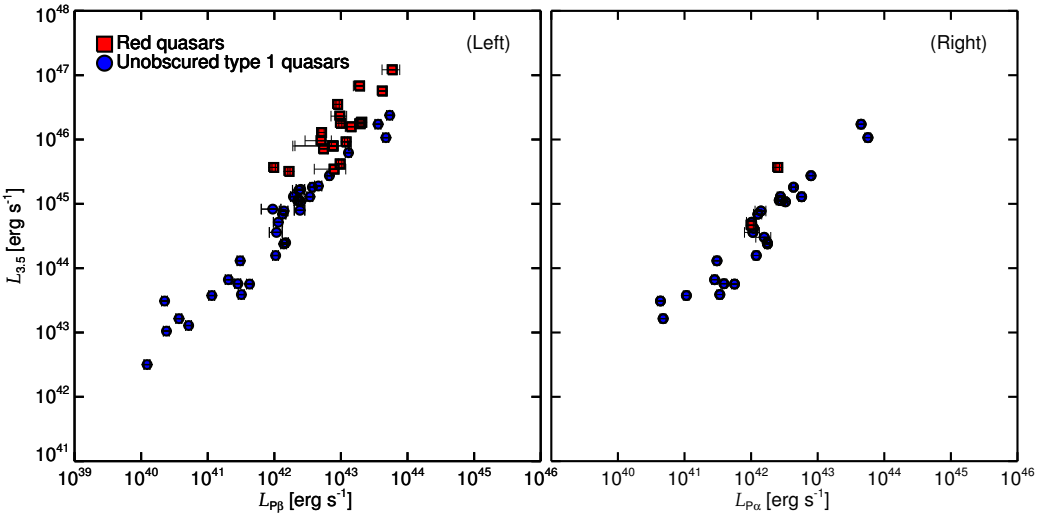

Figure 4.11 Comparisons between $L_{3.5}$ values vs. Paschen line luminosities. The meanings of the symbols are identical to Figure 10.

For the comparison between the CF_{HD} of red quasars and unobscured type 1 quasars, we used 37 unobscured type 1 quasars from Kim et al. (2010). The unobscured type 1 quasars are bright ($K < 14.5$ mag and $M_i < -23$ mag) and located at $z < 0.5$.

Because the L_{bol} and L_{HD} are easily under- or overestimated from the spectral energy distribution (SED) model fitting depending on a set of the dust extinction value and extinction law, we used the Paschen line luminosities and NIR continuum luminosities (L_2 and $L_{3.5}$; λL_λ at 2 μm and 3.5 μm in the rest-frame) as proxies for the L_{bol} and L_{HD}, respectively. Considering previous results that found, first, the temperature of hot dust torus is ∼1000–1500 K (Barvainis 1987; Glikman et al. 2006; Kim et al. 2015a; Hernán-Caballero et al. 2016) and, second, 2 μm and 3.5 μm are closed to the peak wavelengths of blackbody radiation from the hot dust component, L_2 and $L_{3.5}$ can represent L_{HD} (Glikman et al. 2006; Kim et al. 2015a). Although the stellar emission can peak at 1.6 μm, the hot dust component can be a dominant component with its peak at 2–3.5 μm. This is supported by $J - K$ colors of red quasars that are significantly different from those of normal galaxies and star-forming galaxies (e.g., see Figure 1 in Glikman et al. 2012). Although the NIR continuum luminosities of red quasars have a possibility to be overestimated by the stellar emission contamination, the NIR contribution of the stellar emission is known to be ≤10 % for quasars, when NIR continuum luminosity is over than $10^{43.5}$ erg s^{-1} (Hernán-Caballero et al. 2016). There is no plausible reason to believe that the hot and warm dust emission should be much weaker for red quasars than type 1 quasars. If red quasars are red due to unusually high CF_{HD}, this would make the host galaxy contribution to the NIR continuum luminosities even smaller. The Paschen line luminosities are used as a tracer for the L_{bol} (Kim et al. 2015b) by employing the excellent correlation between L_P, $L_{H\alpha}$, L_{5100}, and L_{bol} (Kim et al. 2010; Shen et al. 2011; Jun et al. 2015). The wavelengths of 2 μm and 3.5 μm are

not too far from the Paschen lines (Pβ: 1.2818 μm and Pα: 1.8751 μm) and so the $L_2/L_{\rm P}$ and $L_{3.5}/L_{\rm P}$ are rather insensitive to the exact values of dust extinction.

The NIR continuum luminosities are measured by interpolating the 2MASS (Skrutskie et al. 2006) and *WISE* (Wright et al. 2010) photometric data. The Pβ and Pα luminosities are adopted from Kim et al. (2010) for 37 and 27 unobscured type 1 quasars, respectively.

In this study, we do not consider the Baldwin effect because the Baldwin effect in the Balmer lines is weak (Dietrich et al. 2002), and the Paschen lines have a strong correlation with the Balmer lines (Kim et al. 2010).

Figures 10 and 11 show the comparisons between the NIR continuum luminosities versus Paschen line luminosities of the red quasars and unobscured type 1 quasars. The unobscured type 1 quasars have the mean $\log(L_2/L_{\rm P\beta})$ and $\log(L_{3.5}/L_{\rm P\beta})$ of 2.58±0.01 and 2.64±0.01 with dispersions of 0.55 and 0.51, respectively. The measured luminosity ratios are only slightly smaller than those of red quasars (3.06±0.01 and 3.21±0.01 with dispersions of 0.27 and 0.28). Moreover, the mean $\log(L_2/L_{\rm P\alpha})$ and $\log(L_{3.5}/L_{\rm P\alpha})$ of the unobscured type 1 quasars are 2.51±0.01 and 2.56±0.01 with dispersions of 0.64 and 0.60, respectively, and those of red quasars (2.72±0.02 and 2.97±0.02 with dispersions of 0.32 and 0.35) are almost same.

The result indicates that the covering factor of red quasars are not much different from type 1 quasars, and an unusually large covering factor is not the reason for their red colors. This result is consistent with the viewing angle or torus obscuration scenario, but we address this scenario below.

4.5.3 Viewing angle as a cause for redness

Wilkes et al. (2002) suggested that the redness of red quasars arises from a moderate viewing angle in the quasar unification model when the accretion disk and the BLR are viewed through a dust torus. If so, red quasars should show properties very

similar to unobscured type 1 quasars.

However, previous studies (Urrutia et al. 2012; Kim et al. 2015b) showed that red quasars have significantly higher accretion rates than unobscured type 1 quasars, which cannot be explained by the viewing angle scenario. Among the 19 Pβ luminosity measured red quasars in our sample, the Eddington ratios of 16 red quasars at $z \sim 0.7$ were already studied in Kim et al. (2015b). We have three additional Pβ measured red quasars at $z \sim 0.3$ (0036−0113, 1209−0107, and 1307+2338). Below, we first examine the Eddington ratios of the three additional quasars and then compare the Eddington ratios of 16 red quasars at $z \sim 0.7$ to the $L_{\rm bol}$ matched unobscured type 1 quasars.

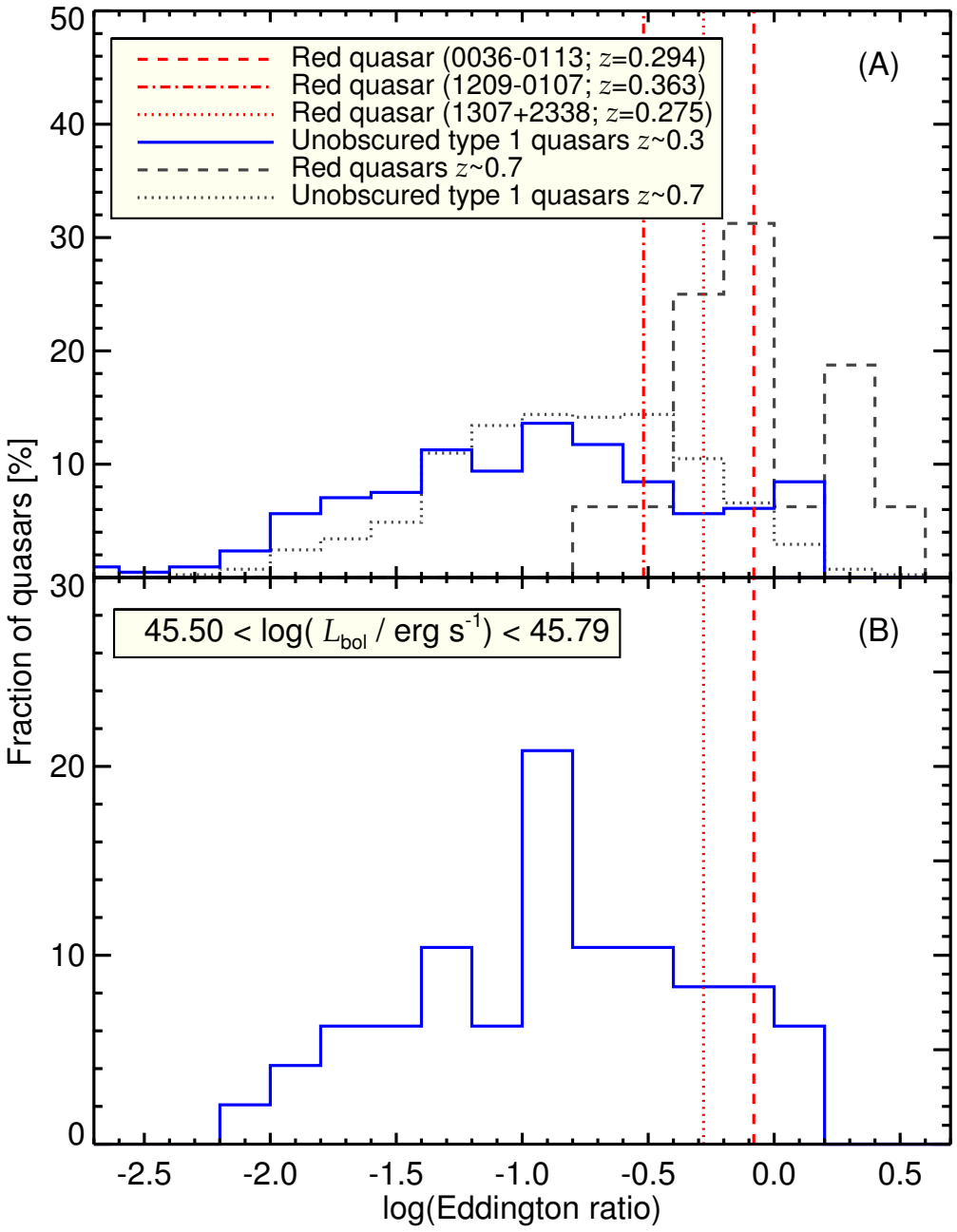

Figure 4.12 (A) Eddington ratios of three red quasars (0036−0113, 1209−0107, and 1307+2338; red lines) and unobscured type 1 quasars $z \sim 0.3$ (blue histograms). The gray dashed and dotted lines represent the Eddington ratio distributions for red quasars and unobscured type 1 quasars at $z \sim 0.7$, respectively, where results are adopted from Kim et al. (2015b). (B) The same figure as above, except that unobscured type 1 quasars have bolometric luminosities similar to the two red quasars (0036−0113 and 1307+2338; $45.50 < \log(L_{\rm bol}/{\rm erg\,s^{-1}}) < 45.79$).

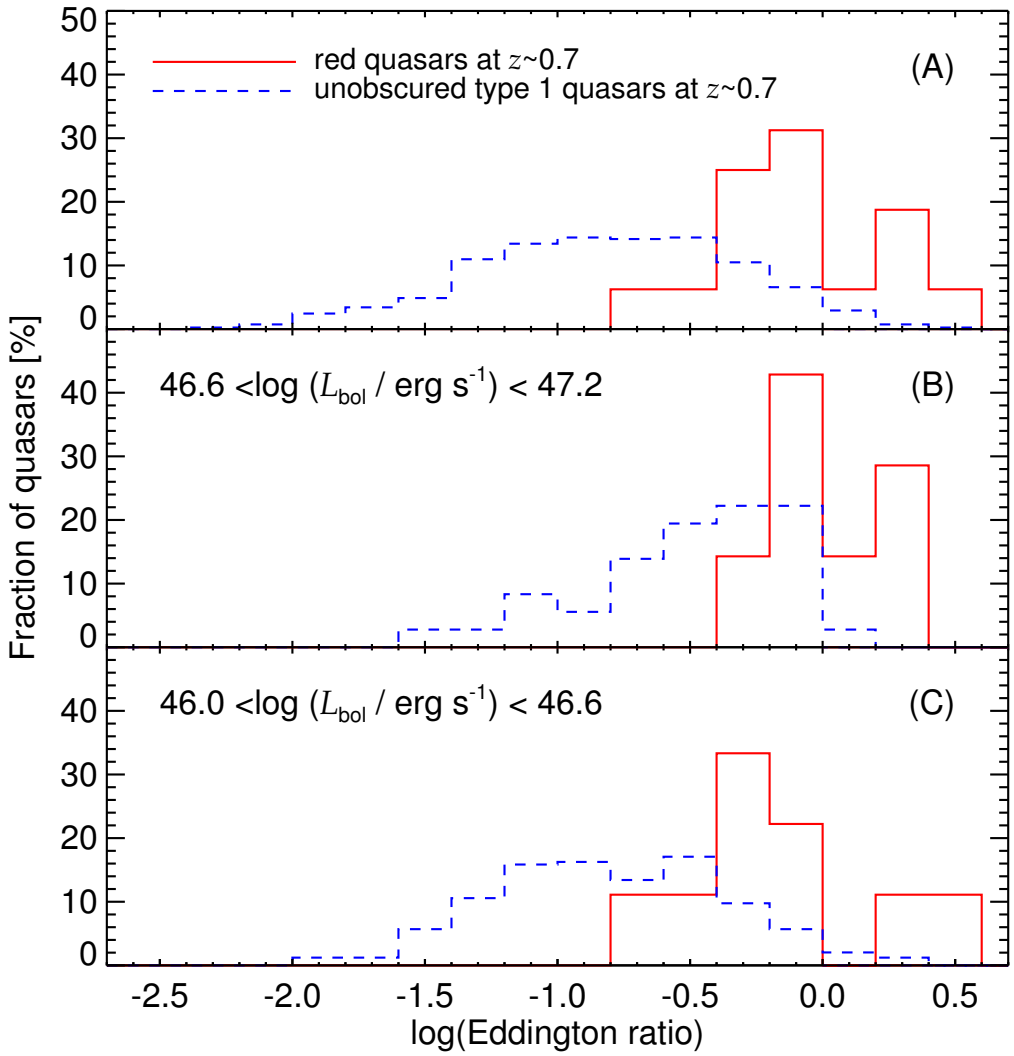

Figure 4.13 (A) Eddington ratio distributions of red quasars and unobscured type 1 quasars at $z \sim 0.7$. The red solid and blue dashed histograms represent red quasars and unobscured type 1 quasars, respectively. The Eddington ratios of red quasars at $z \sim 0.7$ are adopted from Kim et al. (2015b). (B) Eddington ratio distributions for high-luminous quasars ($46.6 < \log(L_{\rm bol}/{\rm erg\,s^{-1}}) < 47.2$). (C) Eddington ratio distributions for low-luminous quasars ($46.0 < \log(L_{\rm bol}/{\rm erg\,s^{-1}}) < 46.6$).

As a comparison sample, we select unobscured type 1 quasars from the quasar catalog (Schneider et al. 2010) of the SDSS Seventh Data Release (DR7; Abazajian et al. 2009). In order to avoid the sample selection bias, the unobscured type 1 quasars are selected by the same selection criteria as red quasars as follows: (i) the same redshift range of the three red quasars ($0.275<z<0.363$), (ii) radio detection in Faint Images of the Radio Sky at Twenty-Centimeters (FIRST) survey (Becker et al. 1995), and (iii) photometric detection in 2MASS. This selection yields 213 unobscured type 1 quasars as the comparison sample.

In order to estimate the BH masses of red quasars, we corrected the Pβ luminosities by adopting $E(B-V)$ values from previous studies (Glikman et al. 2007; Urrutia et al. 2009). The $E(B-V)$ values were determined using their continuum shape. After then, we used the Pβ based $M_{\rm BH}$ estimator from Equation (1) of Kim et al. (2015b), which is modified from the Pβ scaling relation (Kim et al. 2010) by adopting a recent virial coefficient of $\log f = 0.05$ (Woo et al. 2015). For the $M_{\rm BH}$ of unobscured type 1 quasars, we used L_{5100} and $\rm FWHM_{H\beta}$ values from Shen et al. (2011) and the $M_{\rm BH}$ estimator of Equation (2) in Kim et al. (2015b).

The Hβ-based $M_{\rm BH}$ values are lower than the Pβ-based $M_{\rm BH}$ values by 0.45 dex before the extinction correction. No offset can be seen after the Hβ-based $M_{\rm BH}$ values are derived by taking the extinction effect into account, but this introduces a large scatter (rms$\sim$ 0.56 dex) in $M_{\rm BH}$ values from the two methods, justifying the use of Pβ-based $M_{\rm BH}$ here.

To obtain $L_{\rm bol}$ values of the red quasars, we translated the $L_{\rm P\beta}$ using the relationship between the $L_{\rm bol}$ and $L_{\rm P\beta}$ of Equation (4) in Kim et al. (2015b). The $L_{\rm bol}$ values of the unobscured type 1 quasars are converted from the L_{5100} values with a bolometric correction factor of 9.26 (Shen et al. 2011). We note that the measured $M_{\rm BH}$ and $L_{\rm bol}$ values of the red quasars are summarized in Table 2.

The $L_{\rm bol}$ values of the red quasars ($10^{45.50}\,{\rm erg\,s^{-1}} < L_{\rm bol} < 10^{46.51}\,{\rm erg\,s^{-1}}$)

and the comparison sample of unobscured type 1 quasars ($10^{45.04}\,\mathrm{erg\,s^{-1}} < L_{\mathrm{bol}} < 10^{46.55}\,\mathrm{erg\,s^{-1}}$) are similar but not identical. For that reason, we also performed the comparison of the two populations using L_{bol}-matched samples too.

To estimate the Eddington ratio, the Pβ is used as both an indicator of L_{bol} and M_{BH}. Although these two different quantities are derived from the Pβ line and include the same line luminosity term, the M_{BH} has a larger uncertainty than L_{bol} because the M_{BH} values include FWHM square term and the square-rooted line luminosity term. The median uncertainties of the Pβ based L_{bol} and M_{BH} are 0.03 and 0.08 dex, respectively. The Eddington ratio is proportional to $L^{0.5}/\mathrm{FWHM}^2$ and this gives the combined uncertainty of 0.08 dex[2]

We compared the Eddington ratios ($L_{\mathrm{bol}}/L_{\mathrm{Edd}}$, where L_{Edd} is the Eddington luminosity) of red quasars and unobscured type 1 quasars in Figure 12. The median Eddington ratios of unobscured type 1 quasars is 0.12 with an rms scatter of 0.34. Meanwhile, the measured Eddington ratios of three red quasars are 0.83, 0.30, and 0.52 for 0036−0113, 1209−0107, and 1307+2338, respectively. Among 213 unobscured type 1 quasars, only 55 unobscured type 1 quasars have higher Eddington ratios than 0.30. The probability is only 1.7 % that three randomly chosen unobscured type 1 quasars from the comparison sample have the Eddington ratios higher than 0.30. No systematic bias is expected between $L_{\mathrm{bol}}/L_{\mathrm{Edd}}$ from Pβ (red quasars) and L_{5100} with $\mathrm{FWHM}_{\mathrm{H}\beta}$ (unobscured type 1 quasars), except for an added scatter of 0.36 dex that comes from the scatter in the correlation of different quantities (Kim et al. 2015b).

Since several works suggest that the Eddington ratios are dependent on L_{bol} (e.g., Lusso et al. 2012; Suh et al. 2015), we also show the Eddington ratio distribution of the sample in a narrow L_{bol} range that matches the L_{bol} of red quasars. The objects

[2]The uncertainties only consider the uncertainty arising from measurements. If all uncertainties (the intrinsic scatters and uncertainties arising from the correlations between the L_{P}, $L_{\mathrm{H}\alpha}$, L_{5100}, and L_{bol}) are combined together, the combined uncertainty increases to 0.36 dex.

0036−0113 and 1307+2338 have similar $L_{\rm bol}$ of $10^{45.79}\,{\rm erg\,s^{-1}}$ and $10^{45.50}\,{\rm erg\,s^{-1}}$, respectively, but 1209−0107 has a much higher $L_{\rm bol}$ of $10^{46.51}\,{\rm erg\,s^{-1}}$. For comparison, we selected 48 unobscured type 1 quasars with the same $L_{\rm bol}$ range ($10^{45.50} < L_{\rm bol} < 10^{45.79}\,{\rm erg\,s^{-1}}$) of the 2 red quasars 0036−0113 and 1307+2338. The median Eddington ratio of the 48 unobscured type 1 quasars changes to 0.15±0.33, but this is still much lower than those of the red quasars. Among the 48 unobscured type 1 quasars, only 9 unobscured type 1 quasars have higher Eddington ratios than the minimum Eddington ratio, 0.52, of 0036−0113 and 1307+2338. The probability is only 3.2 % that 2 randomly chosen unobscured type 1 quasars from the comparison sample have the Eddington ratios higher than 0.52.

Previous studies (Urrutia et al. 2012; Kim et al. 2015b) showed red quasars at different redshift have higher Eddington ratios than unobscured type 1 quasars. Kim et al. (2015b) measured Eddington ratios for 16 red quasars at $z \sim 0.7$ and the 16 red quasars are included in our 20 red quasars. Kim et al. (2015b) compared the Eddington ratios of the 16 red quasars to those of unobscured type 1 quasars that are matched in $M_{\rm BH}$. We show how the Eddington ratios of 16 red quasars compare with those of $L_{\rm bol}$-matched unobscured type 1 quasars. The unobscured type 1 quasars are selected from the SDSS DR7 quasar catalog (Schneider et al. 2010) with the same redshift range of the 16 red quasars ($0.56 < z < 0.84$). We note that the selection method of the comparison sample is identical to Kim et al. (2015b) and the details of the comparison sample selection are described in Section 2.1 of Kim et al. (2015b).

We divided the red quasars and the unobscured type 1 quasars into two luminosity bins. Figure 13 shows the comparison of the Eddington ratio distributions and our results show that the Eddington ratios of 16 red quasars at $z \sim 0.7$ are significantly higher (factors of ∼3 to 4) than those of unobscured type 1 quasars. Even if we assume a maximal amount of 35 % contamination on the Paschen line

flux by a narrow line (see Section 3), the Eddington ratio decreases by only ∼15 % or 0.07 dex, and we find that the analysis result does not change.

For the low luminosity sample, 9 red quasars and 246 unobscured type 1 quasars are selected, and their $\log(M_{\rm BH}/M_{\odot})$ values have ranges of 7.98–9.07 and 7.71–10.27 for the red quasars and the unobscured type 1 quasars, respectively. The median Eddington ratios of the red quasars and the unobscured type 1 quasars are 0.62 and 0.15, respectively. The D and p values from a K-S test between these two distributions are 0.64 and 7.6×10^{-4}. The high luminosity sample includes 7 red quasars and 36 unobscured type 1 quasars. The $\log(M_{\rm BH}/M_{\odot})$ values have ranges of 8.26–9.09 and 8.58–10.18 for the red quasars and unobscured type 1 quasars, respectively. The median Eddington ratios of the red quasars and unobscured type 1 quasars are 0.97 and 0.35, respectively. The measured D and p values between these two distributions are 0.66 and 5.6×10^{-3}.

Overall, the additional analysis of the three red quasars and the re-analysis of the luminosity matched 16 red quasars in Kim et al. (2015b) strengthens the previous results of Urrutia et al. (2012) and Kim et al. (2015b) that red quasars tend to have higher Eddington ratios than unobscured type 1 quasars. Therefore, we suggest that many of the red quasars, if not all, are not seen as red simply because of the viewing angle (also see Onori et al. 2017).

Table 4.2. Values of $M_{\rm BH}$, $L_{\rm bol}$, and $E(B-V)$ for red quasars

Object name	$M_{\rm BH}$ ($10^8\,M_\odot$)	$L_{\rm bol}$ ($10^{46}\,{\rm erg\,s^{-1}}$)	Eddington ratio	$E(B-V)_{\rm cont}$[a] (mag)	$E(B-V)_{\rm cont}$[b] (mag)	$E(B-V)_{\rm line1}$ (mag)	$E(B-V)_{\rm line2}$ (mag)	$E(B-V)_{\rm BD}$ (mag)
0036−0113	0.60±0.12	0.61±0.03	0.830	0.79	0.96±0.10	>1.58	0.98±0.07	2.54±0.26[d]
0817+4354	–	–	–	0.73	–	–	2.40±0.19	–
0825+4716	12.25±2.98∗	10.40±1.02∗	0.693∗	0.71	0.52±0.10	1.59±0.27	–	–
0911+0143	2.59±0.44∗	1.54±0.16∗	0.486∗	–	0.63±0.17	–	–	–
0915+2418	10.94±4.92∗	12.95±3.18∗	0.967∗	0.68	0.36±0.12	–	–	–
1113+1244	3.09±0.52∗	8.92±0.67∗	2.360∗	1.15	1.41±0.11	0.45±0.09	–	–
1209−0107	8.75±2.71	3.25±0.21	0.303	0.89	–	–	–	–
1227+5053	2.87±1.00∗	2.26±0.49∗	0.644∗	0.38	–	0.23±0.11	–	-0.23±0.07[c]
1248+0531	2.49±0.32∗	1.93±0.12∗	0.633∗	–	0.26±0.07	–	–	–
1307+2338	0.49±0.11	0.32±0.02	0.525	0.58	0.75±0.09	>1.47	1.46±0.08	1.74±0.10[d]
1309+6042	2.37±0.26∗	1.80±0.09∗	0.622∗	–	0.95±0.13	1.29±0.07	–	–
1313+1453	7.62±0.92∗	4.65±0.17∗	0.499∗	–	1.12±0.15	–	–	–
1434+0935	0.95±0.11∗	3.88±0.13∗	3.350∗	–	1.14±0.10	0.81±0.08	–	–

Table 4.2 (cont'd)

Object name	$M_{\rm BH}$ ($10^8\,M_\odot$)	$L_{\rm bol}$ ($10^{46}\,{\rm erg\,s^{-1}}$)	Eddington ratio	$E(B-V)_{\rm cont}$[a] (mag)	$E(B-V)_{\rm cont}$[b] (mag)	$E(B-V)_{\rm line1}$ (mag)	$E(B-V)_{\rm line2}$ (mag)	$E(B-V)_{\rm BD}$ (mag)
1532+2415	6.12±4.87∗	2.24±1.05∗	0.299∗	0.70	–	>2.11	–	–
1540+4923	11.86±7.13∗	2.73±1.11∗	0.188∗	–	0.97±0.10	–	–	–
1600+3522	1.81±0.49∗	4.26±0.63∗	1.927∗	0.22	–	–	–	–
1656+3821	4.87±0.98∗	4.66±0.53∗	0.783∗	0.61	0.88±0.16	>0.30	–	–
1720+6156	1.31±0.33∗	2.58±0.38∗	1.613∗	–	1.50±0.09	0.57±0.28	–	–
2325−1052	2.71±1.59∗	2.02±0.73∗	0.610∗	0.50	–	0.64±0.21	–	0.56±0.01[d]
2339−0912	5.95±0.95∗	8.03±0.55∗	1.102∗	1.06	1.25±0.06	0.53±0.07	–	–

∗$M_{\rm BH}$, $L_{\rm bol}$ values, and Eddington ratios are adopted from Kim et al. (2015b).

[a]$E(B-V)_{\rm cont}$ values are adopted from Glikman et al. (2007), which uncertainties are not available.

[b]$E(B-V)_{\rm cont}$ values are adopted from Urrutia et al. (2009).

[c]$E(B-V)_{\rm BD}$ values are measured with total line luminosities.

[d]$E(B-V)_{\rm BD}$ values are measured with broad line luminosities.

4.6 Conclusions

So far, several explanations for the red colors of red quasars have been suggested; for example, (i) there is dust in their host galaxy, (ii) these quasars are intrinsically red, (iii) the redness is attributable to high CF_{HD}, and (iv) the red color can be attributed to a moderate viewing angle. In order to investigate the origin of the red colors of red quasars, we used 20 red quasars at $z \sim 0.3$ and 0.7 in this study.

We compared the luminosity ratios from hydrogen Balmer to Paschen lines of red quasars to those of unobscured type 1 quasars adopted from Kim et al. (2010). We find that the line luminosity ratios of red quasars are almost six times higher than those of unobscured type 1 quasars, and the extinction correction based on $E(B-V)$ estimated from the continuum shape can bring the similar mean Pβ/Hβ luminosity ratio to that of unobscured type 1 quasars (albeit with a large scatter). This result suggests that dust extinction is responsible for the red colors of red quasars.

Moreover, we examined if the characteristics of red quasars can be explained by other reasons. We examined whether the unusual line luminosity ratios of red quasars can be explained without the dust extinction effects. We compared the observed line luminosity ratios of red quasars to the theoretically expected line luminosity ratios computed from `CLOUDY` code. However, the observed line luminosity ratios of $\sim 63\,\%$ (5 out of 8) red quasars cannot be explained by any physical conditions of BELRs. We also examined whether red quasars have unusually higher CF_{HD} than unobscured type 1 quasars, but we do not find clear evidence of NIR excess for a given Paschen line luminosity. Finally, using a dust-insensitive diagnostic Pβ line, we find that 19 red quasars – three at $z \sim 0.3$ (new measurements) and 16 at $z \sim 0.7$ (Kim et al. 2015b) – have Eddington ratios that are significantly (~ 5 times) higher than those of unobscured type 1 quasars. This result disfavors the scenario in which the red colors of red quasars are caused by a moderate viewing angle that passes though dust torus.

Our results and previous results from studies of red quasars have found that these quasars have (i) high luminosity ratios from Balmer to Paschen lines, (ii) high BH accretion rates (Kim et al. 2015b), (iii) enhanced star formation activities (Georgakakis et al. 2009), (iv) a high fraction of merging features (Urrutia et al. 2008; Glikman et al. 2015), and (v) young radio jets (Georgakakis et al. 2012). Based on these findings, we conclude that red quasars are dust-extincted quasars in the intermediate stage galaxies between ULIRGs and unobscured type 1 quasars and the dust extinction is caused by the remaining dust in their host galaxies.

Table 4.3. Spectrum of 0036−0113

λ (Å)	f_λ (erg s^{-1} cm^{-2} Å^{-1})	f_λ Uncertainty (erg s^{-1} cm^{-2} Å^{-1})
10900	4.470E-18	2.652E-17
10903	5.215E-17	2.763E-17
10905	4.738E-17	2.575E-17
10908	5.146E-17	2.566E-17
10911	7.565E-17	2.431E-17
10913	6.210E-17	2.379E-17
10916	1.274E-17	2.386E-17
10919	2.437E-17	2.621E-17
10921	8.003E-17	2.719E-17
10924	8.594E-17	2.935E-17

Note. — This table lists only a part of the spectrum of 0036−0113. The entire spectra of two red quasars (0036−0113 and 1307+2338) are available in ascii format from the electronic version of the Journal.

References

Abazajian, K. N., Adelman-McCarthy, J. K., Agüeros, M. A., et al. 2009, ApJS, 182, 543

Anderson, S. F., Voges, W., Margon, B., et al. 2003, AJ, 126, 2209

Assef, R. J., Stern, D., Kochanek, C. S., et al. 2013, ApJ, 772, 2

Banerji, M., McMahon, R. G., Hewett, P. C., et al. 2012, MNRAS, 427, 2275

Barvainis, R. 1987, ApJ, 320, 537

Becker, R. H., White, R. L., & Helfand, D. J. 1995, ApJ, 450, 559

Becker, R. H., White, R. L., Gregg, M. D., et al. 2001, ApJS, 135, 227

Benn, C. R., Vigotti, M., Carballo, R., Gonzalez-Serrano, J. I., & Sánchez, S. F. 1998, MNRAS, 295, 451

Boroson, T. A., & Green, R. F. 1992, ApJS, 80, 109

Brusa, M., Civano, F., Comastri, A., et al. 2010, ApJ, 716, 348

Collin-Souffrin, S., Dumont, S., & Tully, J. 1982, A&A, 106, 362

Croom, S. M., Smith, R. J., Boyle, B. J., et al. 2004, MNRAS, 349, 1397

Cushing, M. C., Vacca, W. D., & Rayner, J. T. 2004, PASP, 116, 362

Cutri, R. M., Nelson, B. O., Kirkpatrick, J. D., Huchra, J. P., & Smith, P. S. 2001,

Dietrich, M., Hamann, F., Shields, J. C., et al. 2002, ApJ, 581, 912

Ferland, G. J., Korista, K. T., Verner, D. A., et al. 1998, PASP, 110, 761

Fitzpatrick, E. L. 1999, PASP, 111, 63

Fynbo, J. P. U., Krogager, J.-K., Venemans, B., et al. 2013, ApJS, 204, 6

Georgakakis, A., Clements, D. L., Bendo, G., et al. 2009, MNRAS, 394, 533

Georgakakis, A., Grossi, M., Afonso, J., & Hopkins, A. M. 2012, MNRAS, 421, 2223

Glikman, E., Helfand, D. J., & White, R. L. 2006, ApJ, 640, 579

Glikman, E., Helfand, D. J., White, R. L., et al. 2007, ApJ, 667, 673

Glikman, E., Urrutia, T., Lacy, M., et al. 2012, ApJ, 757, 51

Glikman, E., Urrutia, T., Lacy, M., et al. 2013, ApJ, 778, 127

Glikman, E., Simmons, B., Mailly, M., et al. 2015, arXiv:1504.02111

Grazian, A., Cristiani, S., D'Odorico, V., Omizzolo, A., & Pizzella, A. 2000, AJ, 119, 2540

Greene, J. E., & Ho, L. C. 2005, ApJ, 630, 122

Hernán-Caballero, A., Hatziminaoglou, E., Alonso-Herrero, A., & Mateos, S. 2016, MNRAS, 463, 2064

Hopkins, P. F., Hernquist, L., Cox, T. J., et al. 2005, ApJ, 630, 705

Hopkins, P. F., Hernquist, L., Cox, T. J., et al. 2006, ApJS, 163, 1

Hopkins, P. F., Hernquist, L., Cox, T. J., & Kereš, D. 2008, ApJS, 175, 356

Im, M., Griffiths, R. E., & Ratnatunga, K. U. 1997, ApJ, 475, 457

Im, M., Lee, I., Cho, Y., et al. 2007, ApJ, 664, 64

Ivezić, Ž., Menou, K., Knapp, G. R., et al. 2002, AJ, 124, 2364

Jun, H. D., Im, M., Lee, H. M., et al. 2015, ApJ, 806, 109

Karouzos, M., Im, M., Kim, J.-W., et al. 2014, ApJ, 797, 26

Kim, M., Ho, L. C., & Im, M. 2006, ApJ, 642, 702

Kim, D., Im, M., & Kim, M. 2010, ApJ, 724, 386

Kim, D., Im, M., Kim, J. H., et al. 2015, ApJS, 216, 17

Kim, D., Im, M., Glikman, E., Woo, J.-H., & Urrutia, T. 2015, ApJ, 812, 66

Kim, Y., Im, M., Jeon, Y., et al. 2015, ApJ, 813, L35

Lacy, M., Storrie-Lombardi, L. J., Sajina, A., et al. 2004, ApJS, 154, 166

Lacy, M., Ridgway, S. E., Gates, E. L., et al. 2013, ApJS, 208, 24

Lee, I., Im, M., Kim, M., et al. 2008, ApJS, 175, 116

Lusso, E., Comastri, A., Simmons, B. D., et al. 2012, MNRAS, 425, 623

Maiolino, R., Shemmer, O., Imanishi, M., et al. 2007, A&A, 468, 979

Markwardt, C. B. 2009, Astronomical Data Analysis Software and Systems XVIII, 411, 251

Menci, N., Cavaliere, A., Fontana, A., et al. 2004, ApJ, 604, 12

Netzer, H. 2013, The Physics and Evolution of Active Galactic Nuclei, by Hagai Netzer, Cambridge, UK: Cambridge University Press, 2013,

Norman, C., Hasinger, G., Giacconi, R., et al. 2002, ApJ, 571, 218

Onori, F., Ricci, F., La Franca, F., et al. 2017, MNRAS, 468, L97

Osterbrock, D. E. 1991, Reports on Progress in Physics, 54, 579

Pâris, I., Petitjean, P., Aubourg, É., et al. 2014, A&A, 563, A54

Puchnarewicz, E. M., & Mason, K. O. 1998, MNRAS, 293, 243

Rayner, J. T., Toomey, D. W., Onaka, P. M., et al. 2003, PASP, 115, 362

Rees, M. J., Netzer, H., & Ferland, G. J. 1989, ApJ, 347, 640

Risaliti, G., & Elvis, M. 2005, ApJ, 629, L17

Rose, M., Tadhunter, C. N., Holt, J., & Rodríguez Zaurín, J. 2013, MNRAS, 432, 2150

Rose, M. 2014, American Astronomical Society Meeting Abstracts #223, 223, #321.03

Ruiz, A., Della Ceca, R., Caccianiga, A., Severgnini, P., & Carrera, F. 2014, The X-ray Universe 2014, 314

Sanders, D. B., Soifer, B. T., Elias, J. H., et al. 1988, ApJ, 325, 74

Sanders, D. B., & Mirabel, I. F. 1996, ARA&A, 34, 749

Schlafly, E. F., & Finkbeiner, D. P. 2011, ApJ, 737, 103

Schneider, D. P., Hall, P. B., Richards, G. T., et al. 2005, AJ, 130, 367

Schneider, P. 2006, Extragalactic Astronomy and Cosmology, by Peter Schneider. Berlin: Springer, 2006.,

Schneider, D. P., Richards, G. T., Hall, P. B., et al. 2010, AJ, 139, 2360

Schultz, G. V., & Wiemer, W. 1975, A&A, 43, 133

Shen, Y., Richards, G. T., Strauss, M. A., et al. 2011, ApJS, 194, 45

Skrutskie, M. F., Cutri, R. M., Stiening, R., et al. 2006, AJ, 131, 1163

Stern, D., Assef, R. J., Benford, D. J., et al. 2012, ApJ, 753, 30

Suh, H., Hasinger, G., Steinhardt, C., Silverman, J. D., & Schramm, M. 2015, ApJ, 815, 129

Urrutia, T., Lacy, M., & Becker, R. H. 2008, ApJ, 674, 80

Urrutia, T., Becker, R. H., White, R. L., et al. 2009, ApJ, 698, 1095

Urrutia, T., Lacy, M., Spoon, H., et al. 2012, ApJ, 757, 125

Urry, C. M., & Padovani, P. 1995, PASP, 107, 803

Vacca, W. D., Cushing, M. C., & Rayner, J. T. 2003, PASP, 115, 389

Véron-Cetty, M.-P., & Véron, P. 2006, A&A, 455, 773

Webster, R. L., Francis, P. J., Petersont, B. A., Drinkwater, M. J., & Masci, F. J. 1995, Nature, 375, 469

Whiting, M. T., Webster, R. L., & Francis, P. J. 2001, MNRAS, 323, 718

Wilkes, B. J., Schmidt, G. D., Cutri, R. M., et al. 2002, ApJ, 564, L65

Woo, J.-H., Yoon, Y., Park, S., Park, D., & Kim, S. C. 2015, ApJ, 801, 38

Wright, E. L., Eisenhardt, P. R. M., Mainzer, A. K., et al. 2010, AJ, 140, 1868

Young, M., Elvis, M., & Risaliti, G. 2008, ApJ, 688, 128-147

Young, M., Elvis, M., & Risaliti, G. 2009, ApJS, 183, 17

Chapter 5

Accretion Rates of Red Quasars from the Hydrogen Pβ line

(This chapter has been published in The Astrophysical Journal[1])

5.1 INTRODUCTION

Most of our understanding of quasars is based on normal type 1 quasars found by X-ray, ultraviolet (UV), optical, and radio surveys (Grazian et al. 2000; Becker et al. 2001; Anderson et al. 2003; Croom et al. 2004; Risaliti & Elvis 2005; Schneider et al. 2005; Véron-Cetty & Véron 2006; Young et al. 2009). Moreover, normal type 1 quasars have been studied by using the luminosities in several wavelengths such as X-ray, UV, optical, and radio. However, several studies have suggested that the UV/optical quasar surveys could miss a large number of quasars because some quasars are obscured by intervening dust in their host galaxy (Webster et al. 1995; Cutri et al. 2002) or by the interstellar medium of our galaxy (Im et al. 2007; Lee

[1]Kim et al. 2015, ApJ, 812, 66

et al. 2008).

These dust-obscured quasars would appear to have red colors, requiring different selection techniques to find them. Many studies have been carried out to search for red quasars (e.g., Webster et al. 1995; Benn et al. 1998; Cutri et al. 2001; Glikman et al. 2007, 2012, 2013; Urrutia et al. 2009; Banerji et al. 2012; Stern et al. 2012; Assef et al. 2013; Fynbo et al. 2013; Lacy et al. 2013). Such studies commonly take advantage of large area near-infrared (NIR) surveys such as the Two Micron All-Sky Survey (2MASS; Skrutskie et al. 2006), the UKIRT Infrared Deep Sky Survey (UKIDSS; Lawrence et al. 2007), the *Spitzer* Wide-area Infrared Extragalactic Survey (SWIRE; Londale et al. 2003), or the *Wide field Infrared Survey Explorer* (*WISE*; Wright et al. 2010). In particular, red quasars are found by selecting for objects with very red colors in the optical through NIR based on 2MASS (Cutri et al. 2001; Glikman et al. 2007, 2012; Urrutia et al. 2009), UKIDSS (Banerji et al. 2012; Fynbo et al. 2013; Glikman et al. 2013), SWIRE (Lacy et al. 2007, 2013), or *WISE* (Stern et al. 2012; Assef et al. 2013). In addition, X-ray surveys have been conducted to uncover dust-obscured quasars (Norman et al. 2002; Anderson et al. 2003; Risaliti & Elvis 2005; Young et al. 2009; Brusa et al. 2010).

Pieces of observational evidence suggest that red quasars are a young population based on their (i) enhanced star formation activities (Georgakakis et al. 2009); (ii) a high fraction of merging features (Urrutia et al. 2008; Glikman et al. 2015); (iii) young radio jets (Georgakakis et al. 2012); and (iv) red continuum from dust extinction, possibly caused by their host galaxies (Glikman et al. 2007; Urrutia et al. 2009). These pieces of observational evidence point to a picture in which red quasars are the intermediate population between the merger-driven star-forming galaxies often seen as ultraluminous infrared galaxies (ULIRGs; Sanders et al. 1988; Sanders & Mirabel 1996) and normal blue quasars (Glikman et al. 2007; Urrutia et al. 2008, 2009; Georgakakis et al. 2009, 2012). In particular, simulations (Menci

et al. 2004; Hopkins et al. 2005, 2006, 2008) have shown that a major merger can trigger intense star formation and buried quasar activity. After that, the quasar grows with a high Eddington ratio but is still red because of remaining dust and gas, and the host galaxy is expected to show merger signatures and star formation activity. Finally, the quasar becomes a normal quasar after sweeping away the gas and dust from the quasar-driven wind. Such a scenario suggests that red quasars are in the intermediate stage between merger-driven star-forming galaxies and normal type 1 quasars.

However, other explanations have been proposed to explain the existence of red quasars. Wilkes et al. (2002) suggested that the red colors of red quasars arise from the viewing angle in the quasar unification scheme when the accretion disk and the broad-line region (BLR) are viewed through a dust torus. Another suggestion is that red quasars have intrinsically red colors, i.e. an unusual covering factor of hot dust, a contamination from host galaxy light, or synchrotron emission that peaks at NIR wavelengths from radio jets (Puchnarewicz & Mason 1998; Whiting et al. 2001; Rose 2014; Ruiz et al. 2014).

One observational test for red quasars as an intermediate population, under the merger-driven galaxy evolution scenario, is to investigate whether red quasars exhibit high accretion rates. In this regard, previous studies (Canalizo et al. 2012; Urrutia et al. 2012; Bongiorno et al. 2014) have shown that red quasars could have higher accretion rates than normal quasars and different scaling relations of $M_{\rm BH}$–$L_{\rm B}$ and $M_{\rm BH}$–M_* compared to those of normal quasars. However, the accretion rates of red quasars are still controversial since most of the black hole (BH) mass and the bolometric luminosity estimators are based on flux measured in the UV or optical (Kaspi et al. 2000; Vestergaard 2002; McLure & Dunlop 2004; Greene & Ho 2005).

A major difficulty in estimating BH masses using UV or optical light is that they are easily affected by dust extinction. For example, if a quasar is reddened

by a color excess of $E(B-V) = 2$ mag, its Hβ and Hα line fluxes are suppressed by factors of 860 and 110, respectively, assuming the Galactic extinction law with $R_V = 3.1$ (Cardelli et al. 1989). Furthermore, estimates of $E(B-V)$ values of red quasars can be quite uncertain, where the difference in $E(B-V)$ estimates can be as large as $\Delta E(B-V) = 1.0 - 2.0$ mag for different methods (Glikman et al. 2007; Urrutia et al. 2012). The amount of extinction can also depend on dust properties such as grain sizes and the temperature of the dust, making it more difficult to make an accurate correction for it. Between color excess values of $E(B-V) = 1$ and 2, the amounts of the extinction in Hβ and Hα line fluxes are different by factors of 30 and 10, respectively.

However, the Paschen and Brackett hydrogen lines in the NIR and mid-infrared (MIR) mitigate the disadvantages of the UV/optical measurements. In the case of $E(B-V) = 2$ mag, Pβ, Pα, Brβ, and Brα line fluxes would be suppressed by factors of 3.97, 2.16, 1.62, and 1.31, respectively, which are much less than those for the Hβ and the Hα lines. Consequently, the uncertainties of the NIR flux estimates due to $E(B-V)$ errors are significantly reduced. For these reasons, several NIR BH mass estimators are established by using Paschen (Kim et al. 2010; Landt et al. 2013) and Brackett series lines (Kim et al. 2015).

In this paper, we estimate $M_{\rm BH}$ and $L_{\rm bol}$ values for 16 red quasars at $z \sim 0.7$. The $M_{\rm BH}$ and the $L_{\rm bol}$ values are estimated with Pβ (1.28 μm) line properties (Kim et al. 2010), and we compare the accretion rates of the red quasars to those of normal type 1 quasars, showing that accretion rates are much higher for red quasars. Throughout this paper, we use a standard ΛCDM cosmological model of H_0=70 km s^{-1} Mpc^{-1}, Ω_m=0.3, and Ω_Λ=0.7 (e.g., Im et al. 1997).

5.2 SAMPLE AND OBSERVATION

5.2.1 The Sample

Our sample is drawn from red quasars listed in previous studies (Glikman et al. 2007; Urrutia et al. 2009). The previous studies selected red quasar candidates by using a combination of red colors in the optical through NIR (e.g., $R-K > 4$ and $J-K > 1.7$ in Glikman et al. 2007; $r' - K > 5$ and $J - K > 1.3$ in Urrutia et al. 2009) and FIRST (Becker et al. 1995) radio detection. Then, they confirmed red quasars with spectroscopic follow-up. The previous studies found ∼80 red quasars, whose redshifts ranged from 0.186 to 3.050. These red quasars are very luminous (-31.61< M_i <-23.19; e.g., Urrutia et al. 2009) and obscured by dust (0.186≤ $E(B-V) \leq 3.05$), and they show strong evidence of ongoing interaction (Urrutia et al. 2008; Glikman et al. 2015). Moreover, their spectra are well-fitted by normal type 1 quasar spectrum with a dust reddening law.

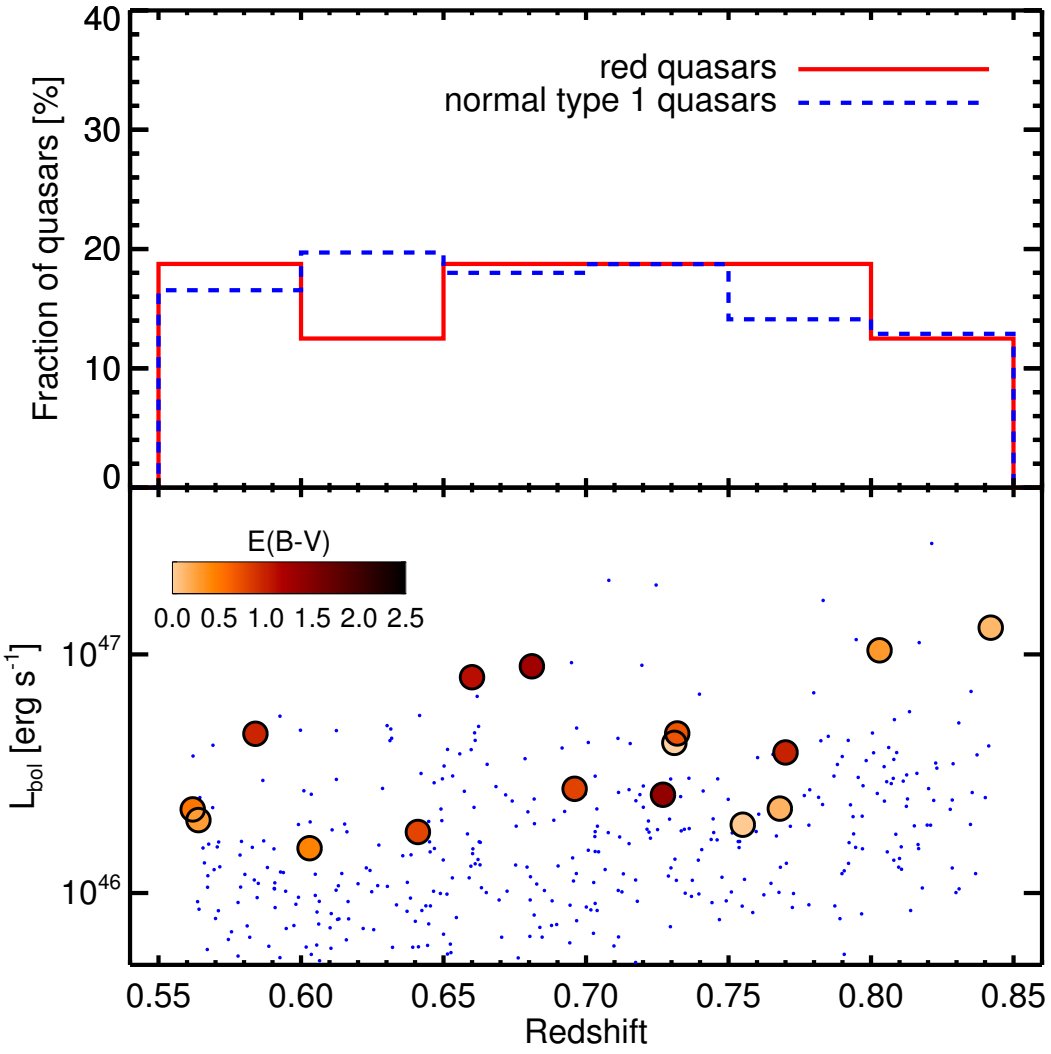

Figure 5.1 Top: redshift distributions of red quasars and normal type 1 quasars normalized by the sample size. The red solid and the blue dashed histograms represent the red quasars and normal type 1 quasars, respectively. Bottom: $L_{\rm bol}$ vs. redshift for red quasars and normal type 1 quasars. The circles and the blue dots represent red quasars and normal type 1 quasars, respectively, and the colors in the circles indicate their dust reddening values as shown in the legend. The $L_{\rm bol}$ values of the red quasars come from Pβ luminosities, and L3000 and L5100 are used for the $L_{\rm bol}$ values of the normal type 1 quasars.

Among the red quasars, we select 20 red quasars at $z \sim 0.7$ (from 0.56 to 0.84) for our study where the redshifted Pβ line is observable in the sky window at the K-band. Moreover, our sample is bright (K <15.5 mag) and has a wide range of luminosities (-31.78< M_K <-26.90 mag).

In order to compare the accretion rates of the red quasars to those of normal type 1 quasars, we select type 1 quasars from the quasar catalog (Schneider et al. 2010) of the Sloan Digital Sky Survey (SDSS) Seventh Data Release (DR7; Abazajian et al. 2009). The catalog contains 105,783 spectroscopically confirmed quasars with wide ranges of redshifts from 0.065 to 5.4, and r' band magnitudes of 15.2< r' <22.9. In order to avoid sample bias effects, we choose quasars with the same selection criteria as the red quasars except for the red colors: (i) the same redshift range of 0.56≤ z ≤0.84; (ii) FIRST radio detection; and (iii) detection in the J-, H-, and K-bands from 2MASS. In the end, 410 SDSS quasars are found and used as the control sample. Figure 1 shows the redshift distribution and the bolometric luminosity (see Section 4.2) vs. redshift of these 16 red quasars and 410 normal type 1 quasars. Note that the red quasars have a bolometric luminosity in the range of $\sim 10^{46}$–10^{47} erg s^{-1}.

Table 5.1. Object List

Objects	Redshift (z)	$E(B-V)$	K (mag)	$r'-K$ (mag)	$J-K$ (mag)
0825+4716	0.803	0.52	14.11	6.42	2.98
0911+0143	0.603	0.63	14.87	6.28	1.59
0915+2418	0.842	0.36	13.79	6.47	2.74
1113+1244	0.681	1.41	13.67	6.06	2.47
1227+5053	0.768	0.38	14.61	4.16[a]	1.71
1248+0531	0.740	0.26	14.63	6.06	3.45
1309+6042	0.641	0.95	14.80	6.77	3.09
1313+1453	0.584	1.12	14.48	5.65	2.30
1434+0935	0.770	1.14	14.90	6.19	2.10
1532+2415	0.562	0.70	14.96	5.13[a]	1.87
1540+4923	0.696	0.97	15.18	5.31	2.28
1600+3522	0.707	0.22	14.17	4.42[a]	2.24
1656+3821	0.732	0.88	15.09	6.91	2.26
1720+6156	0.727	1.50	15.20	6.44	1.95
2325−1052	0.564	0.50	15.24	4.46[a]	2.14
2339−0912	0.660	1.25	14.09	5.16	1.63

Note. — a: $R-K$ mags from Glikman et al. (2007)

5.2.2 Observations

NIR spectra of the 20 red quasars were obtained using the SpeX instrument (Rayner et al. 2003) on the NASA Infrared Telescope Facility (IRTF). Descriptions of the observations of 11 of the 20 red quasars are given in Glikman et al. (2007, 2012). Additionally, we obtained IRTF NIR spectra for the remaining nine sources. In the observation, we used the short cross-dispersion mode (SXD: 0.8–2.5 μm), whose spectral wavelength range includes redshifted Pβ lines. We performed observation with a $0\farcs8$ slit width to achieve a resolution of R ∼750 (400 km s^{-1} in FWHM), which is sufficient for the measurement of the width of broad emission line. Note that this observational setup is nearly identical to that of Glikman et al. (2007, 2012).

For telluric correction, we obtained the spectrum of an A0V star after the observation of each target. The A0V stars were chosen to be near the red quasar (Δairmass < 0.1 and separation $< 15°$). We use the Spextool (Vacca et al. 2003; Cushing et al. 2004) package to produce fully reduced spectra.

Our observations were performed under clear weather conditions and with a sub-arcsecond seeing of ∼$0\farcs7$, and we detect Pβ emission line for five red quasars (0911+0143, 1248+0531, 1309+6042, 1313+1453, and 1434+0935) with a signal-to-noise ratio (S/N) of > 5. We do not detect Pβ line in the remaining four red quasars due to the low S/N of our data (1106+2812, 1159+2914, 1415+0903, and 1523+0030), and they are excluded in the following analysis. In total, we use 16 red quasars at $z \sim 0.7$ (from 0.56 to 0.84) among 20 quasars for which we got IRTF spectra. Table 1 summarizes the basic information of these 16 red quasars.

5.3 ANALYSIS

We shift the fully reduced spectra to the rest frame, and correct the spectrum by adopting $E(B-V)$ values from previous studies (Glikman et al. 2007; Urrutia et al. 2009) in the rest frame for each object. The $E(B-V)$ values were determined by comparing the spectra of the red quasars to the composite spectrum of quasars from the FIRST Bright Quasar Survey (Brotherton et al. 2001) combined with a NIR quasar composite (Glikman et al. 2006). For the reddening law, these studies used the relation from Fitzpatrick (1999) based on an average Galactic extinction curve from the IR through the UV with the conditions of $R_V = 3.1$ and the elimination of a 2175 Å bump, which makes it similar to the Small Magellanic Cloud extinction curve. Although Glikman et al. (2007) provides the $E(B-V)$ values by using the Balmer decrement method for two targets, we use the $E(B-V)$ values by continuum fit because that the continuum based values are available for all of the objects.

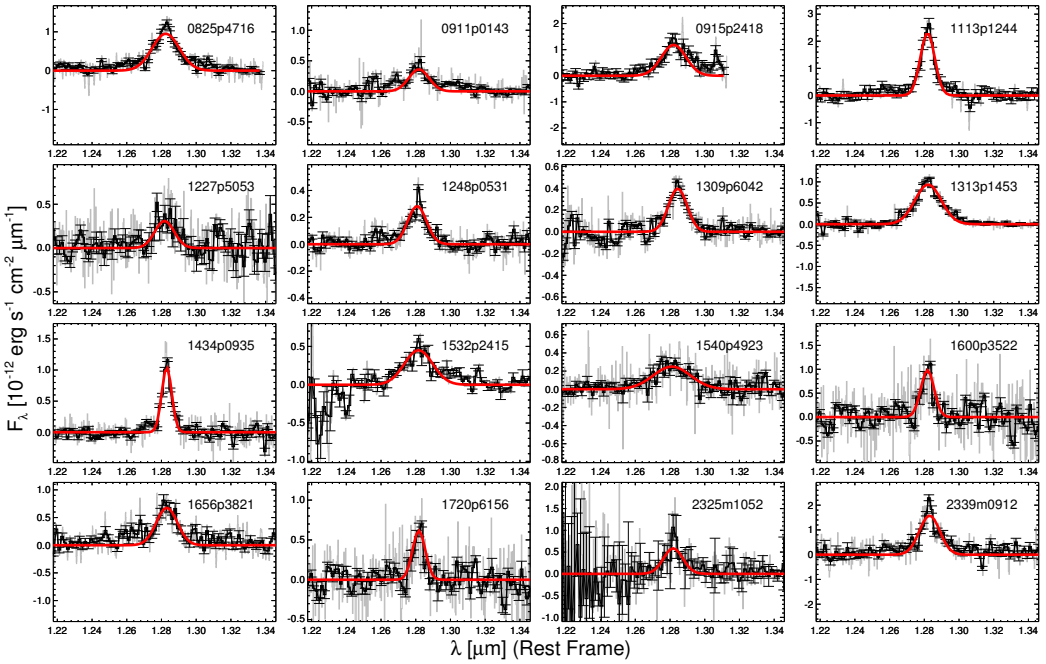

Figure 5.2 Results of the fitting of Pβ lines with a Gaussian function. The continuum is already subtracted. The gray lines indicate observed spectra in the rest frame, and the black lines and the bars indicate binned spectra with a spectral resolution of $R \sim 750$ and associated errors. The red solid lines represent the best-fit model.

After that, we determine the continuum around the Pβ line to estimate the Pβ line full width half maximum (FWHM) and luminosity. The continuum-fitting regions are chosen as 1.21–1.25 μm and 1.31–1.35 μm, with a width of 0.4 μm. The continuum-fitting regions are 0.03 μm away from the Pβ line, where the width of 0.03 μm corresponds to $\sim$7000 km s^{-1}, which is similar to 2$\times$FWHM of a broad-line of a typical type 1 quasar. We fit the continuum with a linear function because the NIR spectrum around Pβ line can be approximated with a power-law component over a limited wavelength range (Glikman et al. 2006; Kim et al. 2010, 2015).

After the continuum subtraction, we fit the Pβ emission line with a single Gaussian function. An IDL procedure, `MPFITEXPR` (Markwardt 2009) code was used to fit the line. For the fit, we set free the central wavelength, integrated flux, and FWHM of the Gaussian component. The fit provides the FWHM and the integrated flux of the Pβ line, and the measured FWHM values were corrected for the dispersion in the wavelength due to the spectral resolution of the instrument through an equation of FHWM $= \sqrt{\mathrm{FWHM_{obs}}^2 - \mathrm{FWHM_{inst}}^2}$ where $\mathrm{FWHM_{inst}} = 400\,\mathrm{km\,s^{-1}}$. The single component fitting can introduce a small systemic bias in the derived values of FWHM and line luminosities. To correct for this bias, we adopted the correction factors of $\mathrm{FWHM_{multi}/FWHM_{single}}$=0.91 and $L_{\mathrm{multi}}/L_{\mathrm{single}}$=1.06, which are derived from higher-resolution Balmer line profiles of other normal type 1 active galactic nuclei (AGNs; Kim et al. 2010; see also the discussion in Kim et al. 2015).

The formal fitting uncertainties are found to be 4.7 % (from 1.0 % to 24.6 %) and 6.9 % (from 1.3 % to 34.7 %) for the FWHM and the flux, respectively. Several high ($>$ 10 %) formal fitting uncertainties are due to the fact that the observed Pβ line is located at the edge of the spectral window of SpeX (for 0915+2418), or the spectrum has a low S/N (for 1227+5053 and 2325$-$1052). An additional uncertainty is considered since the values of the fitted parameter vary with how we define the continuum level. We varied the wavelength regions in the vicinity of the Pβ line for

the continuum fit, and we find that the variation of the continuum level yields to a change of 6.0 % (from 0.9 % to 36.9 %) in the FWHM values and 6.9 % (from 0.9 % to 43.9 %) in the flux values. Overall, we combined these two uncertainties in the quadrature ($\sigma^2_{\rm tot} = \sigma^2_{\rm a} + \sigma^2_{\rm b}$). The combined uncertainties of the FWHM and the flux are 10.0 % (from 2.4 % to 38.0 %) and 10.6 % (from 3.1 % to 45.5 %), respectively, which corresponds to 0.10 dex in $M_{\rm BH}$ value.

5.4 BH Masses and Bolometric Luminosities

5.4.1 BH Masses

For estimating virial masses of red quasars, we adopted the Pβ scaling relation (Kim et al. 2010) after adjusting the relation to have a recent virial coefficient of $\log f = 0.05$ (Woo et al. 2015). The modified relation is

$$\frac{M_{\rm BH}}{M_\odot} = 10^{7.04\pm0.02} \left(\frac{L_{\rm P\beta}}{10^{42}\,{\rm erg\,s^{-1}}}\right)^{0.48\pm0.03} \left(\frac{\rm FWHM_{P\beta}}{10^3\,{\rm km\,s^{-1}}}\right)^2. \quad (5.1)$$

In this scaling relation, the luminosity and the FWHM of the Pβ line represent the radius and the velocity of the BLR. The measured $M_{\rm BH}$ values of the red quasars are listed in Table 2.

For the BH masses of normal type 1 quasars, we use optical or UV spectral properties from Shen et al. (2011) and use the $M_{\rm BH}$ estimators of McLure & Dunlop (2004). Note that we modified their formula so that it gives $\log f = 0.05$ by multiplying by a factor of 1.122. First, we use $\lambda L_{5100\mathring{\rm A}}$ (L5100, hereafter) and FWHM of the Hβ line with the equation of

$$\frac{M_{\rm BH}}{M_\odot} = 5.27 \left(\frac{\rm L5100}{10^{44}\,{\rm erg\,s^{-1}}}\right)^{0.61} \left(\frac{\rm FWHM_{H\beta}}{\rm km\,s^{-1}}\right)^2. \quad (5.2)$$

We use this $M_{\rm BH}$ estimator for 406 normal type 1 quasars with the values of L5100 and FWHM$_{\rm H\beta}$ from Shen et al. (2011). For the remaining four normal type 1

quasars with no Hβ detection, we adopt Mg II and $\lambda L_{3000\mathring{A}}$ (L3000) instead as

$$\frac{M_{\rm BH}}{M_\odot} = 3.59 \left(\frac{\rm L3000}{10^{44}\,{\rm erg\,s^{-1}}} \right)^{0.62} \left(\frac{\rm FWHM_{MgII}}{\rm km\,s^{-1}} \right)^2. \quad (5.3)$$

5.4.2 Bolometric Luminosities

To obtain bolometric luminosities of red quasars, we use several relations between the line luminosity, the continuum luminosity, and the bolometric luminosity. We bootstrap the relations between $L_{\rm P\beta}$ and $L_{\rm H\alpha}$ (Kim et al. 2010), $L_{\rm H\alpha}$ and L5100 (Jun et al. 2015), and L5100 and $L_{\rm bol}$ (Shen et al. 2011) to relate $L_{\rm P\beta}$ to $L_{\rm bol}$. The combined relationship is

$$\log(\frac{L_{\rm bol}}{10^{44}\,{\rm erg\,s^{-1}}}) = 1.29 + 0.969\ \log(\frac{L_{\rm P\beta}}{10^{42}\,{\rm erg\,s^{-1}}}). \quad (5.4)$$

The measured $L_{\rm bol}$ values of the red quasars are listed in Table 2.

For the normal type 1 quasars for which BH masses are estimated by a Hβ BH mass estimator, we convert L5100 to the bolometric luminosity with a bolometric correction factor of 9.26 (Shen et al. 2011) for L5100. We also measure the bolometric luminosities of four normal type 1 quasars without Hβ detection from L3000 with a bolometric correction factor of 5.15 (Shen et al. 2011).

Table 5.2. Pβ parameters, BH masses, and Eddington ratios

Objects	FWHM$_{P\beta}$ (km s^{-1})	log($L_{P\beta}$) (erg s^{-1})	M_{BH} ($10^8\,M_\odot$)	L_{bol} (10^{46} erg s^{-1})	Eddington Ratio	$\dot{M}$ ($M_\odot$ year^{-1})	τ (10^7 years)
0825+4716	3940±393	43.78±0.04	12.25±2.98	10.40±1.02	0.693	18.45	6.64
0911+0143	2907±206	42.93±0.04	2.59±0.44	1.54±0.16	0.486	2.73	9.48
0915+2418	3527±729	43.88±0.09	10.94±4.92	12.95±3.18	0.967	22.96	4.76
1113+1244	2054±107	43.71±0.03	3.09±0.52	8.92±0.67	2.360	15.82	1.95
1227+5053	2781±446	43.10±0.08	2.87±1.00	2.26±0.49	0.644	4.01	7.16
1248+0531	2697±123	43.03±0.02	2.49±0.32	1.93±0.12	0.633	3.43	7.27
1309+6042	2673±89	43.00±0.02	2.37±0.26	1.80±0.09	0.622	3.20	7.40
1313+1453	3793±96	43.42±0.01	7.62±0.92	4.65±0.17	0.499	8.25	9.24
1434+0935	1398±34	43.34±0.01	0.95±0.11	3.88±0.13	3.350	6.89	1.37
1532+2415	4071±1549	43.09±0.16	6.12±4.87	2.24±1.05	0.299	3.98	15.39
1540+4923	5397±1518	43.18±0.14	11.86±7.13	2.73±1.11	0.188	4.85	24.46
1600+3522	1887±228	43.38±0.06	1.81±0.49	4.26±0.63	1.927	7.55	2.39
1656+3821	3028±246	43.42±0.04	4.87±0.98	4.66±0.53	0.783	8.27	5.88
1720+6156	1818±205	43.16±0.06	1.31±0.33	2.58±0.38	1.613	4.58	2.86
2325−1052	2778±772	43.05±0.13	2.71±1.59	2.02±0.73	0.610	3.58	7.55
2339−0912	2927±140	43.67±0.03	5.95±0.95	8.03±0.55	1.102	14.23	4.18

5.4.3 Comparison of the $L_{\rm bol}$ and the $M_{\rm BH}$ from Different Estimators

Five of the red quasars in our sample overlap with the thirteen red quasars studied by Urrutia et al. (2012). We are thus able to compare the $L_{\rm bol}$ and the $M_{\rm BH}$ values of these five red quasars (0825+4716, 0915+2418, 1113+1244, 1532+2415, and 1656+3821) from our method versus the method adopted by Urrutia et al. (2012). Urrutia et al. (2012) obtained $L_{\rm bol}$ by applying a bolometric correction to their monochromatic luminosity at 15 μm (L15, hereafter), and derived $M_{\rm BH}$ values using L15 as a proxy for $R_{\rm BLR}$ and FWHM of broad emission lines (either Balmer or Paschen lines depending on the availability). For comparison, the $M_{\rm BH}$ values of Urrutia et al. (2012) are rescaled to match the virial factor adopted in this paper. Figure 3 shows a comparison of $L_{\rm bol}$ and $M_{\rm BH}$, which show a reasonable agreement between two independent estimates, except for one outlier (1532+2415, a red circle in Figure 3). The Pearson correlation coefficients are 0.863 and 0.370 for the $L_{\rm bol}$ and the $M_{\rm BH}$, respectively, but the Pearson correlation coefficient for $M_{\rm BH}$ values increases to 0.683 if we exclude the outlier. We note that the outlier has the largest uncertainty of the Pβ line properties among the 16 red quasars used in this study, with the fractional errors of the FWHM and the flux as 38 % and 45.5 %, respectively.

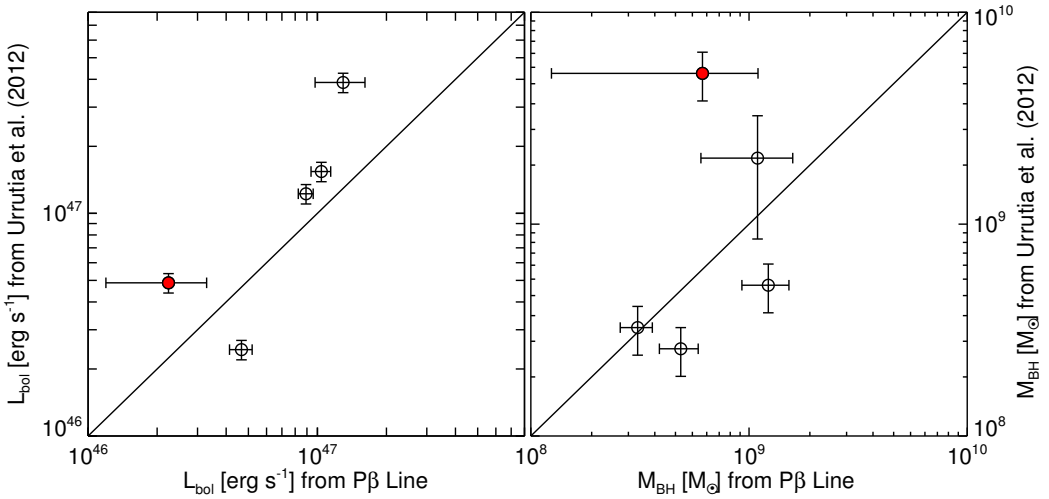

Figure 5.3 (Left): comparison of $L_{\rm bol}$ values derived from Pβ (this work) vs. $L_{\rm bol}$ values derived from L15 (Urrutia et al. 2012). The black solid line indicates the case where the $L_{\rm bol}$ values from the two methods are identical. The outlier (1532+2415, red circle) has the largest uncertainties of the FWHM and the luminosity among Pβ-based measurements. (Right): comparison of $M_{\rm BH}$ values derived from Pβ (this work) vs. $M_{\rm BH}$ values derived from L15 and FWHM of broad emission lines (Urrutia et al. 2012). The meaning of the lines and the red circle are identical to the left panel. The $L_{\rm bol}$ and $M_{\rm BH}$ values agree to within 0.31 dex and 0.48 dex, respectively.

The rms scatters (including measurement uncertainties) of the $L_{\rm bol}$ and the $M_{\rm BH}$ values with respect to the one-to-one correlations are 0.306 dex and 0.479 dex, respectively. In order to derive the intrinsic scatters by removing the contribution from measurement uncertainties, we performed a Monte-Carlo simulation 10000 times by assuming that the $L_{\rm bol}$ and the $M_{\rm BH}$ values from Urrutia et al. (2012) are identical to those from Pβ measurements and adding measurement uncertainties randomly. The median values of the scatters from this simulation are taken to be the contribution to the rms scatter due to measurement uncertainties, and they are subtracted from the original rms scatters in quadrature to obtain intrinsic scatter. Through this process, we find that the intrinsic scatters in the correlations are 0.294 dex and 0.446 dex, respectively, suggesting that the scatters in the two quantities are not due to measurement errors.

In Figure 4, we compare the Eddington ratios from Pβ to those from Urrutia et al. (2012). The comparison shows a reasonable agreement between two values with an rms scatter of 0.514 with respect to the one-to-one correlation. However, if the outlier is excluded, the Eddington ratios from Urrutia et al. (2012) are a bit larger than those from Pβ by a factor of 1.85 (0.267 dex).

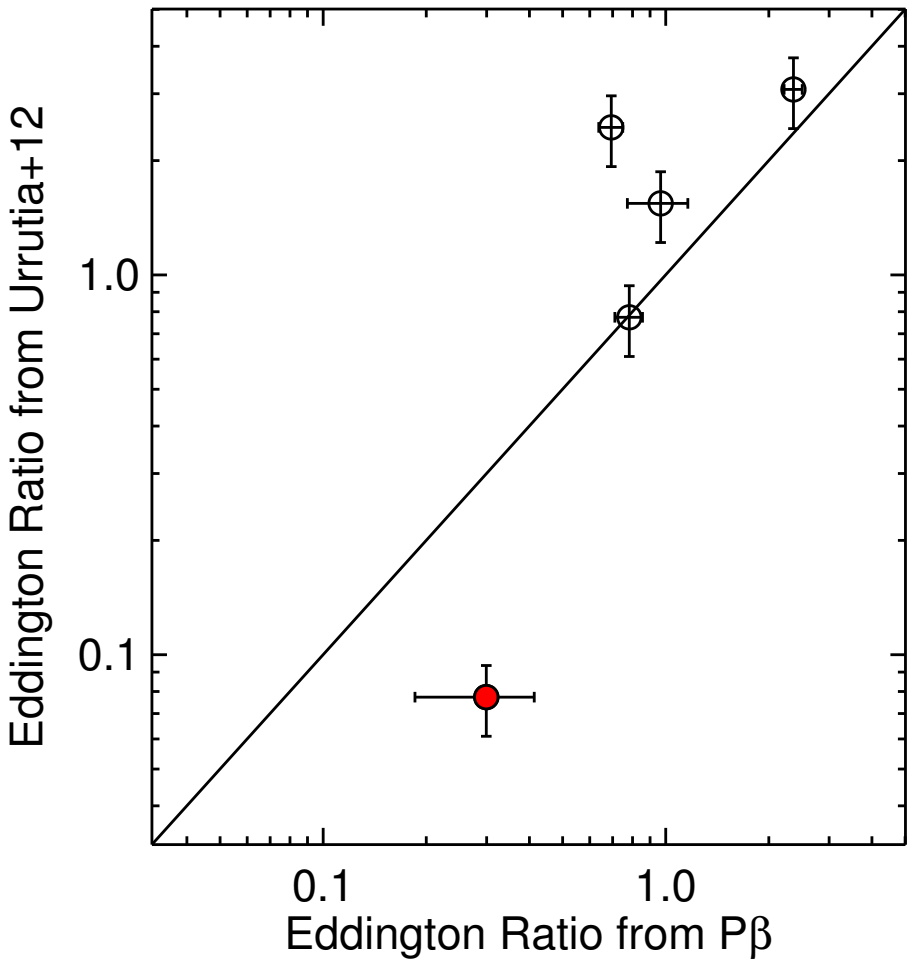

Figure 5.4 Comparison of the Eddington ratios from Urrutia et al. (2012) and those from Pβ. The black solid line indicates the case where the Eddington ratios are identical, and the meaning of the red circle is identical to Figure 3. If the outlier is excluded, the Eddington ratios from Urrutia et al. (2012) are a bit larger than those from Pβ.

5.5 DISCUSSION

5.5.1 Accretion Rates of Red Quasars

In order to characterize the accretion rates of red quasars, we compare the distribution of the Eddington ratios ($L_{\rm bol}/L_{\rm Edd}$, where $L_{\rm Edd}$ denotes the Eddington luminosity) of red quasars and those of normal type 1 quasars. The median Eddington ratios of the red quasars and the normal type 1 quasars are 0.69 and 0.16, respectively. Moreover, Figure 6 shows that the distributions of the Eddington ratios of the red quasars and the normal type 1 quasars are clearly different, with the red quasars having larger $L_{\rm bol}/L_{\rm Edd}$ values than the normal type 1 quasars. In order to quantify how significantly these two distributions differ from each other, we perform the Kolmogorov-Smirnov test (K–S test). For the K–S statistics, the maximum deviation between the cumulative distributions of these two Eddington ratios, D, is 0.71, and the probability of the null hypothesis in which $L_{\rm bol}/L_{\rm Edd}$ values of the two samples are drawn from the same distribution, p, is only 9.07×10^{-8}, confirming that the Eddington ratios of the red quasars are clearly skewed toward higher values in comparison to those of the normal type 1 quasars.

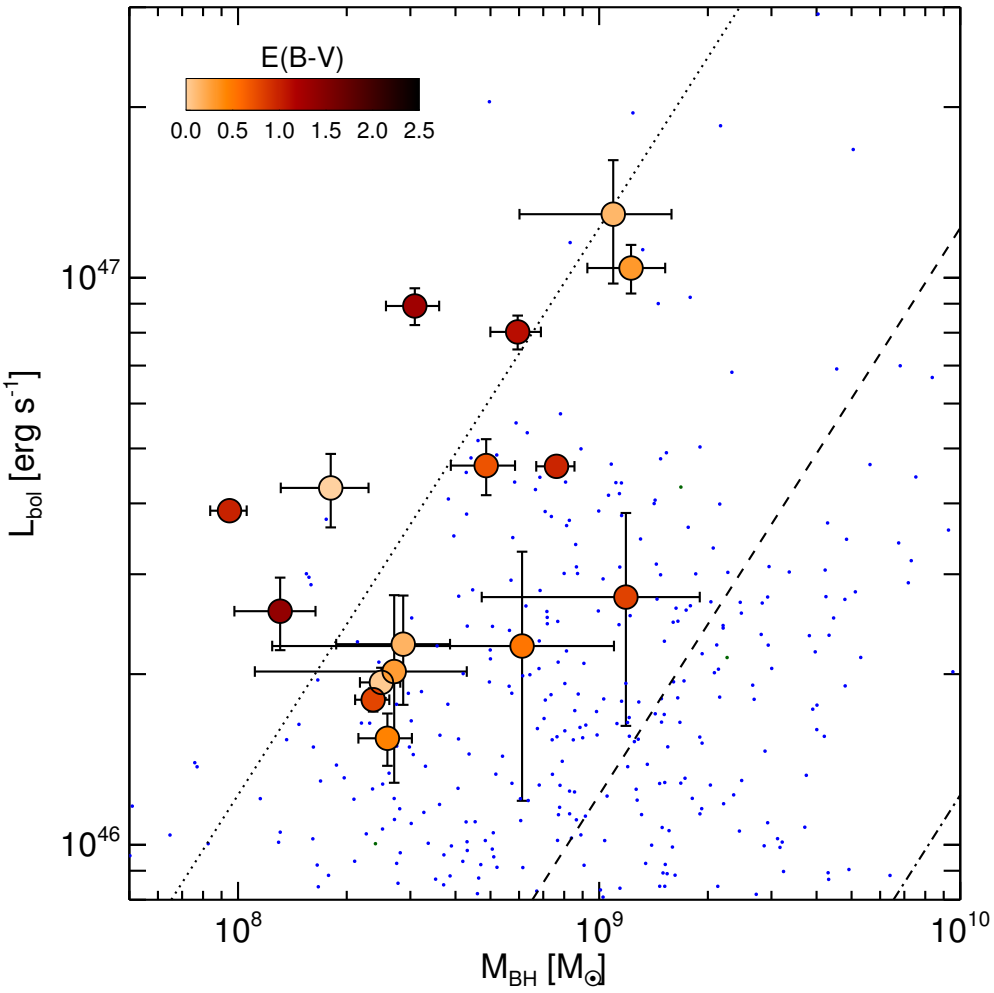

Figure 5.5 The $L_{\rm bol}$ versus $M_{\rm BH}$ of red quasars and normal type 1 quasars. The red quasars are shown with open circles, and the colors in the circles represent their dust reddening values. The blue dots indicate the $L_{\rm bol}$ and the $M_{\rm BH}$ values of normal type 1 quasars. The dotted, dashed, and dash-dotted lines indicate Eddington ratios of 1.0, 0.1, and 0.01, respectively.

Because Eddington ratios can vary with BH mass, we also show the Eddington ratio distribution of the sample divided into BH mass bins to account for any difference in the Eddington ratio distribution arising from the BH mass effect (e.g., Shen et al. 2011). We divided the red quasars and the normal type 1 quasars into a low-mass ($7.9 < \log(M_{\rm BH}/M_{\odot}) < 8.5$) and a high-mass ($8.5 < \log(M_{\rm BH}/M_{\odot}) < 9.1$) sample. For the low-mass sample, 9 red quasars and 67 normal type 1 quasars are selected, and their $\log(L_{\rm bol}/{\rm erg\,s^{-1}})$ values have ranges of 46.19–46.95 and 45.36–46.57 for the red quasars and the normal type 1 quasars, respectively. The D and the p values from a K–S test for these samples are 0.64 and 0.0015, respectively. The high-mass sample includes 7 red quasars and 177 normal type 1 quasars. The $\log(L_{\rm bol}/{\rm erg\,s^{-1}})$ values have ranges of 46.35–47.11 and 45.44–47.31 for the red quasars and the normal type 1 quasars, respectively. The D value is 0.61, and the p is 0.0074 between these two distributions. Again, we find that the Eddington ratio distribution of red quasars is significantly different from that of normal type 1 quasars, independent of the BH mass. The Eddington ratio values of red quasars are about 0.6–0.8 dex larger than those of normal type 1 quasars.

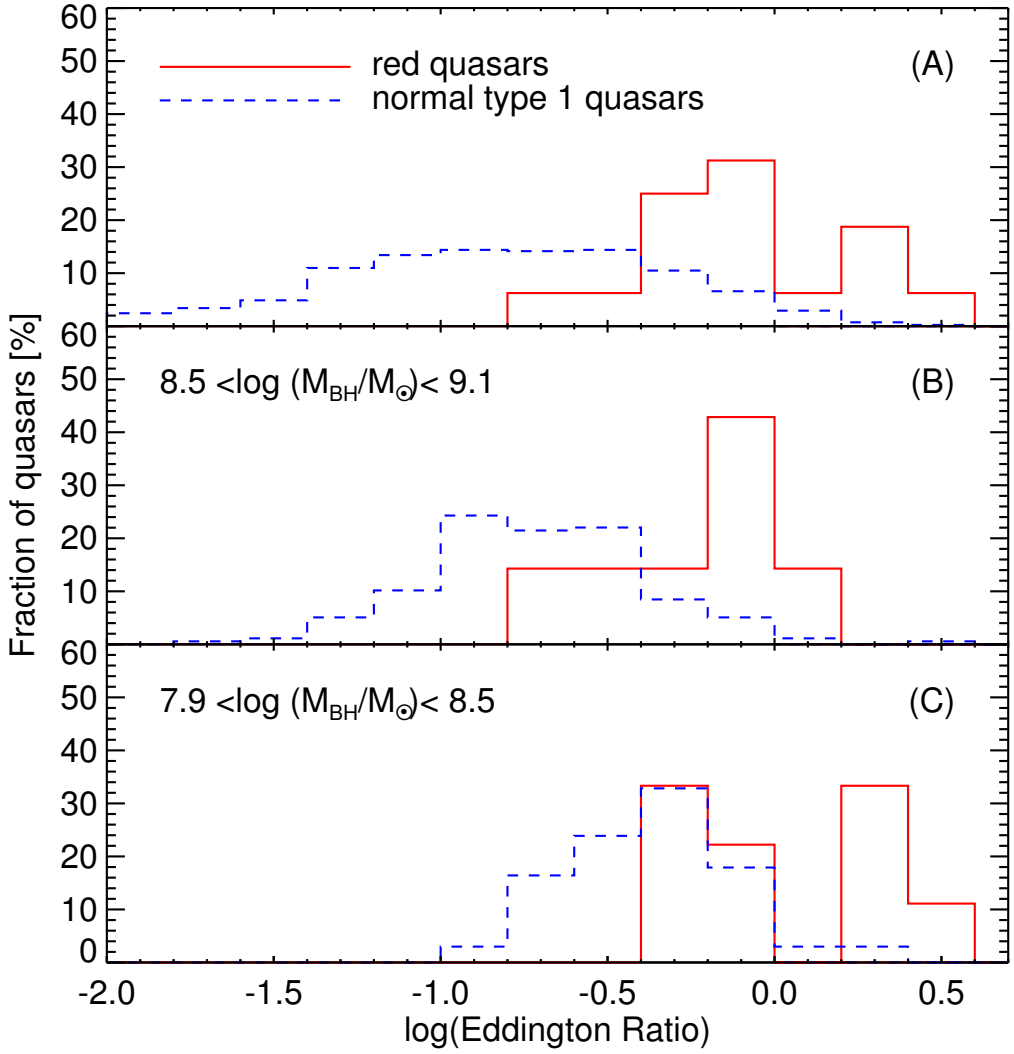

Figure 5.6 (A): distributions of the Eddington ratios of red quasars and normal type 1 quasars. The red solid and the blue dashed histograms represent the red quasars and normal type 1 quasars, respectively. (B): distributions of the Eddington ratios for the high BH mass sample ($10^{8.5} < M_{\rm BH}/M_{\odot} < 10^{9.1}$). (C): distributions of the Eddington ratios for the low BH mass sample ($10^{7.9} < M_{\rm BH}/M_{\odot} < 10^{8.5}$).

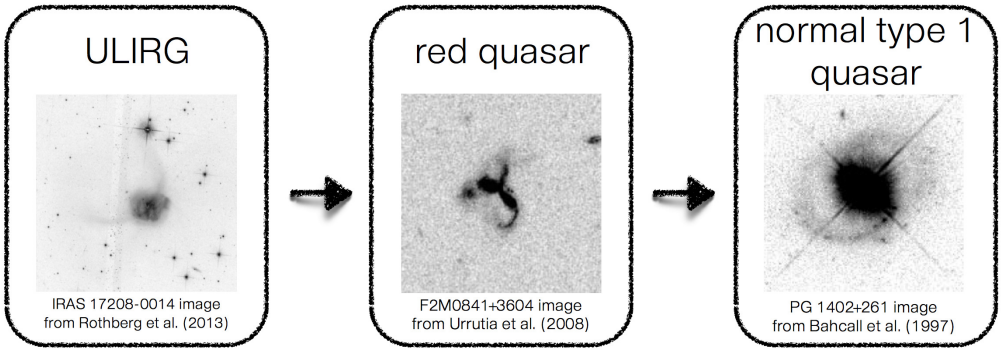

Figure 5.7 Schematic outline of the galaxy evolution scenario from ULIRG to normal type 1 quasars. Image credits belong to Rothberg et al. (2013), Urrutia et al. (2008), and Bahcall et al. (1997).

There are three potential biases that could affect the result–(i) the uncertainty in $E(B-V)$, (ii) the application of the $M_{\rm BH}$ estimator that is derived from normal type 1 quasars, and (iii) the omission of four red quasars without Pβ detection in the analysis. We discuss below how much each item could affect the result.

First, the Eddington ratios of the red quasars could be overestimated or underestimated, since the $E(B-V)$ values (Glikman et al. 2007; Urrutia et al. 2012) of the red quasars can vary by as much as ~ 0.5, depending on how they are derived. For example, for the case of 1227+5053 of which $E(B-V)$ value is 0.38 (continuum-derived) or -0.23 (Balmer decrement-derived)[2], the extinction-corrected Pβ luminosity can be over/underestimated by a factor of 1.6 depending on the method for estimating the $E(B-V)$ value. If we adopt an $E(B-V)$ value of -0.23 from the Balmer decrement, the Eddington ratio of 1227+5053 would decrease from 2.87 to 2.26. Note that this is a rather extreme case. Even if we decrease the Eddington ratios of all of 16 red quasars by a factor of 1.6, the median Eddington ratios of red quasars is 0.55, which is still significantly higher than that of normal type 1 quasars of 0.16. Therefore, the uncertainty in the reddening correction does not affect the result about the Eddington ratios of red quasars, and this demonstrates the power of using the NIR emission line in dusty systems, as outlined also in the introduction.

Second, the Pβ $M_{\rm BH}$ estimator that is derived from normal type 1 quasars may not be applicable to red quasars if the BLR physics of red quasars is very different from that of normal type 1 quasars to the extent that the virial $M_{\rm BH}$ estimator does not hold for red quasars. This is an open question, but we note that our red quasars are moderately obscured quasars for which the BLR is expected to be well-established. Therefore, the characteristics of the BLR physics of red quasars should be very similar to those of normal type 1 quasars.

Third, we omitted four red quasars from our analysis (1106+2812, 1159+2914, 1415+0903, and 1523+0030) because their Pβ lines were not detected with S/N >5, and this may bias the result. Among the four red quasars, we estimated L5100

[2]**Although the $E(B-V)$ value based on the Balmer decrement, -0.23, is unphysical, the negative $E(B-V)$ value is due to the line flux measurement uncertainty, related to the low S/N of the spectrum.**

and $\mathrm{FWHM}_{\mathrm{H}\beta}$ values for 1106+2812, 1415+0903, and 1523+0030 using the optical spectra from Glikman et al. (2006, 2012) and NIR spectra from our IRTF data, but we could not estimate the $\mathrm{FWHM}_{\mathrm{H}\beta}$ for 1159+2914 due to low-quality data (S/N <3). From L5100 and $\mathrm{FWHM}_{\mathrm{H}\beta}$, we computed L_{bol} and M_{BH} values and the Eddington ratios, and we found that the Eddington ratios of 1106+2812, 1415+0903, and 1523+0030 are 0.477, 0.186, and 0.266, respectively. If the Eddington ratios of the three red quasars are included in the Eddington ratio comparison, the D and p values from the K–S test are 0.63 and 4.34×10^{-7}, respectively, which are nearly identical to the result without the three red quasars.

We conclude that red quasars have high accretion rates, with $L_{\mathrm{bol}}/L_{\mathrm{Edd}} \simeq 0.69$. This Eddington ratio is higher than normal type 1 quasars by a factor of 4–5. These results, although limited by the modest size of the sample used in this study, are consistent with the scenario that red quasars are in the intermediate stage between merger-driven star-forming galaxies and the normal type 1 quasars, rather than a scenario in which the red colors of red quasars originate from a viewing angle difference in an AGN unification scheme. Under the merger-driven quasar evolutionary scenario as depicted in Figure 7, the early phase of major mergers drives gas toward the central region of the galaxy due to the loss of the gas' angular momentum through a dissipative, violent merging. This process can fuel the BH activities and a rapid BH growth inside a dust-enshrouded host galaxy (Hopkins et al. 2005, 2008). Such a merger-driven quasar evolutionary scenario also has observational support, especially for luminous quasars (e.g., Hong et al. 2015).

5.5.2 Duration of Red Quasar Phase

The duration period of quasar activity is uncertain, with a wide range of possible values of 10^6–10^8 years (Martini 2004). Quasars shine at the bolometric luminosity of $L_{\mathrm{bol}} = \epsilon \dot{M} c^2$, where ϵ is the radiation efficiency that has a value of $\epsilon \simeq 0.1$ for

luminous quasars (Martini 2004). Under the Eddington-limited accretion (maximal accretion), BH mass can grow exponentially as $\sim \exp(t/\tau_S)$, where τ_s is the Salpeter time, $\tau_S = 4.5\times10^7(\epsilon/0.1)$ years. If the quasar lifetime is $< 10^7$ years, this is less than Salpeter time, and it cannot account for the growth of SMBHs to $M_{\rm BH} \sim 10^9 M_\odot$ from a seed BH with $M_{\rm BH} < 10^6 M_\odot$. Hence, it has been suggested that SMBHs underwent an extended growth period, including a red quasar phase that can last more than a few $\times10^8$ years (Kelly et al. 2010).

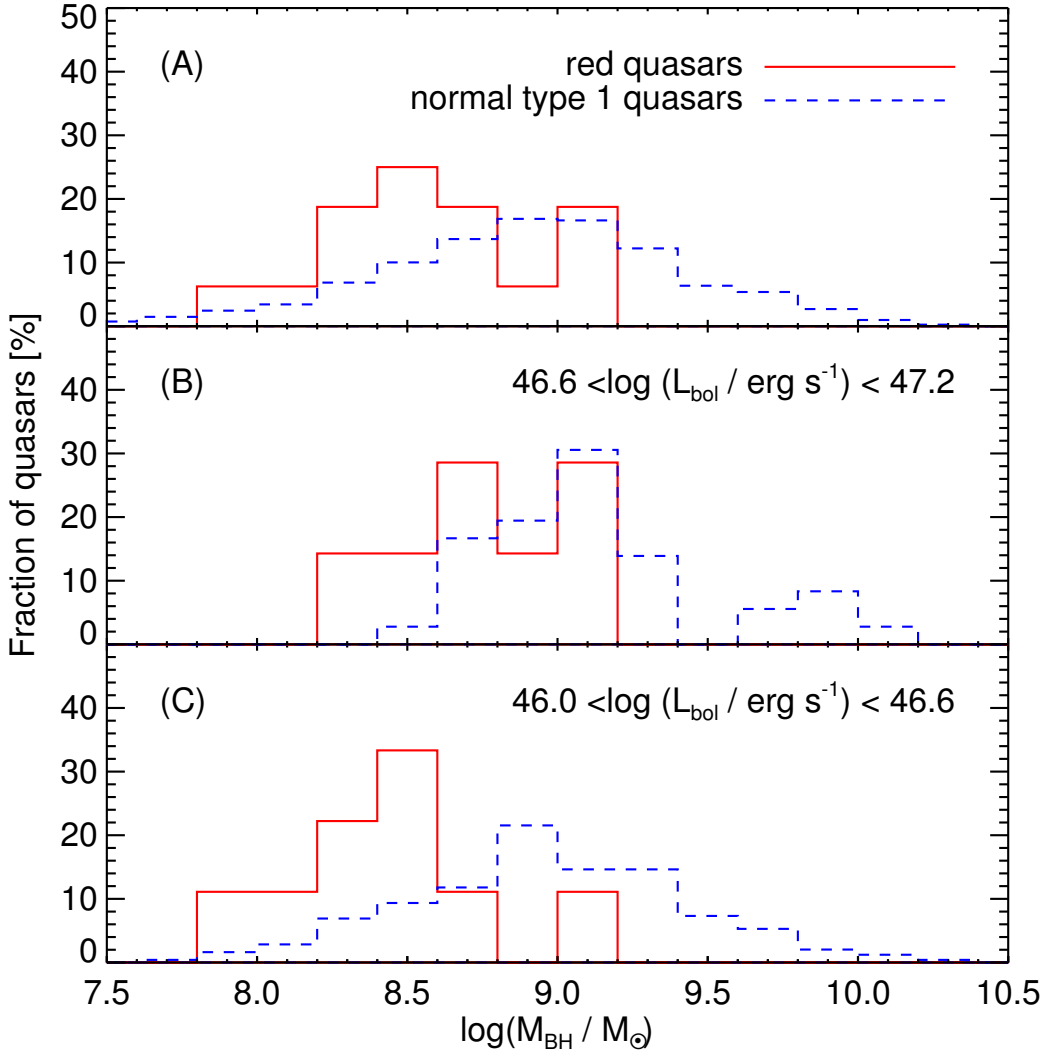

Figure 5.8 (A): $M_{\rm BH}$ distributions of red quasars and normal type 1 quasars. The red solid and the blue dashed histograms represent red quasars and normal type 1 quasars, respectively. (B): $M_{\rm BH}$ distributions for high-luminosity quasars ($10^{46.6} < L_{\rm bol}/{\rm erg\ s^{-1}} < 10^{47.2}$). (C): $M_{\rm BH}$ distributions for low-luminosity quasars ($10^{46.0} < L_{\rm bol}/{\rm erg\ s^{-1}} < 10^{46.6}$).

We can see if such a growth makes sense by estimating the red quasar duration time from the accretion rate and $M_{\rm BH}$ of our red quasar sample. Since the Eddington ratios are roughly 1 for red quasars, we can propose that the BH mass grows exponentially as $\sim \exp(t/\tau)$ and use the characteristic time τ as a rough estimate of the duration of the red quasar phase. Here, $\dot{M}$ is derived using the relations of $L_{\rm bol} = \epsilon \dot{M} c^2$ (assuming $\epsilon = 0.1$), and $\tau = M_{\rm BH}/\dot{M}$.

The derived $\dot{M}$ and τ values are listed in Table 2, and we find that τ values range from 10^7 to 2×10^8 years, or $\sim 7 \times 10^7$ years on average. We see from Figure 8 that the average BH mass of normal type 1 quasars is a few times larger than that of red quasars. To grow the BH mass this much during the red quasar phase, we need only one to two Salpeter time, which supports the use of τ values as estimates of the duration of the red quasar phase.

Our estimate of the red quasar duration time is $\sim$10 times larger than the value presented in Glikman et al. (2012). The estimate in Glikman et al. (2012) relies on the fraction of red quasars to normal type 1 quasars ($\sim 20\%$) and assumes a duration time of 10^7 years for normal type 1 quasars. The difference can be reconciled if we adopt a duration time of $\sim 10^8$ years for normal type 1 quasars as found in Kelly et al. (2010) and Cao (2010). Since the Eddington ratios of normal type 1 quasars are $\times$5 times lower than those of red quasars, the growth rate of BH masses in normal type 1 quasars is much lower than red quasars and the long duration time does not lead to the over-growth of BH mass. Alternatively, we can reconcile the two results if $\epsilon \ll 0.1$ during the red quasar phase.

5.6 SUMMARY

We estimated the Eddington ratios of 16 red quasars at $z \sim 0.7$ ($0.56 < z < 0.84$) using the Pβ line to minimize the extinction due to dust in red quasars. We compared the distribution of the Eddington ratios of the red quasars to those of normal type

Table 5.3. Spectrum of 0911+0143

λ (Å)	f_λ (erg s^{-1} cm^{-2} Å^{-1})	f_λ Uncertainty (erg s^{-1} cm^{-2} Å^{-1})
9381	-3.388E-17	2.237E-17
9384	-7.517E-15	1.877E-17
9387	2.428E-17	2.087E-17
9389	2.050E-17	2.272E-17
9392	1.747E-17	1.711E-17
9395	-7.548E-19	2.203E-17
9398	2.973E-17	1.968E-17
9400	5.394E-17	1.918E-17
9403	3.614E-17	2.249E-17

Note. — This table displays only a part of the spectrum of 0911+0143. The entire spectra of five red quasars are available as a tar file in the electronic version of the Journal.

1 quasars. For the Eddington ratios of normal quasars, 410 normal type 1 quasars at $z \sim 0.7$ in the SDSS DR7 quasar catalog were used. We show that the Eddington ratios of red quasars are significantly higher than those of normal type 1 quasars by a factor of 4.3. Furthermore, for a give Eddington ratio, the average $M_{\rm BH}$ of red quasars is smaller than that of normal type 1 quasars. In other words, red quasars are more active and rapidly growing BHs than normal type 1 quasars, which agrees with the scenario that red quasars are in an intermediate stage between merger-driven star-forming phase and a visible normal quasar phase.

References

Abazajian, K. N., Adelman-McCarthy, J. K., Agüeros, M. A., et al. 2009, ApJS, 182, 543

Anderson, S. F., Voges, W., Margon, B., et al. 2003, AJ, 126, 2209

Assef, R. J., Stern, D., Kochanek, C. S., et al. 2013, ApJ, 772, 2

Bahcall, J. N., Kirhakos, S., Saxe, D. H., & Schneider, D. P. 1997, ApJ, 479, 642

Banerji, M., McMahon, R. G., Hewett, P. C., et al. 2012, MNRAS, 427, 2275

Becker, R. H., White, R. L., & Helfand, D. J. 1995, ApJ, 450, 559

Becker, R. H., White, R. L., Gregg, M. D., et al. 2001, ApJS, 135, 227

Benn, C. R., Vigotti, M., Carballo, R., Gonzalez-Serrano, J. I., & Sánchez, S. F. 1998, MNRAS, 295, 451

Bongiorno, A., Maiolino, R., Brusa, M., et al. 2014, MNRAS, 443, 2077

Brotherton, M. S., Tran, H. D., Becker, R. H., et al. 2001, ApJ, 546, 775

Brusa, M., Civano, F., Comastri, A., et al. 2010, ApJ, 716, 348

Canalizo, G., Wold, M., Hiner, K. D., et al. 2012, ApJ, 760, 38

Cao, X. 2010, ApJ, 725, 388

Cardelli, J. A., Clayton, G. C., & Mathis, J. S. 1989, ApJ, 345, 245

Croom, S. M., Smith, R. J., Boyle, B. J., et al. 2004, MNRAS, 349, 1397

Cushing, M. C., Vacca, W. D., & Rayner, J. T. 2004, PASP, 116, 362

Cutri, R. M., Nelson, B. O., Kirkpatrick, J. D., Huchra, J. P., & Smith, P. S. 2001, The New Era of Wide Field Astronomy, 232, 78

Cutri, R. M., Nelson, B. O., Francis, P. J., & Smith, P. S. 2002, IAU Colloq. 184: AGN Surveys, 284, 127

Fitzpatrick, E. L. 1999, PASP, 111, 63

Fynbo, J. P. U., Krogager, J.-K., Venemans, B., et al. 2013, ApJS, 204, 6

Georgakakis, A., Clements, D. L., Bendo, G., et al. 2009, MNRAS, 394, 533

Georgakakis, A., Grossi, M., Afonso, J., & Hopkins, A. M. 2012, MNRAS, 421, 2223

Glikman, E., Helfand, D. J., & White, R. L. 2006, ApJ, 640, 579

Glikman, E., Helfand, D. J., White, R. L., et al. 2007, ApJ, 667, 673

Glikman, E., Urrutia, T., Lacy, M., et al. 2012, ApJ, 757, 51

Glikman, E., Urrutia, T., Lacy, M., et al. 2013, ApJ, 778, 127

Glikman, E., Simmons, B., Mailly, M., et al. 2015, arXiv:1504.02111

Grazian, A., Cristiani, S., D'Odorico, V., Omizzolo, A., & Pizzella, A. 2000, AJ, 119, 2540

Greene, J. E., & Ho, L. C. 2005, ApJ, 630, 122

Hong, J., Im, M., Kim, M., & Ho, L. C. 2015, ApJ, 804, 34

Hopkins, P. F., Hernquist, L., Cox, T. J., et al. 2005, ApJ, 630, 705

Hopkins, P. F., Hernquist, L., Cox, T. J., et al. 2006, ApJS, 163, 1

Hopkins, P. F., Hernquist, L., Cox, T. J., & Kereš, D. 2008, ApJS, 175, 356

Im, M., Griffiths, R. E., & Ratnatunga, K. U. 1997, ApJ, 475, 457

Im, M., Lee, I., Cho, Y., et al. 2007, ApJ, 664, 64

Jun, H. D., Im, M., Lee, H. M., et al. 2015, arXiv:1504.00058

Kaspi, S., Smith, P. S., Netzer, H., et al. 2000, ApJ, 533, 631

Kelly, B. C., Vestergaard, M., Fan, X., et al. 2010, ApJ, 719, 1315

Kim, D., Im, M., & Kim, M. 2010, ApJ, 724, 386

Kim, D., Im, M., Kim, J. H., et al. 2015, ApJS, 216, 17

Lacy, M., Petric, A. O., Sajina, A., et al. 2007, AJ, 133, 186

Lacy, M., Ridgway, S. E., Gates, E. L., et al. 2013, ApJS, 208, 24

Landt, H., Ward, M. J., Peterson, B. M., et al. 2013, MNRAS, 432, 113

Lawrence, A., Warren, S. J., Almaini, O., et al. 2007, MNRAS, 379, 1599

Lee, I., Im, M., Kim, M., et al. 2008, ApJS, 175, 116

Lonsdale, C. J., Smith, H. E., Rowan-Robinson, M., et al. 2003, PASP, 115, 897

Markwardt, C. B. 2009, Astronomical Data Analysis Software and Systems XVIII, 411, 251

Martini, P. 2004, Coevolution of Black Holes and Galaxies, 169

McLure, R. J., & Dunlop, J. S. 2004, MNRAS, 352, 1390

Menci, N., Cavaliere, A., Fontana, A., et al. 2004, ApJ, 604, 12

Norman, C., Hasinger, G., Giacconi, R., et al. 2002, ApJ, 571, 218

Puchnarewicz, E. M., & Mason, K. O. 1998, MNRAS, 293, 243

Rayner, J. T., Toomey, D. W., Onaka, P. M., et al. 2003, PASP, 115, 362

Risaliti, G., & Elvis, M. 2005, ApJ, 629, L17

Rose, M. 2014, American Astronomical Society Meeting Abstracts #223, 223, #321.03

Rothberg, B., Fischer, J., Rodrigues, M., & Sanders, D. B. 2013, ApJ, 767, 72

Ruiz, A., Della Ceca, R., Caccianiga, A., Severgnini, P., & Carrera, F. 2014, The X-ray Universe 2014, 314

Sanders, D. B., Soifer, B. T., Elias, J. H., et al. 1988, ApJ, 325, 74

Sanders, D. B., & Mirabel, I. F. 1996, ARA&A, 34, 749

Schneider, D. P., Hall, P. B., Richards, G. T., et al. 2005, AJ, 130, 367

Schneider, D. P., Richards, G. T., Hall, P. B., et al. 2010, AJ, 139, 2360

Shen, Y., Richards, G. T., Strauss, M. A., et al. 2011, ApJS, 194, 45

Skrutskie, M. F., Cutri, R. M., Stiening, R., et al. 2006, AJ, 131, 1163

Stern, D., Assef, R. J., Benford, D. J., et al. 2012, ApJ, 753, 30

Urrutia, T., Lacy, M., & Becker, R. H. 2008, ApJ, 674, 80

Urrutia, T., Becker, R. H., White, R. L., et al. 2009, ApJ, 698, 1095

Urrutia, T., Lacy, M., Spoon, H., et al. 2012, ApJ, 757, 125

Vacca, W. D., Cushing, M. C., & Rayner, J. T. 2003, PASP, 115, 389

Véron-Cetty, M.-P., & Véron, P. 2006, A&A, 455, 773

Vestergaard, M. 2002, ApJ, 571, 733

Webster, R. L., Francis, P. J., Petersont, B. A., Drinkwater, M. J., & Masci, F. J. 1995, Nature, 375, 469

Whiting, M. T., Webster, R. L., & Francis, P. J. 2001, MNRAS, 323, 718

Wilkes, B. J., Schmidt, G. D., Cutri, R. M., et al. 2002, ApJ, 564, L65

Woo, J.-H., Yoon, Y., Park, S., Park, D., & Kim, S. C. 2015, ApJ, 801, 38

Wright, E. L., Eisenhardt, P. R. M., Mainzer, A. K., et al. 2010, AJ, 140, 1868

Young, M., Elvis, M., & Risaliti, G. 2009, ApJS, 183, 17

Chapter 6

Conclusion

Dusty red AGNs are thought to be the intermediate stage galaxies, filling the evolutionary sequence between ULIRGs and unobscured type 1 AGNs, which is key in understanding the merger-driven galaxy evolution. However, this scenario has been subject to controversy, since the intrinsic properties of dusty red AGNs have not been studied much yet due to their dust extinction effects.

In this thesis, we perform four research projects for unveiling intrinsic properties of dusty red AGNs. First, we derive the Brackett-line-based $M_{\rm BH}$ estimators (Chapter 2). For this project, we observe 83 local ($0.002 < z < 0.48$) and bright ($K_s < 14$ mag) type 1 AGNs by using IRC on board *AKARI* to obtain 2.5–5.0 μm MIR spectra. These spectra contain Brβ (2.63 μm), Brα (4.05 μm), and PAH (3.3 μm) emission lines, and we derive the Brackett-line-based BH mass estimators using the widths and fluxes of the Brackett lines. Moreover, these spectra include the information of the dust torus. We measure the covering factors and temperatures of the dust torus by adding photometric data of SDSS, 2MASS, *WISE*, and *ISO* to the *AKARI* spectra.

Second, we study a methodology to select dusty red AGNs (Chapter 3). We observe 16 2MASS-selected red AGNs at $z \sim 0.3$ with several telescopes of Keck, Gem-

ini, Magellan, IRTF, and Subaru for obtaining the high S/N (> 100) and medium (~ 2000) optical and NIR spectra. Using these spectra, we measure the $E(B-V)$ values in two ways, based on the line ratios and continuum slopes, and a significant red AGNs are found not to be dusty red AGNs ($E(B-V) > 0.1$). We suppose that optical-NIR color is essential to find dusty red AGNs.

Third, we show that the red colors of red AGNs come from the dust extinction (Chapter 4). Usually red AGNs are believed to have the red colors due to the dust and gas in their host galaxies, but alternative explanations also exist for the red colors: i) an intrinsically red continuum slopes; ii) an unusual high covering factors of the hot dust; and iii) a moderate viewing angle between type 1 and type 2 AGNs. In order to investigate the origin of the red colors, we use optical and NIR spectra of 20 red AGNs at $z \sim 0.3$ and 0.7, and they were selected by the optical-NIR colors with radio detection. Using the spectra, we measure the line ratios from Hβ to Pα line. These line ratios of red AGNs are found to be $\sim$10 times higher than those of unobscured type 1 AGNs. Moreover, by comparing the theoretically expected line ratios of AGNs from `CLOUDY` code, $\sim$55% of the line ratios of red AGNs cannot be explained without adopting the concept of the dust extinction.

Fourth, we compare the BH accretion rates of red AGNs and unobscured type 1 AGNs (Chapter 5). In the merger-driven galaxy evolution scenario, red AGNs are expected to have higher BH accretion rates than unobscured type 1 AGNs, but the BH accretion rates of red AGNs have not been studied much yet due to the dust extinction. In this project, we measure the BH accretion rates using Pβ (1.28 μm) line that has an advantage to alleviate the dust extinction effects than other $M_{\rm BH}$ estimators in UV or optical wavelength range, C IV, Mg II, Hβ, and Hα. We observe 16 red AGNs at $z \sim 0.7$ with SpeX on NASA IRTF to obtain their fluxes and FWHMs of the Pβ line. The measured mean Eddington ratios of red AGNs is ~ 0.69 that is significantly higher than those of unobscured type 1 AGNs by a factor

of ~ 4. This result agrees with the merger-driven galaxy evolution scenario.

To summarize, through these thesis projects, we demonstrate red AGNs are the intermediate stage galaxies between merger-driven star-forming galaxies and unobscured type 1 AGNs, as expected in the merger-driven galaxy evolution scenario, based on two investigations for the origin of the red colors and the BH accretion rates of red AGNs. Moreover, we also provide Brackett-line-based BH mass estimators that will be very useful for extremely dust obscured system. After the Space Infrared Telescope for Cosmology and Astrophysics (SPICA) and James Webb Space Telescope (*JWST*) are launched, we believe the Brackett lines will be detected easily and used as the BH mass estimator broadly. Furthermore, we provide a hint that dusty red AGNs should be selected by optical-NIR colors, which will be useful for follow-up studies.

From these studies, we show that red AGNs are young AGNs due to that red AGNs have (i) more rapidly growing BHs than unobscured type 1 AGNs and (ii) the red colors by the dust extinction. This result implies that we can understand how galaxies evolve using these young AGNs by studying several projects. For example, first, co-evolution of BHs and host galaxies. The BHs are considered to play an important role in galaxy evolution by a feedback mechanism. The rapidly growing BHs in red AGNs would be the perfect testbed to understand the co-evolution of BHs and host galaxies. Second, dust torus evolution. The unification model expects that the BH is surrounded by a dust torus. Although the dust torus geometries (e.g., height, width, and size) are believed to be affected by the BH activity, the geometric evolution has not been studied much yet. From this project, the colors of young AGNs can be expected, and the population of young AGNs can be studied correctly.

초 록

은하들은 병합을 통해 성장한다고 예측된다. 이 모델에 따르면, 병합된 은하는 별 생성 은하로 성장한다. 이후에 일반적인 활동성 은하핵으로 진화하며, 그 중간 과정에서 붉은 활동성 은하핵이 나타날 것이라고 생각된다. 은하 병합 과정에서 미처 정리되지 못한 모 은하의 먼지들이 성간 소광을 통해 붉은 활동성 은하핵의 붉은 색을 만들어 내는 것이라 생각되나, 관측 적으로 이 사실이 명확히 밝혀지진 않았다. 이러한 가설들이 맞는지 알아보기 위해 붉은 활동성 은하핵의 블랙홀 활동성 연구가 필수적이나, 성간 소광의 영향으로 블랙홀 질량과 활동성이 아직 정확히 측정되지 않았다. 그리고, 현재까지 붉은 활동성 은하핵을 분류하는데 여러가지 방법이 있었지만, 어떤 방법이 붉은 활동성 은하핵을 분류하는 정확한 방법인지는 아직 제대로 연구되지 않았다.

본 학위논문에서는 붉은 활동성 은하핵의 숨겨진 특성을 알아내기위해 크게 세 가지 주제로 연구를 진행했다. 첫째, 블랙홀 질량 측정법을 새롭게 정립하는 것, 둘째, 붉은 활동성 은하핵 분류법에 대한 고찰, 그리고 셋째, 붉은 활동성 은하핵의 특성들을 조사해보고, 이 결과가 병합을 통한 은하 성장 예측 모델과 잘 맞아떨어지는 지를 비교해 보는 것이다.

하나씩 자세히 설명하면, 첫째로, 적외선을 이용해 블랙홀 질량 측정법을 정립했다. 현재까지는 먼지의 영향을 많이 받는 자외선 혹은 가시광선을 이용해 블랙홀 질량을 측정해 왔으나, 성간 소광이 많이 일어나리라 생각되는 붉은 활동성 은하핵을 연구하기에는 부적합한 방법이었다. 하지만, 적외선은 성간 소광의 영향을 거의 받지 않기에, 붉은 활동성 은하핵의 블랙홀 질량을 측정하기에 매우 유용하다. 이 연구는 아카리 우주 망원경으로 촬영한 일반적인 활동성 은하핵의 적외선 분광 자료를 이용해 진행되었고, 이 결과, 0.20~0.36dex의 정밀도를 가지고 있는 브라켓 라인을 기반으로 한 블랙홀 질량 측정법을 새로 정립할 수 있었다. 뿐만 아니라, 이러한 적외선 분광 데이터를

이용해 여러가지 연구를 더 진행했다. 발머/파셴/브라켓 라인의 밝기 비율을 통해 활동성 은하핵의 물리적 환경이 어떨지 예측해 보았고, 여러 종류의 측광 데이터들을 함께 이용해 활동성 은하핵의 먼지 띠 온도도 측정해 보았다. 측정된 먼지 띠의 온도는 ~1100K 였으며, 이는 기존에 측정된 값 (~1500K)에 비하면 다소 낮은 온도였다.

둘째, 붉은 활동성 은하핵의 분류법에 대해 연구해 보았다. 붉은 활동성 은하핵을 분류하기 위해서는 근적외선 색을 이용하는 방법과 가시광-근적외선의 색을 이용하는 두가지 방법이 있다. 어떠한 방법을 통해 붉은 활동성 은하핵을 분류하는 것이 좋은지에 대해 연구하기 위해, 근적외선 색 ($J-K > 2$) 과 가시광-근적외선 색 ($r' -K > 4$ 그리고 $J-K > 1.3$)으로 분류된 두가지 천체들을 연구해 보았다. 각각의 대상들에 대해 성간 소광이 얼마나 일어났는지를 알 수 있는 $E(B-V)$값들을 구해 보았고, 근적외선 색으로 분류된 대상들에 비해 가시광-근적외선 색을 통해 분류한 대상들의 $E(B-V)$가 훨씬 크게 측정되었음을 알 수 있었다.

셋째, 붉은 활동성 은하핵의 특성들이 병합을 통한 은하 성장 모델과 잘 맞아 떨어지는지를 확인해 보았다. 이 연구는 가시광-근적외선 색을 통해 분류된 붉은 활동성 은하핵을 근적외선 분광 관측한 자료를 기반으로 진행되었다. 근적외선으로 측정한 붉은 활동성 은하핵의 블랙홀 활동성이 (Edd ratio ~0.69) 일반적인 활동성 은하핵의 그것에 비해 약 4배 가량 컸음을 보여주었다. 뿐만 아니라, 붉은 활동성 은하핵의 발머-파셴 선의 밝기 비율을 조사해본 결과, 이들의 붉은 빛이 성간 소광 현상의 결과로 나타났음을 알 수 있었다. 위 결과들은 병합을 통한 은하 성장 모델과 완벽히 부합함을 알 수 있었다.

결론적으로, 본 학위논문을 통해 적외선 블랙홀 질량 측정법을 정립할 수 있었고, 이를 이용해 붉은 활동성 은하핵의 블랙홀 질량과 활동성을 정확하게 측정했다. 그리고 근적외선의 색보다는 가시광-근적외선의 색을 이용하는 것이 붉은 활동성 은하핵을 분류하는데 효과적임을 보여주었다. 뿐만 아니라, 붉은 활동성 은하핵의 특성들은 은하 병합을

통한 은하 성장 모델에서 예측했던 어린 활동성 은하핵의 특성과 잘 부합하며, 이는 붉은 활동성 은하핵이 은하 병합으로 촉발된 은하 성장의 한 과정에 해당하는 은하임을 보여주는 중요한 결과이다.

주요어: 은하: 진화 - 활동성 은하핵: 방출선 - 활동성 은하핵: 일반 - 활동성 은하핵: 초거대 질량 블랙홀 - 관측: 분광
학 번: 2011-30126